



UNIVERSITÉ DE LIÈGE  
FACULTÉ DES SCIENCES  
DÉPARTEMENT DE PHYSIQUE  
UNITÉ DE RECHERCHE CESAM – IPNAS

# Weak localisation in the transport of interacting Bose–Einstein condensates across random media

Renaud Chrétien

**Supervisor:** Prof. Peter Schlagheck

**Jury:** Prof. N. D. Nguyen, Université de Liège (President)  
Prof. T. Bastin, Université de Liège (Secretary)  
Prof. A. Buchleitner, Universität Freiburg, Germany  
Prof. N. Cherroret, Université P. et M. Curie, France  
Prof. J. Martin, Université de Liège

A thesis submitted in partial fulfilment of the requirements  
for the degree of Doctor of Philosophy in Sciences  
ACADEMIC YEAR 2020–2021

Copyright ©2021 Renaud Chrétien, Université de Liège – Faculté des Sciences, Place du 20 août, 7, B-4000 Liège, Belgium

Tous droits réservés. Aucune partie de ce document ne peut être reproduite sous forme d'imprimé, photocopie ou par n'importe quels autres moyens, sans l'autorisation écrite de l'auteur ou du promoteur.

All Rights Reserved. No part of this publication may be reproduced in any form by print, photo print or any other means without permission in writing from the author or the supervisor.

# Abstract

Quantum simulation with ultracold atoms gained a lot of traction recently by proposing a framework with a lot of flexibility, versatility and tunability to emulate diverse quantum effects. It indeed provides the ideal playground to study many-body effects in a well-controlled environment and is particularly useful in the domain of quantum coherent transport of waves in random media. The purpose of this thesis is to study several configurations of coherent transport within random media with Bose-Einstein condensates and to investigate the interplay between coherence and interaction effects. In particular, we start by numerically studying Aharonov-Bohm oscillations in the transmission of particles across the eponymous rings in a 1D configuration. When exposed to a suitably chosen disorder potential, those rings yield oscillations with double frequency, which are routinely encountered in solid-state physics where they are referred to as Al'tshuler-Aronov-Spivak oscillations, similar in essence to coherent backscattering and weak localisation. We then study the behaviour of those oscillations in the presence of interaction within Aharonov-Bohm rings and find that in the mean-field regime, they are inverted for finite interaction. Truncated Wigner simulations are then carried out in the same scenario and indicate that the inversion should be observable for realistic atomic and experimental parameters with  $^{39}\text{K}$  atoms, although dephasing of the oscillations is observed at strong interaction owing to interaction-induced inelastic scattering. A first-order nonlinear diagrammatic theory is then presented and benchmarks our numerical findings. The question of the inversion prevalence is then investigated in a 2D scenario, following state-of-the-art observations in the literature. It has indeed been numerically observed that coherent backscattering is inverted in the mean-field approximation for finite interaction strength. We numerically confirm this observation with our study and extend it beyond the mean-field approximation by applying the truncated Wigner method. These simulations show that the inversion prevails beyond the mean-field regime and should moreover be observable experimentally with  $^{87}\text{Rb}$  atoms for realistic parameters, despite a partial dephasing. This dephasing however completely eclipses interference effects and washes out this signature of antilocalisation for stronger interaction.



# Résumé

La simulation quantique avec des atomes ultrafroids connaît ces dernières années un franc succès notamment en raison de l'écosystème qu'elle propose. Dans ce contexte, il est ainsi possible d'étudier et de simuler divers effets quantiques avec un degré de flexibilité, de polyvalence et d'ajustabilité impressionnant. En effet, la simulation quantique fournit le cadre idéal pour étudier des effets quantiques à  $N$  corps dans un environnement bien contrôlé et est particulièrement indiquée pour étudier des problèmes de transport cohérent d'ondes de matière dans des milieux aléatoires. L'objet de cette thèse de doctorat est d'investiguer plusieurs scénarios s'inscrivant dans cette thématique à l'aide de condensats de Bose–Einstein et d'examiner la compétition entre les effets d'interférence et d'interaction. En particulier, nous commençons par nous intéresser aux oscillations, dites d'Aharonov–Bohm, de la transmission de particules au travers des anneaux portant le même nom, à une dimension. En présence d'un désordre adéquat au sein de tels anneaux, ces oscillations laissent place à des oscillations d'une fréquence double, connues comme oscillations d'Al'tshuler–Aronov–Spivak, dans la transmission moyennée de particules. Ces oscillations, fréquemment rencontrées en physique de l'état solide, ont un mécanisme sous-jacent très similaire à celui de la localisation faible ou encore de la rétrodiffusion cohérente. Ensuite, nous examinons le comportement de telles oscillations en présence d'interaction au sein d'anneaux d'Aharonov–Bohm et montrons une inversion de ces oscillations dans l'approximation à champ moyen. Des simulations truncated Wigner réalisées dans le même contexte indiquent que l'inversion devrait être observable expérimentalement pour des atomes de  $^{39}\text{K}$  avec un jeu de paramètres réalistes, malgré que la diffusion inélastique ne mène à un déphasage des effets d'interférence pour une interaction plus intense. Nous présentons ensuite une théorie diagrammatique nonlinéaire du premier ordre qui confirme ces observations. La prévalence de cette inversion est enfin examinée dans un scénario à deux dimensions, conformément à la littérature qui indique une inversion de la rétrodiffusion cohérente. Nous confirmons ce résultat dans l'approximation à champ moyen et étendons les simulations dans un contexte plus général au moyen de la méthode "truncated Wigner". Cette méthode indique que l'inversion prévaut au-delà du régime à champ moyen et devrait être observable expérimentalement avec des atomes de  $^{87}\text{Rb}$ , malgré la présence d'un déphasage partiel. À plus forte interaction, ce dernier éclipse d'ailleurs complètement la signature d'antilocalisation observée.



# Acknowledgments

My journey as a PhD student is about to end and what an adventure it was! At the conclusion of this journey and although it is not in my nature to be demonstrative, I better realise that some people were/are/shall be very important to me and I would like to thank them hereby.

I first would like to express my deep gratitude to my advisor Prof. Peter Schlagheck for many reasons. The most obvious one is for having given me the opportunity to carry out a PhD thesis under your guidance. I consider myself as very lucky to have benefited from your profound knowledge of physics and mathematics, but also from the wide freedom and flexibility of work you encouraged within the group. Despite your busy schedule, you have always found some time for helping me by answering my numerous questions. I also thank you for the proofreading of this manuscript and your criticisms. It was a real honour to be your PhD student.

My thanks also go to Prof. Andreas Buchleitner, Prof. Nicolas Cherroret, Prof. Ngoc Duy Nguyen, Prof. John Martin and Prof. Thierry Bastin who kindly accepted to constitute my jury of thesis. I wish you a reading as pleasant as possible.

The next person I would like to thank is Dr. Julien Dujardin, who most kindly welcomed me in the group when I was a young graduate student. Entering the research world is kind of intimidating, but you introduced me smoothly to the domain of ultracold atoms and I really enjoyed the working atmosphere with Cyril around Aharonov–Bohm rings. I also would like to thank you for proofreading this manuscript, so many years after your defence. . .

By the way, I also thank Dr. Cyril Petitjean for the precious help he provided me regarding Aharonov–Bohm rings and also for his friendliness and good mood.

I now would like to thank Dr. Josef Rammensee from the university of Regensburg. Your help regarding the diagrammatic theory around Al'tshuler–Aronov–Spivak oscillations was very precious. I have been very impressed by your mastery of diagrammatic techniques and express you my gratitude for having worked with us on this challenging topic. I hope Chapter 6 honours your work as it should.

My thanks go now to my office mates, Emeline, Antoine and Lionel. It was a real pleasure to have so kind and friendly colleagues at my sides and also, to meet the woman of my life. I enjoyed all the discussions we had regarding various topics such as video games, tennis, sports in general, politics, “why LaTeX or inkscape is still bugging again?” and . . . about

physics of course! Such a nice working atmosphere is rare and I'm glad I was involved in.

My next thanks go to the other PhD students in the building. First of all, to Guillaume with whom I had to pleasure to teach the programming lessons. It was a pleasure to work with you and I'm glad we were so often on the same wavelength. I also appreciated all the discussions we had regarding our mutual passion for physics. I want to thank Elodie for her kindness and her permanent good mood. It is always a pleasure to hear someone knocking at the door and to discover that you has simply come to ask how it is going. I also want to thank Céline for all the discussions we had that often ranged beyond physics and that were always pleasant. I also would like to thank Pierre and Florence with whom it is also always a pleasure to discuss. I also want to thank Thomas for his friendship, for the regular lifts from office back to home and for his careful proofreading of this manuscript. Your meticulous work has contributed to enhance the quality of this document. I am very grateful for that and intend to return the favour in proper time. My only regret is that we did not have more time to spend, and maybe to collaborate, together. I would like to thank Dr. Quirin Hummel who worked as a postdoc. I would have appreciated to have more regular conversations with you in German, but unfortunately, the epidemic decided otherwise.

Finally, I have to thank my family. My parents, first, who have encouraged and stimulated my eager to learn from the very early childhood and have put me in the best conditions to carry out my studies. Last, but not least, I want to thank Emeline simply for who she is. I am very glad to have met you at the office. My life has changed since then and I enjoy every second spent on your side. You have indirectly contributed a lot to this thesis, but also and above all, you have made me a happy man.

Computational resources have been provided by the Consortium des Équipements de Calcul Intensif (CÉCI, see <http://www.cec-hpc.be/>), funded by the Fonds de la Recherche Scientifique de Belgique (F.R.S.-FNRS) under Grant No. 2.5020.11 and by the Walloon Region.



# Contents

|  |            |
|--|------------|
| <b>Abstract</b>  | <b>iii</b> |
| <b>Résumé</b>  | <b>v</b>   |
| <b>Acknowledgments</b>   | <b>vii</b> |
| <b>Introduction</b>  | <b>1</b>   |
| <b>1 Wave propagation in disordered media</b>  | <b>9</b>   |
| 1.1 Absorption and scattering of light . . . . .                                     | 10         |
| 1.1.1 Wave absorption by the medium . . . . .  | 10         |
| 1.1.2 Scattering by the medium and the different transport regimes . . . . .         | 10         |
| 1.2 Multiple scattering of coherent waves in disordered media . . . . .              | 13         |
| 1.2.1 Incoherent transport . . . . .   | 16         |
| 1.3 Interference-induced enhancement of the return probability . . . . .             | 20         |
| 1.3.1 Phase coherence length . . . . .   | 20         |
| 1.3.2 Paths pairings that are robust to disorder averaging . . . . .                 | 21         |
| 1.3.3 Weak localisation . . . . .  | 23         |
| 1.3.4 Coherent backscattering . . . . .  | 25         |
| 1.3.5 Nonlinear weak localisation and coherent backscattering . . . . .              | 27         |
| 1.4 Anderson localisation . . . . .  | 28         |
| 1.4.1 Coherent forward scattering as an indicator of Anderson localisation . . . . . | 31         |
| <b>2 Bose–Einstein condensates: a source of coherent matter waves</b>                | <b>35</b>  |
| 2.1 From Maxwell–Boltzmann to Bose–Einstein distribution . . . . .                   | 35         |
| 2.2 Bose–Einstein condensation of an ideal gas in a harmonic trap . . . . .          | 37         |
| 2.3 Quantum scattering theory and atom–atom interaction . . . . .                    | 42         |
| 2.3.1 Quantum scattering theory for a dilute gas at low temperature . . . . .        | 42         |
| 2.3.2 Low energy scattering in the far–field limit . . . . .                         | 45         |
| 2.3.3 Tuning the effective interaction by leveraging Feshbach resonances . . . . .   | 48         |
| 2.4 Mean–field description of Bose–Einstein condensates . . . . .                    | 49         |
| 2.5 Atom lasers . . . . .  | 52         |
| 2.5.1 Theoretical description of an atom laser . . . . .                             | 54         |
| 2.6 Quantum transport with atom lasers in open systems . . . . .                     | 57         |
| 2.6.1 Transparent boundary conditions . . . . .                                      | 57         |
| 2.6.2 Smooth exterior complex scaling . . . . .                                      | 60         |

|          |  |            |
|----------|--|------------|
| 2.6.3    | Application to atom lasers . . . . .   | 62         |
| <b>3</b> | <b>Description of many-body effects beyond the mean-field regime</b>           | <b>65</b>  |
| 3.1      | Phase-space formulation of classical mechanics . . . . .                       | 66         |
| 3.2      | Phase-space formulation of quantum mechanics . . . . .                         | 67         |
| 3.2.1    | Properties of the Wigner function . . . . .                                    | 70         |
| 3.2.2    | Gallery of Wigner functions . . . . .  | 71         |
| 3.2.3    | Time evolution of the Wigner function and operator correspondences .           | 75         |
| 3.2.4    | Truncated Wigner method . . . . .  | 77         |
| 3.3      | Truncated Wigner method applied to open quantum systems . . . . .              | 79         |
| 3.3.1    | Sampling of the initial quantum state . . . . .                                | 79         |
| 3.3.2    | Evolution equation . . . . .   | 80         |
| 3.3.3    | Computation of observables . . . . .   | 81         |
| 3.3.4    | Validity of the truncated Wigner method . . . . .                              | 83         |
| <b>4</b> | <b>Transport of Bose-Einstein condensate through Aharonov-Bohm rings</b>       | <b>85</b>  |
| 4.1      | Aharonov-Bohm effect . . . . .   | 85         |
| 4.1.1    | Aharonov-Bohm Gedankenexperiment . . . . .                                     | 87         |
| 4.1.2    | Aharonov-Bohm effect in condensed-matter physics . . . . .                     | 89         |
| 4.2      | Description of the scattering region and Aharonov-Bohm rings . . . . .         | 90         |
| 4.2.1    | Description of the scattering region . . . . .                                 | 91         |
| 4.3      | Mean-field equations of the system . . . . .                                   | 94         |
| 4.4      | Reflection and transmission across an Aharonov-Bohm ring . . . . .             | 94         |
| 4.5      | Aharonov-Bohm oscillations in the transmission . . . . .                       | 98         |
| 4.5.1    | Interaction effects . . . . .  | 99         |
| <b>5</b> | <b>AAS oscillations of interacting bosonic matter wave beams</b>               | <b>105</b> |
| 5.1      | From Webb to Sharvin-Sharvin experiment . . . . .                              | 105        |
| 5.2      | Theory of Al'tshuler-Aronov-Spivak oscillations . . . . .                      | 108        |
| 5.2.1    | Formulation of the scattering problem in terms of Green's functions .          | 109        |
| 5.2.2    | Green's function of a 1D infinite lattice . . . . .                            | 111        |
| 5.2.3    | Green's function of the ring . . . . .   | 111        |
| 5.2.4    | Theory of Al'tshuler-Aronov-Spivak oscillations . . . . .                      | 116        |
| 5.3      | From Aharonov-Bohm to Al'tshuler-Aronov-Spivak oscillations . . . . .          | 121        |
| 5.4      | Inversion of AAS oscillations . . . . .  | 124        |
| 5.4.1    | Al'tshuler-Aronov-Spivak oscillations beyond the mean-field regime .           | 125        |
| 5.4.2    | Experimental observability of the AAS oscillations inversion . . . . .         | 128        |
| <b>6</b> | <b>Diagrammatic theory for AAS oscillations in the presence of interaction</b> | <b>131</b> |
| 6.1      | Fundamental building blocks of the diagrammatic theory . . . . .               | 132        |
| 6.2      | Resummation of diagrams in the noninteracting case . . . . .                   | 133        |
| 6.2.1    | Diagrams related to effective reflection and transmission at a junction        | 133        |
| 6.2.2    | Families of diagrams that join the junctions . . . . .                         | 136        |
| 6.2.3    | Family of diagrams connecting the ring to the leads . . . . .                  | 138        |
| 6.2.4    | Total reflection and transmission amplitudes in the noninteracting case        | 140        |
| 6.3      | Resummation of diagrams in the interacting case . . . . .                      | 142        |
| 6.3.1    | First-order correction to the reflection and transmission amplitudes .         | 147        |

|          |  |            |
|----------|--|------------|
| 6.3.2    | Ensemble average of the reflection and transmission probabilities . . .      | 149        |
| 6.4      | Confrontation of the diagrammatic theory to the numerical results . . . . .  | 150        |
| <b>7</b> | <b>Inversion of CBS with interacting ultracold bosons: a tW approach</b>     | <b>155</b> |
| 7.1      | Description of the scattering geometry . . . . .                             | 156        |
| 7.2      | Numerical discretisation procedure . . . . .                                 | 159        |
| 7.3      | Coherent backscattering peak . . . . .                                       | 163        |
| 7.4      | Angular resolved current . . . . .   | 166        |
| 7.5      | Inversion of coherent backscattering beyond the mean-field regime . . . . .  | 170        |
|          | <b>Conclusion</b>  | <b>177</b> |
| <b>A</b> | <b>Numerical integration routine</b>   | <b>183</b> |
| A.1      | Taylor’s method for numerical integration . . . . .                          | 183        |
| A.2      | Numerical routine for integrating the 1D field equations . . . . .           | 185        |
| A.3      | Numerical routine for integrating the 1D field equations (tW method) . . . . | 187        |
| A.4      | Numerical routine for integrating the 2D field equations . . . . .           | 191        |
| A.5      | Numerical routine for integrating the 2D field equations (tW method) . . . . | 192        |
| <b>B</b> | <b>Introduction to Green’s functions</b>                                     | <b>197</b> |
| B.1      | Green’s function of an ordinary differential equation . . . . .              | 197        |
| B.1.1    | Green’s function of the classical harmonic oscillator . . . . .              | 199        |
| B.2      | Green’s function of a partial differential equation . . . . .                | 201        |
| B.2.1    | Green’s function of the Schrödinger equation . . . . .                       | 201        |
| B.3      | Perturbative series for the full Green’s function . . . . .                  | 203        |
| <b>C</b> | <b>Analytical expression for the quantum noise</b>                           | <b>205</b> |
| C.1      | Propagation on a semi-infinite lattice . . . . .                             | 205        |
| C.2      | Quantum noise in two dimensions . . . . .                                    | 206        |
| <b>D</b> | <b>Derivation of the motion equation for the truncated Wigner method</b>     | <b>211</b> |
| <b>E</b> | <b>Overview of the numerical integration package</b>                         | <b>213</b> |
| E.1      | Data preparation layer . . . . .   | 214        |
| E.2      | Propagation layer . . . . .  | 215        |
| E.3      | Postprocessing layer . . . . .   | 216        |
|          | <b>List of publications</b>  | <b>217</b> |
|          | <b>Bibliography</b>  | <b>219</b> |



# Introduction

Until the very end of the 19<sup>th</sup> century, the description of nature essentially rested on two classical theories supposed to explain all observed phenomena. On the one hand, in combination with the Lorentz's expression of the electromagnetic force acting on a charged particle, Maxwell's equations describe wave propagation of electromagnetic waves. They provide the suitable framework to study the electromagnetic component of the surrounding world. On the other hand, Newton's equations for motion describe the time evolution of a set of particles, provided that the proper initial conditions are known. With these two sets of equations (although their resolution can be tedious), physics was perceived as a nearly mature and fully-mastered science [1], since solving those equations is a problem rather algebraic than physical. It was actually believed at that epoch that new significant discoveries were exceedingly remote and that the next progress in physics would only consist in more precise estimations of some fundamental constants [2].

However, some phenomena observed by researchers were unexplainable in terms of classical mechanics: the blackbody radiation, the Compton effect, the stability of the atom, the photoelectric effect or the Stern and Gerlach experiment, to mention some famous examples. For instance, this latter experiment only finds an explanation by introducing a quantity that does not have any classical analogy: the intrinsic spin angular momentum. The photoelectric effect was explained in 1905 by Einstein who assumed that light is composed of small energy packets (later called photons) and that energy exchanges are discrete, as was postulated earlier by Planck. It gave rise to the famous Planck–Einstein relation that describes electromagnetic waves with a particle model, thereby introducing the wave–particle duality of light, that led to a certain confusion in the conception of light, and paving the way for quantum mechanics.

Louis De Broglie extended in 1924 the wave–particle duality to matter, indicating that to every massive particle is associated a wave of wavelength  $\lambda_{dB} = h/p$ , where  $h$  is the Planck constant and  $p$  the momentum of the particle. This hypothesis, quickly confirmed experimentally by the diffraction of electrons by Davisson and Germer, constitutes the foundation of quantum mechanics. This new branch of physics describes a particle by a complex-valued function  $\psi(\mathbf{r}, t)$  called the wavefunction. Its physical meaning is revealed by its square modulus which provides the probability density of finding the particle at the position  $\mathbf{r}$  and the time  $t$  [3]. Therefore, the knowledge of  $\psi(\mathbf{r}, t)$  supplies all the possible information about the particle. Knowing the initial state  $\psi(\mathbf{r}, t_0)$ , the state of the particle at time  $t$  is provided by

the Schrödinger equation

$$i\hbar\frac{\partial}{\partial t}\psi(\mathbf{r}, t) = -\frac{\hbar^2}{2m}\Delta\psi(\mathbf{r}, t) + V(\mathbf{r}, t)\psi(\mathbf{r}, t),$$

with  $m$  the mass of the particle and  $V(\mathbf{r}, t)$  an external potential.

The advent of quantum mechanics allowed physicists to make tremendous progress in the understanding of nature, from the very fundamental level with a fully-fledged description of the atom, to a more applied level with the explanation of the laser process or the transistor-based electronics. It has also provided a suitable framework to study light-matter interaction, which has been since then a very active field of research. Light and matter have always been closely related in our conception of nature. From the foundations of quantum mechanics to the advent of the laser, it played a crucial role both from the theoretical and applied points of view. For instance, one of the lowest temperatures ever measured in the universe results from the fine control of this interaction. As we shall address in this manuscript, it has allowed one to reach Bose-Einstein condensation, a very peculiar state of matter that shall be of central relevance in this manuscript.

This new state of matter, as it is sometimes called, is obtained thanks to sophisticated techniques that bring the temperature of an atomic vapour very close to the absolute zero. At those temperatures, particles actually exhibit a very different behaviour, as is illustrated with a gas made of  $N$  indistinguishable particles. This system is described by a wavefunction  $\psi(\mathbf{r}_1\sigma_1, \dots, \mathbf{r}_N\sigma_N)$  with  $|\psi(\mathbf{r}_1\sigma_1, \dots, \mathbf{r}_N\sigma_N)|^2$  giving the probability density to find the particle  $i$  with the spin  $\sigma_i$  at the position  $\mathbf{r}_i$ , with  $i = 1, 2, \dots, N$ . As a result of the symmetrisation postulate [3], any observable related to such a system of  $N$  indistinguishable quantum particles should be left unchanged after permutation of two particles. The wavefunction of the system should also be left unchanged after two permutations of the same pair of particles. This implies that the many-body wavefunction describing the system is either entirely symmetric or entirely antisymmetric under particles permutation. The symmetric or antisymmetric feature of the many-body wavefunction is dependent on the integer or half-integer feature of the particle intrinsic spin. As a result of the spin-statistics theorem [4], particles with half-integer spin are referred to as fermions whilst those with integer spin are referred to as bosons. They obey the following statistical distribution

$$n_i = \frac{g_i}{\exp\left(\frac{E_i - \mu}{k_B T}\right) \pm 1}, \quad (1)$$

where the positive sign stands for the Fermi-Dirac statistics (for fermions) and the negative sign stands for the Bose-Einstein statistics (for bosons). Those statistical distributions provide the average number  $n_i$  of particles of energy  $E_i$  (with degeneracy  $g_i$ ) at thermal equilibrium for a system at the temperature  $T$  and the chemical potential  $\mu$ . Both of which are well approximated by the Maxwell-Boltzmann distribution for high temperatures so that the effect of the specific statistics is only significant at low temperatures. This feature is however absolutely remarkable, as we discuss below for bosons.

Indeed, based on the seminal work of Bose [5], Einstein predicted theoretically [6, 7] in 1925 that for a bosonic gas at temperatures very close from the absolute zero, a large fraction of

---

the particles occupy the ground state of the many-body system and populate it macroscopically, forming a giant matter wave called a Bose–Einstein condensate. The first experimental observation of Bose–Einstein condensation in 1995, with  $^{87}\text{Rb}$  atoms by Cornell and Wieman [8] at Boulder and with  $^{23}\text{Na}$  atoms by Ketterle [9] at MIT, confirmed this prediction and paved the way for a very rich and new physics. This scientific feat was rewarded by the Nobel prize in physics in 1997.

Since its experimental realisation, Bose–Einstein condensation has gained traction, both from the theoretical and experimental point of views. It indeed opens a new dimension in the area of precision measurements [10–13], provides a useful tool in quantum information [14–16], allows to address various questions related to many-body physics [17] and opens new prospects in many other domains.

There are actually lots of possible applications in the context of precision measurements. Bose–Einstein condensates can be for instance used in accelerometers or gravimeters to improve their precision. They can also be used to improve the most accurate setup for measuring time: atomic fountains [11]. In this regard, the NASA Cold Atom Laboratory [18] very recently obtained a Bose–Einstein condensate in the International Space Station [19]. This realisation is an astonishing tour de force: it was realised in a hostile environment within a setup that has the dimension of a mini-fridge, controlled remotely from the Earth and allowed to achieve colder temperatures compared to Earth-bound facilities. This realisation is a major milestone, opening new prospects in terms of the definition of the time unit and the related practical applications, such as the establishment of the international atomic time, tests of General Relativity, guiding per satellite, synchronisation of telecommunication networks, to mention a few examples.

At a more fundamental level, quantum information may also benefit from the use of Bose–Einstein condensates. They are proposed by some research teams to be used as a communication channel between the many cores of a quantum computer. This approach would allow to reduce the number of bits required for a computer and thereby to address decoherence, which is a major problem faced in the realisation of a such a device and that increases with the number of bits [20–26].

Another most prominent research area related to Bose–Einstein condensation (and more generally to ultracold gases) is quantum simulation of many-body phenomena that generally arise in condensed-matter systems [27]. Ultracold atoms provide an unprecedented degree of flexibility, tunability and control [28] that allows one to purely focus on many-body phenomena by getting rid of undesirable side effects, such as those induced by impurities or dislocations of the lattice-like structure or electrons–phonons coupling, that are common, for example in the field of condensed matter physics. Some new prospects towards a novel range of phenomena related to condensed matter physics and otherwise unattainable are then rendered possible, as well as to address issues that nowadays remain open.

It is for instance possible to create an optical lattice, in analogy with a tight-binding model, by forming a standing wave obtained by properly interfering counterpropagating lasers. It thus creates a potential landscape made of spatially periodic minima in which particles can

be trapped. Those trapped particles can move from one site to another through quantum tunnelling, thereby providing a setup very similar to electrons moving in a conductor sample. The power of quantum simulation is revealed when one wants to study the effects of changing parameters of the system. Whereas ultracold atoms allow very easily to, for example, modify the on-site atomic density or to tune the lattice spacing, a variation of one of those parameters in a solid-state system would require the creation of a new sample with the desired properties. Ultracold atoms allow to tune the atom-atom interaction from attractive to repulsive or from short to long range by leveraging the Feshbach tuning [29]. They also make possible to engineer more complicated geometries and to envisage various scattering and disorder potentials or to create artificial gauge fields [30, 31] that act on neutral atoms as a magnetic field would on electrons.

Ultracold atoms thus provide a formidable toolbox to study complex situations originating from solid-state physics such as effects related to mesoscopic quantum transport, giving rise to an emerging subfield of atomic physics: atomtronics [32–35], the ultimate goal of which being to realise logical devices and operations with ultracold atoms (see Ref. [36] for a roadmap of this intriguing and exciting field of research). An example of the atomtronic equivalent of a simple electronic circuit, consisting in a wire connected to a power input, is provided in FIG. 1, where the role of the battery poles is played by two reservoirs at the chemical potentials  $\mu_L$  and  $\mu_R$  and that of the resistor is played by an optical lattice. A chemical potential bias induces a current from the higher to the lower chemical potential reservoir, as particles are injected in the optical lattice and tunnel from one site to a neighbour site in a situation totally analogous to the quantum transport of current carriers in a metallic sample.

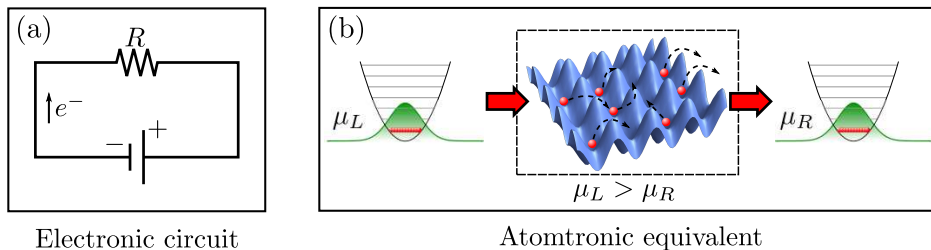


Figure 1 – Panel (a): a simple electronic circuit. Panel (b): atomtronic equivalent consisting in two reservoirs, maintained at the chemical potentials  $\mu_L$  and  $\mu_R$ , that are connected to an optical lattice. As a result of a chemical potential bias between the reservoirs, a net atomic current that follows this bias is induced. This kind of atomtronic setup provides a very flexible and tunable model to study mesoscopic electronic transport.

As FIG. 1 illustrates in a simple situation, atomtronics provides a framework to study a wide variety of mesoscopic phenomena. Those are of particular relevance not only at the fundamental level but also at the applied level. The increase of processors speed indeed faces nowadays the limit of miniaturisation: at several nanometers (silicon atomic radius is about 0.21 nm), quantum effects related to the transport of electrons become more and more significant [37]. Below those scales, as the size of such structures becomes comparable with the electronic wavelength, further miniaturisation of logical electronic devices such as transistors,



---

which are the building blocks of microprocessors, demands a fully-fledged understanding of mesoscopic transport of electrons [38, 39], upon which the working principle is based. In this context, the study of source-drain transport processes is of particular relevance because they represent a probe that can be used to explore coherence or interaction effects in various situations, such as quantum dots [40] or Aharonov-Bohm rings [41–44], to mention a few.

Several experiments have been successfully carried out by the group of Esslinger using fermionic  ${}^6\text{Li}$  atoms [45–48]. As a starting point of their source-drain transport experiments, they studied the ohmic conduction attributed to a narrow channel linking the two reservoirs. They then examined the advent of superfluidity in the latter scenario and showed how a bias in the chemical potential between the two reservoirs of atoms could be leveraged to create an atomic thermoelectric heat engine. They also observed a quantised conductance of the channel as is predicted by the Landauer-Büttiker formalism [38, 49] and as is experimentally observed with a two-dimensional electron gas through a quantum point contact [50].

These impressive experiments have demonstrated the power of atomtronics but also yield a lot of open questions related to interaction effects because they were realised with weakly interacting fermions. From the theoretical point of a view, addressing those effects demands a substantial effort and remains nowadays considerably unfathomed. As a matter of fact, such a study requires to be able to account for many-body correlation and quantum coherence within a complex geometry consisting of a finite scattering region in the presence of interaction joining two (possibly macroscopic) reservoirs without interaction, as Ref. [51] indicates.

Those coherence effects, and more specifically their interplay with the above-mentioned interaction effects, constitute a research field on their own and encompass a lot of intriguing phenomena and open questions. Indeed, as a result of quantum interferences, coherent waves crossing a weakly disordered region show a noteworthy increase of the related (macroscopic) reflection and a concomitant drop in the related transmission, which is known in mesoscopic physics as weak localisation [52, 53]. The same mechanism is also encountered with coherent light crossing a disordered sample made of point-like scatterers, where interferences are responsible for an increase of the backscattered current, which is referred to as coherent backscattering [54–56].

Coherent backscattering was also experimentally observed in 2012 with ultracold bosonic atoms propagating towards a 2D disorder potential [57, 58]. Investigating interaction effects, that are most naturally present within a Bose-Einstein condensate, is a complex task in this context. This was studied with a nonlinear diagrammatic theory of coherent backscattering [59]. This has also been numerically studied in the idealised scenario of a matter plane wave propagation obtained by an atom laser that emits bosonic atoms propagating towards a 2D disorder potential. The numerical integration of the mean-field equations arising in the mean-field approximation in a quasi-steady context yields an interaction-induced inversion of the coherent backscattering peak [60]. This peak inversion is also found for Bose-Einstein condensates that propagate towards irregularly shaped billiard geometries [61]. Many-body diagrammatic approaches indicate that this inversion only prevails in the mean-field regime of very weak interaction and that a dephasing should appear in a more realistic context of stronger interaction [62]. Questions related to the experimental observability of this effect

thus arise and we try to shed more light on this issue in this manuscript.

The in-depth study and understanding of the interplay between coherent and interaction effects in the context of quantum transport of ultracold bosonic particles is fundamental. It allows to (at least partially) answer some of the above fundamental and general many-body related questions, which is already most satisfactory as such. It is also essential for the design and implementation of atomtronic devices that encompass source-drain scenarios, where a coherent flow of atoms is produced between several reservoirs as a result of chemical potential bias, like for instance transistors or diodes whose working principle would lie on atom-atom interaction effects [32–35]. Any logical operation performed with such atomtronic devices would prevent heat generation and preserve quantum coherence, thereby paving the way for the design and realisation of quantum computing schemes, which are the holy Grail for many researchers (see the nice and recent review article about atomtronics [63]).

## Outline of the manuscript

The focus of this thesis is brought on the intriguing competition between coherent and interaction effects with matter waves obtained with Bose-Einstein condensates. We made an effort in proposing a pedagogical approach, without sacrificing the rigour, of the underlying concepts with the hope that this manuscript benefits to a great number of readers. We also note that the present work – more specifically the methodologies developed in Chapters 2 and 3 – is based on the work of Dr. Julien Dujardin who brought significant progress in the context of coherence and interaction effects with Bose-Einstein condensates [51]. In this context, our work exploits the framework built by Dr. Dujardin in a different, although similar, context.

In the *first chapter*, we introduce the physics related to the transport of coherent waves in random media. We start by the incoherent, classical, description of transport that neglects interference effects based on the assumption that they do not contribute to averaged transport observables. This approach, that portrays waves transport as a diffusive process, allows us to introduce fundamental transport lengths, such as the scattering mean free path or the transport mean free path. We then show how in certain scenarios, namely weak localisation and coherent backscattering, interference effects alter the classical diffusive picture. Anderson localisation and the underlying theories are then discussed as a spectacular suppression of diffusion solely owing to interference effects.

The *second chapter* is dedicated to an introduction to Bose-Einstein condensates that are a central thematic of this manuscript. The quantum scattering theory is then investigated in details as it allows us to model atom-atom interaction whose importance is here primordial. Those condensates are usually described in the mean-field approximation which is then adapted to model atom lasers that can be seen as a source of quasi monochromatic matter waves. We finally conclude the chapter by introducing the numerical mean-field discretisation of the equations governing atom lasers including how to implement smooth exterior complex scaling, a technique employed to model open systems.

---

In the *third chapter*, we introduce the truncated Wigner method that allows us to describe quantum transport beyond the mean-field approximation by mimicking quantum fluctuations that are not captured by this approximation. In particular, this supplies the proper framework to address the dephasing-related questions, as it models both elastic and inelastic scattering. We start by introducing phase-space techniques in the familiar context of classical mechanics. This appealing formulation is then extended to quantum mechanics, which introduces the Wigner function as an extension of the classical probability density related to the system state. The related motion equation is then particularised to atom lasers, as a foundation of subsequent studies using the truncated Wigner method. This chapter, as well as Chapter 2, is based on the work of Dr. Julien Dujardin [51].

The *fourth chapter* marks the starting point of the study of quantum transport across Aharonov-Bohm rings. The related Aharonov-Bohm effect is first introduced as a consequence of the gauge invariance of the Schrödinger equation. Aharonov-Bohm rings, that we model as a two-arms interferometer penetrated by an artificial gauge flux, are then discussed. The scattering region that we study is made of an Aharonov-Bohm ring connected to two semi-infinite matter wave guides, one of which being coupled to a reservoir, following the principle of atom lasers. Interaction effects are finally investigated on the transmission of atoms across the ring.

In the *fifth chapter*, we present Al'tshuler-Aronov-Spivak oscillations that occur in the ensemble averaged transmission across Aharonov-Bohm rings in the presence of a weak and smooth disorder. A semiclassical theory of Al'tshuler-Aronov-Spivak oscillations based on a formulation of the scattering problem in terms of Green's functions is derived and reveals the intimate connection between those oscillations, weak localisation and coherent backscattering. It also lays the foundations for the diagrammatic theory developed in Chapter 6. Numerical results related to the study of interaction effects on Al'tshuler-Aronov-Spivak oscillations are then presented first in the mean-field approximation and then by means of the truncated Wigner method. We conclude the chapter by examining the experimental observability for realistic atomic species.

In the *sixth chapter*, we expose the diagrammatic theory of Al'tshuler-Aronov-Spivak oscillations mainly developed by our collaborator, Dr. Josef Rammensee. Based on a Green's function formulation of the scattering problem, Dr. Rammensee derived a full resummation of scattering paths involved in the semiclassical noninteracting Green's function, instead of focussing only on the leading order terms. After that, the resummation technique is generalised to a perturbative expansion of the Green's function in terms of the interaction parameter, up to the first order. A comparison between the numerical and the diagrammatic results is then finally performed.

The *seventh and last chapter* is finally dedicated to a study of quantum transport of Bose-Einstein condensates in 2D disorder in the presence of atom-atom interaction. This work positions itself as a natural extension of the work initiated by Hartung [60] in the mean-field approximation. We first present the scattering region we study and how coherent backscattering emerges in the mean-field simulations both in the ensemble averaged momentum distribution and backscattered current. As expected from Ref. [60], an inversion of the coherent

backscattering peak is found in the presence of interaction. We then extend the description of this problem by using the truncated Wigner method that once again allows us to model inelastic scattering on top of elastic scattering. We conclude this chapter by examining the experimental observability of the peak inversion, regarding the presence of dephasing for finite interaction strengths.

# Chapter 1

## Wave propagation in disordered media

In this chapter, we begin by introducing absorption and scattering of waves that take place when a wave crosses a medium. We specifically focus on scattering, which is a central thematic of this manuscript, and whose different regimes may be primarily characterised by a fundamental quantity: the scattering mean free path. This quantity allows to identify three main regimes of transport. The first regime consists in a ballistic motion where the wave essentially propagates in the sample in straight line, without any scattering event. The second one is called the single scattering regime and consists in a single scattering event during the traversal of the sample. The third and most intricate is the regime of multiple scattering that typically occurs in random media. Such media, which are equivalently referred to as disordered media, can be colloquially described as media whose physical properties are random functions of both position and time, for instance owing to the presence of scatterers at random positions.

The physics emerging from the transport of coherent waves in such random media is very rich but also challenging to describe. As a starting point, we formalise the problem by a complex field, representing the wave, that obeys a Helmholtz equation. This applies in many transport situations, such as for instance to describe the transport of electrons within a solid or the transport of light in a cloud. The complex field that solves the wave equation has the physical picture of a summation over all possible scattering paths within the random medium and is leveraged to obtain observables. However, owing to the complexity of the propagation, such a deterministic description must be abandoned to the profit of a stochastic description of waves transport. This method consists in an ensemble averaging of the observables of relevance over several scattering configurations.

A first approach is to assume that interferences between scattering paths, that are for instance contained in the wave intensity, cancel each other and do not survive ensemble averaging. Based on that assumption, they are neglected to simplify the description. This boils down to a classical sum of intensities that results in a diffusive motion. We show that this diffusive motion finds applications for instance in deriving Ohm's law or describing heat transport in solids, but also completely fails in some contexts.

Indeed, the diffusion can be mitigated or even completely suppressed as a result of interference effects which are of primal importance in some contexts. Weak localisation and coherent backscattering that occur in the weak disorder limit are then discussed as an illustration of the importance of interference effects. We also discuss the strong disorder limit that is related to Anderson localisation and present the related theories. We finally briefly introduce coherent forward scattering, which is a higher order interference effect that is, in some contexts, a key indicator of Anderson localisation in the momentum space.

## 1.1 Absorption and scattering of light

When a wave propagates within a certain medium, two main phenomena generally enter into competition: absorption and scattering. They can both have significant effects and applications.

### 1.1.1 Wave absorption by the medium

We consider for simplicity the propagation of an incident beam of light. Provided the incident light traversing the medium possesses an energy compatible with a transition energy of the particles constituting the medium, a transition can occur. This transition may take the simple form of an electronic transition, where a photon from the incident beam is absorbed by an atom of the crossed medium, or a more complicated transition, for instance rotational, vibrational or both (Raman transition). The incident beam loses energy during such a transition and is globally attenuated because the exchanged energy is dissipated through either radiative or non-radiative processes. The global attenuation of the incident light beam is described by the Beer–Bouguer–Lambert law that provides the intensity as

$$I(x) = I_0 e^{-\kappa x}, \quad (1.1)$$

where  $x$  is the direction of propagation of the incident beam,  $I_0$  its initial intensity and  $\kappa$  the absorption coefficient that depends on the absorption cross-section and on the number of absorbers.

### 1.1.2 Scattering by the medium and the different transport regimes

Another mechanism for the attenuation of the incident light beam is scattering by the medium. In case of light transport, several mechanisms are responsible for scattering, depending on the size  $\sigma$  of the scatterer compared with the wavelength  $\lambda$  of the waves, as is illustrated in FIG. 1.1.

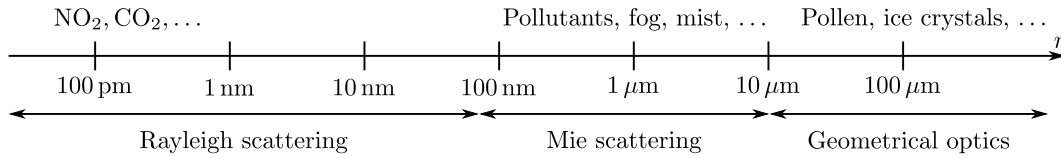


Figure 1.1 – Different scattering limits and the related models are considered, depending on the wavelength  $\lambda$  of the incident light and the characteristic dimension  $\sigma$  of the scatterer.

The first limit is obtained when the wavelength of the incident beam is much larger than the dimension of the scatterer,  $\lambda \gg \sigma$  which is described by Rayleigh scattering [64–67]. This model predicts a scattered intensity that scales as  $1/\lambda^4$  and is mostly isotropic. It results that Rayleigh scattering is very wavelength–selective, as for instance, a blue light of  $\lambda \approx 400$  nm yields a scattered intensity ten times larger than a red light of  $\lambda \approx 700$  nm. It provides an explanation for the blue colour of the sky at midday, as the blue component of the incident sun light is scattered much more than the red one. On the other hand, it also explains why the sky appears red by the end of the day, as every component of the incident light beam but the red one has been previously scattered.

If the size of the scatterer is of the same order of magnitude as the incident wavelength, namely  $\lambda \approx \sigma$ , scattering processes are best described by Mie theory [68]. Contrarily to Rayleigh scattering, Mie scattering is not as wavelength–selective but is strongly anisotropic as it favours forward scattering. This is the scattering process that produces the milky white light by misty and foggy days (or when a high concentration of pollutants is present), as the incident light is scattered by the large water droplets in suspension in the surrounding air.

When the wavelength of the incident wave is much smaller than the dimension of the scatterer, namely  $\lambda \ll \sigma$ , geometrical optics is applicable and the waves are treated in terms of rays. The subsequent reflection and refraction occurring at the interface separating two media of different refractive indices are described by means of Snell–Descartes laws for reflection and refraction. It provides for instance an explanation for halos, as sunlight or moonlight is refracted by ice crystals in cirrus clouds.

### Regimes of scattering

We now distinguish several scattering regimes and for that purpose, we introduce the elastic scattering mean free path  $l_s = 1/(\rho_s \sigma_s)$ , where  $\rho_s$  is the density of scatterers and  $\sigma_s$  the related scattering cross section<sup>1</sup>. The scattering mean free path is the average distance that separates two successive elastic scattering events. Depending on the ratio between  $l_s$  and the characteristic length  $L$  of the medium, three different scattering regimes emerge, as is sketched in Fig. 1.2.

<sup>1</sup>We note that strictly speaking, this expression for the scattering mean free path related to an incident wave of wavevector  $\mathbf{k}$  crossing a medium with a density of scatterers  $\rho_s$  is valid only in the weak disorder limit (or dilute regime) characterised by  $\rho_s/k^3 \ll 1$ . This regime is to be opposed to the strong disorder regime.

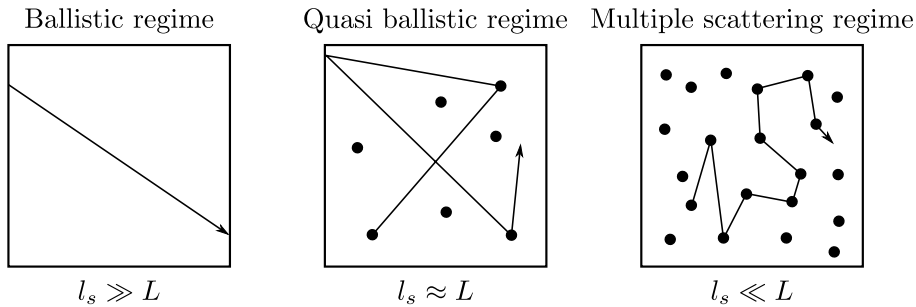


Figure 1.2 – Sketch of the possible waves transport regimes. If the elastic mean free path  $l_s$  is much larger than the sample size  $L$ , then the transport is ballistic. If they are comparable, then the transport is said quasi ballistic and propagating waves are essentially scattered once during their traversal of the sample. If the mean free path is much smaller than the sample size, the transport turns to the multiple scattering regime made of many scattering events.

### The ballistic regime $l_s/L \gg 1$

When the scattering mean free path is much larger than the characteristic length of the sample, the waves propagate as a projectile does. Such a motion typically occurs in very pure media where the scatterers density is small or for systems with low characteristic size. It is for instance achieved in ballistic point contacts [50, 69], in InSb mesoscopic structures [70], in InGaAs open quantum dots [71, 72], in carbon nanotubes [73, 74] or in graphene nanoribbons [75]. However, besides those very specific systems related to mesoscopic physics, such ballistic transport does not generally occur owing to the complexity of disordered media.

### The single scattering regime $l_s/L \approx 1$

When the scattering mean free path is comparable with the dimension of the system, waves are typically scattered once across their traversal of the medium. This scattering regime is in general not the most common one. It is however frequently encountered in optically thin media, because the photons exit the medium very quickly, without many scattering events. It can also occur in artificial situations, for instance in scattering experiments involving a single scattering centre.

Such a scattering regime yields a random direction for the scattered wave, as it strongly depends on the specific details of the collision which are not exactly known and might additionally evolve in time. This random feature is to be opposed to the following regime of scattering that, kind of counterintuitively, appears as more deterministic owing to the smoothing that results from the numerous scattering events that average this randomness out. This regime of multiple scattering, which we extensively discuss in the following, lies at the heart of our work.



**The multiple scattering regime  $l_s/L \ll 1$** 

In the third case where the scattering mean free path is much smaller than the size of the sample, the incident wave is likely to be scattered many times before exiting the medium. Such situations occur for instance in the radiative transfer, for X-rays that are scattered by a crystal, for acoustic waves propagating across porous media, or regarding the irregularities in the ionosphere that multiply scatter radio waves, to name a few examples.

From the point of view of the incident beam, such a medium is then qualified as random because of the multiple random scattering taking place during its traversal of the disordered sample, either because the position of the scatterers is not known or because they slightly move with time. More formally, those disordered media are described in terms of a quantity that displays pronounced spatial variations [76], such as the refraction index for the transport of light or the density of matter for acoustic waves. As a consequence, it is not very useful nor desirable to deterministically describe such transport problems in terms of a fixed configuration of the scatterers. A statistical approach describing the scattering in terms of an ensemble average over many different configurations of the scatterers is therefore more suitable.

A lot of very interesting phenomena occur in the context of coherent transport of waves through random media, which we understand as transport processes capable of giving rise to interference effects, owing to their sensitivity with respect to the phase of the wavefunction  $\psi(\mathbf{r})$ . In the context of solid-state physics for instance, those interference effects may have dramatic effects. Anderson showed in 1958 that interference can render a metallic conductor insulating due to a sufficiently strong disorder that localises waves, which is referred to as Anderson (or strong) localisation [77]. It has been later shown that Anderson localisation goes well beyond solid-state physics and is a universal effect of coherent waves propagating within a random medium.

**1.2 Multiple scattering of coherent waves in disordered media**

One very important and fundamental aspect of waves is their ability to exhibit interferences, as a result of an existing phase coherence relationship which is revealed when superposing the interfering waves. This ability is exacerbated in a random medium, which can be modelled as a collection of point scatterers at random positions. In the context of electronic transport within a solid, the role of the scatterers is played by the imperfections in the crystal lattice structure, such as vacancies, dislocations, or impurities. In the present context of the transport of light, scattering occurs owing to random changes in the refractive index of the medium, for instance because of the presence of fat molecules or proteins in a glass of milk or due to the presence of water droplets that scatter the light in a thick cloud. Waves propagating in such media are described by the complex field  $\psi(\mathbf{r}) \in \mathbb{C}$  which, as indicated in Ref. [78], obeys the wave equation

$$(\Delta + k^2)\psi(\mathbf{r}) = -k^2V(\mathbf{r})\psi(\mathbf{r}), \quad (1.2)$$

and where

$$V(\mathbf{r}) = V_0 \sum_{n=0}^N \delta(\mathbf{r} - \mathbf{r}_n), \quad (1.3)$$

accounts for the presence of a scattering potential made of identical isotropic scatterers at random positions. Equation (1.2) applies as well for describing electronic transport as for the transport of light. Indeed, under certain assumptions Eq. (1.2) is equivalent to the stationary Schrödinger equation<sup>2</sup> and to the Helmholtz equation for electromagnetic waves [78]. In the former case, the complex field  $\psi(\mathbf{r})$  is called the wavefunction whilst in the latter, it refers to the electric field. Relevant transport quantities such as the conductance of a disordered sample in the electronic context or such as the light intensity in the transport of light are related to the square modulus of  $\psi(\mathbf{r})$  which can be obtained by solving Eq. (1.2) for a particular disorder configuration. The formulation of the wave equation (1.2) stimulates to treat the right hand side as an inhomogeneity and to elaborate a solution by using the Green's function method<sup>3</sup>, which yields the formal solution

$$\psi(\mathbf{r}) = \psi_0 e^{i\mathbf{k}_i \cdot \mathbf{r}} - k^2 \int G_0(\mathbf{r}, \mathbf{r}') V(\mathbf{r}') \psi(\mathbf{r}') d^3 r', \quad (1.4)$$

which is a self-consistent equation known as the Lippmann–Schwinger equation, where  $\psi_0$  is the amplitude of the incident wave and  $\mathbf{k}_i$  is the related wavevector. The first term in the right hand side of Eq. (1.4) is the solution of  $(\Delta + k^2)\psi(\mathbf{r}) = 0$ , that is, Eq. (1.2) in the absence of scattering potential. This homogeneous wave equation describes in this case the propagation in free space. In the second term of the right hand side of Eq. (1.4), we have introduced  $G_0(\mathbf{r}, \mathbf{r}')$ , the Green's function obtained as the solution of

$$(\Delta + k^2)G_0(\mathbf{r}, \mathbf{r}') = \delta(\mathbf{r} - \mathbf{r}'), \quad (1.5)$$

which is an equation very similar to Eq. (1.2), with the right hand side corresponding to a point source at  $\mathbf{r} = \mathbf{r}'$  described by a delta distribution. This technique allows to convert the partial differential equation (1.2) into an integral equation (1.4), in principle easier to solve or at least, more prone to allow the use of approximation techniques. Indeed, the self-consistent shape of Eq. (1.4) motivates a solution obtained iteratively that can be written, assuming an incident plane wave, as

$$\begin{aligned} \psi(\mathbf{r}) = & \psi_0 e^{i\mathbf{k}_i \cdot \mathbf{r}} \\ & - k^2 \int G_0(\mathbf{r}, \mathbf{r}') V(\mathbf{r}') \psi_0 e^{i\mathbf{k}_i \cdot \mathbf{r}'} d^3 r' \\ & + k^4 \iint G_0(\mathbf{r}, \mathbf{r}') V(\mathbf{r}') G_0(\mathbf{r}', \mathbf{r}'') V(\mathbf{r}'') \psi_0 e^{i\mathbf{k}_i \cdot \mathbf{r}''} d^3 r' d^3 r'' \\ & - \dots, \end{aligned} \quad (1.6)$$

which is known as a Born series and which has a quite intuitive physical interpretation. The inspection of the Born series in Eq. (1.6) actually shows that the different terms appearing in the summation have a common structure. They consist in free propagations described by  $G_0(\mathbf{r}, \mathbf{r}')$  separated by scattering events described by the interaction with the scattering potential at a given position, as is sketched in FIG. 1.3. The integration over the dummy

---

<sup>2</sup>The equivalence is straightforwardly shown by defining  $k^2 \equiv 2m\omega/\hbar$  and  $V(\mathbf{r}) \equiv -\tilde{V}(\mathbf{r})/(\hbar\omega)$ . The resulting stationary Schrödinger equation describes a quantum particle of energy  $E = \hbar\omega$  that propagates towards the disorder potential  $\tilde{V}(\mathbf{r})$ , for instance an electron within a disordered metallic sample.

<sup>3</sup>This method is very commonly used in this manuscript. The reader can find a (hopefully) pedagogical introduction to this technique in Appendix B.

variables appearing in a specific term of Eq. (1.6) is then understood as an integration over all paths that end at position  $\mathbf{r}$  and implies the exact number of scattering events contained in this specific term. For instance, the last line of Eq. (1.6) describes all imaginable paths that consist in two scattering events of the incident wave and ends up at position  $\mathbf{r}$ . This term is represented by the third term in the first line of FIG. 1.3, where the integration appearing in Eq. (1.6) is implicitly understood in this diagram, so that this term contains all paths featuring two scattering events.

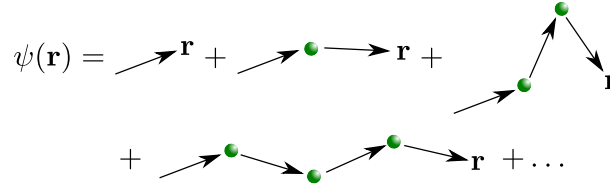


Figure 1.3 – Physical picture of the terms appearing in the Born series (1.6). The solution  $\psi(\mathbf{r})$  of the Lippmann–Schwinger equation (1.4) is written as a sum of many scattering paths consisting in free propagations interrupted by various scattering events. An implicit summation over the fixed scattering centres positions is understood for each diagram.

The physical picture portrayed in FIG. 1.3 incites to reformulate the solution (1.6) of Eq. (1.4) in a very intuitive form. The wave at position  $\mathbf{r}$  is then explicitly expressed as

$$\psi(\mathbf{r}) = \sum_{\gamma} \psi_{\gamma}, \quad (1.7)$$

that is, a summation of partial waves along all possible and imaginable scattering paths  $\gamma$  that end at position  $\mathbf{r}$ , irrespective of the number of scattering events they encompass. This writing is perfectly equivalent to Eq. (1.6) provided the sum over all paths  $\gamma$  is understood as the sum of all paths that end at position  $\mathbf{r}$  in every possible manner. The square modulus of  $\psi(\mathbf{r})$  written in the form (1.7) is given by the pictorial equation

$$|\psi(\mathbf{r})|^2 = \sum_{\gamma, \gamma'} \rightarrow \quad (1.8)$$

where the green circles represent the point scatterers, the blue line denotes a path  $\gamma$  and the red line the complex conjugate of the partial wavefunction along path  $\gamma'$ . The double sum appearing in Eq. (1.8) can be split into two contributions

$$|\psi(\mathbf{r})|^2 = \sum_{\gamma} |\psi_{\gamma}|^2 + \sum_{\gamma \neq \gamma'} \psi_{\gamma'}^* \psi_{\gamma}, \quad (1.9)$$

where the first term corresponds to the classical contribution, which pairs of paths are in the specialised literature referred to as Diffuson, whilst the second one encompasses contributions giving rise to interferences.

Eq. (1.9) provides an explicit solution to the Lippmann–Schwinger equation. This solution in terms of a particular disorder landscape provides a rather complicated structure which is a signature of the underlying specific scattering configuration. This solution is not particularly relevant in a transport experiment since the exact positions  $\mathbf{r}_1, \dots, \mathbf{r}_N$  of the scatterers are not precisely known and those scatterers can also be in motion. This highlights the need of a statistical approach to obtain average properties. Since the motion occurs on a timescale typically much larger than the duration of the experiment, the principle of the statistical approach is to determine  $\psi(\mathbf{r})$  for several static realisations of the disorder potential that differ from one another and to average over those disorder landscapes. This leads us to define the ensemble average of  $|\psi(\mathbf{r})|^2$ , which reads

$$\langle |\psi(\mathbf{r})|^2 \rangle = \int \dots \int |\psi(\mathbf{r})|^2 dr_1^3 \dots dr_N^3, \quad (1.10)$$

where the angled brackets  $\langle \cdot \rangle$  indicate the ensemble average, obtained by averaging over all scattering centres positions, which boils down to averaging over many static disorder configurations.

### 1.2.1 Incoherent transport

A first approach to determine  $\langle |\psi(\mathbf{r})|^2 \rangle$  is to simplify the expression for  $\psi(\mathbf{r})$  by neglecting the interference terms in Eq. (1.9), based on the assumption that the coherent contribution gets randomised from one disorder configuration to another, so that they cancel each other and finally yield a zero average contribution. In fact, the minimum phase difference between two different paths is of the order of  $kl_s$  and is obtained with two paths that are identical to each other, apart from one different scattering centre. As Ref. [76] indicates, in most situations<sup>4</sup>,  $kl_s \gg 2\pi$  and the overall phase difference therefore fluctuates from one disorder realisation to another by an amount much larger than  $2\pi$ . The overall phase of the second term in Eq. (1.9) is therefore treated as a random number uniformly distributed in  $[0, 2\pi[$  from which we expect no contribution in average.

This leaves us with  $|\psi(\mathbf{r})|^2$  defined as a sum of probabilities to follow each individual path ending at position  $\mathbf{r}$ . Such a classical pairing of paths is illustrated in FIG. 1.4. In this approximation, the phases acquired along  $\psi_\gamma$  and  $\psi_\gamma^*$  are identical and yield a vanishing phase difference between them.

---

<sup>4</sup>This is indeed the case for instance for light propagation within clouds where  $kl_s \sim 10^8$  but also for electronic transport within gold for which  $kl_s > 100$  [76].

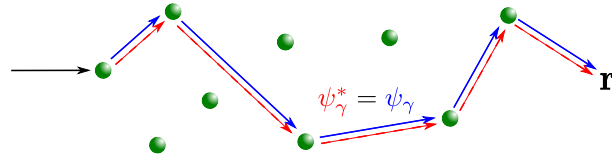


Figure 1.4 – Example of a classical pairing of paths, referred to as Diffuson, which further gives an interpretation of the transport of waves in terms of a random walk process where the total intensity at point  $\mathbf{r}$  is obtained by adding up the intensities of each individual path.

In this classical picture, the transport shall be later understood as a random walk process where the intensities of the involved paths are basically summed up. Despite its rather crude and peremptory assumption that interferences between paths do not contribute to ensemble averaged transport quantities, this approach knew some great success. It was for instance applied by Drude [79–81] for evaluating the conductance of a metallic sample or by Chandrasekhar in the radiative transfer [82]. It also spectacularly fails in some contexts, as we shall show later.

Putting aside those failures of the description of wave transport in random media in terms of a sum of classical intensities for the moment, we briefly develop this approach in order to introduce certain quantities relevant in a waves transport context and to provide a base-moment for the discussion of interference effects. In the weak disorder regime  $kl_s \gg 1$ , which corresponds to a situation where the distance that separates the scattering centres is large compared to the wavelength of the incoming wave, it is possible to provide an expression for the ensemble average of  $|\psi(\mathbf{r})|^2$ . In the following, we note  $I(\mathbf{r}) \equiv \langle |\psi(\mathbf{r})|^2 \rangle$  the intensity at point  $\mathbf{r}$  and  $I_0(\mathbf{r}) \equiv |\langle \psi_0(\mathbf{r}) \rangle|^2$  the incident intensity at the same position. In the case of isotropic point scatterers that we considered upon here,  $I(\mathbf{r})$  is given by

$$\begin{aligned} I(\mathbf{r}) &= I_0(\mathbf{r}) + \frac{4\pi}{l_s} \int |\langle G_0(\mathbf{r}, \mathbf{r}') \rangle|^2 I(\mathbf{r}') d^3 r' \\ &= I_0(\mathbf{r}) + \frac{1}{4\pi l_s} \int \frac{e^{-|\mathbf{r}-\mathbf{r}'|/l_s}}{|\mathbf{r}-\mathbf{r}'|^2} I(\mathbf{r}') d^3 r', \end{aligned} \quad (1.11)$$

which is referred to as the Bethe–Salpeter equation [83], that consists here in a sum of two contributions [78]. The first contribution is the square modulus of the ensemble averaged incident intensity that propagates towards  $\mathbf{r}$  without scattering. In the case of an incident plane wave  $\psi_0 = \exp(ikz)$  of wavevector  $\mathbf{k}$  propagating in the  $z$ -direction within a semi-infinite medium with boundary at  $z = 0$ , it is given by  $I_0(\mathbf{r}) = I_0 \exp(-z/l_s)$ . This expression recalls Beer–Bouguer–Lambert law that describes the global exponential attenuation of an incident wave by a factor related to the elastic scattering mean free path. It translates the depletion of the incident beam into the various scattered modes. The second contribution represents the scattered intensity  $I(\mathbf{r}')$  at position  $\mathbf{r}'$  that propagates towards position  $\mathbf{r}$ . This propagation is described by a factor related to the specific radiation pattern of the scatterers that weights the intensity. In the simple case of isotropic scattering that we consider here, this factor describes an isotropic spherical propagation of  $I(\mathbf{r}')$  towards position  $\mathbf{r}$ , but more sophisticated radiation patterns can be readily envisaged.

Since only the square modulus of  $\psi(\mathbf{r})$  enters Eq. (1.11), we qualify as incoherent the kind of transport processes described by this equation. We already highlighted that as such, this contribution is not affected by any dephasing mechanism. Under the assumption that it does not vary appreciably over the elastic scattering mean free path, the intensity  $I(\mathbf{r})$  can be expanded in Taylor series

$$I(\mathbf{r} + \mathbf{r}') = I(\mathbf{r}) + \mathbf{r}' \cdot \nabla I(\mathbf{r}) + \frac{1}{2!} (\mathbf{r}' \cdot \nabla)^2 I(\mathbf{r}) + \dots \quad (1.12)$$

and inserted into Eq. (1.11) with the substitution  $\mathbf{r}' \rightarrow \mathbf{r}' - \mathbf{r}$ . This readily yields the following stationary diffusion equation [78]

$$\frac{l_s^2}{3} \Delta I(\mathbf{r}) + I_0(\mathbf{r}) = 0 \quad (1.13)$$

for the ensemble averaged intensity, with a source term  $I_0(\mathbf{r}) = I_0 \exp(-z/l_s)$ .

Very similarly, it is possible to obtain a time-dependent version of Eq. (1.11) that may be used with time-varying sources [39] and which is given by

$$\frac{\partial}{\partial t} \langle I(\mathbf{r}, t) \rangle = D_B \Delta \langle I(\mathbf{r}, t) \rangle + J_0(\mathbf{r}, t), \quad (1.14)$$

where  $J_0(\mathbf{r}, t)$  is the flux density at position  $\mathbf{r}$  and time  $t$ . We have introduced the Boltzmann diffusion coefficient  $D_B = vl_B/d$ , with  $v$  the group velocity of the wave,  $d$  the space dimension and  $l_B$  the Boltzmann transport mean free path that shall be discussed in detail later. This Boltzmann diffusion coefficient characterises for instance how a wavepacket spreads in time in such a medium, as we have the linear relation  $(\Delta \mathbf{r})^2 = 2dD_B t$  which is typical for a diffusion process [84]. Eq. (1.14) essentially tells us that the average intensity for the wave under consideration undergoes a random walk [39]. This kind of equations finds applications in the description of heat conduction, in which context it is referred to as heat equation, or in the description of Brownian motion. In the context of electronic transport, this equation which emerges in the Drude model, predicts a linear relation between the current density and the electric field, with the Drude conductivity as proportionality coefficient. It thereby yields a microscopic picture for the well known Ohm's law [81, 85].

On top of the first length scale introduced earlier, namely the elastic scattering mean free path, the Boltzmann diffusion coefficient introduces a second length scale which is referred to as the Boltzmann transport mean free path and denoted by  $l_B$ . This new length scale is related to the elastic mean free path  $l_s$  through

$$\frac{l_s}{l_B} = 1 - \langle \cos \theta \rangle_f = 1 - \int_0^{2\pi} \cos \theta f(k, \theta) d\theta, \quad (1.15)$$

where  $\theta$  denotes the scattering angle,  $\langle \cdot \rangle_f$  is the average over the phase function  $f(k, \theta)$  that parametrises the radiation pattern by providing the scattering intensity in the direction indicated by  $\theta$ . This phase function encodes the potential anisotropy of the scatterers (or the scattering potential). For perfectly isotropic scattering, this function is equal to one and the cosine averages to zero, yielding  $l_B = l_s$ . For more correlated disorder potentials,  $l_s < l_B$  and forward scattering is enhanced. This provides an intuitive interpretation of the Boltzmann

transport mean free path. Indeed, after a scattering event, the direction and phase of the wave are modified. This Boltzmann transport mean free path is the length required for the wave to get randomised and forget about its initial direction. In the context of the random walk undergone by the average intensity, we therefore associate the Boltzmann transport mean free path with the average step of this random walk [86].

The anisotropy of the scattering depends on how the de Broglie wavelength  $\lambda_{\text{dB}} = 2\pi/k$  compares with the typical size  $\sigma$  of the scatterers, which in the context of a correlated continuous disorder is referred to as the correlation length of the disorder. As a general condition, we note that  $l_s \leq l_B$ , as we have already highlighted. In most situations, several scattering events are required to significantly bend the trajectory of the wave and deflect it from the initial direction, which implies that  $l_s \ll l_B$ . This is the case when  $k\sigma \gg 1$  and implies that forward scattering is clearly favoured compared to scattering in other directions of space. In that case, scattering occurs in a cone centred around the forward direction and whose aperture is  $2\theta$ , where  $\theta$  is the angle between the incident and the scattered direction. On the other hand, in very limited situations, a single scattering event can totally scramble the incident direction, which implies that  $l_s \lesssim l_B$ . This happens when the de Broglie wavelength is much larger than the typical size of the scatterers (or the correlation length for a continuous disorder potential), that is when  $k\sigma \ll 1$ . In such situations, scattering centres are perceived as point-like scatterers by the wave and scattering is almost perfectly isotropic (see FIG. 1.5 for a sketch of the two scattering regimes).

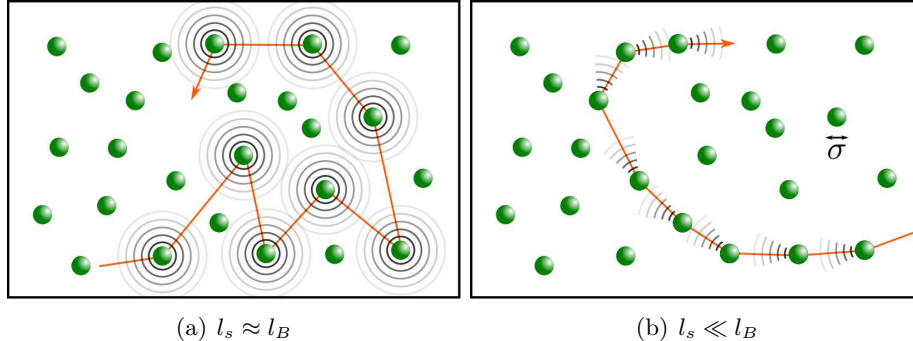


Figure 1.5 – Panel (a): When the de Broglie wavelength of the incident wave is much larger than the typical size  $\sigma$  of the scatterers, *i.e.*  $k\sigma \ll 1$ , scattering is almost isotropic, so that after a single scattering event, the direction of propagation gets totally randomised, leading to  $l_s \approx l_B$ . Panel (b): When  $k\sigma \gg 1$ , scattering is strongly anisotropic and forward scattering is favoured leading to  $l_s \ll l_B$ : several scattering events are required in order to scramble the initial direction and phase of the wave. Adapted from [87].

Related to the two mean free path scales, it is possible to introduce two time scales, namely the elastic scattering time  $\tau_s = l_s/v$  and the Boltzmann transport time  $\tau_B = l_B/v$ . They respectively represent the time separating two subsequent elastic scattering events and the time required for the initial direction of the wave to get randomised. Those two transport

quantities are related through [39]

$$\tau_B = \frac{\tau_s}{1 - \langle \cos \theta \rangle_f}. \quad (1.16)$$

Following the previous discussion, it is not surprising that  $\tau_s \leq \tau_B$ . Indeed, when  $k\sigma \ll 1$ , elastic scattering is isotropic and  $\langle \cos \theta \rangle_f \simeq 0$  because  $\theta$  is uniformly distributed in  $[0, 2\pi]$ . This implies that a single scattering event is likely to fully randomise the incoming direction and we have  $\tau_s \approx \tau_B$ . On the other hand, when  $k\sigma \gg 1$ , forward scattering is enhanced and  $\theta \simeq 0$ , which implies that  $\langle \cos \theta \rangle_f \simeq 1$  and  $\tau_s \ll \tau_B$ .

### 1.3 Interference-induced enhancement of the return probability

#### 1.3.1 Phase coherence length

In addition to the two length scales previously discussed, we now introduce the phase coherence length  $L_\phi$ . It can be defined as the length over which a phase coherence relation can be maintained, in the sense that over that distance, any existing phase relation between two waves gets destroyed owing to inelastic processes introducing irreversibility. It plays a crucial role as a threshold to the advent of coherent effects.

As we have indeed seen in the previous discussion, even with an assumption as crude as to neglect all interference terms when computing ensemble averages, it is possible to introduce several microscopic quantities relevant in a transport of waves context and to provide satisfactory descriptions of macroscopic phenomena based on those concepts. This works particularly well provided the system is at high temperature. In this case, the phase coherence length  $L_\phi$  is usually much smaller than the typical size  $L$  of the system, rendering the related interference effects negligible [88]. However, as we develop below, interference effects can play a major role in the context of transport within random media as soon as  $L \lesssim L_\phi$ .

When interference effects are involved, the notion of phase coherence between the interfering waves indeed emerges. Because elastic scattering by the disorder potential is not the only scattering mechanism in play in such a context, we note that phase coherence is fragile and subject to destruction in the presence of inelastic scattering or any other dephasing mechanism.

Such inelastic processes indeed modify the phase of the wave in a non deterministic manner because they randomly occur, consequently randomising the underlying phase. The loss of coherence is due to such inelastic processes which encompass all interaction processes between the coherent wave and its surrounding. For example, in the context of electronic transport, those scattering events can take the form of an interaction between the electron and an impurity that possesses internal degrees of freedom or an electron-phonon coupling between the electron and the phonon sea (which is strongly enhanced by the temperature) or, more simply, an electron-electron interaction through the Coulomb potential.

This highlights the crucial relevance of the phase coherence length, since it determines the length scale beyond which quantum interference effects are destroyed by the irreversibility



caused by inelastic scattering. Therefore, in the limit where  $L \lesssim L_\phi$ , the system is in a coherent regime governed by phase coherent effects, whilst in the limit where  $L \gg L_\phi$ , interference effects are largely destroyed and the system is in a classical incoherent regime for which we provide introductory details in the previous section. This regime is frequently encountered at high temperatures that favour irreversibility mechanisms (for instance, the coupling of electrons with phonons is significantly enhanced with  $T$ ), thereby reducing  $L_\phi$ .

We now describe in which context those coherence effects may play a role that can dramatically alter the classical transport picture. In Eq. (1.9), which we recall here for convenience,

$$|\psi(\mathbf{r})|^2 = \sum_{\gamma} |\psi_{\gamma}|^2 + \sum_{\gamma \neq \gamma'} |\psi_{\gamma'}^*| \cdot |\psi_{\gamma}| e^{i(\phi_{\gamma} - \phi_{\gamma'})}, \quad (1.17)$$

and where the second term is written in polar notation, the square modulus of  $\psi(\mathbf{r})$  is expressed as a sum of classical contributions, which we discussed in details in the previous section, and a second term. This term is expressed as a sum of interfering pairs of different paths. In the presence of dephasing mechanisms that yield a phase coherence length smaller than  $l_s$  and  $l_B$ , any initially existing phase relation between such paths cannot be maintained, not even between two successive scattering events. Consequently, interference effects play absolutely no role in this regime of dominant dephasing. In order to be able to observe interference effects, it is indeed necessary that the phase coherent length  $L_\phi$  be much larger than the elastic scattering mean free path, so that  $l_s, l_B \ll L_\phi$  in order for phase coherence to be preserved for multiple scattering events.

### 1.3.2 Paths pairings that are robust to disorder averaging

In the following, we implicitly assume that we work in a regime of large phase coherence length  $l_s, l_B \ll L_\phi$  and we examine the implications of interference effects on wave transport. In that case, interfering paths mostly display ordinary structures such as the two paths sketched in FIG. 1.6(a). The phase difference  $\phi_{\gamma} - \phi_{\gamma'}$  between those paths is a signature of the very specific scattering sequence they describe. Such contributions yield a complicated structure for the intensity  $I(\mathbf{r})$  that is therefore a signature of the specific disorder landscape. Because of their random nature, they do not survive the ensemble average, contrarily to very particular pairings, as we show by closely following the discussion in Refs. [87, 89].

To understand the emergence of pairings robust to ensemble averaging, we consider a plane wave of incident wavevector  $\mathbf{k}_i$  propagating in a disordered medium made of point scatterers. The complex amplitude related to an incident wave of wavevector  $\mathbf{k}_i$  diffracted into a wave pointing in the direction  $\mathbf{k}_f$  reads

$$A(\mathbf{k}_i, \mathbf{k}_f) = \sum_{\mathbf{r}_i, \mathbf{r}_f} f(\mathbf{r}_i, \mathbf{r}_f) e^{i(\mathbf{k}_i \cdot \mathbf{r}_i - \mathbf{k}_f \cdot \mathbf{r}_f)}, \quad (1.18)$$

where  $\mathbf{r}_i$  (resp.  $\mathbf{r}_f$ ) is the first (resp. last) encountered scatterer and

$$f(\mathbf{r}_i, \mathbf{r}_f) = \sum_{\Gamma} f_{\Gamma} e^{i\delta_{\Gamma}} \quad (1.19)$$

is the complex amplitude related to the propagation from  $\mathbf{r}_i$  to  $\mathbf{r}_f$ . This amplitude is expressed as a sum of the complex amplitudes  $f_{\Gamma} \exp(i\delta_{\Gamma})$  associated with each path  $\Gamma_{\mathbf{r}_i \rightarrow \mathbf{r}_f} \equiv \Gamma$

beginning at position  $\mathbf{r}_i$  and ending at position  $\mathbf{r}_f$ . Introducing the points  $\mathbf{r}'_i$  and  $\mathbf{r}'_f$ , the intensity of the scattered wave is yielded as

$$|A(\mathbf{k}_i, \mathbf{k}_f)|^2 = \sum_{\mathbf{r}_i, \mathbf{r}_f} \sum_{\mathbf{r}'_i, \mathbf{r}'_f} f^*(\mathbf{r}'_i, \mathbf{r}'_f) f(\mathbf{r}_i, \mathbf{r}_f) e^{i(\mathbf{k}_i \cdot \mathbf{r}_i - \mathbf{k}_f \cdot \mathbf{r}_f)} e^{-i(\mathbf{k}_i \cdot \mathbf{r}'_i - \mathbf{k}_f \cdot \mathbf{r}'_f)}. \quad (1.20)$$

The double summation encompasses a lot of contributions that are encoded in the pairings  $f^*(\mathbf{r}'_i, \mathbf{r}'_f) f(\mathbf{r}_i, \mathbf{r}_f)$ . Most of them average out for a large number of disorder configurations and bring no average contribution, but some of them are robust to ensemble averaging, as we highlight below. To stress this, we explicitly write

$$f^*(\mathbf{r}'_i, \mathbf{r}'_f) f(\mathbf{r}_i, \mathbf{r}_f) = \sum_{\Gamma} \sum_{\Gamma'} f_{\Gamma} f_{\Gamma'}^* e^{i(\delta_{\Gamma} - \delta_{\Gamma'})} \quad (1.21)$$

which reveals the phase difference  $\delta_{\Gamma} - \delta_{\Gamma'}$  between two paths  $\Gamma$  and  $\Gamma'$ . As we already discussed, this phase difference displays in general large fluctuations, at least of an amount  $kl_s$ , which is the minimum phase difference obtained by two paths that differ only by one scattering centre. As we already pointed out, Ref. [76] indicates that  $kl_s$  can range from  $kl_s \approx 10^2$  for the electronic transport across relatively clean metals to  $kl_s \approx 10^8$  for light propagation through a foggy atmosphere.

Consequently, those fluctuations average out for most pairings, except, for instance, for those such that  $\Gamma = \Gamma'$ , which gives rise to the previously described incoherent contribution<sup>5</sup>. In the absence of any time-reversal symmetry breaking mechanism<sup>6</sup>, another contribution for which the amplitudes of the paired paths is the same is found when  $\Gamma$  and  $\Gamma'$  represent paths which are time-reversed of each other and thus contain visits of the same sequence of scattering centres in the reversed order. Such pairings yield a phase difference  $\delta_{\Gamma} - \delta_{\Gamma'} = 0$  owing to the symmetry of the experienced elastic scattering events and provided the length of the paired paths does not exceed the phase coherence length<sup>7</sup>. Such paths correspond to  $\mathbf{r}_i = \mathbf{r}'_f$  and  $\mathbf{r}_f = \mathbf{r}'_i$  and their pairing provides the ensemble averaged intensity of the scattered wave as

$$\langle |A(\mathbf{k}_i, \mathbf{k}_f)|^2 \rangle = \left\langle \sum_{\mathbf{r}_i, \mathbf{r}_f} |f(\mathbf{r}_i, \mathbf{r}_f)|^2 \left( 1 + e^{i(\mathbf{k}_i + \mathbf{k}_f) \cdot (\mathbf{r}_i - \mathbf{r}_f)} \right) \right\rangle. \quad (1.23)$$

This equation still features the presence of a phase difference  $\Delta\phi = (\mathbf{k}_i + \mathbf{k}_f) \cdot (\mathbf{r}_i - \mathbf{r}_f)$  that results from the diffraction of the incident wave from  $\mathbf{k}_i$  to  $\mathbf{k}_f$ . This phase difference vanishes for instance when  $\mathbf{r}_i = \mathbf{r}_f$ , as in FIG. 1.6(b) or when  $\mathbf{k}_i = -\mathbf{k}_f$ , as in FIG. 1.6(c).

<sup>5</sup>We note that  $\Gamma_{\mathbf{r}_i \rightarrow \mathbf{r}_f} = \Gamma'_{\mathbf{r}'_f \rightarrow \mathbf{r}'_i}$  implicitly implies that  $\mathbf{r}_i = \mathbf{r}'_i$  and  $\mathbf{r}_f = \mathbf{r}'_f$ , yielding exponentials equal to one in Eq. (1.20). We recover the classical contribution of an overall intensity obtained as a sum of classical intensities, as discussed previously.

<sup>6</sup>Such as a (if needed synthetic) magnetic field.

<sup>7</sup>This may also be explained following the argument developed in [90]. The Green's function appearing in Eq. (1.4) turns out to be

$$G_0(\mathbf{r}, \mathbf{r}') = \frac{e^{ik|\mathbf{r} - \mathbf{r}'|}}{4\pi|\mathbf{r} - \mathbf{r}'|} = G_0(\mathbf{r}', \mathbf{r}), \quad (1.22)$$

and, owing to the presence of a strongly fluctuating factor  $|\mathbf{r} - \mathbf{r}'|$  in the exponential, yields robust to disorder averaging contributions when it is paired with itself (its complex conjugate). On top of the obvious Diffuson contributions that such an argument involves, the symmetry of the Green's function also indicates the presence of Cooperon contributions originating from the pairing between  $G_0^*(\mathbf{r}', \mathbf{r}) = G_0^*(\mathbf{r}, \mathbf{r}')$  and  $G_0(\mathbf{r}, \mathbf{r}')$ .

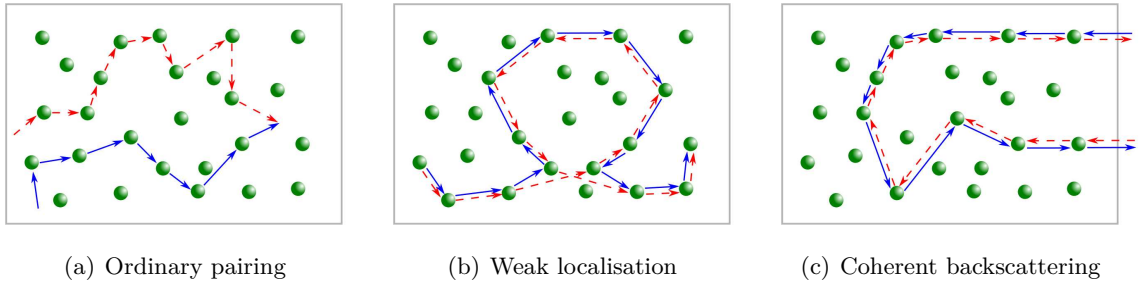


Figure 1.6 – Panel (a): Pairing of ordinary scattering paths which do not survive the ensemble average owing to their sensitivity to a specific disorder configuration. Panel (b): pairs of path forming closed loops giving rise to weak localisation. Panel (c): pairs of paths increasing the backscattered intensity and giving rise to coherent backscattering.

In the former case, the probability to return to the origin is enhanced due to closed loop structures, which is known as weak localisation [52,91]. In the latter case, the intensity is increased in the backscattered direction, which is known as coherent backscattering [54,92,93]. We also note that either for weak localisation or coherent backscattering, the probability to return to origin or to be scattered in the backwards direction is twice the classical probability, as is clear from Eq. (1.23). Both weak localisation and coherent backscattering are closely related phenomena, as they share the same underlying mechanism of constructive interferences between counterpropagating loops. This mechanism is also responsible for Al'tshuler–Aronov–Spivak oscillations [94–96] in Aharonov–Bohm rings [41,42,44], as is thoroughly discussed in Chapter 5. In the weak disorder limit  $kl_s \gg 1$ , which is to be opposed to the strong scattering regime  $kl_s \ll 1$  that shall be discussed in Section 1.4 dedicated to Anderson localisation, only the Diffuson<sup>8</sup> and Cooperon<sup>9</sup> contribute to the ensemble averaged observables in leading order of  $1/(kl_s)$  [90]. Higher order interference effects originating from pairings of more sophisticated scattering paths do not significantly contribute in this limit and can be therefore neglected in a first approach. They are however much more significant in a strong disorder regime.

### 1.3.3 Weak localisation

Due to the closed loops sketched in FIG. 1.6(b), diffusive transport faces localisation effects because of which the waves tend to remain at their initial position. This mitigates the diffusion, as the underlying diffusion constant  $D = D_B + \delta D$  is reduced compared to Drude–Boltzmann incoherent propagation [39], because the (small) weak localisation correction  $\delta D$  is negative. This reduction of the diffusion constant highlights the outcome of microscopic quantum interference phenomena on macroscopic quantities. As was shown around 1980 in two theoretical studies [52,91], positive corrections to the classically predicted resistivity of a disordered mesoscopic sample must indeed be added owing to weak localisation effects.

<sup>8</sup>Which produces the mostly angle-independent incoherent background.

<sup>9</sup>Which is responsible for weak localisation and coherent backscattering.

Weak localisation was already experimentally studied at the same time in the context of solid–state physics, as it explains the unexpected dependence of resistivity of thin metallic films with respect to the temperature. For instance, Ref. [97] is dedicated to experimental measurements of the magnetoresistance of a two–dimensional electron gas in several Si MOSFETs, which are reported in FIG. 1.7(a). At low temperatures, a classically unexpected high resistance is observed as a result of weak localisation effects. A clear decrease of the resistance is encountered with increasing temperature, as is expected owing to the reduction of weak localisation effects. This reduction results from the drop of  $L_\phi$  with temperature, thereby reducing the number of scattering trajectories participating to weak localisation, as paths longer than  $L_\phi$  lose phase coherence. The same reduction of weak localisation effects is also observed in the presence of an increasing perpendicular magnetic field  $H$ . Magnetic fields are indeed known for breaking the time–reversal symmetry in the sense that the phases related to time–reversed paths become different in the presence of a magnetic field.

This particularity may be experimentally leveraged in order to distinguish the classical resistance from weak localisation corrections. From simple arguments indeed, one can estimate which magnetic field intensity starts to destroy weak localisation effects by dephasing interfering trajectories. Amongst all paths  $\Gamma$  that give rise to weak localisation, those encircling the largest area are the most sensitive to the presence of a perpendicular magnetic field as each path acquires a phase shift proportional to the enclosed surface. This largest area is most often obtained with paths of maximal length, comparable with the phase coherence length<sup>10</sup>.

Based on this observation and considering for simplicity that the surfaces begot by such paths are circle–like surfaces, one can derive an expression for the experienced phase shift as a function of the perpendicularly applied magnetic field. It serves as a starting point to estimate which field intensity starts to dephase those paths and to mitigate weak localisation effects. As the magnetic field is further increased, shorter paths giving rise to smaller enclosed areas are also affected and get dephased. This yields a smaller correction for weak localisation effects that can even be suppressed for sufficiently high magnetic field. Nevertheless, a robust to disorder averaging maximum of resistivity still prevails as a signature of weak localisation for field intensities close to zero because the system is in this case time–reversal invariant. This dependence of weak localisation with respect to an external magnetic field motivates a magnetic field–dependent weak localisation correction to the resistivity [88].

---

<sup>10</sup>All paths of length comparable with the phase coherence length do not necessarily enclose the largest area possible. One can for instance think of a path withdrawn into itself, yielding a shrivelled enclosed area. The class of largest possible enclosed areas is however most likely obtained with paths of maximal length, dictated by  $L_\phi$ , that describe in two dimension circle–like surfaces.

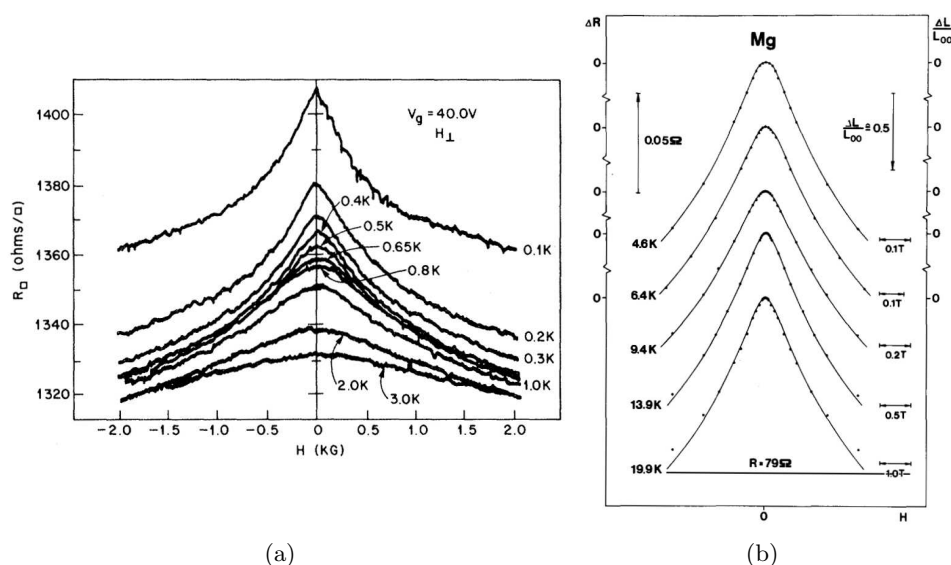


Figure 1.7 – Decrease of the magnetoresistance of a (a) 2DEG in MOSFET structures (extracted from [97]) and (b) thin Mg films (extracted from [53]) with increasing perpendicular magnetic field  $H$  and temperature  $T$ . This reduction of weak localisation effects results from phase coherence length limiting mechanisms (temperature) or time-reversal symmetry breaking mechanisms (magnetic field).

This reduction – and even cancellation – of weak localisation effects by time-reversal symmetry breaking mechanisms, such as an external magnetic field, offers a possibility to separate the classical magnetoresistance from the corrections due to quantum interference effects, highlighting the importance of the latter. Another experimental study of this issue is also reported in Ref. [53] whose main results are reproduced in Fig. 1.7(b) that shows the magnetoresistance of a thin Mg film as a function both of the temperature and of the magnetic field. Similar results are obtained both regarding the dependence with respect to the temperature as well as for regarding the dependence with respect to the magnetic field. The same experimental study of weak localisation is also provided for thin Cu films [98], for thin Cs films [99] or for InSb thin films [100], to name a few of the numerous experimental evidences of weak localisation in the context of solid-state physics.

### 1.3.4 Coherent backscattering

A manifestation of weak localisation in the context of transport of light across random media is coherent backscattering. Indeed, pairings of time-reversed paths yield a robust to disorder averaging constructive interference that increases the probability of backscattering, and thereby the backscattered current. This enhancement is much easier to observe as such than the enhancement of the probability of coming back to the origin in a weak localisation scenario.

The scattering paths depicted in FIG. 1.6(c) display a phase shift that can be written  $\Delta\phi \simeq k|\mathbf{r}_i - \mathbf{r}_f|\theta$  for small angles  $\theta$  between  $\mathbf{k}_i$  and  $\mathbf{k}_f$ . It is clear that a perfectly zero phase

shift is obtained for  $\theta = 0$ , as we already highlighted. Owing to the diffusive behaviour of the averaged intensity,  $|\mathbf{r}_i - \mathbf{r}_f|$  behaves as the square root of the number of scattering events experienced along the path. Several interference patterns for different pairings of time-reversed paths are sketched in FIG. 1.8 in coloured dash-dotted lines. As expected, all those patterns display a maximum at  $\theta = 0$ , whilst the other maxima depend on the number of scattering events contained in the scattering sequence. The total averaged intensity is obtained as a weighted sum of all those interference patterns. The weighting factor is provided by  $|f(\mathbf{r}_i, \mathbf{r}_f)|^2$  in Eq. (1.23) and is all the lower as the path is long, which indicates that short length paths have more importance than long ones in the summation appearing in Eq. (1.23).

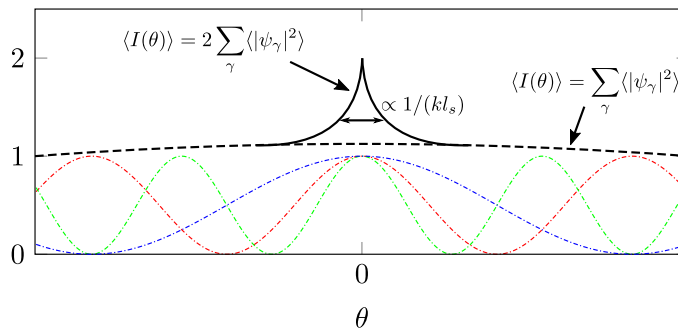


Figure 1.8 – Qualitative sketch of interference patterns related to individual pairings of time-reversed paths and of the coherent backscattering peak that results from the weighted superposition of those patterns. Coloured dash-dotted lines: interference pattern produced by specific path pairings. Black dotted line: diffusive background arising from averaged classical contributions (Diffusons). Solid black line: coherent backscattering peak due to constructive interferences around  $\theta = 0$  (Cooperons). Adapted from [76].

As a result of the superposition of all those interference patterns, the structure depicted in black solid line in FIG. 1.8 emerges. Away from  $\theta = 0$ , a flat diffusive background is encountered as results from the classical contributions. Close to  $\theta = 0$  however, as all interference patterns show constructive interferences, a peak of conic shape, which is referred to as the coherent backscattering cone, is encountered. The width of this cone is proportional to  $1/(kl_s)$  and is governed by short length scattering paths [39]. Its measurement can be leveraged to measure the elastic mean free path experimentally. As is obvious from Eq. (1.23), this peak is theoretically exactly twice as bright as the diffusive background. In practice however, short length scattering paths consisting in an immediate backreflection at the first scattering event mitigate this picture. Those paths of large importance in the summation in Eq. (1.23) are actually identical to their time-reversed twin and hence do not participate to coherent backscattering.

Long before the advent of the nowadays frequently admitted explanation detailed above, coherent backscattering was already observed in 1893 in the opposition surge in the rings of Saturn [101]. Indeed, light emitted from the Sun gets multiply scattered by small particles in the rings of Saturn and causes the rings to appear much brighter in the backscattered direction, as has for instance been photographed in the early 2000's by Cassini.

It has emerged at approximately the same epoch as weak localisation, as a theoretical study [92], immediately followed by experimental observations [54, 93], reported an increase of the scattered current in the backscattered direction. Those experimental evidences were obtained by illuminating an aqueous medium containing small polystyrene spheres in suspension with visible light. Both references report an enhancement of the backscattered intensity within a narrow cone, however less pronounced than the expected factor 2 enhancement owing to the angular dependence of the scattering of light by the polystyrene spheres. Ten years later, this factor enhancement was achieved by illuminating BaSO<sub>4</sub>, ZnO and TiO<sub>2</sub> powders with laser light [102].

Since then, coherent backscattering is observed and studied in a very wide array of domains. It has for instance been theoretically studied for light propagating across 3D disordered slabs obtained with speckle fields [103], or experimentally observed with classical waves such as acoustic waves [104] or elastic waves [105] and can even be exploited to characterise human bones [106]. Another potential and less expected application is found in the petroleum search and deep underground probing. Signatures of coherent backscattering and weak localisation have indeed been found by recording the ground motion with a series of geophones after striking a sledgehammer on the ground [107, 108].

Coherent backscattering of light by ultracold atoms was first reported in 1999 in Nice [109], as a laser illuminating a scattering sample made of laser-cooled gas of Rubidium atoms showed an increased backscattered intensity, paving the way for numerous studies of coherent backscattering with ultracold atoms. More recently, ultracold atoms were used not as scattering medium but directly as a coherent source. Indeed, following the theoretical proposal in Ref. [110], a group of experimental physicists in Palaiseau reported the direct observation of coherent backscattering of ultracold atoms in the presence of a 2D disorder landscape created by means of optical speckle fields [57]. Similar results were also found at the same time in Nice [58]. Time-of-flight imaging shows that a Bose-Einstein condensate, initially in a well-defined momentum state  $\mathbf{p}_i$ , gets elastically scattered and hence populates all states of constant energy in the momentum space, with a higher population encountered in the momentum state corresponding to  $-\mathbf{p}_i$ . These studies initiated a large number of other studies related to coherent backscattering in the context of ultracold atoms.

### 1.3.5 Nonlinear weak localisation and coherent backscattering

A very legitimate question that immediately arises in the context of coherent backscattering with ultracold atoms is the effect of a many-body interaction that is most naturally present within Bose-Einstein condensates. Both coherent backscattering and weak localisation are indeed affected by nonlinearities, as a general diagrammatic theory indicates [59], both for the propagation of light across a nonlinear Kerr medium [111, 112] and for the transport of ultracold atoms towards disordered potentials [60, 61].

In the context of light transport, the presence of a nonlinearity trivially mitigates phase coherence and the related peak height, as is found in Ref. [113] for backscattering of light by cold atoms. More spectacularly, a narrow dip in the backscattered direction is encountered in the angular profile of the light scattered by a disordered opaque medium, owing to the presence of

a nonlinearity [114]. The phase coherence length in this reference scales as  $L_\phi \propto 1/\theta$ , which indicates that the lower  $\theta$ , the longer the involved relevant paths. The emergence of the dip is then attributed to a path length selective nonlinearity that increases the sensitivity to absorption of long paths, that mostly play a role around  $\theta = 0$ , more than the one of short paths.

In the context of quantum transport of matter waves, the presence of a many-body atom-atom interaction gives rise, in the mean-field description, to an effective interaction energy which is accounted by a nonlinearity in the Gross-Pitaevskii equation. Numerical mean-field studies related to the transport of a Bose-Einstein condensate across a 2D disordered slab [60] or through irregularly shaped billiard geometries [61], both performed in the context of a quasi-stationary reachable scattering state, indicate that owing to the presence of a finite nonlinearity in the related Gross-Pitaevskii equation, coherent backscattering gets inverted.

These mean-field studies suffer however a drawback in the sense they are only valid in the limit of a very weak interaction strength. It therefore appears reasonable to question the extension of the validity of the mean-field approach, more specifically to which extent the predicted peak inversion prevails in a regime extending beyond the mean-field description. A dephasing of coherent backscattering is indeed expected for strong interaction, a study based on diagrammatic many-body techniques indicates [115]. As a matter of fact, in the presence of interaction, inelastic scattering processes which are beyond the scope of the mean-field approach yield an energy redistribution amongst the interacting particles. This energy spectrum causes the production of an incoherent contribution to the current which can, for sufficiently strong interaction, dominate the coherent contribution and wash out coherent interference effects. This inelastic scattering-induced coherence loss and the resulting thermalisation are indeed confirmed in Ref. [116] which is dedicated to the theoretical and numerical study of an out-of-equilibrium Bose-Einstein condensate prepared in a configuration very similar to that in Ref. [57].

## 1.4 Anderson localisation

As is clearly evidenced by weak localisation and the related coherent backscattering, interferences between scattering paths have significant effects on the transport, as those microscopic phenomena diminish the classically expected macroscopic conductivity, which is translated into a reduced diffusion constant. Yet more astonishing is the annihilation of transport that takes place in the context of Anderson localisation and which turns a metallic conductor into an insulator of zero conductivity.

In his famous seminal paper [77], Anderson theoretically studied the electronic transport within a semiconductor as a result of scattering by crystal defects and investigated to what extent the Drude-Boltzmann theory remains valid in the presence of a strong disorder. He used a tight binding formulation of noninteracting electrons propagating on a lattice with uniform hopping term and randomly distributed on-site energies that model a disorder potential.

For sufficiently strong disorder, he showed that any electron gets localised at its initial position in the sense of an exponentially vanishing probability of escaping its initial lattice site by diffusive motion, resulting, in the words of Anderson, in the “absence of diffusion”. This



annulation of the diffusion constant and the resulting annihilation of transport is entirely due to coherent interference effects that, in the context of a sufficiently strong disorder, lead to an elastic scattering mean free path which is comparable to the de Broglie wavelength of the electrons. In such a context of a mean free path becoming comparable to – and even shorter than – the wavelength, the wave picture starts to get qualitatively deprived of its substance [117, 118]. It indicates that the electron is constantly scattered before any propagation can occur, so that the treatment of a diffusive propagation resulting from a plane wave motion interrupted by many scattering events collapses. This situation occurs as soon as  $kl_s \approx C \sim 1$  which is known as the Ioffe–Regel criterion [119] that defines the strong scattering regime and which applies in the infinite space.

This Ioffe–Regel criterion appears as a selective criterion that allows to discriminate between a regime of parameters giving rise to spatially localised waves and a regime of parameters that yields spatially extended waves that propagate diffusively, portraying Anderson localisation as a phase transition between those two regimes [120]. This transition which, in the context of electronic transport across a metal, turns this metallic sample into a perfect insulator [77], appears at the so-called mobility edge [118]. This localised regime introduces a new length scale  $\xi_{\text{loc}}$ , which is referred to as the localisation length and most naturally appears as the characteristic length parameter in the spatial exponential decay of the modulus square of the localised wavefunction.

As the discussion above highlights, in the strong scattering regime, the semiclassical picture of a plane wave motion between scattering events breaks down and fails at describing strong localisation. In this context, a new phenomenological approach was proposed by the gang of four (Abrahams, Anderson, Licciardello, Ramakrishnan) in 1979 [121] who followed the works of Thouless [122]. This approach consists in considering that the localisation properties of the system under study are governed by a single parameter, which is referred to as the dimensionless conductance  $g(L)$ , and its dependence with respect to the system size  $L$ . This dimensionless conductance is expressed as

$$g(L) = \frac{\tau_{\text{H}}}{\tau_{\text{Th}}}, \quad (1.24)$$

that is, as the Heisenberg time  $\tau_{\text{H}}$  which is the time scale required by the system to resolve its discrete energy spectrum and where quantum effects become inevitable [123] divided by the Thouless time  $\tau_{\text{Th}}$ , required for an electron to diffusively traverse the sample and reach the system boundary. This dimensionless conductance reveals two opposite regimes. On the one hand, when  $g \gg 1$ , or equivalently  $\tau_{\text{H}} \gg \tau_{\text{Th}}$ , quantum interference effects are suppressed before playing a significant role and classical diffusive transport is obtained. On the other hand, when  $g \ll 1$ , or equivalently  $\tau_{\text{H}} \ll \tau_{\text{Th}}$ , strong localisation is achieved and the wave does not reach the boundary of the system.

The scaling theory is devoted to linking those two limits and to describing what happens between them. For that purpose, the scaling parameter is defined as the logarithmic derivative of the dimensionless conductance with respect to the size of the system

$$\beta = \frac{d \ln g}{d \ln L} \equiv \beta(g), \quad (1.25)$$

where a strong assumption has been made, namely that  $\beta$  depends only on  $g$  (and on the dimensionality by extension) and not upon the microscopic transport properties of the medium. Despite its crudeness, this hypothesis has been verified by renormalisation group studies [124] and a self-consistent theory of Anderson localisation [125]. This approach of a single parameter scaling law provides a unified framework in which transport properties are described by  $\beta(L)$  both in the weak and strong scattering regimes. FIG. 1.9, which is extracted from [126], shows the dependence of  $\beta(g)$  as a function of the dimensionless conductance  $g$  in dimension 1, 2 and 3.

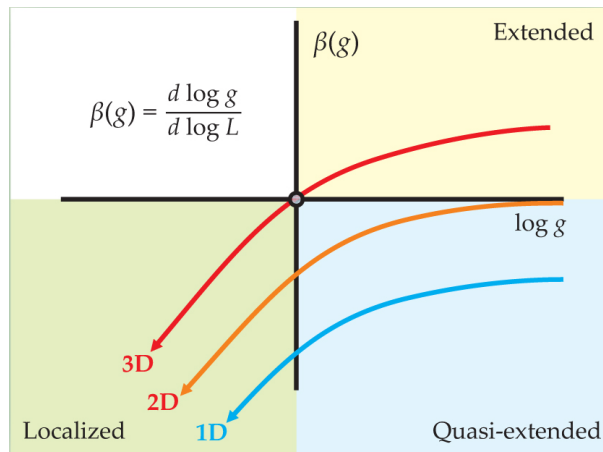


Figure 1.9 – Dependence of  $\beta(g)$  as a function of the dimensionless conductance  $g$  in dimension 1, 2 and 3. In 1D and 2D, Anderson localisation always occurs whilst in 3D, there is a phase transition from a spatially localised to an extended regime which occurs at the mobility edge, when the red curve crosses the  $\log g$  axis. This figure is extracted from [126].

The curves depicted in FIG. 1.9 are very interesting and reveal that a genuine (second order) phase transition from a spatially localised regime to an extended regime only occurs in 3D (and beyond) at the mobility edge, which separates the weak from the strong scattering regimes for which the Ioffe–Regel criterion can be used as a discriminating criterion. Conversely, for a disordered system in 1D or 2D, there is no such phase transition and there are no extended states. The scaling parameter  $\beta(g)$  is indeed always found negative and implies that the dimensionless conductance  $g$  monotonically decreases with the system size  $L$ , which in turn indicates that  $g \ll 1$  and that a strongly localised regime is achieved, irrespective of the size of the system. However, the related localisation length is usually very large for such systems, exceeding the size of the system within which waves propagate in the extended regime so that weak localisation effects remain nonetheless observable. Anderson localisation is however granted to occur when the system is large enough, irrespective of the disorder regime.

Although very satisfactory from the qualitative point of view, the scaling theory fails at predicting the critical exponents around the critical point. This theory was extended by Vollhardt and Wölfle to give rise to the microscopic self-consistent theory of Anderson localisation [125] that predicts very precise localisation lengths in 1D and 2D and is satisfactory in

3D but fails at predicting the critical exponent of the related phase transition. Very recently, the emergence of the landscape theory as a universal mechanism for Anderson and weak localisation [127, 128] provides perspectives of a more accurate prediction of the mobility edge and of the critical exponent, which nowadays remains an open and challenging question.

Despite its current profound implications on the physics of waves transport within random media, the paper of Anderson largely went under the radar of the scientific community before 1970, as it was cited only 30 times the first ten years that followed its publication [126], whereas it is nowadays cited more than 5000 times. Anderson localisation has indeed been observed and studied in a wide variety of contexts, both for classical or quantum waves, which is not surprising considering the ubiquity of Anderson localisation as an interference phenomenon. It was for instance experimentally observed with light<sup>11</sup> in disordered media [129, 130] or within photonic crystals [131]. It has also been encountered in the acoustics domain for ultrasound [132, 133] but also with microwaves [134]. Experimental signatures in the direct space for ultracold atoms were recently evidenced by a research group in Palaiseau [135] and by another research group in Florence [136]. Finally, it has also been studied in the momentum space [110, 137–140].

#### 1.4.1 Coherent forward scattering as an indicator of Anderson localisation

As we have highlighted below, Anderson localisation is an extremely active field of research, especially in the framework of ultracold atoms where signatures of Anderson localisation are actively sought, particularly in the momentum space. The idea of such studies is to prepare a wavepacket narrowly centred around an initial momentum state and to analyse how the ensemble averaged momentum distribution evolves in time. In this context and driven by the signature of weak localisation in this space (coherent backscattering), a group led by C. Miniatura searched for an equivalent signature of Anderson localisation in the momentum space. A first numerical study [141], dedicated to the investigation of a wavepacket propagating towards a 2D disordered potential in a configuration very similar to that in Ref. [110], reports the time evolution of the ensemble averaged momentum distribution of Ref. [110], for which a signature of Anderson localisation is expected at long times. Beyond the localisation time  $t_{\text{loc}}$ , they noticed the emergence in the forward direction of a peak very similar to the coherent backscattering peak, which effect is referred to as coherent forward scattering. At long times, those peaks form a twin structure which is shown in FIG. 1.10.

---

<sup>11</sup>Photons do not interact contrarily to electrons, which constitutes a simplified context of work.

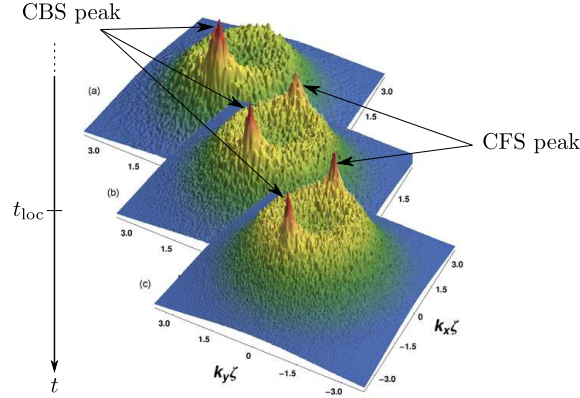


Figure 1.10 – Disorder average of the momentum distribution of matter waves with initial momentum  $\mathbf{k}_i = (1.5/\zeta, 0)$  that displays the twin peaks structure featuring coherent back and forward scattering. The latter peak that appears around the localisation time  $t_{loc}$ , which corresponds to the time required to reach the localisation length  $\xi_{loc}$ , is a signature of Anderson localisation in the momentum space. Adapted from [141] and [142].

Contrarily to coherent backscattering which is nowadays well understood in terms of constructive interferences between time-reversed scattering paths, coherent forward scattering is more complicated to portray. Ref. [143] indicates that this effect appears as a consequence of higher order interferences, such as for instance paths which yield back and forth scattering sequences between the back and forward directions, two examples of which being sketched in FIG. 1.11 for the second order. Those paths can be understood as higher order interference terms compared to the Cooperon that give rise to weak localisation and coherent backscattering. Indeed, as we mentioned earlier, those terms are only the leading order terms in a weak disorder scenario.

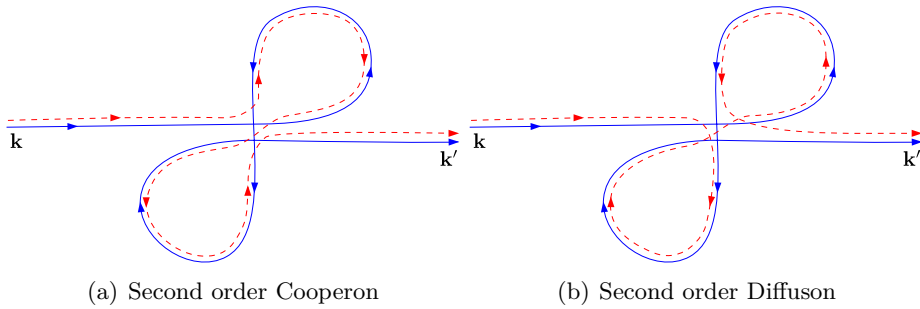


Figure 1.11 – Scattering paths related to second order Cooperon and Diffuson, adapted from [76].

This mechanism of back and forth scattering does not play a significant role in the diffusive regime, contrarily to the case of a localised regime, which typically occurs for Anderson localisation for which interference accumulate to yield a notable peak in the forward direction. Ref. [143] further indicates that this peak should also be visible in a confined region of space

---

of extension less than the localisation length. Beyond its fundamental relevance as such, this effect is particularly interesting as it is, as we have highlighted, a key indicator and signature in the momentum space of the onset of Anderson localisation [144, 145] under the condition that the atomic motion is not constrained by any artificial mechanism in the propagation direction [143].

The experimental observation of coherent forward scattering poses a substantial problem owing to the lack of experimental realisations of energy-filtering methods, although there exists a proposal of such for ultracold atoms [146]. Indeed, as Ref. [147] states, those methods are necessary to target a very narrow energy window to circumvent the scrambling of the dependence of the diffusion constant and the localisation length with respect to the energy. This reference suggests that, despite those practical difficulties, the experimental observation of coherent forward scattering should indeed nowadays be possible for a quantum kicked rotor system. It has nevertheless to our knowledge for the moment not been observed yet.



## Chapter 2

# Bose–Einstein condensates: a source of coherent matter waves

In this chapter, we introduce the framework of ultracold atoms through Bose–Einstein condensates that provide a formidable toolbox for quantum simulation of many–body physics systems. We start by introducing how Bose–Einstein condensation naturally emerges from the related distribution when an ideal gas of bosonic particles in a trap is cooled down to very low temperatures, following Einstein’s theoretical model. Bosonic particles forming a condensate in this context however do exhibit interaction, which brings us to the quantum scattering theory that finally results in the famous Gross–Pitaevskii equation describing atom–atom interaction within the condensate in the mean–field approximation. With those tools at our disposal, we shall be in a position to discuss atom lasers that are a key ingredient to produce highly coherent quantum matter waves that can be used in the context of the transport of coherent waves within random media.

### 2.1 From Maxwell–Boltzmann to Bose–Einstein distribution

The description of a macroscopic system containing a large number of particles in terms of microscopic quantities requires a statistical approach. Indeed, solving Newton’s law for each particle not only comprises a prohibitively large number of equations<sup>1</sup> but also involves errors on the collisions between particles that propagate exponentially in the presence of particle–particle interaction.

A first statistical approach arose by the end of the 19<sup>th</sup> century with the kinetic theory of gases and is due to Boltzmann who derived a statistical distribution referred to as Maxwell–Boltzmann distribution (see Refs. [149, 150] for more information). This law describes the distribution of discernable<sup>2</sup> particles of a classical gas in thermal equilibrium amongst the

---

<sup>1</sup>For a room of volume  $V = 100 \text{ m}^3$  and particles density  $n = p/k_B T \approx 2 \cdot 10^{25}$  per unit volume, where  $p$  is the ambient pressure,  $T$  the ambient temperature and  $k_B = 1.38 \times 10^{-23} \text{ m}^2 \text{ kg s}^{-2} \text{ K}^{-1}$  is the Boltzmann constant, each particle being completely defined by its position  $\mathbf{r}(t)$  and momentum  $\mathbf{p}(t)$  at time  $t$ , this amounts to considering approximately  $10^{28}$  coupled ordinary differential equations [148]!

<sup>2</sup>The notion of discernibility is intuitively understood as the possibility to label and monitor the time evolution of each particle.

energy levels at disposal and is, in the absence of degeneracy, yielded as

$$\langle \hat{n}_k \rangle_{\text{MB}} = \frac{1}{e^{\beta(E_k - \mu)}}, \quad (2.1)$$

where  $\langle \hat{n}_k \rangle_{\text{MB}}$  is the average population of the state with energy  $E_k$ ,  $\mu$  is the chemical potential of the particles gas and  $\beta = 1/(k_B T)$ , with  $k_B = 1.38 \times 10^{-23} \text{ m}^2 \text{ kg s}^{-2} \text{ K}^{-1}$  the Boltzmann constant and  $T$  the temperature of the gas.

Some time later, Bose wrote a paper about a new derivation of Planck’s law for black body radiation. In this novel approach, he treated the thermal radiation as originating from a gas made of identical and indistinguishable particles later called photons. This novel concept of indistinguishability, although natural in quantum mechanics<sup>3</sup>, is totally innovative and contrasts with the treatment of Boltzmann. It has also deep consequences on the equilibrium state that is attained as it originates from the number of possible manners to distribute the particles amongst the reachable energy states. Indistinguishability decreases the number of accessible configurations and hence enhances the importance of a given configuration, thereby favouring condensed configurations, as the problem of distributing  $N$  particles in two boxes illustrates [151].

Bose sent his work to Einstein who translated the article into German and published it in *Zeitschrift für Physik* [5]. Short after, Einstein extended Bose’s work to a gas of indistinguishable and noninteracting atoms, leading to Bose–Einstein distribution that provides the number of atoms of energy  $E_k$  as

$$\langle \hat{n}_k \rangle_{\text{BE}} = \frac{1}{e^{\beta(E_k - \mu)} - 1} = \frac{z}{e^{\beta E_k} - z}, \quad (2.2)$$

where we have introduced the fugacity  $z = \exp(\beta\mu)$  that is sometimes used to write Bose–Einstein distribution. An important physical constraint comes with this distribution, namely that the chemical potential is such that  $\mu < E_0$  (or equivalently in terms of the fugacity that  $0 < z < \exp(\beta E_0)$ ), where  $E_0$  is the lowest eigenvalue of the Hamiltonian describing the system under study, in order to prevent the occupation number of a hypothetical state of energy less than  $\mu$  to be negative. It provides an upper bound on the number of particles populating the excited states

$$\langle \hat{N} \rangle_{\text{exc}} = \sum_{k>0} \frac{1}{e^{\beta(E_k - \mu)} - 1} < \langle \hat{N} \rangle_{\text{exc}}^{\text{max}} = \sum_{k>0} \frac{1}{e^{\beta(E_k - E_0)} - 1} \quad (2.3)$$

obtained by setting  $\mu$  to its maximal value  $E_0$ . The value  $\langle \hat{N} \rangle_{\text{exc}}^{\text{max}}$  is called the *saturation number* and indicates that if the average number  $\langle \hat{N} \rangle$  of particles in the system is larger than  $\langle \hat{N} \rangle_{\text{exc}}^{\text{max}}$ , then  $\langle \hat{N} \rangle_0 = \langle \hat{N} \rangle - \langle \hat{N} \rangle_{\text{exc}}^{\text{max}}$  necessarily lie in the ground state, as a preliminary signature of Bose–Einstein condensation [152]. In particular, this accumulation in the ground state does not depend upon the energy spacing between the ground state and the first excited state and occurs at every temperature. It requires however all the more particles that the temperature is high to significantly populate the ground state.

---

<sup>3</sup>Owing to the possible overlap of the wavepackets related to various particles, it is impossible to discriminate one particle amongst the others. Evaluating the probability that a specific particle occupies a given position is abandoned to the benefit of determining the probability of finding a particle at position  $\mathbf{r}$ .



FIG. 2.1(a) shows the average ground state population as a function the energy difference  $E_0 - \mu$  and FIG. 2.1(b) shows the average population as predicted by the Bose–Einstein distribution (2.1) versus the energy  $E_k$  for different values of the fugacity  $z$ .

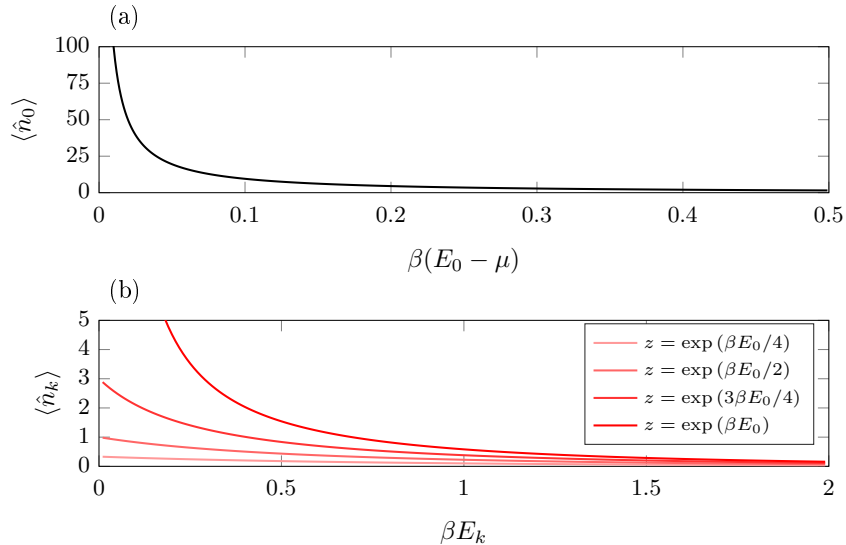


Figure 2.1 – Upper panel: average population of the ground state as a function of the energy difference  $E_0 - \mu$ . As  $\mu \rightarrow E_0$ , the population of the ground state becomes infinitely large and diverges. Lower panel: Bose–Einstein distribution as a function of the energy  $E_k$  for different values of the fugacity  $z$ . The higher the fugacity, the more particles populate the low energy modes.

FIG. 2.1(a) highlights that the average ground state population

$$\langle \hat{n}_0 \rangle = \frac{1}{e^{\beta(E_0 - \mu)} - 1} \quad (2.4)$$

becomes infinite when the chemical potential reaches its upper bound,  $\mu \rightarrow E_0$ , which is a key ingredient of Bose–Einstein condensation. This is confirmed by FIG. 2.1(b) which illustrates that, when  $z \rightarrow \exp(\beta E_0)$  (or equivalently  $\mu \rightarrow E_0$ ), the low energy states feature a much higher population than the high energy states, indicating a tendency to aggregate in the low energy states when the fugacity (or the chemical potential) tends to its upper bound.

## 2.2 Bose–Einstein condensation of an ideal gas in a harmonic trap

Bose–Einstein condensation as predicted by Einstein is expected to occur in free space. Temperatures required for a significant population of the ground state to emerge are nevertheless extremely low, so that cooling and trapping<sup>4</sup> techniques must be used to be able to experimentally produce a Bose–Einstein condensate [153]. For this reason, we describe in the following

<sup>4</sup>For those very low temperatures, material boundaries such as a glass container are not suitable to confine the gas as all particles would immediately stick to the walls.

how this phenomenon occurs in a harmonic trap modelled by the harmonic potential

$$V(\mathbf{r}) = \frac{1}{2}mr^2\omega^2, \quad (2.5)$$

with  $r$  being the distance from the centre of the trap,  $\omega \equiv \omega_x = \omega_y = \omega_z$  is the uniform confinement frequency and  $m$  the mass of the bosonic particles. The Hamiltonian related to this system reads

$$\hat{H} = \frac{\hat{\mathbf{p}}^2}{2m} + V(\mathbf{r}) \quad (2.6)$$

for which the eigenvalues read

$$E_{\mathbf{n}} = \left( n_x + n_y + n_z + \frac{3}{2} \right) \hbar\omega, \quad (2.7)$$

where  $n_x, n_y, n_z \in \mathbb{N}$  are the mode indices of the trap. The average number of particles contained within the Bose gas is provided as a sum over all average occupation numbers  $\langle n_{n_x, n_y, n_z} \rangle$  of each mode  $n_{n_x, n_y, n_z}$ , with  $n_x, n_y, n_z \in \mathbb{N}$ . This is yielded as

$$\langle \hat{N} \rangle = \sum_{\mathbf{n}} \frac{1}{e^{\beta(E_{\mathbf{n}} - \mu)} - 1} = \sum_{\mathbf{n}} \frac{z}{e^{\beta E_{\mathbf{n}}} - z}, \quad (2.8)$$

whilst the average occupation number of the specific  $\langle n_{n_x, n_y, n_z} \rangle$  state is provided by the Bose–Einstein distribution (2.2) that yields the constraint that the fugacity must take values in the range  $[0, \exp(3\beta\hbar\omega/2)]$ . As a matter of convenience and following the discussion in Ref. [154], the ground state energy can be absorbed in a rescaled chemical potential  $\tilde{\mu} = \mu - 3\hbar\omega/2$  which in turn modifies the eigenvalues as  $\tilde{E}_{\mathbf{n}} = (n_x + n_y + n_z)\hbar\omega$  and also yields rescaled fugacity  $\tilde{z} = z \exp(-3\beta\hbar\omega/2)$  varying between 0 and 1. This transformation preserves the Bose–Einstein distribution provided one expresses it in terms of the rescaled eigenvalues, chemical potential and fugacity.

Separating the average population of the ground state from the other states, the average number of particles in the trap is written

$$\langle \hat{N} \rangle = \frac{1}{e^{-\beta\tilde{\mu}} - 1} + \sum_{\mathbf{n} \neq \mathbf{0}} \frac{1}{e^{\beta(\tilde{E}_{\mathbf{n}} - \mu)} - 1} = \frac{\tilde{z}}{1 - \tilde{z}} + \sum_{\mathbf{n} \neq \mathbf{0}} \frac{\tilde{z}}{e^{\beta E_{\mathbf{n}}} - \tilde{z}}, \quad (2.9)$$

and highlights once again an unbounded growth of the average ground state population in the limit  $\tilde{z} \rightarrow 1$ . As we earlier discussed, the excited states population gets bounded in this limit by the critical (or saturation) number

$$N_{\text{cr}} \equiv \langle \hat{N} \rangle_{\text{exc}}^{\text{max}} = \sum_{\mathbf{n} \neq \mathbf{0}} \frac{1}{e^{\beta E_{\mathbf{n}}} - 1}, \quad (2.10)$$

which is referred to as the saturation of the excited states. A direct consequence is that, at fixed temperature  $T$ , if the trap contains an average number of particles higher than the critical number  $N_{\text{cr}}$ , the difference between those two quantities necessarily populates the ground state. Furthermore, the injection of a new particle into the trap leads to a very high probability to condense in the ground state. The excited population is then referred to as the *thermal cloud* whilst the ground state population is referred to as the *condensate*. It

is important to note that the critical number  $N_{\text{cr}}$  remains finite, whereas the ground state population can be arbitrarily large compared to that of the thermal cloud. In the formal limit  $\tilde{z} \rightarrow 1$  and when  $\beta\hbar\omega \ll 1$ , the critical number can be computed as  $N_{\text{cr}} = [k_B T / (\hbar\omega)]^3 \zeta(3)$  and the average number of particles is yielded [154] as

$$\langle \hat{N} \rangle = \frac{\tilde{z}}{1 - \tilde{z}} + N_{\text{cr}}, \quad (2.11)$$

where  $\zeta(3) \approx 1.202$  is the Riemann zeta function and where we have once again separated the ground state contribution from the thermal cloud, because of the divergence of the ground state population in the limit  $\tilde{z} \rightarrow 1$ .

Conversely, condensation is also highlighted when the number of particles is constant and the temperature lowered. This is a common situation since Bose–Einstein condensation is usually achieved by first loading traps with  $N$  particles and then progressively lowering the temperature. Indeed, the critical number  $N_{\text{cr}}$  is an increasing function of the temperature that allows us to define a corresponding critical temperature by setting  $\langle \hat{N} \rangle = N_{\text{cr}}$ , which yields

$$k_B T_{\text{cr}} = \hbar\omega \sqrt[3]{\frac{N}{\zeta(3)}}. \quad (2.12)$$

This critical temperature corresponds to a threshold below which bosonic particles deplete the thermal cloud and feed the condensate by significantly populating the ground mode, as is qualitatively illustrated in FIG. 2.2.

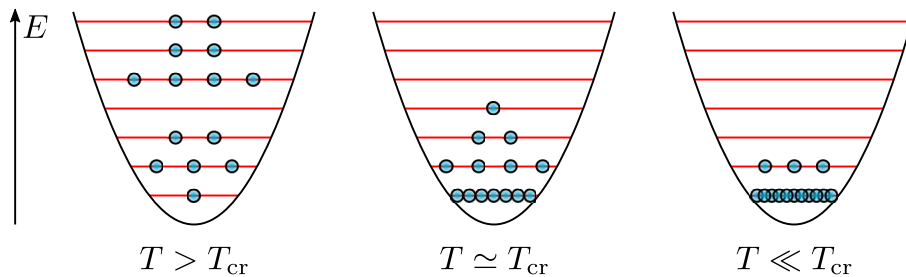


Figure 2.2 – Schematic population of the energy levels of a trapped gas of bosonic particles. When  $T \gg T_{\text{cr}}$ , bosons populate the energy levels similarly as would be prescribed by the Maxwell–Boltzmann distribution. Around the critical temperature  $T \approx T_{\text{cr}}$ , bosons start to condense in the ground state and when  $T \ll T_{\text{cr}}$ , the majority of the bosonic particles occupy the ground state.

As FIG. 2.2 illustrates, for high temperatures such that  $T \gg T_{\text{cr}}$  bosonic particles populate the energy levels as would be prescribed by the Maxwell–Boltzmann distribution, as the Bose–Einstein distribution is safely approximated by the latter in this limit. As the temperature is lowered to reach to the critical temperature  $T \approx T_{\text{cr}}$ , the formation of the condensate is triggered and a non negligible fraction of the total particles condense in the ground state. In the limit  $T \ll T_{\text{cr}}$ , the majority of the particles lie in the ground state and populate it macroscopically. The thermal cloud can even be entirely emptied and the condensate made of all trapped particles in the theoretical limit  $T \rightarrow 0$ .

The related de Broglie wavelength

$$\lambda_{\text{dB}}(T) = \sqrt{\frac{2\pi\hbar^2}{mk_B T}} \quad (2.13)$$

at temperature  $T$  also provides qualitative information of the system behaviour at low temperatures. Indeed, at high temperature  $T \gg T_{\text{cr}}$ , the de Broglie wavelength  $\lambda_{\text{dB}}$  of the particles is extremely short compared with the mean distance separating the particles and they can be safely described in terms of point-like particles following the Maxwell–Boltzmann distribution. However, around the critical temperature, one can show [29] that both thermal the de Broglie wavelength (2.13) and the mean spacing  $d$  between particles are of the same order of magnitude, whilst below  $T_{\text{cr}}$ , the de Broglie wavelength spreads and overlaps with that of other bosonic particles. That portrays Bose–Einstein condensation as the emergence of a giant matter wave of bosonic particles at low temperatures. This behaviour is illustrated in FIG. 2.3 which shows a graphical illustration of the de Broglie wavelength in different temperature regimes.

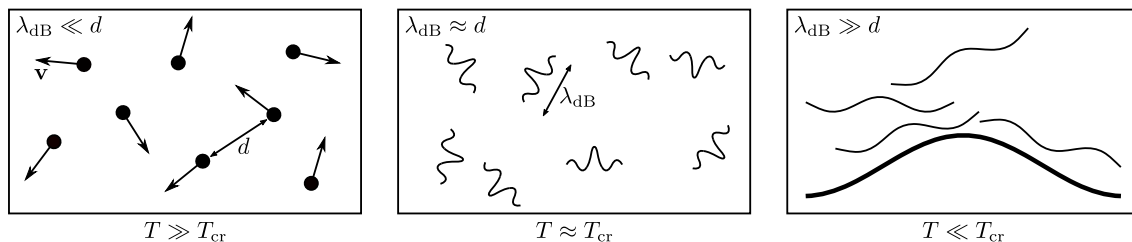


Figure 2.3 – Scheme of the de Broglie wavelength in different regimes of temperature. When  $T \gg T_{\text{cr}}$ , bosonic particles can be safely treated as classical point-like particles obeying Maxwell–Boltzmann distribution. When  $T \approx T_{\text{cr}}$ , atomic wavepackets start to overlap to form a giant matter wave when  $T \ll T_{\text{cr}}$ , referred to as Bose–Einstein condensate. Adapted from [155].

Temperatures required to obtain Bose–Einstein condensation experimentally, that are typically hundreds of nanokelvin, rendered its observation totally impossible until the advent of laser cooling techniques. One had thus to wait for 70 years for the first experimental observation with  $^{87}\text{Rb}$  atoms in 1995 by the group of Cornell and Wieman [8] at Boulder (JILA) and with  $^{23}\text{Na}$  atoms by the group of Ketterle [9] at MIT. The famous picture of the Nobel lecture [156] illustrating the experimental velocity distribution of a gas  $^{87}\text{Rb}$  atoms in three typical temperature regimes is shown in FIG. 2.4.

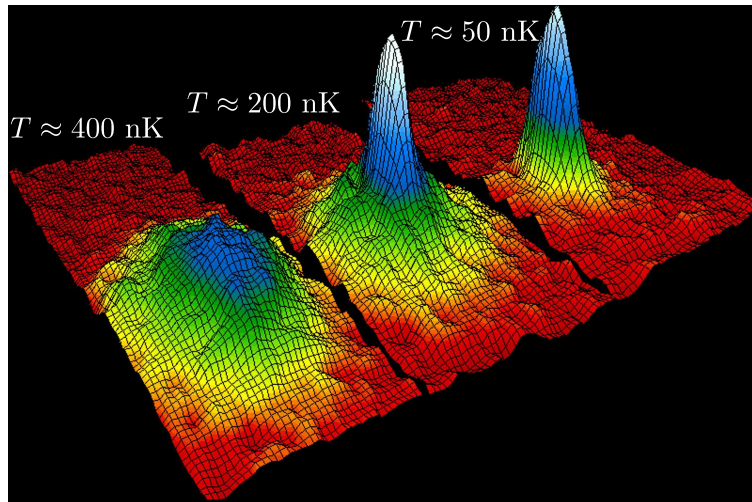


Figure 2.4 – First experimental observation of Bose–Einstein condensation by imaging the velocity distribution of a Bose gas of  $^{87}\text{Rb}$  atoms at different temperature regimes. The left panel for which  $T \gg T_{\text{cr}}$  shows a statistical population of the energy states. The atomic cloud is still quite hot and the velocity distribution wide. In the middle panel corresponding to  $T \approx T_{\text{cr}}$ , a strong blue peak appears as a signature of a high population of the ground state that indicates the formation of the condensate. For  $T \ll T_{\text{cr}}$ , as in the right panel, a quite pure condensate is obtained and only the ground state is appreciably populated. Picture adapted from [156].

FIG. 2.4 shows the velocity distribution of the trapped atoms that first statistically populate the energy levels of the trap at high temperatures (left panel). The thermal cloud is largely populated as the width of the velocity distribution indicates and no emergence of a significantly high population of the ground state is yet to be noticed. As the temperature is progressively lowered by evaporative cooling, a macroscopic population of the ground state (middle panel) emerges and highlights the formation of the condensate around  $T_{\text{cr}}$ . A lower temperature further depletes the thermal cloud to yield a very pure condensate, where nearly all  $^{87}\text{Rb}$  atoms contained in the trap populate the ground state (right panel). For this spectacular achievement, Cornell and Wieman together with Ketterle were rewarded by the Nobel prize in physics in 2001.

However, far from being an ultimate accomplishment, this observation stimulated many other subsequent experiments and paved the way for a very rich physics. Amongst those early experiments, a significant part were devoted to alkali atoms, mainly for three reasons. Indeed, owing to the presence of an intrinsic magnetic moment, they can be easily confined within a magnetic trap. Furthermore, the energy difference between the ground state and the first excited state of alkali atoms lies in the optical or near-infrared regime for which lasers are readily available to cool them down. Finally, alkali atoms are characterised by the presence of an unpaired electron that most naturally results in a weak atom–atom interaction (that can be exploited as a probe to study many–body interaction effects or to realise evaporative cooling). For those reasons, alkali atoms are a suitable candidate for Bose–Einstein conden-

sation and it is thus not surprising that the first Bose–Einstein condensates are made of alkali atoms, although other kinds of species have also been used.

Bose–Einstein condensates were indeed obtained with numerous bosonic species such as  $^1\text{H}$  [157],  $^4\text{He}$  [158, 159],  $^7\text{Li}$  [160, 161],  $^{23}\text{Na}$  [9],  $^{39}\text{K}$  [162],  $^{40}\text{Ca}$  [163],  $^{41}\text{K}$  [164],  $^{52}\text{Cr}$  [165],  $^{85}\text{Rb}$  [166],  $^{87}\text{Rb}$  [8],  $^{84}\text{Sr}$  [167],  $^{86}\text{Sr}$  [168],  $^{88}\text{Sr}$  [169],  $^{133}\text{Cs}$  [170, 171],  $^{160}\text{Dy}$  [172],  $^{162}\text{Dy}$  [172],  $^{164}\text{Dy}$  [173],  $^{168}\text{Er}$  [174],  $^{170}\text{Yb}$  [175] and  $^{174}\text{Yb}$  [176]. Bose–Einstein condensates of mixtures of different isotopes of the same element were also obtained, as for instance sympathetic cooling of a mixture of  $^{87}\text{Sr}$  and  $^{88}\text{Sr}$  [169]. Mixtures of different species were also cooled down and trapped to reach Bose–Einstein condensatation like  $^{84}\text{Sr}$  or  $^{88}\text{Sr}$  with evaporatively cooled  $^{87}\text{Rb}$  [177], or  $^{41}\text{K}$  with  $^{87}\text{Rb}$  [164] or even a mixture of  $^{133}\text{Cs}$  still with  $^{87}\text{Rb}$  [178] to name a few.

The ideal picture of a noninteracting Bose–Einstein condensate depicted until here is nevertheless modified by atom–atom interaction. Indeed, contrarily to the prediction by Einstein of Bose–Einstein condensation of an ideal gas in free space, atom–atom interaction plays a major role within traps. Owing to the accumulation of bosonic particles in the ground state of the confining trap, a high density is obtained in the centre of the trap and interaction plays in this context an important role, deforming the harmonic potential experienced by the atoms and increasing the critical value  $N_{\text{cr}}$  [29].

## 2.3 Quantum scattering theory and atom–atom interaction

As we have highlighted, atom–atom interaction plays an important role in trapped Bose–Einstein condensates. However, at the very opposite naive conception one might have, this interaction should not be considered as an inconvenience but rather as a probe to explore many–body effects in a highly controlled environment. It is especially valuable in the context of quantum simulation where ultracold atoms provide an unprecedented framework for the emulation of complex many–body systems, for instance originated from condensed matter physics.

Quantum scattering theory provides the suitable framework for describing atom–atom interaction within ultracold gases. Scattering experiments indeed generally supply a remarkable investigation tool for atomic and nuclear physics, as they provide not only information about fundamental matter (the discovery of the atomic nucleus or some elementary particles, ...) but also about fundamental interactions between particles. The principle lies in illuminating a target with an incident beam and measuring the deflection of that beam by the target, which makes it a quite simple experiment to carry out. Depending on the experiment, the incident beam can be either light or massive particles, the (de Broglie, in case of massive particles) wavelength of which being comparable to that of the scatterers.

### 2.3.1 Quantum scattering theory for a dilute gas at low temperature

In this section, we consider the collision in free space of two identical atoms of mass  $m$  at positions  $\mathbf{r}_1$  and  $\mathbf{r}_2$  and interacting in the dilute regime via the two–body van der Waals

interaction potential that is asymptotically described by

$$U(|\mathbf{r}_1 - \mathbf{r}_2|) \sim \begin{cases} 1/|\mathbf{r}_1 - \mathbf{r}_2|^\alpha & \text{for } |\mathbf{r}_1 - \mathbf{r}_2| \rightarrow 0 \\ -C_6/|\mathbf{r}_1 - \mathbf{r}_2|^6 & \text{for } |\mathbf{r}_1 - \mathbf{r}_2| \rightarrow \infty \end{cases}, \quad (2.14)$$

where  $C_6 > 0$  is a constant related to the specific particles under study and  $\alpha$  is a constant. This potential vanishes as  $1/r^6$  for large  $r$  whilst it diverges for short atom–atom distances owing to the Coulomb repulsive force between each atomic nucleus. It indicates that at large distance, it acts as an attractive potential whilst at short distance, it is strongly repulsive owing to the overlap of the atomic electronic clouds. Repulsive and attractive forces equilibrate somewhere between those two asymptotic regimes, which results in a global minimum that features the possibility to form a diatomic molecule. The exact and detailed shape of the van der Waals potential is unfortunately in general not known analytically.

A gas with a density  $n$  of atoms in the trap is said dilute in the sense of an average interatomic distance  $d = n^{-1/3}$  much larger than the typical range  $r_0$  of the atom–atom interaction [153]. As a consequence, three–body or higher order collision processes are much less likely than atom–atom collisions, which justifies the restriction to a two–body interaction potential [29]. Because the dilute regime allows to work with asymptotic expressions for the scattering wavefunction we are interested in, the scattering properties shall be entirely described in this context by the scattering amplitude. Therefore, the fine details of the scattering potential are not required for a reliable description of the collision process.

The two–body Hamiltonian describing this system is given by

$$\hat{\mathcal{H}} = -\frac{\hbar^2}{2m} \left( \frac{\partial^2}{\partial \mathbf{r}_1^2} + \frac{\partial^2}{\partial \mathbf{r}_2^2} \right) + U(\mathbf{r}_1 - \mathbf{r}_2). \quad (2.15)$$

Given that the interaction potential only depends on the distance between the two particles, it is then quite natural to decouple the centre–of–mass motion from the dynamics of the relative motion through a change of reference frame. In the centre–of–mass reference frame, where we note the relative position  $\mathbf{r} = \mathbf{r}_1 - \mathbf{r}_2$ , the Hamiltonian governing the relative motion is provided by

$$\hat{H} = \frac{\hat{\mathbf{p}}^2}{2\mu} + U(\mathbf{r}) \quad (2.16)$$

and describes the motion of a particle with reduced mass  $\mu = m/2$  and relative momentum  $\mathbf{p} = (\mathbf{p}_1 - \mathbf{p}_2)/2$  in the presence of a central scattering potential  $U(\mathbf{r})$ . This change of reference frame casts the two–body problem into an effective one–body scattering problem described by the following time–dependent Schrödinger equation

$$i\hbar \frac{\partial}{\partial t} \Psi(\mathbf{r}, t) = \left( -\frac{\hbar^2}{2\mu} \Delta + U(\mathbf{r}) \right) \Psi(\mathbf{r}, t), \quad (2.17)$$

generated by the Hamiltonian (2.16), with  $\Psi(\mathbf{r}, t)$  the wavefunction for the relative motion. In the steady–state regime and if the incident matter waves have well–defined energy  $E_k = \hbar^2 k^2 / 2\mu$ , with  $k \in \mathbb{R}$ , we can treat them as plane waves and make the Ansatz  $\Psi(\mathbf{r}, t) =$

$\psi(\mathbf{r})e^{-iE_k t/\hbar}$ . The scattering states  $\psi(\mathbf{r})$  of the relative motion are then solution of the stationary Schrödinger equation

$$\left(-\frac{\hbar^2}{2\mu}\Delta + U(\mathbf{r})\right)\psi(\mathbf{r}) = E_k\psi(\mathbf{r}). \quad (2.18)$$

In view of applying the technique of Green's functions to solve Eq. (2.18), in a fashion very similar to that in Chapter 1, we rewrite Eq. (2.18) under the following form

$$(\Delta + k^2)\psi(\mathbf{r}) = \frac{2\mu}{\hbar^2}U(\mathbf{r})\psi(\mathbf{r}), \quad (2.19)$$

where we treat the right hand side as an inhomogeneity, although it is proportional to  $\psi(\mathbf{r})$ . This equation can be solved by the technique of Green's functions which yields the solution under the integral form

$$\psi(\mathbf{r}) = \phi_0(\mathbf{r}) + \frac{2\mu}{\hbar^2} \int G(\mathbf{r} - \mathbf{r}')U(\mathbf{r}')\psi(\mathbf{r}')d\mathbf{r}', \quad (2.20)$$

where the first term  $\phi_0(\mathbf{r})$  corresponds to the incident wave and satisfies the homogeneous Helmholtz equation  $(\Delta + k^2)\phi_0(\mathbf{r}) = 0$ . Since we treat the incident waves as plane waves, we write

$$\phi_0(\mathbf{r}) = \phi_0 e^{i\mathbf{k}\cdot\mathbf{r}} = \phi_0 e^{ikz} \quad (2.21)$$

with  $\phi_0$  the incident amplitude of a wave propagating, without loss of generality, along the  $z$ -axis. The second term of Eq. (2.20) is obtained thanks to the Green's function  $G(\mathbf{r} - \mathbf{r}')$  which satisfies

$$(\Delta + k^2)G(\mathbf{r} - \mathbf{r}') = \delta(\mathbf{r} - \mathbf{r}'), \quad (2.22)$$

where the inhomogeneous part of Eq. (2.19) has been replaced by a delta distribution. This equation, that just involves a delta distribution instead of the (possibly complicated) scattering potential is much easier to solve than the original equation (2.19) and allows one to write Eq. (2.19) under the formally equivalent self-consistent integral form (2.20). The Green's function in Eq. (2.22) is given by

$$G^\pm(\mathbf{r} - \mathbf{r}') = -\frac{1}{4\pi} \frac{e^{\pm ik|\mathbf{r}-\mathbf{r}'|}}{|\mathbf{r} - \mathbf{r}'|}, \quad (2.23)$$

that describes a spherical wave and where the  $\pm$  sign delineates the existence of a Green's function related to ingoing waves ( $-$ ) and another one to outgoing waves ( $+$ ). The choice between those depends upon the problem one wants to solve. Since we are looking here for scattering states, we are looking for states corresponding to outgoing waves, which amounts to keeping the positive sign in the exponential, that is the ( $+$ ) Green's function in (2.23). It turns out that Eq. (2.20) can be written as

$$\psi(\mathbf{r}) = \phi_0 e^{ikz} - \frac{\mu}{2\pi\hbar^2} \int \frac{e^{ik|\mathbf{r}-\mathbf{r}'|}}{|\mathbf{r} - \mathbf{r}'|} U(\mathbf{r}')\psi(\mathbf{r}') d^3r', \quad (2.24)$$

which is known as the *Lippmann–Schwinger equation* [179]. This self-consistent equation remains implicit for the solution  $\psi(\mathbf{r})$ , but marks the starting point for an iterative solution



based on successive approximations

$$\begin{aligned}
\psi(\mathbf{r}) &= \phi_0 e^{ikz} \\
&\quad - \frac{\mu}{2\pi\hbar^2} \int G(\mathbf{r} - \mathbf{r}') U(\mathbf{r}') \phi_0(\mathbf{r}') d^3r' \\
&\quad + \left( \frac{\mu}{2\pi\hbar^2} \right)^2 \iint G(\mathbf{r} - \mathbf{r}') U(\mathbf{r}') G(\mathbf{r}' - \mathbf{r}'') U(\mathbf{r}'') \phi_0(\mathbf{r}'') d^3r' d^3r'' \\
&\quad - \dots, \\
&= \phi_0 e^{ikz} + \sum_{n=1}^{\infty} \left[ \left( -\frac{\mu}{2\pi\hbar^2} \right)^n \int \dots \int G(\mathbf{r} - \mathbf{r}_1) U(\mathbf{r}_1) \right. \\
&\quad \left. \dots G(\mathbf{r}_{n-1} - \mathbf{r}_n) U(\mathbf{r}_n) \phi_0(\mathbf{r}_n) d^3r_1 \dots d^3r_n \right]. \quad (2.25)
\end{aligned}$$

We observe that each contribution describes a sequence of free propagations from point  $\mathbf{r}_n$  to point  $\mathbf{r}_{n-1}$  described by the Green's function that are interrupted by scattering events, those contributions forming a so-called Born series. This reflects that  $\psi(\mathbf{r})$  is composed of a sum of contributions ranging from the direct contribution of the incident wave that directly reaches  $\mathbf{r}$  to the contribution that includes an infinite number of scattering events of the incident wave before reaching  $\mathbf{r}$ , as is diagrammatically shown in Eq. (2.26)

$$\psi(\mathbf{r}) = \text{---} \rightarrow \mathbf{r} + \text{---} \xrightarrow{U(\mathbf{r}')} \bullet_{\mathbf{r}'} \text{---} \rightarrow \mathbf{r} + \text{---} \xrightarrow{U(\mathbf{r}'')} \bullet_{\mathbf{r}''} \xrightarrow{U(\mathbf{r}')} \bullet_{\mathbf{r}'} \text{---} \rightarrow \mathbf{r} + \dots \quad (2.26)$$

In practice, one truncates the Born series, which amounts to writing the approximation of order  $n$  of the solution as

$$\psi^{(n)}(\mathbf{r}) = \phi_0 e^{ikz} - \frac{\mu}{2\pi\hbar^2} \int G(\mathbf{r} - \mathbf{r}') U(\mathbf{r}') \psi^{(n-1)}(\mathbf{r}') d^3r', \quad (2.27)$$

and iterating step by step to obtain this approximation of order  $n$  of the solution from that of order  $n - 1$ . It is common to truncate the Born series at the first order, hence putting  $\psi(\mathbf{r}') \equiv \phi_0(\mathbf{r}')$  in the right-hand-side of (2.27), thus giving rise to the so-called *Born approximation* [180] that is given by

$$\psi^{(1)}(\mathbf{r}) = \phi_0 e^{ikz} - \frac{\mu}{2\pi\hbar^2} \int G(\mathbf{r} - \mathbf{r}') U(\mathbf{r}') \phi_0(\mathbf{r}') d^3r'. \quad (2.28)$$

Although this method is approximative, since it describes the scattered wave only in terms of the incident wave and waves issued from a single scattering event, it is used in various configurations [181, 182].

### 2.3.2 Low energy scattering in the far-field limit

Since in a dilute gas the relevant length scale for interaction is much lower than the average atom–atom distance [29], we are interested in the asymptotic behaviour of the solution  $\psi(\mathbf{r})$  in the far-field limit, corresponding to  $r \rightarrow \infty$ . Because the integration in (2.24) is in practice restricted to a spatial extension given by the finite range  $R$  of the scattering potential, we

can safely write in the limit  $R \ll r$  that  $|\mathbf{r} - \mathbf{r}'| \simeq r - \mathbf{r}' \cdot \mathbf{e}_r$ , where  $\mathbf{e}_r$  is a unit vector pointing in the direction carried by  $\mathbf{r}$ . This allows us to express the Green's function (5.8) as

$$G^\pm(\mathbf{r} - \mathbf{r}') \approx -\frac{1}{4\pi} e^{ikr} e^{-ik\mathbf{r}' \cdot \mathbf{e}_r}, \quad (2.29)$$

and the Lippmann–Schwinger equation (2.24) exhibits the asymptotic expression given by

$$\psi(\mathbf{r}) \stackrel{R \ll r}{\approx} \phi_0 e^{ikz} + \underbrace{\left[ -\frac{\mu}{2\pi\hbar^2} \int e^{-ik\mathbf{r}' \cdot \mathbf{e}_r} U(\mathbf{r}') \psi(\mathbf{r}') d^3r' \right]}_{f(\mathbf{k}, \mathbf{k}')} \frac{e^{ikr}}{r}, \quad (2.30)$$

where we have introduced the scattering amplitude  $f(\mathbf{k}, \mathbf{k}')$  that characterises the angular dependence of the scattering state in the direction carried by  $\mathbf{k}'$ . This expression for the asymptotic behaviour for  $R \ll r$  of the scattering state shows that the scattering state consists in the sum of the incident wave and an outgoing spherical wave weighted by a directional factor  $f(\mathbf{k}, \mathbf{k}')$  that encodes all the physics related to the scattering potential, as illustrated in FIG. 2.5.

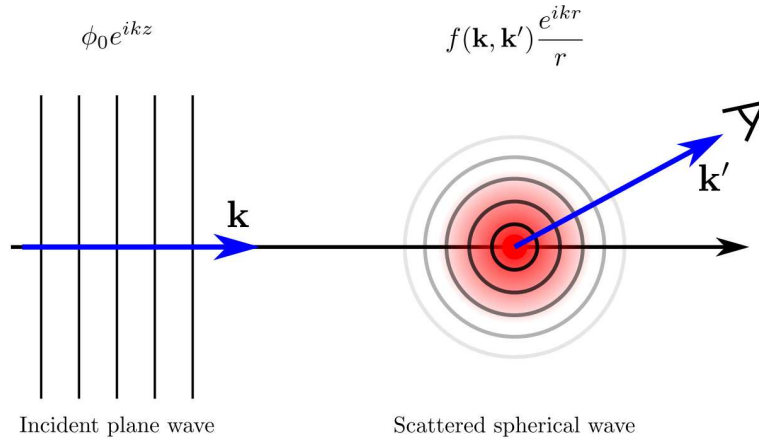


Figure 2.5 – In the far-field limit, an incident plane wave  $e^{ikz}$  is scattered as an outgoing spherical  $e^{ikr}/r$  wave weighted by the scattering amplitude  $f(\mathbf{k}, \mathbf{k}')$  that encodes the directional dependence of the scattered wavefunction owing to the details of the scattering potential.

Due to the very low temperatures involved with Bose–Einstein condensates, the associated average kinetic energy and wavevector are also very small. In the limit of low energy collisions where both  $k \rightarrow 0$  and  $k' \rightarrow 0$ , we can write that  $e^{ikz} \rightarrow 1$ ,  $e^{ikr} \rightarrow 1$  and consequently that  $e^{-ik\mathbf{r}' \cdot \mathbf{e}_r} \rightarrow 1$ . In this formal combined limit, the scattering amplitude reads

$$f(\mathbf{k}, \mathbf{k}') \stackrel{k \rightarrow 0}{\approx} -\frac{\mu}{4\pi\hbar^2} \int U(\mathbf{r}') \psi(\mathbf{r}') d^3r' \equiv -a_S, \quad (2.31)$$

where  $a_S$  is the so-called *s-wave scattering length*. In the low energy limit,  $a_S$  entirely governs the scattering, since the wavefunction provided in Eq. (2.30) reads

$$\psi(\mathbf{r}) \stackrel{k \rightarrow 0}{\approx} 1 - \frac{a_S}{r}, \quad (2.32)$$

where we have set the amplitude  $\phi_0$  of the incident wave to one for simplicity. Since the scattering amplitude is perfectly isotropic, the scattered wavefunction acquires a perfectly spherical symmetry, irrespective of the exact shape and details of the scattering potential. Therefore, in the low–energy limit, any scattering potential that is designed to provide the same scattering length also yields the same wavefunction (for  $R \ll r$ ) as the true interaction potential. This can be leveraged to replace the complicated (and whose analytical expression is lacking) van der Waals interaction potential with a pseudopotential that is carefully designed to produce the same s–wave scattering length. Amongst all pseudopotentials that yield the same s–wave scattering length, we should choose one that renders the calculations easy.

Owing to the diluteness of the gas, that implies an interparticle distance much larger than the length scale relevant for interaction, it is most natural to choose a contact pseudopotential, as was first proposed by Fermi [183]. This pseudopotential reads

$$U_F(\mathbf{r}) = g\delta(\mathbf{r}), \quad (2.33)$$

where the interaction strength  $g$  must be determined so that a scattering process in the presence of the pseudopotential (2.33) in the low energy limit ends up with the same value for  $a_s$  as would arise in the presence of the true interaction potential. This appealing pseudopotential however raises a divergence when inserted in the Lippmann–Schwinger equation (2.24), owing to the presence of a  $1/r$  singularity in the resulting equation.

The Fermi–Huang pseudopotential provides a solution to that issue. It is quite similar in essence to the Fermi pseudopotential and essentially consists in a regularisation of this pseudopotential in such a way that it can handle the presence of a  $1/r$  singularity. Its action in position representation on the total wavefunction  $\psi(\mathbf{r})$  reads

$$U_{FH}(\mathbf{r})\psi(\mathbf{r}) = g\delta(\mathbf{r})\frac{\partial r\psi(\mathbf{r})}{\partial r} \quad (2.34)$$

and provides the following wavefunction when inserted in the Lippmann–Schwinger equation (2.24)

$$\psi(\mathbf{r}) = e^{ikz} - \frac{1}{\frac{2\pi\hbar^2}{g\mu} + ik} \frac{e^{ikr}}{r}, \quad (2.35)$$

that is, the same form as Eq. (2.30). In the low–energy scattering limit where  $k, k' \rightarrow 0$  and provided that we define the interaction strength as

$$g = \frac{2\pi\hbar^2 a_S}{\mu} = \frac{4\pi\hbar^2 a_S}{m}, \quad (2.36)$$

we can write the wavefunction  $\psi(\mathbf{r})$  in the same way as in Eq. (2.32). The interaction strength defined in Eq. (2.36) governs entirely the atom–atom interaction in the low–energy limit without requiring the knowledge and full details of the atom–atom interaction potential: it only depends upon the s–wave scattering length. The same definition of the interaction strength  $g$  would have been obtained by computing the scattering amplitude in the Born approximation

$$f^{(1)}(\mathbf{k}, \mathbf{k}') = -\frac{\mu}{2\pi\hbar^2} \int G(\mathbf{r} - \mathbf{r}') U_{FH}(\mathbf{r}') \phi(\mathbf{r}') d^3r' \quad (2.37)$$

with the Fermi–Huang pseudopotential  $U_{\text{FH}}(\mathbf{r})$  used instead of the exact scattering potential  $U(\mathbf{r})$ . Therefore, for such a pseudo–potential, the scattered part of the wavefunction can be considered as a small perturbation in comparison to the incident wave and the Fermi–Huang pseudopotential gives always rise to scattering only in the s–wave channel, not only when  $k \rightarrow 0$ .

### 2.3.3 Tuning the effective interaction by leveraging Feshbach resonances

When there exists a closed channel that possesses a bound state whose energy matches the kinetic incident energy  $E \rightarrow 0$  of the free colliding particles, as is shown in FIG. 2.6, a coupling between that closed channel and the entrance channel may be realised, provided such a coupling exists. In that case, there is a non negligible probability that the particles collide in the closed scattering channel to form a metastable state of short lifetime. This coupling between the entrance and the closed channels may dramatically alter the atomic s–wave scattering length and is known as Feshbach resonances [184,185] (see the nice review articles [17,186]).

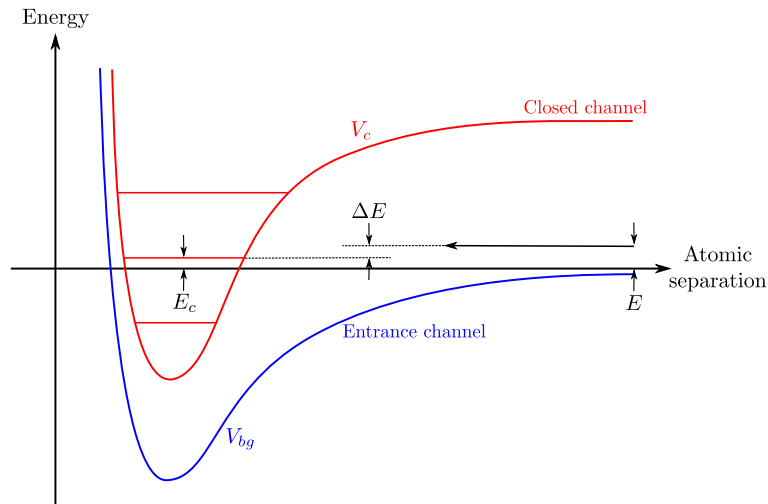


Figure 2.6 – Working principle of Feshbach resonances where a controlled coupling between the entrance channel and a closed channel may be realised to tune the s–wave scattering length and the effective atom–atom interaction strength. Figure adapted from [29].

The closed channel is referred to as closed because asymptotically, it is unreachable due to its energy that is forbidden for the colliding particles that most naturally scatter in the entrance channel. The coupling may be achieved by any mechanism that connects the two channels. The most frequent mechanism is to use an external magnetic field  $B$  that modifies the energy of the bound state in the closed channel due to the Zeeman effect. This magnetic dependence of the bound state energy allows one to finely tune the energy gap  $\Delta E$  and by extension the s–wave scattering length whose expression is given in Ref. [187], that is,

$$a_s = a_{\text{bg}} \left( 1 + \frac{\Delta B}{B - B_0} \right), \quad (2.38)$$

where  $a_{\text{bg}}$  is the background scattering length,  $B_0$  is the resonant magnetic field and  $\Delta B$  is the so-called resonance width. Since no constraint act on the sign of neither  $a_{\text{bg}}$  nor  $\Delta B$ , the s-wave scattering length can be tuned positive or negative by leveraging those magnetically-induced Feshbach resonances. The atomic gas can therefore switch from a repulsive to an attractive interaction and vice-versa. There exists other coupling mechanisms, such as for instance by laser light (optically-induced Feshbach resonances) that can be useful when the tuning by a magnetic field is not present.

## 2.4 Mean-field description of Bose–Einstein condensates

Bose–Einstein condensation has been qualitatively described, as well as how to handle the presence of an atom–atom interaction in the low energy limit. In this section, we establish the suitable mathematical framework to describe Bose–Einstein condensates in the mean-field limit, which is of fundamental relevance in the context of this manuscript. To that end, we consider a dilute gas of bosonic particles that interact through the two-body interaction potential  $U(|\mathbf{r} - \mathbf{r}'|)$  and that is under the influence of an external potential  $V(\mathbf{r}, t)$ . This potential can be for instance a confinement potential that models a trap and/or a disorder potential towards which the bosonic particles propagate. Such a system is governed by the many-body Hamiltonian

$$\begin{aligned} \hat{H} = & \int \hat{\psi}^\dagger(\mathbf{r}, t) \left( \frac{-\hbar^2}{2m} \Delta + V(\mathbf{r}, t) \right) \hat{\psi}(\mathbf{r}, t) d\mathbf{r} \\ & + \frac{1}{2} \iint \hat{\psi}^\dagger(\mathbf{r}, t) \hat{\psi}^\dagger(\mathbf{r}', t) U(|\mathbf{r} - \mathbf{r}'|) \hat{\psi}(\mathbf{r}', t) \hat{\psi}(\mathbf{r}, t) d\mathbf{r} d\mathbf{r}', \end{aligned} \quad (2.39)$$

where  $\hat{\psi}(\mathbf{r}, t)$  (resp.  $\hat{\psi}^\dagger(\mathbf{r}, t)$ ) is the annihilation (resp. creation) field operator that destroys (resp. creates) a particle at position  $\mathbf{r}$  and time  $t$ . As bosonic operators, they satisfy the following commutation relations

$$[\hat{\psi}(\mathbf{r}, t), \hat{\psi}^\dagger(\mathbf{r}', t)] = \delta(\mathbf{r} - \mathbf{r}'), \quad (2.40)$$

$$[\hat{\psi}(\mathbf{r}, t), \hat{\psi}(\mathbf{r}', t)] = [\hat{\psi}^\dagger(\mathbf{r}, t), \hat{\psi}^\dagger(\mathbf{r}', t)] = 0. \quad (2.41)$$

Field operators are related to creation and annihilation operators associated with an orthonormal single-particle basis  $|\phi_k\rangle$  through

$$\hat{\psi}(\mathbf{r}, t) = \sum_{k=0}^{\infty} \langle \mathbf{r} | \phi_k \rangle \hat{a}_k \quad (2.42)$$

$$\hat{\psi}^\dagger(\mathbf{r}', t) = \sum_{k=0}^{\infty} \langle \mathbf{r}' | \phi_k \rangle^* \hat{a}_k^\dagger, \quad (2.43)$$

where  $\hat{a}_k$  (resp.  $\hat{a}_k^\dagger$ ) is the annihilation (resp. creation) operator related to the mode  $k$

$$\hat{a}_k |n_0, n_1, \dots, n_k, \dots\rangle = \sqrt{n_k} |n_0, n_1, \dots, n_k - 1, \dots\rangle \quad (2.44)$$

$$\hat{a}_k^\dagger |n_0, n_1, \dots, n_k, \dots\rangle = \sqrt{n_k + 1} |n_0, n_1, \dots, n_k + 1, \dots\rangle, \quad (2.45)$$

where  $n_k$  is the eigenvalue of the number operator  $\hat{n}_k = \hat{a}_k^\dagger \hat{a}_k$  corresponding to the occupation number of the  $k$  mode. As bosonic operators, they also have to obey

$$\begin{aligned} [\hat{a}_k, \hat{a}_{k'}^\dagger] &= \delta_{kk'} \\ [\hat{a}_k, \hat{a}_{k'}] &= [\hat{a}_k^\dagger, \hat{a}_{k'}^\dagger] = 0. \end{aligned}$$

The total number of particles can be expressed via those operators through

$$N = \sum_{k=0}^{\infty} \hat{a}_k^\dagger \hat{a}_k = \int \hat{\psi}^\dagger(\mathbf{r}, t) \hat{\psi}(\mathbf{r}, t) d\mathbf{r}. \quad (2.46)$$

Following the prescription of the previous section, we replace the true van der Waals interaction potential  $U(|\mathbf{r} - \mathbf{r}'|)$  by the Fermi–Huang pseudopotential which results in the following two-body Hamiltonian

$$\hat{H} = \int \hat{\psi}^\dagger(\mathbf{r}, t) \left( \frac{-\hbar^2}{2m} \Delta + V(\mathbf{r}, t) \right) \hat{\psi}(\mathbf{r}, t) d\mathbf{r} + \frac{g}{2} \iint \hat{\psi}^\dagger(\mathbf{r}, t) \hat{\psi}^\dagger(\mathbf{r}', t) \hat{\psi}(\mathbf{r}', t) \hat{\psi}(\mathbf{r}, t) d\mathbf{r} d\mathbf{r}', \quad (2.47)$$

with the interaction strength  $g$  defined in Eq. (2.36). The time evolution for the field operators is given by the Heisenberg equation

$$i\hbar \frac{\partial}{\partial t} \hat{\psi}(\mathbf{r}, t) = [\hat{\psi}(\mathbf{r}, t), \hat{H}] \quad (2.48)$$

which allows us to write, owing to the commutation relations of the bosonic fields prescribed in Eq. (2.41), that

$$i\hbar \frac{\partial}{\partial t} \hat{\psi}(\mathbf{r}, t) = \left[ \frac{-\hbar^2}{2m} \Delta + V(\mathbf{r}, t) + g \int \hat{\psi}^\dagger(\mathbf{r}', t) \hat{\psi}(\mathbf{r}', t) d\mathbf{r}' \right] \hat{\psi}(\mathbf{r}, t). \quad (2.49)$$

Solving this equation for a reasonable number of particles demands a formidable amount of numerical resources and justifies that we simplify the description by using a mean-field theory that provides the behaviour of the interacting condensate in terms of physical parameters.

As we already highlighted, the ground state of a Bose–Einstein condensate is much more populated than any other mode so that  $n_0 \gg n_i$  for every  $i > 0$ . This justifies to decompose the creation field operator as

$$\hat{\psi}(\mathbf{r}, t) = \langle \mathbf{r} | \phi_0 \rangle \hat{a}_0 + \sum_{k=1}^{\infty} \langle \mathbf{r} | \phi_k \rangle \hat{a}_k = \phi_0(\mathbf{r}, t) \hat{a}_0 + \delta\hat{\psi}(\mathbf{r}, t), \quad (2.50)$$

where we have noted  $\phi_0(\mathbf{r}, t) = \langle \mathbf{r} | \phi_0 \rangle$  and separated the ground state from the excited states, following the same argument as previously. Because only the ground state contributes significantly to the total population, we can treat the contribution of the other modes constituting the thermal cloud as a small perturbation  $\delta\hat{\psi}(\mathbf{r}, t)$  to the field operator  $\hat{\psi}(\mathbf{r}, t)$ .

The essence of the mean-field approximation is to replace quantum operators by c-numbers. To that end, we neglect the perturbation  $\delta\hat{\psi}(\mathbf{r}, t)$  to the field operator  $\hat{\psi}(\mathbf{r}, t)$  in Eq. (2.50) and define the condensate wavefunction [153, 154] as

$$\psi(\mathbf{r}, t) = \langle \dots, \mathcal{N} - 1, \dots | \hat{\psi}(\mathbf{r}, t) | \dots, \mathcal{N}, \dots \rangle \approx \sqrt{\mathcal{N}} \phi_0(\mathbf{r}, t). \quad (2.51)$$

We then apply the Bogoliubov prescription and replace the field operator  $\hat{\psi}(\mathbf{r}, t)$  by the condensate wavefunction  $\psi(\mathbf{r}, t)$  defined in Eq. (2.51). This replacement is justified in the limit of a very large number  $\mathcal{N}$  in the ground state, since the action of  $\hat{a}_0$  or  $\hat{a}_0^\dagger$  (which are the only surviving operator in Eq. (2.50) and its complex conjugate if one neglects the perturbation  $\delta\hat{\psi}(\mathbf{r}, t)$  compared to  $\phi_0(\mathbf{r}, t)\hat{a}_0$ ) onto the ground state yields  $\mathcal{N} \pm 1 \approx \mathcal{N}$ , which mostly preserves the condensate. The field operator now matches a classical field and thus describes the system as a classical object, following exactly the same procedure as in electrodynamics, where the electromagnetic field description replaces a description in terms of photons. This treatment works particularly well for dilute gases at extremely low temperatures [29].

If we inject the expression of the wavefunction condensate defined in Eq. (2.51) in the Hamiltonian in Eq. (2.49), we obtain

$$i\hbar \frac{\partial}{\partial t} \psi(\mathbf{r}, t) = \left[ \frac{-\hbar^2}{2m} \Delta + V(\mathbf{r}, t) + g|\psi(\mathbf{r}, t)|^2 \right] \psi(\mathbf{r}, t), \quad (2.52)$$

which is referred to as the time-dependent Gross–Pitaevskii equation [188, 189] that describes the ground state of a Bose–Einstein condensate in the mean-field limit. It appears as a nonlinear Schrödinger equation with a nonlinear interaction energy  $g|\psi(\mathbf{r}, t)|^2$  that results from the mean-field description of the many-body problem in terms of an effective one-body problem. This interaction energy is proportional to the interaction strength  $g$  and to the local density of particles at position  $\mathbf{r}$  and acts as an effective potential generated by the other particles. It works particularly well for very weak interaction strengths for which the depletion of the condensate due to interaction to the benefit of the thermal cloud is negligible.

Provided that the nonlinearity is small enough and the external potential is static, a stationary scattering state is found by using the separation Ansatz

$$\psi(\mathbf{r}, t) = \psi(\mathbf{r}) e^{-i\mu t/\hbar}, \quad (2.53)$$

where  $\mu$  is the chemical potential, and which, after insertion in Eq. (2.52), yields

$$\left( \frac{-\hbar^2}{2m} \Delta + V(\mathbf{r}) + g|\psi(\mathbf{r})|^2 \right) \psi(\mathbf{r}) = \mu \psi(\mathbf{r}). \quad (2.54)$$

A major drawback of this equation is that the convergence towards a stable steady scattering state is limited to very weak interaction strengths [190], as for higher nonlinearities, a steady state might be unreachable, owing to the presence of dynamical instabilities [191, 192]. Furthermore, the mean-field approximation does not take into account inelastic scattering that plays a major role in the presence of finite interaction, as we discussed in Chapter 1. The truncated Wigner method that we extensively discuss in Chapter 3 offers a solution to those drawbacks.

Despite those limitations, the Gross–Pitaevskii equation has been successfully applied in a wide variety of contexts, ranging from the description of Bose–Einstein condensates in optical lattices [193] or the propagation of solitons [194] to the study of Josephson effect with Bose–Einstein condensates [195, 196], to name a few.

## 2.5 Atom lasers

Amongst all their fascinating properties, Bose–Einstein condensates exhibit a high degree of coherence related to the phase of the condensate wavefunction. That high degree of coherence can be highlighted through the ability of the condensate to display interference effects, in great analogy with interference effects that occur with coherent light. This has been for instance demonstrated by measurements of the spatial coherence of Bose–Einstein condensates in a double slit–like experiment [197] (usually referred to as the Munich experiment) or by the interference between two freely expanding Bose–Einstein condensates [198]. As we explain in the following, those properties of coherence are leveraged to produce coherent matter wave beams referred to as *atom lasers*.

Indeed, motivated by the optical laser that allows to produce a beam of photons that is highly monochromatic, coherent, directional and that can be sharply focussed, researchers were in the 90’s interested in realising a device with similar properties but which emits matter waves instead of photons. The exceptional degree of coherence featured by Bose–Einstein condensates makes it an ideal candidate to produce such coherent matter waves, as the above discussion highlights. Condensates indeed contain a large number of bosonic particles that macroscopically occupy the ground state, all of which thus sharing the same wavefunction with a well–defined phase. It is then not surprising that Bose–Einstein condensates were used as a coherent source of matter waves in the first experimental atom laser that was realised by the end of 1996 [199] and was quickly followed by experimental realisations of other research groups [200–202].

The notion of coherence in this context is to be understood in terms of the ability for the bosonic matter wave from a Bose–Einstein condensate to display interference effects resulting from the interference of the various wave components that form the matter wave beam, as in Refs. [197, 198]. This offers a very sensitive probe to explore interference effects in complex many–body systems. It indeed opens immediate applications in the context of atom optics, atom interferometry and even atom holography [203] but also offers new perspectives for the realisation of bosonic atomtronic components [204–206] as well as to allow comparison with their fermionic equivalent [45, 207, 208]. Beside this high coherence degree, atom lasers are also an ideal source producing nearly monochromatic matter waves [209] which can be approximately described as plane waves. Compared to the transport of a wavepacket, this description of the matter waves in terms of plane waves allows to put aside an additional complexity, for instance related to the width of the wavepacket, in the scattering arising in transport processes and settles an idealised context for their theoretical description.

The principle of an atom laser is to outcouple atoms from a trapped Bose–Einstein condensate into a waveguide in a finely controlled manner. Depending on whether the trap used to confine the atoms is optical or magnetic, several outcoupling methods are envisaged. In the



case of optical traps, the outcoupling can be performed by varying the depth of the optical trap so that atoms can tunnel out [209]. For magnetic traps, the principle is to transfer atoms from the hyperfine trapped state to an untrapped state. This transfer can be performed either via a multiphoton optical transition, which is known as Raman atom lasers [201, 210, 211] or by applying a monochromatic radio-frequency radiation (the so-called radio-frequency knife [199, 202, 212, 213]). It consists in sending an electromagnetic radiation that couples the trapped hyperfine state with a state that is not affected by the trapping potential and which is then referred to as untrapped state, so that the radiation “cuts” atoms from the trap to the free space.

Because atoms possess a mass, they fall under the action of gravity so that their de Broglie wavelength  $\lambda_{dB} = h/mv$  decreases quickly as a result of their fall. This is a major drawback because a large and well-defined de Broglie wavelength is required in various studies related to quantum transport. The solution proposed in Ref. [212] is to superimpose to the magnetic trap a horizontal matter wave guide, which can be obtained by illuminating the released atoms by a far detuned laser beam, that cancels the effects of gravity and squeezes the motion of the atoms in the  $x$ -direction. In great analogy with an optical laser, this setup, which is sketched in FIG. 2.7, provides a one-dimensional flux of atoms that is highly coherent and whose de Broglie wavelength can be adjusted by varying the frequency of the radio-frequency radiation, although some atoms ( $\sim 15\%$  in Ref. [214]) are found in some transverse excited states of the waveguide.

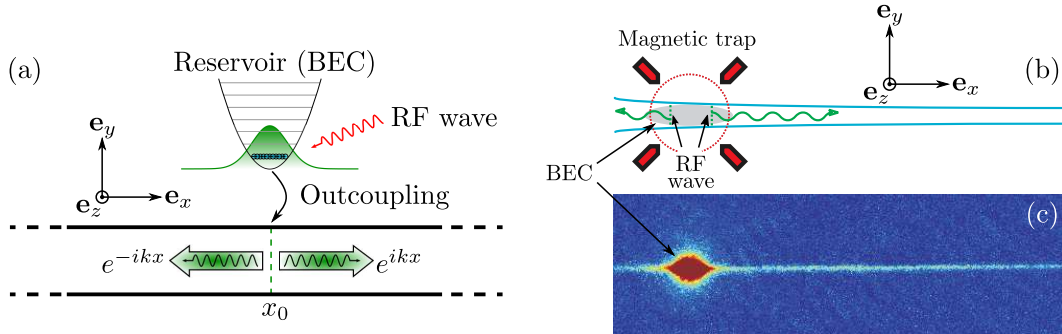


Figure 2.7 – Panel (a): Sketch of a typical atom laser where atoms are outcoupled from a Bose–Einstein condensate to a one-dimensional matter wave guide where plane waves  $e^{\pm ikx}$  are injected, forming a one-dimensional beam of monochromatic coherent matter waves of tunable wavelength  $\lambda_{dB}$ . Panels (b)–(c): Experimental realisation [212] of an atom laser where a horizontal optical potential is superimposed to the magnetic trap, allowing that outcoupled atoms are squeezed in the  $x$ -direction to form an atom laser. Right panel adapted from [212].

In the experimental realisation depicted in FIG. 2.7(b)–(c), the experimental setup produces a condensate containing a high number  $\mathcal{N}$  of  $^{87}\text{Rb}$  atoms at a very low temperature  $T$  and the chemical potential  $\mu$  and which are in the hyperfine  $|F, m_F\rangle = |1, -1\rangle$  trapped state. We treat this condensate in the idealised limit  $\mathcal{N} \rightarrow \infty$  and  $T \rightarrow 0$ . The outcoupling of atoms from the condensate consists in flipping the spin of the atoms, thereby coupling the “low-field seeker”  $|F, m_F\rangle = |1, -1\rangle$  trapped state to the  $|F, m_F\rangle = |1, 0\rangle$  state, which is not

affected by the presence of a magnetic trap. This coupling is performed by applying a radio-frequency radiation [202] which releases atoms in the matter wave guide with the kinetic energy  $mv^2/2 = \mu$ . The matter wave guide is obtained by imposing a strong confinement realised in the presence of the following optical potential

$$V_{\text{wg}}(\mathbf{r}) = \frac{1}{2}m\omega_{\perp}^2(x)(y^2 + z^2) \quad (2.55)$$

that squeezes the motion of the untrapped atoms along the  $x$ -direction.

### 2.5.1 Theoretical description of an atom laser

In order to provide a set of evolution equations for the field operators related to the atoms of the system under study, we introduce the field operator  $\hat{\Psi}(\mathbf{r}, t)$  of the atoms in the matter wave guide, which are in the hyperfine  $|F, m_F\rangle = |1, 0\rangle$  untrapped state. We also introduce  $\hat{\Phi}(\mathbf{r}, t)$ , the field operator of the atoms which are still confined within the source, in the hyperfine  $|F, m_F\rangle = |1, -1\rangle$  trapped state. In the absence of interaction between the atoms within the trap, as well as in the absence of interaction between trapped and untrapped atoms, the many-body Hamiltonian related to this system reads [215]

$$\begin{aligned} \hat{H} = & \int \hat{\Psi}^\dagger(\mathbf{r}, t) \left( -\frac{\hbar^2}{2m}\Delta + V(\mathbf{r}) \right) \hat{\Psi}(\mathbf{r}, t) d^3r + \int \hat{\Phi}^\dagger(\mathbf{r}, t) \left( -\frac{\hbar^2}{2m}\Delta + V_{\text{trap}}(\mathbf{r}) \right) \hat{\Phi}(\mathbf{r}, t) d^3r \\ & + \iint U(|\mathbf{r} - \mathbf{r}'|) \hat{\Psi}^\dagger(\mathbf{r}, t) \hat{\Psi}^\dagger(\mathbf{r}', t) \hat{\Psi}(\mathbf{r}', t) \hat{\Psi}(\mathbf{r}, t) d^3r d^3r' \\ & + \int C(t) \hat{\Psi}^\dagger(\mathbf{r}, t) \hat{\Phi}(\mathbf{r}, t) d^3r + \int C^*(t) \hat{\Phi}^\dagger(\mathbf{r}, t) \hat{\Psi}(\mathbf{r}, t) d^3r, \end{aligned} \quad (2.56)$$

where  $U(|\mathbf{r} - \mathbf{r}'|)$  is the atom–atom interaction term between outcoupled atoms,  $C(t)$  is the coupling strength between the source and the matter wave guide and  $V(\mathbf{r}) = V_{\text{ext}}(\mathbf{r}) + V_{\text{wg}}(\mathbf{r})$  is the total potential. The coupling strength between the source and the matter wave guide is adiabatically ramped from zero to a constant value which is related to the strength of the applied radio-frequency field. The Heisenberg equation provides equations of motion for the field operators which evolve according to

$$i\hbar \frac{\partial \hat{\Psi}(\mathbf{r}, t)}{\partial t} = \left( -\frac{\hbar^2}{2m}\Delta + V(\mathbf{r}) \right) \hat{\Psi}(\mathbf{r}, t) + U(|\mathbf{r} - \mathbf{r}'|) \hat{\Psi}^\dagger(\mathbf{r}, t) \hat{\Psi}(\mathbf{r}, t) \hat{\Psi}(\mathbf{r}, t) + C(t) \hat{\Phi}(\mathbf{r}, t) \quad (2.57)$$

$$i\hbar \frac{\partial \hat{\Phi}(\mathbf{r}, t)}{\partial t} = \left( -\frac{\hbar^2}{2m}\Delta + V_{\text{trap}}(\mathbf{r}) \right) \hat{\Phi}(\mathbf{r}, t) + C^*(t) \hat{\Psi}(\mathbf{r}, t). \quad (2.58)$$

In the idealised limit of  $\mathcal{N} \rightarrow \infty$  and  $T \rightarrow 0$  that we initially considered, we can neglect the population of the thermal cloud and assume that all atoms are in the ground state. We thus make the single mode decomposition Ansatz for the field operator of the atoms in the reservoir  $\hat{\Phi}(\mathbf{r}, t) = \phi_0(\mathbf{r}) \hat{\phi}_{\mathcal{S}}(t)$ , where  $\phi_0(\mathbf{r})$  is the ground state wavefunction of energy  $\mu$  and  $\hat{\phi}_{\mathcal{S}}(t)$  the related field operator.

Similarly, we also assume that the propagation in the matter wave guide occurs in the transverse ground state  $\chi_0(y, z)$ . We thus decompose the field operator  $\hat{\Psi}(\mathbf{r}, t)$  of the atoms in the

matter wave guide as  $\hat{\Psi}(\mathbf{r}, t) = \chi_0(y, z)\hat{\psi}(x, t)$ , with  $\hat{\psi}(x, t)$  the field operator related to that decomposition [51]. This allows us to rewrite the evolution equations for the field operators as

$$i\hbar\frac{\partial\hat{\psi}(x, t)}{\partial t} = \left(-\frac{\hbar^2}{2m}\frac{\partial^2}{\partial x^2} + V(x)\right)\hat{\psi}(x, t) + g(x)\hat{\psi}^\dagger(x, t)\hat{\psi}(x, t)\hat{\psi}(x, t) + K(x, t)\hat{\phi}_S(t) \quad (2.59)$$

$$i\hbar\frac{\partial\hat{\phi}_S(t)}{\partial t} = \mu\hat{\phi}_S(t) + \int K^*(x, t)\hat{\psi}(x, t)dx, \quad (2.60)$$

where we have defined the coupling strength as

$$K(x, t) = C(t) \iint \chi_0^*(y, z)\phi_0(\mathbf{r})dydz \quad (2.61)$$

and  $g(x)$  the effective 1D interaction strength. The short-range atom-atom interaction is modelled by a contact potential that, in the presence of a strong harmonic confinement of frequency  $\omega_\perp(x)$ , yields an effective 1D interaction strength given by

$$g(x) = \frac{m\omega_\perp(x)}{2\pi\hbar}U = 2\hbar\omega_\perp(x)a_S. \quad (2.62)$$

In order to simplify the description, we suppose that the source is strongly localised at position  $x_S$ , which amounts to choosing an idealised profile for the coupling and make the separation Ansatz  $K(x, t) = \kappa(t)\delta(x - x_S)$ , where  $\kappa(t)$  is a function that describes how the coupling strength evolves with time. Considering the macroscopic population of the condensate and a reasonably weak coupling, we can assume that for finite time evolution, the condensate is not significantly altered by its depletion into the matter wave guide. This argument motivates to perform the Ansatz  $\phi_S(t) = \langle\hat{\phi}_S(t)\rangle = \phi_S e^{-i\mu t/\hbar}$  which enables to get rid of the specific equation related to the source, as Eqs. (2.59) and (2.60) are written

$$i\hbar\frac{\partial\hat{\psi}(x, t)}{\partial t} = \left(-\frac{\hbar^2}{2m}\frac{\partial^2}{\partial x^2} + V(x)\right)\hat{\psi}(x, t) + g(x)\hat{\psi}^\dagger(x, t)\hat{\psi}(x, t)\hat{\psi}(x, t) + \kappa(t)\delta(x - x_S)\phi_S(t)e^{-i\mu t/\hbar} \quad (2.63)$$

$$i\hbar\frac{\partial\phi_S(t)}{\partial t} = \kappa^*(t)\hat{\psi}(x_S, t). \quad (2.64)$$

Indeed, we make the assumption that the coupling  $\kappa(t)$  is vanishingly weak such that  $\kappa(t) \rightarrow 0$  in such a manner that the product  $\mathcal{N}|\kappa(t)|^2$  remains finite. In that formal limit, we can write  $\phi_S = \sqrt{\mathcal{N}}[1 + \mathcal{O}(|\kappa(t)|^2)]$  for any  $t$ , so that in first approximation, the source population remains constant and the matter wave guide does not influence it, as Refs. [51, 216] indicate. In practice, this corresponds to a reservoir that contains a large number of particles submitted to a very weak radio frequency field. This allows us to rewrite the equation for the field operators related to the atom in the matter wave guide as

$$i\hbar\frac{\partial\hat{\psi}(x, t)}{\partial t} = \left(-\frac{\hbar^2}{2m}\frac{\partial^2}{\partial x^2} + V(x)\right)\hat{\psi}(x, t) + g(x)\hat{\psi}^\dagger(x, t)\hat{\psi}(x, t)\hat{\psi}(x, t) + \sqrt{\mathcal{N}}\kappa\delta(x - x_S)e^{-i\mu t/\hbar}, \quad (2.65)$$

and to neglect the time evolution of  $\phi_S(t)$ .

This equation does in general not possess an analytical solution, which motivates a numerical integration. To this end, we discretise the continuous scattering region of length  $\mathcal{L}$  in a 1D grid of  $L$  sites which we label by  $\alpha \in \mathbb{Z}$  and spaced by  $\delta$ . In this framework, the kinetic energy operator appearing in Eq. (2.65) is expressed in terms of a finite–difference scheme

$$\begin{aligned} -\frac{\hbar^2}{2m} \frac{\partial^2}{\partial x^2} \hat{\psi}(x) &\simeq -\frac{\hbar^2}{2m} \frac{\hat{\psi}(x+\delta) + \hat{\psi}(x-\delta) - 2\hat{\psi}(x)}{\delta^2} \\ &= E_\delta \hat{\psi}(x) - \frac{E_\delta}{2} [\hat{\psi}(x+\delta) + \hat{\psi}(x-\delta)], \end{aligned}$$

where we have introduced the on–site energy  $E_\delta = \hbar^2/m\delta^2$  and a nearest–neighbour hopping term  $-E_\delta/2$ . The discretised version of Eq. (2.65) takes the form

$$i\hbar \frac{\partial \hat{\psi}_\alpha(t)}{\partial t} = (E_\alpha + V_\alpha) \hat{\psi}_\alpha(t) - \frac{E_\delta}{2} [\hat{\psi}_{\alpha-1}(t) + \hat{\psi}_{\alpha+1}(t)] + g_\alpha \hat{\psi}_\alpha^\dagger(t) \hat{\psi}_\alpha(t) \hat{\psi}_\alpha(t) + \sqrt{\mathcal{N}} \kappa \delta_{\alpha, \alpha_S} e^{-i\mu t/\hbar}, \quad (2.66)$$

where the field operator  $\hat{\psi}_\alpha(t)$  at site  $\alpha$  corresponding to position  $x = \delta\alpha$  is defined according to  $\hat{\psi}_\alpha(t) \equiv \hat{\psi}(\delta\alpha, t) \sqrt{\delta}$ . With this discretisation scheme, the disorder and the interaction strength also acquire an on–site expression which are yielded as  $V_\alpha \equiv V(\delta\alpha)$  and  $g_\alpha \equiv g(\delta\alpha)/\delta$  in Eq. (2.66).

As we already explained, we consider here the formal limit of a very weak coupling  $\kappa(t)$  between the source and the lead that is adiabatically and smoothly ramped on with time and reaches a value  $\kappa \rightarrow 0$  such that  $\mathcal{N}|\kappa(t)|^2$  remains constant [212, 217, 218]. Consequently, this combined limit yields a constant number of atoms in the scattering region. A stationary many–body scattering state with energy  $\mu$  establishes after a long enough propagation time. This scattering state corresponds to a coherent superposition of plane waves of wavenumber given by

$$k = \frac{1}{\delta} \arccos \left( 1 - \frac{\mu}{E_\delta} \right) \quad (2.67)$$

and directly related to the dispersion relation of the lattice

$$\mu = E_\delta [1 - \cos(k\delta)]. \quad (2.68)$$

It is also characterised by a stationary density and current of atoms which are given by

$$\rho^\varnothing = \frac{1}{\delta} \frac{\mathcal{N}|\kappa|^2}{\mu(2E_\delta - \mu)} \quad (2.69)$$

$$j^\varnothing = \frac{1}{\hbar} \frac{\mathcal{N}|\kappa|^2}{\sqrt{\mu(2E_\delta - \mu)}}, \quad (2.70)$$

as can be obtained by solving Eq. (2.66) for a 2–sites system and computing the related density and current [51].

## 2.6 Quantum transport with atom lasers in open systems

The infinite extension system described by Eq. (2.65) can be conceived in terms of an open quantum system provided we restrict the presence of disorder and interaction to a specific finite region of space, which, along with its surrounding, we refer to as *scattering region*. This approach is particularly useful as we are very interested in the interplay between interference and interaction effects which occur in a finite region of space. Following the terminology used in mesoscopic physics and in Refs. [51, 218] that inspire the present discussion, we name *left* and *right leads* the spatial regions situated at the left and the right of the scattering region, as is depicted in FIG. 2.8(a).

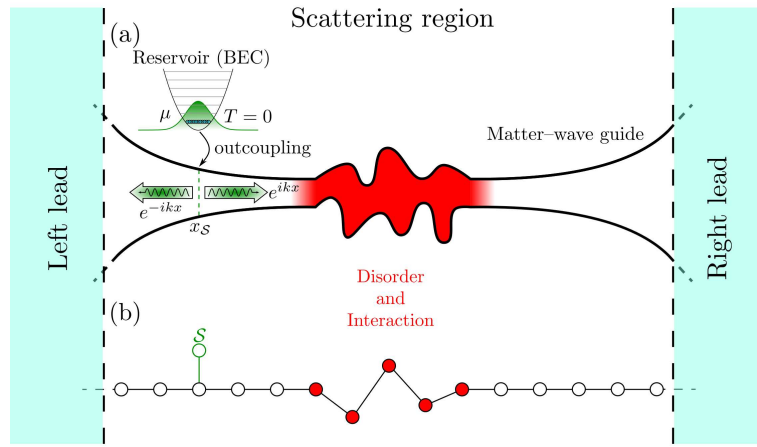


Figure 2.8 – Panel (a): Typical atom laser configuration modelled as an open system where only a finite extension scattering region is relevant. Panel (b): Discretisation of the scattering region.

This separation follows from the spatial dependence of the confinement potential resulting from the far detuned laser beam used to create the waveguide. Indeed, the waist of this laser beam is very narrow in a specific region of space which results in a locally stronger confinement that increases the atomic density and consequently the interaction energy. It allows us to model the scattering region as an open system and thus to focus on a finite region of space instead of the infinite extension system described in Eq. (2.65). We now explain how this quantum open system is modelled.

### 2.6.1 Transparent boundary conditions

Following the approach developed in [51, 218], we start by regrouping all the local field operators  $\hat{\psi}_\alpha$  into a vector of field operators denoted by  $\hat{\psi}$  and whose expression in the basis  $|\alpha\rangle$  is yielded as

$$\hat{\psi} = \sum_{\alpha=-\infty}^{\infty} \hat{\psi}_\alpha |\alpha\rangle, \quad (2.71)$$

where the orthonormal local sites are such that  $\langle \alpha | \alpha' \rangle = \delta_{\alpha\alpha'}$ . This allows us to compactly express Eq. (2.66) in Dirac notation

$$i\hbar \frac{\partial}{\partial t} \hat{\psi} = \left( \hat{H}_k + \hat{V} + \hat{U} \right) \hat{\psi} + |S\rangle, \quad (2.72)$$

with  $\hat{H}_k$  the kinetic Hamiltonian describing a free propagation,  $\hat{V}$  the scattering potential,  $\hat{U}$  an operator related to the effective potential due to the nonlinear interaction term in Eq. (2.66) and a coherent source term  $|S\rangle = \kappa\sqrt{N}e^{-i\mu t/\hbar} |\alpha_S\rangle$ , with  $|\alpha_S\rangle$  being the source site.

We choose to note  $\alpha = 0$  the first site of the scattering region and  $\alpha = N$  the last one, which allows us to separate the total wavefunction as

$$\hat{\psi} = \hat{P}_{\mathcal{L}_L} \hat{\psi}_{\alpha_{\mathcal{L}_L}} + \hat{P}_{\mathcal{Q}} \hat{\psi}_{\alpha_{\mathcal{Q}}} + \hat{P}_{\mathcal{L}_R} \hat{\psi}_{\alpha_{\mathcal{L}_R}}, \quad (2.73)$$

with the projectors  $\hat{P}_{\mathcal{L}_L}$ ,  $\hat{P}_{\mathcal{Q}}$  and  $\hat{P}_{\mathcal{L}_R}$  being defined on the local orthonormal grid basis states  $|\alpha\rangle$  as

$$\hat{P}_{\mathcal{L}_L} = \sum_{\alpha=-\infty}^{-1} |\alpha\rangle \langle \alpha|, \quad \hat{P}_{\mathcal{Q}} = \sum_{\alpha=0}^N |\alpha\rangle \langle \alpha|, \quad \hat{P}_{\mathcal{L}_R} = \sum_{\alpha=N+1}^{\infty} |\alpha\rangle \langle \alpha|, \quad (2.74)$$

and satisfying  $\hat{P}_X \hat{P}_Y = \delta_{XY} \hat{P}_X$ , with  $X, Y = \mathcal{L}_L, \mathcal{Q}, \mathcal{L}_R$  as well as  $\hat{P}_{\mathcal{L}_L} + \hat{P}_{\mathcal{Q}} + \hat{P}_{\mathcal{L}_R} = \hat{1}$ . The scattering region is labelled by  $\mathcal{Q}$  whilst the left and right lead are labelled by  $\mathcal{L}_L$  and  $\mathcal{L}_R$ . This separation of the system between the scattering region and the rest of the infinite space, as well as the possibility to solve Eq. (2.72) outside the scattering region more easily, motivates the use of the *Feshbach projection operator formalism* [184, 185], also called Feshbach–Fano separation, which reveals why we introduced projectors in Eq. (2.74). In the local basis  $|\alpha\rangle$ , the Hamiltonian in Eq. (2.72) yields matrix elements given by

$$\langle \alpha | \hat{H}_k | \alpha' \rangle = E_\delta \delta_{\alpha, \alpha'} - \frac{E_\delta}{2} (\delta_{\alpha, \alpha'-1} + \delta_{\alpha, \alpha'+1}) \quad (2.75)$$

$$\langle \alpha | \hat{V} | \alpha' \rangle = \delta_{\alpha, \alpha'} V_\alpha \quad (2.76)$$

$$\langle \alpha | \hat{U} | \alpha' \rangle = \delta_{\alpha, \alpha'} g_\alpha |\psi_\alpha|^2. \quad (2.77)$$

The spatial separation of the system in three regions gives rise to a set of three coupled evolution equations that are given by

$$i\hbar \frac{\partial \hat{\psi}_{\mathcal{L}_L}}{\partial t} = \hat{H}_{\mathcal{L}_L} \hat{\psi}_{\mathcal{L}_L} + \hat{W}_{\mathcal{L}_L \mathcal{Q}} \hat{\psi}_{\mathcal{Q}} \quad (2.78)$$

$$i\hbar \frac{\partial \hat{\psi}_{\mathcal{Q}}}{\partial t} = \left( \hat{H}_{\mathcal{Q}} + \hat{V}_{\mathcal{Q}} + \hat{U}_{\mathcal{Q}} \right) \hat{\psi}_{\mathcal{Q}} + \hat{W}_{\mathcal{Q} \mathcal{L}_L} \hat{\psi}_{\mathcal{L}_L} + \hat{W}_{\mathcal{Q} \mathcal{L}_R} \hat{\psi}_{\mathcal{L}_R} + |S\rangle \quad (2.79)$$

$$i\hbar \frac{\partial \hat{\psi}_{\mathcal{L}_R}}{\partial t} = \hat{H}_{\mathcal{L}_R} \hat{\psi}_{\mathcal{L}_R} + \hat{W}_{\mathcal{L}_R \mathcal{Q}} \hat{\psi}_{\mathcal{Q}}, \quad (2.80)$$

where  $|\psi_X\rangle = \hat{P}_X |\psi\rangle$  denotes the wavefunction projected on the  $X = \mathcal{L}_L, \mathcal{Q}, \mathcal{L}_R$  region,  $\hat{H}_X = \hat{P}_X \hat{H} \hat{P}_X$  the Hamiltonian related to the  $X = \mathcal{L}_L, \mathcal{Q}, \mathcal{L}_R$  region and finally

$$\hat{W}_{\mathcal{L}_L \mathcal{Q}} = -\frac{E_\delta}{2} |-1\rangle \langle 0| = \hat{P}_{\mathcal{L}_L} \hat{H} \hat{P}_{\mathcal{Q}} = \hat{W}_{\mathcal{Q} \mathcal{L}_L}^\dagger \quad (2.81)$$

$$\hat{W}_{\mathcal{L}_R \mathcal{Q}} = -\frac{E_\delta}{2} |N\rangle \langle N+1| = \hat{P}_{\mathcal{L}_R} \hat{H} \hat{P}_{\mathcal{Q}} = \hat{W}_{\mathcal{Q} \mathcal{L}_R}^\dagger. \quad (2.82)$$

The power of the Feshbach projection operator formalism lies in that Eqs. (2.78) and (2.80) are linear equations that describe free propagation. Their solution is thus readily obtained by formal integration and may hence be injected in Eq. (2.79) yielding

$$\begin{aligned}
i\hbar \frac{\partial \hat{\psi}_{\mathcal{Q}}}{\partial t} &= \left( \hat{H}_{\mathcal{Q}} + \hat{V}_{\mathcal{Q}} + \hat{U}_{\mathcal{Q}} \right) \hat{\psi}_{\mathcal{Q}} + |S\rangle \\
&- \frac{i}{\hbar} \int_{t_0}^t \hat{W}_{\mathcal{Q}\mathcal{L}_L} e^{-i(t-t')\hat{H}_{\mathcal{L}_L}/\hbar} \hat{W}_{\mathcal{L}_L\mathcal{Q}} \hat{\psi}_{\mathcal{Q}}(t') dt' \\
&- \frac{i}{\hbar} \int_{t_0}^t \hat{W}_{\mathcal{Q}\mathcal{L}_R} e^{-i(t-t')\hat{H}_{\mathcal{L}_R}/\hbar} \hat{W}_{\mathcal{L}_R\mathcal{Q}} \hat{\psi}_{\mathcal{Q}}(t') dt' \\
&+ \hat{W}_{\mathcal{Q}\mathcal{L}_L} e^{-i(t-t')\hat{H}_{\mathcal{L}_L}/\hbar} \hat{\psi}_{\mathcal{L}_L}(t_0) \\
&+ \hat{W}_{\mathcal{Q}\mathcal{L}_R} e^{-i(t-t')\hat{H}_{\mathcal{L}_R}/\hbar} \hat{\psi}_{\mathcal{L}_R}(t_0),
\end{aligned} \tag{2.83}$$

where the second and third lines describe the flow of bosonic particles exiting the scattering region into the two leads whilst the fourth and fifth lines describe the entrance of bosonic particles that were initially present in the left and right leads and penetrate the scattering region after some time.

We now evaluate the integrals appearing in the second and third lines of Eq. (2.83) by computing

$$\hat{W}_{\mathcal{Q}\mathcal{L}_L} e^{-i(t-t')\hat{H}_{\mathcal{L}_L}/\hbar} \hat{W}_{\mathcal{L}_L\mathcal{Q}} = \frac{E_{\delta}^2}{4} \int_0^{\pi} |\langle -1 | k^{(\mathcal{L}_L)} \rangle|^2 e^{-i(t-t')E_k/\hbar} |0\rangle \langle 0| dk \tag{2.84}$$

$$\hat{W}_{\mathcal{Q}\mathcal{L}_R} e^{-i(t-t')\hat{H}_{\mathcal{L}_R}/\hbar} \hat{W}_{\mathcal{L}_R\mathcal{Q}} = \frac{E_{\delta}^2}{4} \int_0^{\pi} |\langle k^{(\mathcal{L}_R)} | N+1 \rangle|^2 e^{-i(t-t')E_k/\hbar} |N\rangle \langle N| dk, \tag{2.85}$$

where we have introduced the normalised continuum eigenstates of each waveguide  $|k^{(\mathcal{L}_L)}\rangle$  and  $|k^{(\mathcal{L}_R)}\rangle$ . In the local basis  $|\alpha\rangle$ , they take on a form related to Bessel integrals which, for the left lead, is yielded as

$$\langle \alpha | k^{(\mathcal{L}_L)} \rangle = \sqrt{\frac{2}{\pi}} \sin[\alpha k] \quad \text{with } \alpha < 0 \tag{2.86}$$

and, for the right lead, as

$$\langle \alpha | k^{(\mathcal{L}_R)} \rangle = \sqrt{\frac{2}{\pi}} \sin[(\alpha - N)k] \quad \text{with } \alpha > N, \tag{2.87}$$

with  $0 \leq k\delta \leq \pi$ . Those eigenstates are related to the following continuous eigenvalues

$$E_k = E_{\delta}[1 - \cos(k\delta)] - \mu \tag{2.88}$$

and are such that  $\langle k^{(\mathcal{L}_L)} | \tilde{k}^{(\mathcal{L}_L)} \rangle = \langle k^{(\mathcal{L}_R)} | \tilde{k}^{(\mathcal{L}_R)} \rangle = \delta(k - \tilde{k})$ . Since  $1 - \cos(k\delta) \simeq (k\delta)^2/2$  for  $k\delta \ll 1$  and since  $E_{\delta} = \hbar^2/(m\delta^2)$ , we find that  $E_k \simeq \hbar^2 k^2/2m - \mu$ , hence, up to the constant shift  $\mu$ , tends to the continuous dispersion relation of a free wave. As a result of the discretisation procedure we used, Eq. (2.88) imposes that  $0 < \mu < 2E_{\delta}$  in order to give rise to a wave that propagates in the lead. We are finally left with a set of integro-differential

equations for each of the  $N + 1$  sites of the scattering region which are given by

$$\begin{aligned}
i\hbar \frac{\partial \hat{\psi}_\alpha}{\partial t} &= (E_\delta + V_\alpha) \hat{\psi}_\alpha - \frac{E_\delta}{2} \left[ \hat{\psi}_{\alpha-1}(1 - \delta_{\alpha,0}) + \hat{\psi}_{\alpha+1}(1 - \delta_{\alpha,N}) \right] + g_\alpha \hat{\psi}_\alpha^\dagger \hat{\psi}_\alpha \hat{\psi}_\alpha + \sqrt{N} \kappa \delta_{\alpha,\alpha_S} e^{-i\mu t/\hbar} \\
&\quad - \frac{i}{\hbar} (\delta_{\alpha,0} + \delta_{\alpha,N}) \frac{E_\delta^2}{2} \int_{t_0}^t M_\alpha(t-t') \hat{\psi}_\alpha(t') dt' \\
&\quad + \delta_{\alpha,0} \hat{\chi}_0(t) + \delta_{\alpha,N} \hat{\chi}_N(t),
\end{aligned} \tag{2.89}$$

where we have introduced

$$\hat{\chi}_0(t) = E_\delta \sum_{\alpha'=-\infty}^{-1} M_{\alpha'}(t-t_0) \hat{\psi}_{\alpha'}(t_0) \tag{2.90}$$

$$\hat{\chi}_N(t) = -E_\delta \sum_{\alpha'=N+1}^{\infty} M_{\alpha'-N}(t-t_0) \hat{\psi}_{\alpha'}(t_0), \tag{2.91}$$

as well as

$$M_\alpha(\tau) = \frac{i^\alpha}{2} \left[ J_{\alpha-1} \left( \frac{E_\delta \tau}{\hbar} \right) + J_{\alpha+1} \left( \frac{E_\delta \tau}{\hbar} \right) \right] e^{-i(E_\delta - \mu)\tau/\hbar}, \tag{2.92}$$

where  $J_\alpha$  is the Bessel function of the first kind and order  $\alpha$ . The details of the derivation can be found in Appendix C.

Eq. (2.89) describes exactly the time evolution of the field operators  $\hat{\psi}_\alpha$  since, until now, no approximation has been performed. The second line of Eq. (2.89) describes the depletion of the scattering region by particles leaving in one of the two leads whilst the third line Eq. (2.89) describes the injection of particles initially in one of the two leads into the scattering region, thereby corresponding to transparent boundary conditions. Although exact with respect to the discrete equation (2.66), this approach faces the major drawback of being extremely slow in practice. Indeed, integrals in the second line of Eq. (2.89) have to be computed at each time step, which demands a huge numerical effort since the  $1/\sqrt{z}$  decrease of  $J_\alpha(z)$  renders any cutoff in the related integrals impossible [51, 218]. In the following, we introduce smooth exterior complex scaling to efficiently replace those integrals.

## 2.6.2 Smooth exterior complex scaling

The idea when dealing with a quantum open system numerically is to absorb the outgoing flux of atoms. There are several possibilities of doing so, for instance by implementing absorbing boundary conditions through the so-called one-way wave equation method [219]. The underlying idea is to modify the dispersion relation at the boundaries so that only outgoing waves are allowed whilst those in the opposite direction are not permitted. This method is straightforwardly implemented in combination with a Crank–Nicolson integration scheme [60] but is sharply  $\mu$ -dependent. This is a major drawback in the context of our work, since inelastic scattering occurring for finite interaction is responsible for creating a broad spectrum of energies associated to outgoing waves. Another possibility is to use complex absorbing potentials [220, 221], where a finite imaginary part is added to the potential in order to damp out outgoing waves. However, the introduction of this imaginary part can be responsible for non desirable backreflection and must therefore be suitably chosen.



These drawbacks can be circumvented by employing the method of complex scaling [222–227] that allows to deal with a broad variety of energies and that is more efficient than complex absorbing potentials [218]. In one dimension, it consists in introducing the complex path  $z = F(x) \mapsto z = xe^{i\theta}$  in the complex plane with  $\theta$ , the rotation angle that should be suitably chosen to damp outgoing waves. For simplicity, we perform this transformation onto the  $x$  coordinate of a one-dimensional Schrödinger equation

$$i\hbar \frac{\partial}{\partial t} \psi(x, t) = -\frac{\hbar^2}{2m} \frac{\partial^2}{\partial x^2} \psi(x, t), \quad (2.93)$$

describing the free 1D propagation of a particle, instead of Eq. (2.65). Solutions of the time-independent Schrödinger equation (2.93) for a fixed energy  $E$  are readily found out to be

$$\psi(x) = A_+ e^{ikx} + A_- e^{-ikx}, \quad (2.94)$$

with  $A_{\pm}$  the amplitude related to the left and right propagating plane waves. The rotation considered here yields

$$\psi(z) = A_+ e^{ikxe^{i\theta}} + A_- e^{-ikxe^{i\theta}} = A_+ e^{ikx \cos \theta} e^{-kx \sin \theta} + A_- e^{-ikx \cos \theta} e^{kx \sin \theta}. \quad (2.95)$$

This transformation has rendered outgoing solutions elements of the Hilbert space  $\mathbb{L}^2(\mathbb{R})$ , whereas ingoing solutions are not square integrable, yielding  $A_- = 0$  [218]. The complex scaling proposed here thus solves the problem of outgoing waves but generally poses difficulties, because an external potential cannot necessarily be expressed in terms of complex coordinates and nonlinearities arising in a nonlinear Schrödinger equation can furthermore cause numerical troubles [228–230].

Smooth exterior complex scaling [231, 232] solves this problem by considering a position-dependent rotation angle  $\theta \equiv \theta(x)$ . The idea is to leave the spatial coordinate unchanged within the scattering region (so that both external potential and nonlinearity are not affected) and to smoothly ramp the rotation angle from 0 to a suitable value  $\theta$  at the boundaries. We formally write the coordinate transformation in the context of smooth exterior complex scaling as  $\hat{U}_\theta$  and its action on the wavefunction is given by

$$\hat{U}_\theta \psi(x, t) = \sqrt{\frac{\partial z(x)}{\partial x}} \psi[z(x), t] \quad (2.96)$$

with the complex coordinate  $z(x)$  being defined as

$$z(x) = \int_{x_0}^x q(x') dx'. \quad (2.97)$$

The function  $q(x)$  is written as

$$q(x) = 1 + (e^{i\theta} - 1)u(x), \quad (2.98)$$

with  $u(x)$  a smooth switching function that goes from zero to 1 over a certain spatial distance, as is shown in FIG. 2.9(c). The Schrödinger equation (2.93) governing the evolution of the wavefunction is then transformed according to

$$i\hbar \frac{\partial \hat{U}_\theta \psi(x, t)}{\partial t} = \hat{U}_\theta \hat{H} \hat{U}_\theta^{-1} \hat{U}_\theta \psi(x, t) \quad (2.99)$$

which leaves us with the evaluation of the transformed Hamiltonian  $\hat{U}_\theta \hat{H} \hat{U}_\theta^{-1}$ . The derivatives transform with respect to  $z$  according to [51, 218]

$$\begin{aligned}\frac{\partial}{\partial x} &= \frac{\partial z}{\partial x} \frac{\partial}{\partial z} = \frac{1}{f(z)} \frac{\partial}{\partial z} \\ \frac{\partial^2}{\partial x^2} &= \frac{1}{f(z)} \frac{\partial}{\partial z} \left( \frac{1}{f(z)} \frac{\partial}{\partial z} \right) = \frac{1}{f^2(z)} \left( \frac{\partial^2}{\partial z^2} - \frac{f'(z)}{f(z)} \frac{\partial}{\partial z} \right)\end{aligned}$$

and allow to write the transformed Schrödinger equation as

$$i\hbar \frac{\partial \hat{U}_\theta \psi(x, t)}{\partial t} = -\frac{\hbar^2}{2m} \frac{1}{f^2(z)} \left( \frac{\partial^2}{\partial z^2} - \frac{f'(z)}{f(z)} \frac{\partial}{\partial z} \right) \hat{U}_\theta \psi(x, t). \quad (2.100)$$

Before applying this procedure to the study of atom lasers, we finally note that smooth exterior complex scaling was first introduced with a very different purpose from absorbing outgoing waves in quantum open systems. The idea was to unmask resonance states of Hamiltonians featuring a structure intertwining bound states, resonance states and a continuum of states. Indeed, as the Hamiltonian is transformed according to  $\hat{U}_\theta \hat{H} \hat{U}_\theta^{-1}$ , the bound states are left unchanged, the continuum of states is rotated in the complex plane along a straight line with the angle  $2\theta$ , whereas the resonance states acquire a complex energy that allows to separate them from the continuum [233].

### 2.6.3 Application to atom lasers

Smooth exterior complex scaling provides a convenient way of modelling the infinite extension system described in Eq. (2.89) as a finite extension open system. The implementation of smooth exterior complex scaling allows us to rewrite Eq. (2.89) as

$$\begin{aligned}i\hbar \frac{\partial \hat{\psi}_\alpha}{\partial t} &= (E_\delta/q_\alpha + V_\alpha - \mu q_\alpha) \hat{\psi}_\alpha - \frac{E_\delta}{2} [J_{\alpha-} \hat{\psi}_{\alpha-1} + J_{\alpha+} \hat{\psi}_{\alpha+1}] + g_\alpha \hat{\psi}_\alpha^\dagger \hat{\psi}_\alpha \hat{\psi}_\alpha + \sqrt{\mathcal{N}} \kappa(t) \delta_{\alpha, \alpha_S} \\ &+ \delta_{\alpha, 0} \hat{\chi}_0(t) + \delta_{\alpha, N} \hat{\chi}_N(t),\end{aligned} \quad (2.101)$$

where we introduced the effective hopping term

$$J_{\alpha\pm} = \left( \frac{1}{q_{\alpha\pm 1}} - \frac{\delta q'_{\alpha\pm 1}}{2 q_{\alpha\pm 1}^2} \right) \quad (2.102)$$

with  $q_\alpha = q(x = \alpha\delta)$ . The on-site potential  $V_\alpha$  and the on-site interaction strength  $g_\alpha$  are preserved by this transformation because they are only present within the scattering region that is left unchanged by smooth exterior complex scaling. The third line of Eq. (2.89), that describes the decay of outgoing waves by means of transparent boundary conditions applied at the most left and right sites of the scattering region, is now handled by smooth exterior complex scaling which damps outgoing waves out over a certain distance. The last line of Eq. (2.89), that is not modified by smooth exterior complex scaling, is still present in Eq. (2.101) and describes how an initial population outside the scattering region penetrates into it after some finite time.

In order to provide a mean-field description of Eq. (2.101), in the limit of a large number of atoms  $\mathcal{N} \rightarrow \infty$  and very weak interaction strength, we apply Bogoliubov's prescription and

replace the field operators by c–numbers  $\hat{\psi}_\alpha \rightarrow \psi_\alpha \equiv \langle \hat{\psi}_\alpha \rangle$  and  $\hat{\psi}_\alpha^\dagger \rightarrow \psi_\alpha^* \equiv \langle \hat{\psi}_\alpha^\dagger \rangle$ . This allows us to cast the many–body problem into an effective one–body problem described by

$$i\hbar \frac{\partial \psi_\alpha}{\partial t} = \left( \frac{E_\delta}{q_\alpha} + V_\alpha - \mu q_\alpha \right) \psi_\alpha - \frac{E_\delta}{2} [J_{\alpha-} \psi_{\alpha-1} + J_{\alpha+} \psi_{\alpha+1}] + g_\alpha |\psi_\alpha|^2 \psi_\alpha + \sqrt{N} \kappa \delta_{\alpha, \alpha_S}, \quad (2.103)$$

that contains a nonlinear interaction energy and where the last line of Eq. (2.101) has vanished owing to the initially perfectly empty leads  $\chi_0(t_0) = \chi_N(t_0) = 0$ .

This equation is numerically integrated in the absence of disorder potential and interaction from an initially empty waveguide to reach a stationary scattering state whose spatial density is shown in FIG. 2.9(d), for illustration of smooth exterior complex scaling purposes.

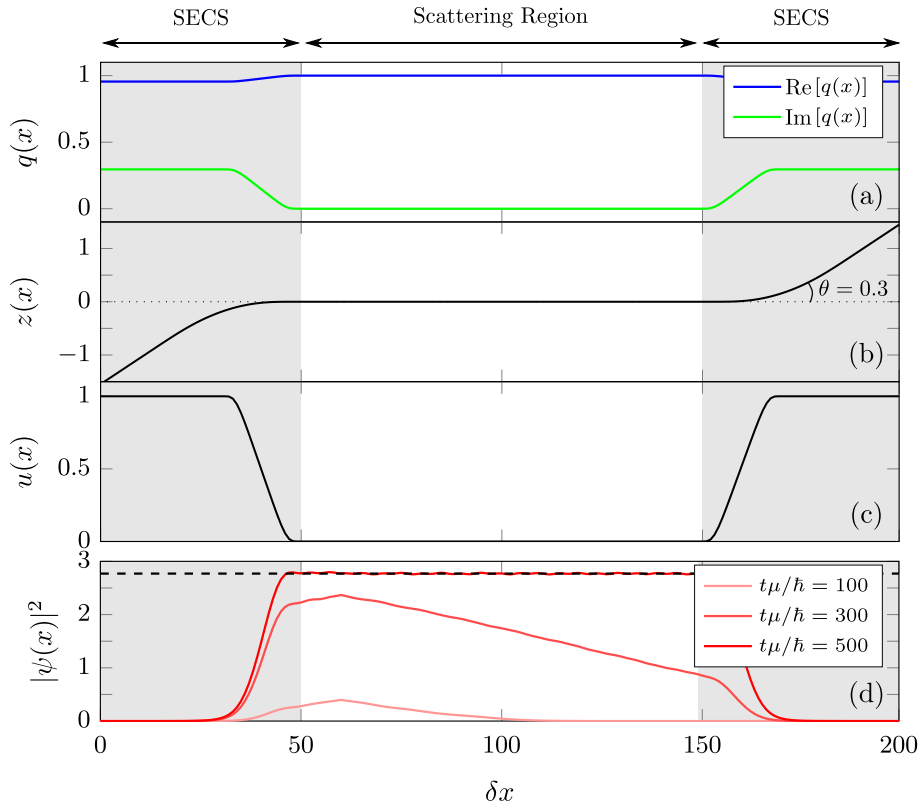


Figure 2.9 – Implementation of smooth exterior complex scaling to an atom laser scenario. The three upper (a)–(c) panels show the complex function  $q(x)$  that is used in mean–field equations, the complex coordinate  $z(x)$  and the smooth switching function  $u(x)$  used to model the  $x$ –dependence of  $q(x)$ . Panel (d) shows a typical atom laser scenario in the absence of disorder potential and nonlinearity. After some transient time, a steady density establishes to the value predicted by Eq. (2.69) as shown in dashed line. Outside the scattering region, outgoing particles are efficiently damped over  $\approx 25$  sites by smooth exterior complex scaling. Numerical parameters:  $\mu/E_\delta = 0.2$  and  $\theta = 0.3$ .

FIG. 2.9(d) illustrates the density  $|\psi(x)|^2$  of the steady scattering state  $\psi(x)$  that is reached after some transient time related to the chemical potential of the source and the extension of the scattering region. Smooth exterior complex scaling absorbs outgoing waves over a distance of  $\approx 25$  sites, which settles the typical scenario studied in the following chapters, in the presence of more sophisticated geometries, of disorder potential and interaction.

## Chapter 3

# Description of many–body effects beyond the mean–field regime

In this chapter, we introduce the truncated Wigner method that is a recurrent tool used in our work to describe many–body effects beyond the traditional mean–field approximation. More specifically, the truncated Wigner method mimics the initial quantum fluctuations that are not captured by a mean–field description and provides a suitable description of inelastic scattering processes that arise in the presence of finite interaction. Indeed, it has been shown that the presence of a weak atom–atom interaction in the context of quantum transport towards disorder potentials generates inelastic scattering processes [62, 115] which can compromise coherent effects.

We start by recalling some basic concepts of classical phase–space mechanics. Those concepts are useful to build the Wigner function, a quasiprobability distribution used in the quantum formulation of phase–space that provides a description of a quantum system state equivalent to that provided by a density operator  $\hat{\rho}$ . We show some of the underlying key properties and give some examples of Wigner functions that are considered in our work, namely those of a vacuum state and, more generally, of a coherent state. We also provide the Wigner function of a thermal state and of a Fock state, which is an example of a non–classical state that highlights the possible negativity of the Wigner function, in contrast to a classical probability distribution. For this reason, the Wigner function is referred to as a quasiprobability distribution.

We then derive the evolution for the Wigner function and show where the truncated part of the method name comes from. This truncation is necessary to allow numerical integration of the underlying evolution equation and gives rise to a set of coupled Langevin equations for each mode of the system. It allows one to compute expectation values of observables through an average over trajectories evolved along those Langevin equations and whose initial conditions are sampled according to the Wigner function of the system at initial time  $t_0$ . The formalism developed in this chapter is then used and particularised to atom lasers, setting the framework we work with for the rest of this manuscript. A discussion related to the validity of the truncated Wigner method is finally performed.

### 3.1 Phase-space formulation of classical mechanics

A classical system with  $2N$  degrees of freedom can be described in terms of its generalised coordinates  $\mathbf{q} \in \mathbb{R}^N$  and the related canonically conjugated momentum  $\mathbf{p} \in \mathbb{R}^N$ . The underlying space of dimension  $2N$  spanned by  $(\mathbf{q}, \mathbf{p})$  is called the *phase space*. The data of both  $\mathbf{q}$  and  $\mathbf{p}$  at time  $t$  gives a point in that phase space. That point represents the whole dynamics of the system at time  $t$  and we call it a *microstate* of the system. It evolves with  $t$  in the phase space as prescribed by Hamilton equations

$$\begin{cases} \frac{dq_i}{dt} = \frac{\partial H}{\partial p_i} \\ \frac{dp_i}{dt} = -\frac{\partial H}{\partial q_i} \end{cases} \quad \text{with } i = 1, \dots, N, \quad (3.1)$$

where  $H$  is the Hamiltonian related to the system. In the simple case of a system displaying one-dimensional motion, such as a 1D mass-spring system, the underlying phase space is a plane and the trajectory that solves Eqs. (3.1) is readily representable in the 2D phase space (in this example of a 1D mass-spring system, the trajectory is an ellipse of constant energy), but it is in general not so easily drawable because of the dimension of the underlying phase space.

Following the principle of a statistical (Gibbs) ensemble, we now consider a collection of virtual copies of the system under study at the same energy. Those copies are macroscopically identical but microscopically different and represent a possible state that the system might occupy, thereby forming a probability distribution for the state of the system. The replacement of the Dirac peaks associated to the microstates of the system expresses statistical uncertainties or the lack of knowledge of the system [234]. We therefore define a probability distribution  $\rho(\mathbf{q}, \mathbf{p}; t)$  that is positive and normalised such that

$$\iint \rho(\mathbf{q}, \mathbf{p}; t) d^N q d^N p = 1 \quad (3.2)$$

and which gives the probability that the system is in the state  $(\mathbf{q}, \mathbf{p})$ . The conjugated variables  $\mathbf{q}$  and  $\mathbf{p}$  are hence considered as random variables following the probability density  $\rho(\mathbf{q}, \mathbf{p}; t)$ . The latter can be used to compute the ensemble average at time  $t$  of an observable  $A(\mathbf{q}, \mathbf{p})$  through

$$\langle A(t) \rangle = \iint A(\mathbf{q}, \mathbf{p}) \rho(\mathbf{q}, \mathbf{p}; t) d^N q d^N p, \quad (3.3)$$

and can also, by means of partial integration over one of the two conjugated variables, yield the marginal distribution over the other one

$$\rho_{\mathbf{p}}(\mathbf{q}; t) = \int \rho(\mathbf{q}, \mathbf{p}; t) d^N p \quad \text{and} \quad \rho_{\mathbf{q}}(\mathbf{p}; t) = \int \rho(\mathbf{q}, \mathbf{p}; t) d^N q. \quad (3.4)$$

As is usually done in probability theory, a probability distribution can be described by its characteristic function  $\chi(\boldsymbol{\xi}_1, \boldsymbol{\xi}_2) = \langle e^{i(\boldsymbol{\xi}_1 \cdot \mathbf{p} + \boldsymbol{\xi}_2 \cdot \mathbf{q})} \rangle = \text{Tr}(e^{i(\boldsymbol{\xi}_1 \cdot \mathbf{p} + \boldsymbol{\xi}_2 \cdot \mathbf{q})})$  through its Fourier transform

$$\rho(\mathbf{q}, \mathbf{p}; t) = \frac{1}{\pi^{2N}} \iint \chi(\boldsymbol{\xi}_1, \boldsymbol{\xi}_2) e^{-i(\boldsymbol{\xi}_1 \cdot \mathbf{p} + \boldsymbol{\xi}_2 \cdot \mathbf{q})} d^N \xi_1 d^N \xi_2, \quad (3.5)$$

and vice-versa. The characteristic function entirely describes the probability distribution because its value for  $\boldsymbol{\xi}_1 = \boldsymbol{\xi}_2 = \mathbf{0}$  is one and its derivatives at that point yield all the moments of the conjugated variables  $\mathbf{q}$  and  $\mathbf{p}$ .

The time evolution of  $\rho(\mathbf{q}, \mathbf{p}; t)$  can be inferred by means of the Liouville theorem which states that the phase–space distribution function  $\rho(\mathbf{q}, \mathbf{p}; t)$  is constant along the trajectories of the system

$$\frac{d\rho(\mathbf{q}, \mathbf{p}; t)}{dt} = \frac{\partial\rho(\mathbf{q}, \mathbf{p}; t)}{\partial t} + \{\rho(\mathbf{q}, \mathbf{p}; t), H(\mathbf{q}, \mathbf{p})\} = 0, \quad (3.6)$$

where

$$\{A, B\} = \sum_{i=1}^N \left[ \frac{\partial A}{\partial q_i} \frac{\partial B}{\partial p_i} - \frac{\partial A}{\partial p_i} \frac{\partial B}{\partial q_i} \right] \quad (3.7)$$

are Poisson brackets [235, 236]. The time evolution of  $\rho(\mathbf{q}, \mathbf{p})$  with respect to  $t$  is prescribed by

$$\frac{\partial\rho(\mathbf{q}, \mathbf{p}; t)}{\partial t} = -\{\rho(\mathbf{q}, \mathbf{p}; t), H(\mathbf{q}, \mathbf{p}; t)\}, \quad (3.8)$$

which is known as Liouville equation [3]. This partial differential equation contains the time evolution of the system as a result of external forces and of the coupling with its environment.

## 3.2 Phase–space formulation of quantum mechanics

The procedure developed for classical mechanics can be straightforwardly generalised to quantum mechanics<sup>1</sup>, as was first proposed by Wigner in 1932 [240, 241]. We aim at defining a probability distribution  $\rho(\mathbf{q}, \mathbf{p})$  in the quantum phase space that describes the quantum system that is in a state characterised by the density operator  $\hat{\rho}$ . This ideal probability distribution, that would yield only positive numbers and that would be normalised to unity, could then be used to compute expectation values of an observable  $A$  as

$$\langle A(t) \rangle = \iint A(\mathbf{q}, \mathbf{p}) \rho(\mathbf{q}, \mathbf{p}; t) d\mathbf{p} d\mathbf{q}, \quad (3.9)$$

exactly as in classical mechanics. This appealing formulation allows to use functions rather than quantum operators. However, even in the absence of statistical uncertainties, it faces the impossibility to simultaneously determine conjugated variables of the same system with an arbitrary accuracy, as is stated by Heisenberg uncertainty relations.

It is nevertheless possible to deal with some functions that play an analogous role to probability distributions in the classical phase space. The price to pay being that those functions do not fulfil all properties required to be named a probability distribution: they are referred to as quasiprobability distributions.

To obtain such a quasiprobability distribution, we start by introducing  $\boldsymbol{\alpha} = \mathbf{q} + i\mathbf{p}$  and  $\boldsymbol{\xi} = \frac{1}{2}(\boldsymbol{\xi}_1 + i\boldsymbol{\xi}_2)$ , with  $\boldsymbol{\alpha} \equiv \alpha_1, \dots, \alpha_\nu, \dots, \alpha_N$  and  $\nu = 1, 2, \dots, N$  the mode index. This

---

<sup>1</sup>We recommend to the interested reader the reading of the nice review articles dedicated to phase–space quantum mechanics [237] and its applications in the context of the truncated Wigner method [238, 239].

allows us to rewrite Eq. (3.9) as

$$\langle A(t) \rangle = \text{Tr} [\hat{\rho} \hat{A}] = \iint f_{\mathcal{W}}^{(\hat{A})}(\boldsymbol{\alpha}, \boldsymbol{\alpha}^*) W^{(\hat{\rho})}(\boldsymbol{\alpha}, \boldsymbol{\alpha}^*, t) d^N \alpha d^N \alpha^*, \quad (3.10)$$

that is an integral over the phase space of a function  $f_{\mathcal{W}}^{(\hat{A})}(\boldsymbol{\alpha}, \boldsymbol{\alpha}^*)$  related to the observable of interest and weighted by the Wigner distribution  $W^{(\hat{\rho})}(\boldsymbol{\alpha}, \boldsymbol{\alpha}^*, t)$  that contains all information about the state of the system and which we still need to properly define. It thus appears that there exists a link between quantum expectation values of observables and phase-space averages. In order to exploit this link in Eq. (3.10), the function  $f_{\mathcal{W}}^{(\hat{A})}(\boldsymbol{\alpha}, \boldsymbol{\alpha}^*)$  of the operator  $\hat{A}$  related to the observable under study must be written in a way that we try to make clear in the following.

The rule for determining the function  $f_{\mathcal{W}}^{(\hat{A})}(\boldsymbol{\alpha}, \boldsymbol{\alpha}^*, t)$  is to use the Weyl correspondence rule that prescribes to express the operator related to the observable of interest in terms of power series of the creation and annihilation operators which are symmetrically, or Weyl, ordered

$$\hat{A} = \prod_{\nu=0}^N \sum_{n_{\nu}=0}^{\infty} \sum_{m_{\nu}=0}^{\infty} c_{n_{\nu} m_{\nu}}^{(\hat{A})} (\hat{a}_{\nu}^{\dagger n_{\nu}} \hat{a}_{\nu}^{m_{\nu}})_{\mathcal{W}}, \quad (3.11)$$

where  $c_{n_{\nu} m_{\nu}}^{(\hat{A})}$  are coefficients related to the decomposition of the operator  $\hat{A}$  in terms of symmetrically ordered products of the creation and annihilation operators related to each mode  $\nu$ . In Eq. (3.11),  $(\hat{a}_{\nu}^{\dagger n_{\nu}} \hat{a}_{\nu}^{m_{\nu}})_{\mathcal{W}}$  designs the symmetric, or Weyl, ordering<sup>2</sup> of non-commuting operators which gives, if we take the simple example of the single-mode operator  $\hat{A}(\hat{\mathbf{a}}, \hat{\mathbf{a}}^{\dagger}) = \hat{a}_{\nu}^{\dagger} \hat{a}_{\nu}^2$ ,

$$\hat{A}(\hat{\mathbf{a}}, \hat{\mathbf{a}}^{\dagger}) = \hat{a}_{\nu}^{\dagger} \hat{a}_{\nu}^2 \quad \Rightarrow \quad (\hat{a}_{\nu}^{\dagger} \hat{a}_{\nu}^2)_{\mathcal{W}} = \frac{1}{3} (\hat{a}_{\nu}^{\dagger} \hat{a}_{\nu}^2 + \hat{a}_{\nu} \hat{a}_{\nu}^{\dagger} \hat{a}_{\nu} + \hat{a}_{\nu}^2 \hat{a}_{\nu}^{\dagger}), \quad (3.12)$$

where we have introduced the vector  $\hat{\mathbf{a}} = [\hat{a}_0, \dots, \hat{a}_{\nu}, \dots, \hat{a}_N]^T$  (resp.  $\hat{\mathbf{a}}^{\dagger} = [\hat{a}_0^{\dagger}, \dots, \hat{a}_{\nu}^{\dagger}, \dots, \hat{a}_N^{\dagger}]^T$ ) that contains all annihilation (resp. creation) operators related to each mode  $\nu$ . In general, such a symmetric ordering contains  $\mathcal{N}_{\nu} = (n_{\nu} m_{\nu})! / (n_{\nu}! m_{\nu}!)$  terms per mode  $\nu$  associated with all possible permutations of the  $n_{\nu}$  creation operators and the  $m_{\nu}$  annihilation operators and must hence be normalised by  $\mathcal{N}_{\nu}$ . Following Weyl correspondence rule for writing the operator  $\hat{A}$  related to observable  $A$ , we express the corresponding function as

$$f_{\mathcal{W}}^{(\hat{A})}(\boldsymbol{\alpha}, \boldsymbol{\alpha}^*) = \prod_{\nu=0}^N \sum_{n_{\nu}=0}^{\infty} \sum_{m_{\nu}=0}^{\infty} c_{n_{\nu} m_{\nu}}^{(\hat{A})} \boldsymbol{\alpha}^{* n_{\nu}} \boldsymbol{\alpha}^{m_{\nu}}, \quad (3.13)$$

where  $c_{n_{\nu} m_{\nu}}^{(\hat{A})}$  are the same coefficients appearing in the decomposition of  $\hat{A}$  in terms of Weyl ordered products of the creation and annihilation operators related to each mode  $\nu$  in Eq. (3.11).

---

<sup>2</sup>Since creation and annihilation operators do not commute, there are as many different quasiprobability distributions as they are different orderings. Another frequently used ordering is the Wick, or normal, ordering where all creation operators are at the left of the annihilation operators. This yields the so-called Glauber–Sudarshan P distribution [242, 243]. One can also define the antinormal ordering where all annihilations operators are at the left of creation operators, thereby giving rise to Husimi Q distribution [244].



To obtain the Wigner function that links phase–space averages to quantum expectation values, we introduce the (Weyl ordered) characteristic function<sup>3</sup>, as was done in the classical phase–space formulation,

$$\chi_{\mathcal{W}}^{(\hat{\rho})}(\boldsymbol{\xi}, \boldsymbol{\xi}^*, t) = \langle \hat{D}(\boldsymbol{\xi}, \boldsymbol{\xi}^*) \rangle = \langle \hat{\rho} e^{\boldsymbol{\xi} \cdot \hat{\mathbf{a}}^\dagger - \boldsymbol{\xi}^* \cdot \hat{\mathbf{a}}} \rangle = \text{Tr} \left[ \hat{\rho} e^{\boldsymbol{\xi} \cdot \hat{\mathbf{a}}^\dagger - \boldsymbol{\xi}^* \cdot \hat{\mathbf{a}}} \right] = \text{Tr} \left[ \hat{\rho} \prod_{\nu=0}^N e^{\xi_\nu \hat{a}_\nu^\dagger - \xi_\nu^* \hat{a}_\nu} \right], \quad (3.14)$$

the latter being the expectation value of the Glauber displacement operator  $\hat{D}(\boldsymbol{\xi}, \boldsymbol{\xi}^*)$  of the system in the  $\hat{\rho}$  state.

The Wigner function can be obtained by means of the Fourier transform of the Weyl ordered characteristic function, yielding

$$\begin{aligned} W^{(\hat{\rho})}(\boldsymbol{\alpha}, \boldsymbol{\alpha}^*, t) &= \frac{1}{\pi^{2N}} \iint \text{Tr} \left[ \hat{\rho} e^{\boldsymbol{\xi} \cdot \hat{\mathbf{a}}^\dagger - \boldsymbol{\xi}^* \cdot \hat{\mathbf{a}}} \right] e^{-i(\boldsymbol{\xi} \cdot \boldsymbol{\alpha} + \boldsymbol{\xi}^* \cdot \boldsymbol{\alpha}^*)} d^{2N} \boldsymbol{\xi} \\ &= \frac{1}{\pi^{2N}} \iint \text{Tr} \left\{ \hat{\rho} \exp \left[ \sum_{\eta=0}^N (\xi_\eta \hat{a}_\eta^\dagger - \xi_\eta^* \hat{a}_\eta) \right] \right\} \exp \left[ -i \sum_{\nu=0}^N (\xi_\nu \alpha_\nu + \xi_\nu^* \alpha_\nu^*) \right] d^{2N} \boldsymbol{\xi} \\ &= \frac{1}{\pi^{2N}} \prod_{\nu=0}^N \iint \text{Tr} \left[ \hat{\rho} \prod_{\eta=0}^N e^{\xi_\eta \hat{a}_\eta^\dagger - \xi_\eta^* \hat{a}_\eta} \right] e^{-i(\xi_\nu \alpha_\nu + \xi_\nu^* \alpha_\nu^*)} d^2 \xi_\nu. \end{aligned} \quad (3.15)$$

The characteristic function  $\chi_{\mathcal{W}}^{(\hat{\rho})}(\boldsymbol{\xi}, \boldsymbol{\xi}^*, t)$  can, similarly to the Wigner function, be used to compute quantum expectation values of Weyl ordered products of creation and annihilation operators through

$$\begin{aligned} \langle (\hat{a}_\nu^\dagger)^{n_\nu} \hat{a}_{\nu'}^{m_{\nu'}} \rangle_{\mathcal{W}} &= \text{Tr} \left[ \hat{\rho} (\hat{a}_\nu^\dagger)^{n_\nu} \hat{a}_{\nu'}^{m_{\nu'}} \right]_{\mathcal{W}} \\ &= \frac{\partial^{n_\nu + m_{\nu'}}}{\partial (i \xi_\nu^*)^{n_\nu} \partial (i \xi_{\nu'})^{m_{\nu'}}} \chi(\boldsymbol{\xi}, \boldsymbol{\xi}^*) \Big|_{\boldsymbol{\xi} = \boldsymbol{\xi}^* = \mathbf{0}} \\ &= \frac{\partial^{n_\nu + m_{\nu'}}}{\partial (i \xi_\nu^*)^{n_\nu} \partial (i \xi_{\nu'})^{m_{\nu'}}} \int W^{(\hat{\rho})}(\boldsymbol{\alpha}, \boldsymbol{\alpha}^*, t) e^{i(\boldsymbol{\xi} \cdot \boldsymbol{\alpha} + \boldsymbol{\xi}^* \cdot \boldsymbol{\alpha}^*)} \Big|_{\boldsymbol{\xi} = \boldsymbol{\xi}^* = \mathbf{0}} d^{2N} \boldsymbol{\alpha} \\ &= \int \alpha_\nu^{*n_\nu} \alpha_{\nu'}^{m_{\nu'}} W^{(\hat{\rho})}(\boldsymbol{\alpha}, \boldsymbol{\alpha}^*, t) d^{2N} \boldsymbol{\alpha}, \end{aligned} \quad (3.16)$$

illustrating that differentiation in the direct space becomes multiplication by the complex numbers  $\alpha_\nu$  and  $\alpha_\nu^*$  in the reciprocal space [51]. As already stated, we observe that phase–space averages such as Eq. (3.10) and Eq. (3.16) are associated to quantum expectation values of symmetrically ordered observables expressed in terms of creation and annihilation operators. Weyl correspondence rule thus provides a very powerful tool to compute quantum

---

<sup>3</sup>As a Taylor series expansion of the displacement operator  $\hat{D}$  shows, it is already Weyl ordered. It is nonetheless possible to define different characteristic functions that are normal or antinormal ordered and which Fourier transform yields the Glauber–Sudarshan P distribution and the Husimi Q distribution. Those characteristic functions are closely related one to each other and so are the resulting distributions which are formally equivalent one to each other [245, 246]. Each representation may have its advantages and drawbacks with respect to the studied system.

expectation values by means of phase-space averages that involve functions instead of operators.

As an example, let us show how this formalism can be used to compute the expectation value of the single-mode occupation number operator  $\hat{N}_\nu = \hat{a}_\nu^\dagger \hat{a}_\nu$  of mode  $\nu$ . The expectation value  $\langle (\hat{N}_\nu)_\mathcal{W} \rangle$  of the Weyl ordered operator is directly obtained as

$$\langle (\hat{N}_\nu)_\mathcal{W} \rangle = \iint f_{\mathcal{W}}^{(\hat{N}_\nu)}(\boldsymbol{\alpha}, \boldsymbol{\alpha}^*) W^{(\hat{\rho})}(\boldsymbol{\alpha}, \boldsymbol{\alpha}^*, t) d^N \alpha d^N \alpha^*, \quad (3.17)$$

but is not exactly the quantum expectation value we are looking for, namely  $\langle N_\nu \rangle$ . We make use of the bosonic commutation relation  $[\hat{a}_\nu, \hat{a}_{\nu'}^\dagger] = \delta_{\nu\nu'}$  and symmetrise the number operator related to the mode  $\nu$  as

$$\hat{N}_\nu = \hat{a}_\nu^\dagger \hat{a}_\nu = \frac{1}{2} (\hat{a}_\nu^\dagger \hat{a}_\nu - \hat{a}_\nu \hat{a}_\nu^\dagger) - \frac{1}{2} = (\hat{a}_\nu^\dagger \hat{a}_\nu)_\mathcal{W} - \frac{1}{2} = (N_\nu)_\mathcal{W} - \frac{1}{2}. \quad (3.18)$$

The expectation value of interest is thus related to the expectation value of the Weyl ordered number operator related to the mode  $\nu$  as  $\langle \hat{N}_\nu \rangle = \langle (\hat{a}_\nu^\dagger \hat{a}_\nu)_\mathcal{W} \rangle - \frac{1}{2}$  and we can use Eq. (3.17) to compute it, thereby yielding

$$\langle \hat{N}_\nu(t) \rangle = \langle (\hat{a}_\nu^\dagger \hat{a}_\nu)_\mathcal{W} \rangle - \frac{1}{2} = \iint \boldsymbol{\alpha}^* \boldsymbol{\alpha} W^{(\hat{\rho})}(\boldsymbol{\alpha}, \boldsymbol{\alpha}^*, t) d^N \alpha d^N \alpha^* - \frac{1}{2} \quad (3.19)$$

$$= \iint \alpha_\nu^* \alpha_\nu W^{(\hat{\rho})}(\boldsymbol{\alpha}, \boldsymbol{\alpha}^*, t) d^N \alpha d^N \alpha^* - \frac{1}{2}. \quad (3.20)$$

We have therefore mapped the computation of the expectation value of a quantum observable to a phase-space average thanks to the Weyl correspondence rule. As we have already stated earlier, although this formulation resembles very much to a classical formulation of phase-space, the difference lies in that the Wigner function  $W^{(\hat{\rho})}(\boldsymbol{\alpha}, \boldsymbol{\alpha}^*)$  describing the state of the system is not a probability distribution. It indeed does not fulfil all the properties required to be named a probability distribution: it contains the whole quantum feature of the system.

### 3.2.1 Properties of the Wigner function

- The Wigner function is real-valued

$$\begin{aligned} (W^{(\hat{\rho})})^*(\boldsymbol{\alpha}, \boldsymbol{\alpha}^*, t) &= \frac{1}{\pi^{2N}} \iint \text{Tr} \left[ \hat{\rho} e^{\boldsymbol{\xi}^* \cdot \hat{\mathbf{a}} - \boldsymbol{\xi} \cdot \hat{\mathbf{a}}^\dagger} \right] e^{i(\boldsymbol{\xi}^* \cdot \boldsymbol{\alpha}^* + \boldsymbol{\xi} \cdot \boldsymbol{\alpha})} d^{2N} \boldsymbol{\xi} \\ &= \frac{1}{\pi^{2N}} \iint \text{Tr} \left[ \hat{\rho} e^{\boldsymbol{\lambda} \cdot \hat{\mathbf{a}}^\dagger - \boldsymbol{\lambda}^* \cdot \hat{\mathbf{a}}} \right] e^{-i(\boldsymbol{\lambda} \cdot \boldsymbol{\alpha} + \boldsymbol{\lambda}^* \cdot \boldsymbol{\alpha}^*)} d^{2N} \boldsymbol{\lambda} = W^{(\hat{\rho})}(\boldsymbol{\alpha}, \boldsymbol{\alpha}^*, t), \end{aligned} \quad (3.21)$$

as could be inferred from its definition by performing the variable substitution  $\boldsymbol{\lambda} \rightarrow -\boldsymbol{\xi}$  and  $\boldsymbol{\lambda}^* \rightarrow -\boldsymbol{\xi}^*$ .

- The Wigner function is normalised

$$\iint W^{(\hat{\rho})}(\boldsymbol{\alpha}, \boldsymbol{\alpha}^*, t) d^N \alpha d^N \alpha^* = \text{Tr}(\hat{\rho}) = 1, \quad (3.22)$$

as could be deduced by setting  $\hat{A} \equiv \hat{I}$  in Eq. (3.10) and exploiting that the trace of the density operator  $\hat{\rho}$  is known to be equal to one.

- The marginal distribution of the Wigner function related to one of the two canonically conjugated variables yields the probability distribution associated with that variable, as can be proved by partial integration over one of those two variables. Let us write  $\boldsymbol{\alpha} = \boldsymbol{\alpha}_r + i\boldsymbol{\alpha}_i$  and  $\boldsymbol{\xi} = \boldsymbol{\xi}_r + i\boldsymbol{\xi}_i$  and integrate  $W(\boldsymbol{\alpha}_r, \boldsymbol{\alpha}_i)$  over  $\boldsymbol{\alpha}_i$ . We can write

$$\begin{aligned}
\int W^{(\hat{\rho})}(\boldsymbol{\alpha}_r, \boldsymbol{\alpha}_i, t) d\boldsymbol{\alpha}_i &= \frac{1}{\pi^{2N}} \iiint \text{Tr} \left[ \hat{\rho} e^{(\hat{\mathbf{a}}^\dagger - i\boldsymbol{\alpha}_r + \boldsymbol{\alpha}_i) \cdot (\boldsymbol{\xi}_r + i\boldsymbol{\xi}_i) - (\hat{\mathbf{a}} + i\boldsymbol{\alpha}_r + \boldsymbol{\alpha}_i) \cdot (\boldsymbol{\xi}_r - i\boldsymbol{\xi}_i)} \right] d\boldsymbol{\xi}_r d\boldsymbol{\xi}_i d\boldsymbol{\alpha}_i \\
&= \frac{1}{\pi^{2N}} \iiint e^{-2i\boldsymbol{\alpha}_r \cdot \boldsymbol{\xi}_r + 2i\boldsymbol{\alpha}_i \cdot \boldsymbol{\xi}_i} \text{Tr} \left[ \hat{\rho} e^{\hat{\mathbf{a}}^\dagger \cdot (\boldsymbol{\xi}_r + i\boldsymbol{\xi}_i) - \hat{\mathbf{a}} \cdot (\boldsymbol{\xi}_r - i\boldsymbol{\xi}_i)} \right] d\boldsymbol{\xi}_r d\boldsymbol{\xi}_i d\boldsymbol{\alpha}_i \\
&= \frac{1}{\pi^N} \int e^{-2i\boldsymbol{\alpha}_r \cdot \boldsymbol{\xi}_r} \text{Tr} \left[ \hat{\rho} e^{(\hat{\mathbf{a}}^\dagger - \hat{\mathbf{a}}) \cdot \boldsymbol{\xi}_r} \right] d\boldsymbol{\xi}_r \\
&= \frac{1}{\pi^N} \int e^{-2i\boldsymbol{\alpha}_r \cdot \boldsymbol{\xi}_r} \int e^{2i\mathbf{p} \cdot \boldsymbol{\xi}_r} \langle \mathbf{p} | \hat{\rho} | \mathbf{p} \rangle d\mathbf{p} d\boldsymbol{\xi}_r \\
&= \frac{1}{\pi^N} \iint e^{2i(\mathbf{p} - \boldsymbol{\alpha}_r) \cdot \boldsymbol{\xi}_r} \langle \mathbf{p} | \hat{\rho} | \mathbf{p} \rangle d\mathbf{p} d\boldsymbol{\xi}_r \\
&= \langle \boldsymbol{\alpha}_r | \hat{\rho} | \boldsymbol{\alpha}_r \rangle = \text{Pr}(\boldsymbol{\alpha}_r), \tag{3.23}
\end{aligned}$$

where we have used twice the identity

$$\int e^{\pm 2i\mathbf{a} \cdot \mathbf{b}} d\mathbf{b} = \pi^N \delta(\mathbf{a}). \tag{3.24}$$

As Eq. (3.23) shows, partial integration over  $\boldsymbol{\alpha}_r$  (resp. over  $\boldsymbol{\alpha}_i$ , as could be similarly proven) renders the probability distribution of  $\boldsymbol{\alpha}_i$  (resp. of  $\boldsymbol{\alpha}_r$ ) and the Wigner function thus resembles very much in this respect to a joint probability distribution for  $\boldsymbol{\alpha}_i$  and  $\boldsymbol{\alpha}_r$  (or two any other canonically conjugated variables such as  $\boldsymbol{\alpha}$  and  $\boldsymbol{\alpha}^*$ ). It can however contain negative values (examples of which are given below) as a result of quantum interferences, explicitly violating one of Kolmogorov axioms a probability distribution must fulfil and is thereby referred to as quasiprobability distribution.

### 3.2.2 Gallery of Wigner functions

We show in the following the one mode Wigner function for several common states, namely coherent, thermal and Fock states, based on their density operator.

#### Coherent states

The symmetric characteristic function associated to the coherent state  $|\alpha_0\rangle$  described by the density operator  $\hat{\rho}_{\text{coh}} = |\alpha_0\rangle \langle \alpha_0|$  is given by

$$\begin{aligned}
\chi_{\mathcal{W}}^{(|\alpha_0\rangle \langle \alpha_0|)}(\boldsymbol{\xi}, \boldsymbol{\xi}^*) &= \text{Tr} \left[ |\alpha_0\rangle \langle \alpha_0| e^{\boldsymbol{\xi} \cdot \hat{\mathbf{a}}^\dagger - \boldsymbol{\xi}^* \cdot \hat{\mathbf{a}}} \right] = \langle \alpha_0 | e^{\boldsymbol{\xi} \cdot \hat{\mathbf{a}}^\dagger - \boldsymbol{\xi}^* \cdot \hat{\mathbf{a}}} | \alpha_0 \rangle \\
&= e^{\frac{1}{2}(\boldsymbol{\xi} \cdot \boldsymbol{\alpha}_0^* - \boldsymbol{\xi}^* \cdot \boldsymbol{\alpha}_0)} \langle \alpha_0 | \alpha_0 + \boldsymbol{\xi} \rangle = e^{\boldsymbol{\xi} \cdot \boldsymbol{\alpha}_0^* - \boldsymbol{\xi}^* \cdot \boldsymbol{\alpha}_0} e^{-|\boldsymbol{\xi}|^2/2},
\end{aligned}$$

whose Fourier transform yields the Wigner function

$$W^{(|\alpha_0\rangle \langle \alpha_0|)}(\boldsymbol{\alpha}, \boldsymbol{\alpha}^*) = \frac{1}{\pi^2} \iint e^{\boldsymbol{\xi} \cdot \boldsymbol{\alpha}_0^* - \boldsymbol{\xi}^* \cdot \boldsymbol{\alpha}_0} e^{-|\boldsymbol{\xi}|^2/2} e^{-i(\boldsymbol{\xi} \boldsymbol{\alpha} + \boldsymbol{\xi}^* \boldsymbol{\alpha}^*)} d\boldsymbol{\xi} d\boldsymbol{\xi}^* \tag{3.25}$$

$$= \frac{2}{\pi} e^{-2|\boldsymbol{\alpha} - \boldsymbol{\alpha}_0|^2}, \tag{3.26}$$

which is a Gaussian of mean  $\mu = \alpha_0$ , standard deviation  $\sigma = 1/2$  and peak value  $2/\pi$  at  $\alpha = \alpha_0$ . As a Gaussian, the Wigner function related to coherent states is positive definite everywhere and qualifies as a true phase-space probability distribution. Three examples for different values of  $\alpha_0$  are shown in FIG. 3.1.

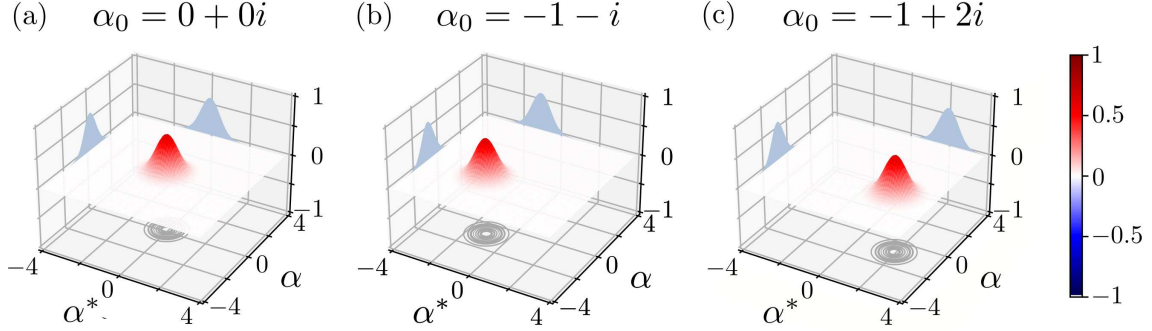


Figure 3.1 – Wigner functions of three coherent states for different values of  $\alpha_0$ .

When  $\alpha_0 = 0 + 0i$ , as in FIG. 3.1(a), the related coherent state is referred to as a vacuum state, which has probably the most simple Wigner function one can think of. As Ref. [247] indicates, such a probability distribution in the phase space classically corresponds to the phase-space density of a collection of oscillators, with statistical fluctuations of zero mean and isotropic  $1/2$  variance. Those statistical fluctuations naturally emerge as vacuum fluctuations in a quantum mechanical context, even if the system lies in a pure vacuum state. Those isotropic vacuum, or quantum, fluctuations and the related  $1/2$  variance, are not described by a mean-field method that assumes a perfectly zero field for a vacuum state. FIGS. 3.1(b) and 3.1(c) show two coherent states that correspond to vacuum states translated by the Glauber displacement operator in the phase space. They exhibit the same behaviour and variance as the vacuum state in FIG. 3.1(a), but display a translated mean  $\alpha_0$ . Ref. [247] indicates that this variance also originates from vacuum fluctuations that, for instance, would inevitably arise in the coherent state produced by a high quality laser of coherent amplitude. In some cases, especially if  $\alpha_0 \rightarrow \infty$ , one might neglect the fluctuations around the mean value, which amounts to approximate the state of the system by a purely classical field with well defined amplitude and phase.

### Fock states

The density operator of the Fock state  $|n\rangle$  is given by  $\hat{\rho}_{|n\rangle} = |n\rangle \langle n|$  and leads to the characteristic function

$$\begin{aligned} \chi_{\mathcal{W}}^{(|n\rangle\langle n|)}(\xi, \xi^*) &= \text{Tr} \left[ |n\rangle \langle n| e^{\xi \cdot \hat{a}^\dagger - \xi^* \cdot \hat{a}} \right] = \sum_{j=0}^{\infty} \langle j|n\rangle \langle n| e^{\xi \cdot \hat{a}^\dagger - \xi^* \cdot \hat{a}} |j\rangle = \langle n| e^{\xi \cdot \hat{a}^\dagger - \xi^* \cdot \hat{a}} |n\rangle \\ &= e^{-|\xi|^2/2} \langle n| \sum_{k=0}^{\infty} \frac{(\xi \cdot \hat{a}^\dagger)^k}{k!} \sum_{l=0}^{\infty} \frac{(-\xi^* \cdot \hat{a})^l}{l!} |n\rangle = e^{-|\xi|^2/2} \mathcal{L}_n(|\xi|^2), \end{aligned} \quad (3.27)$$

where  $\mathcal{L}_n(x)$  is the  $n^{\text{th}}$  Laguerre polynomial. This allows for the determination of the related Wigner function through the Fourier transform

$$W^{(|n\rangle\langle n|)}(\alpha, \alpha^*) = \frac{2}{\pi}(-1)^n e^{-2|\alpha|^2} \mathcal{L}_n(4|\alpha|^2). \quad (3.28)$$

Three examples for the Fock states  $|1\rangle$ ,  $|3\rangle$  and  $|5\rangle$  are shown in FIG. 3.2.

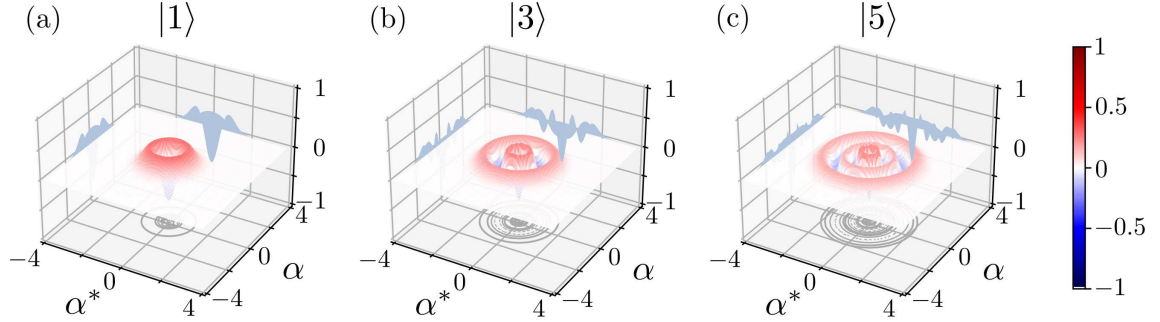


Figure 3.2 – Wigner functions of three different Fock states.

Owing to the property that the  $n^{\text{th}}$  Laguerre polynomial  $\mathcal{L}_n(x)$  possesses  $n$  real roots, the related Wigner function oscillates strongly, all the more with high  $n$ . This also implies that the Wigner function of Fock states takes negative values which disqualifies it as a probability distribution. This negativity can be on the other hand leveraged as an indicator of the nonclassicality of the underlying physical state [248].

### Thermal states

The density operator for a thermal state at thermal equilibrium with chemical potential  $\mu$  and reservoir temperature  $T = 1/(\beta k_B)$ , with  $k_B$  the Boltzmann constant, is provided by

$$\hat{\rho}_{\text{th}} = \left(1 - e^{-\beta(E_1 - \mu)}\right) \sum_{n=0}^{\infty} e^{-n\beta(E_1 - \mu)} |n\rangle \langle n|, \quad (3.29)$$

where  $E_i$  are the eigenenergies of the system in the grand canonical ensemble. The density operator thus consists in a statistical mixture of Fock states weighted by coefficients that depend upon the population of the energy levels. The related characteristic function then

reads

$$\begin{aligned}
\chi_{\mathcal{W}}^{(\hat{\rho}_{\text{th}})}(\xi, \xi^*) &= (1 - e^{-\beta(E_i - \mu)}) \text{Tr} \left[ \sum_{n=0}^{\infty} e^{-n\beta(E_i - \mu)} |n\rangle \langle n| e^{\xi \cdot \hat{a}^\dagger - \xi^* \cdot \hat{a}} \right] \\
&= (1 - e^{-\beta(E_i - \mu)}) \sum_{j=0}^{\infty} \langle j| \sum_{n=0}^{\infty} e^{-n\beta(E_i - \mu)} |n\rangle \langle n| e^{\xi \cdot \hat{a}^\dagger - \xi^* \cdot \hat{a}} |j\rangle \\
&= (1 - e^{-\beta(E_i - \mu)}) \sum_{j=0}^{\infty} e^{-j\beta(E_i - \mu)} \langle j| e^{\xi \cdot \hat{a}^\dagger - \xi^* \cdot \hat{a}} |j\rangle \\
&= (1 - e^{-\beta(E_i - \mu)}) e^{-|\xi|^2/2} \sum_{j=0}^{\infty} e^{-j\beta(E_i - \mu)} \langle j| \sum_{k=0}^{\infty} \frac{(\xi \cdot \hat{a}^\dagger)^k}{k!} \sum_{l=0}^{\infty} \frac{(-\xi^* \cdot \hat{a})^l}{l!} |j\rangle \\
&= (1 - e^{-\beta(E_i - \mu)}) e^{-|\xi|^2/2} \sum_{j=0}^{\infty} e^{-j\beta(E_i - \mu)} \sum_{k=0}^j \frac{(-1)^k |\xi|^{2k}}{(k!)^2} j(j-1) \dots (j-k+1) \\
&= (1 - e^{-\beta(E_i - \mu)}) e^{-|\xi|^2/2} \sum_{j=0}^{\infty} e^{-j\beta(E_i - \mu)} \mathcal{L}_j(|\xi|^2), \tag{3.30}
\end{aligned}$$

where

$$\mathcal{L}_n(x) = \sum_{m=0}^n (-1)^m \frac{n!}{(m!)^2 (n-m)!} x^m \tag{3.31}$$

is the  $n^{\text{th}}$  Laguerre polynomial. Since the generating function of Laguerre polynomials reads

$$\sum_{n=0}^{\infty} t^n \mathcal{L}_n(x) = \frac{1}{1-t} e^{tx/(1-t)}, \tag{3.32}$$

we can finally write

$$\chi_{\mathcal{W}}^{(\hat{\rho}_{\text{th}})}(\xi, \xi^*) = e^{-\frac{|\xi|^2}{2} \coth[\beta(E_i - \mu)/2]}. \tag{3.33}$$

This allows us to write the Wigner function for a thermal state as

$$W^{(\hat{\rho}_{\text{th}})}(\alpha, \alpha^*) = \frac{2}{\pi} \frac{1}{\coth\left(\frac{\beta(E_i - \mu)}{2}\right)} e^{-2|\alpha|^2 / \coth[\beta(E_i - \mu)/2]}. \tag{3.34}$$

Three examples for different values of  $\Gamma_k = \coth[\beta(E_i - \mu)/2]$  are shown in FIG. 3.3.

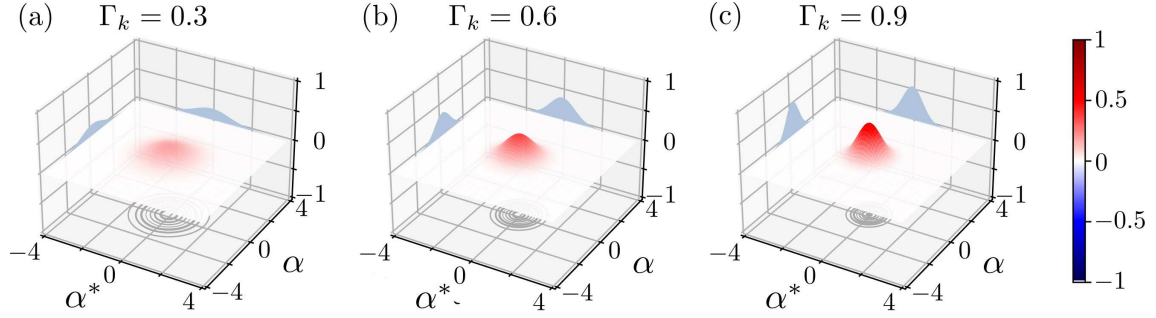


Figure 3.3 – Wigner functions of three thermal states for different values of  $\Gamma_k = \coth[\beta(E_i - \mu)/2]$ .

Because of the underlying density operator that is obtained as a sum of Fock states, which are purely quantum states whose Wigner function may be negative as we highlight in the following, it should appear natural that the Wigner function of a thermal state would also be oscillatory and takes negative values. However, the weighted sum over Fock states yields the Wigner functions shown in FIG. 3.3, for three different values of  $\Gamma_k$ . They are also Gaussian that are everywhere positive definite and that are more spread than the Gaussian related to coherent states which reflects the classicality of the related thermal field.

### 3.2.3 Time evolution of the Wigner function and operator correspondences

Still following the analogy with classical mechanics, the time evolution equation for the density operator is found through canonical quantisation. The classical variables are replaced by quantum operators and Poisson brackets by commutators, which yields

$$i\hbar \frac{\partial \hat{\rho}}{\partial t} = [\hat{H}, \hat{\rho}], \quad (3.35)$$

which is known as the von Neumann equation [3], the quantum analogue of the Liouville equation. The linear mapping we have introduced between quantum operators and their associated function renders possible to write the time evolution equation for the Wigner function based on the von Neumann equation. If the Hamiltonian of the system is expressed in terms of  $\hat{a}_\nu^\dagger$  and  $\hat{a}_\nu$ , the commutator appearing in the von Neumann equation involves products of the density operator and annihilation/creation operators. One should then compute the Wigner functions of those quantities and relate them to the Wigner function of the system described by the density operator  $\hat{\rho}$ , which is achieved by Fourier transforming  $\text{Tr}[\hat{a}_\nu \hat{\rho} e^{\xi \cdot \hat{a}^\dagger - \xi^* \cdot \hat{a}}]$ . We first note, by using the invariance of the trace under circular permutation and using the Baker–Hausdorff formula [249, 250] that

$$\text{Tr}[\hat{a}_\nu \hat{\rho} e^{\xi \cdot \hat{a}^\dagger - \xi^* \cdot \hat{a}}] = \text{Tr}[\hat{\rho} e^{\xi \cdot \hat{a}^\dagger} e^{-\xi^* \cdot \hat{a}} e^{-|\xi|^2/2} \hat{a}_\nu] = \left( \frac{\xi}{2} - \frac{\partial}{\partial \xi^*} \right) \chi_{\mathcal{W}}^{(\hat{\rho})}(\xi, \xi^*), \quad (3.36)$$

whose Fourier transform provides

$$\begin{aligned}
W^{(a_\nu \hat{\rho})}(\boldsymbol{\alpha}, \boldsymbol{\alpha}^*) &= \iint \text{Tr} \left[ \hat{a}_\nu \hat{\rho} e^{\boldsymbol{\xi} \cdot \hat{\mathbf{a}}^\dagger - \boldsymbol{\xi}^* \cdot \hat{\mathbf{a}}} \right] e^{-i(\boldsymbol{\xi} \cdot \boldsymbol{\alpha} + \boldsymbol{\xi}^* \cdot \boldsymbol{\alpha}^*)} d^{2N} \boldsymbol{\xi} \\
&= \iint \left( \frac{\boldsymbol{\xi}}{2} - \frac{\partial}{\partial \boldsymbol{\xi}^*} \right) \chi_{\mathcal{W}}^{(\hat{\rho})}(\boldsymbol{\xi}, \boldsymbol{\xi}^*) e^{-i(\boldsymbol{\xi} \cdot \boldsymbol{\alpha} + \boldsymbol{\xi}^* \cdot \boldsymbol{\alpha}^*)} d^{2N} \boldsymbol{\xi} \\
&= \left( \alpha_\nu + \frac{1}{2} \frac{\partial}{\partial \alpha_\nu^*} \right) W^{(\hat{\rho})}(\boldsymbol{\alpha}, \boldsymbol{\alpha}^*), \tag{3.37}
\end{aligned}$$

after integrating by parts [239, 251]. It thereby highlights a functional rule that is used to establish a link between the Wigner function associated to the action of annihilation/creation operators on the density operator (and vice-versa) and the corresponding effect on the Wigner function of the system. They are four such combinations and the effect on the Wigner function is obtained similarly as in Eq. (3.37), yielding a set of correspondence rules

$$W^{(\hat{a}_\nu \hat{\rho})}(\boldsymbol{\alpha}, \boldsymbol{\alpha}^*) = \left( \alpha_\nu + \frac{1}{2} \frac{\partial}{\partial \alpha_\nu^*} \right) W^{(\hat{\rho})}(\boldsymbol{\alpha}, \boldsymbol{\alpha}^*) \tag{3.38}$$

$$W^{(\hat{a}_\nu^\dagger \hat{\rho})}(\boldsymbol{\alpha}, \boldsymbol{\alpha}^*) = \left( \alpha_\nu^* - \frac{1}{2} \frac{\partial}{\partial \alpha_\nu} \right) W^{(\hat{\rho})}(\boldsymbol{\alpha}, \boldsymbol{\alpha}^*) \tag{3.39}$$

$$W^{(\hat{\rho} \hat{a}_\nu)}(\boldsymbol{\alpha}, \boldsymbol{\alpha}^*) = \left( \alpha_\nu - \frac{1}{2} \frac{\partial}{\partial \alpha_\nu^*} \right) W^{(\hat{\rho})}(\boldsymbol{\alpha}, \boldsymbol{\alpha}^*) \tag{3.40}$$

$$W^{(\hat{\rho} \hat{a}_\nu^\dagger)}(\boldsymbol{\alpha}, \boldsymbol{\alpha}^*) = \left( \alpha_\nu^* + \frac{1}{2} \frac{\partial}{\partial \alpha_\nu} \right) W^{(\hat{\rho})}(\boldsymbol{\alpha}, \boldsymbol{\alpha}^*). \tag{3.41}$$

This set of correspondence rules allows to derive a motion equation for the Wigner function. We consider for instance a typical discrete two-body Hamiltonian

$$\hat{H} = -\frac{J}{2} \sum_{\nu=0}^N \left( \hat{a}_\nu^\dagger \hat{a}_{\nu+1} + \hat{a}_{\nu+1}^\dagger \hat{a}_\nu \right) + \sum_{\nu=0}^N V_\nu \hat{a}_\nu^\dagger \hat{a}_\nu + \frac{1}{2} \sum_{\nu=0}^N U_\nu \hat{a}_\nu^\dagger \hat{a}_\nu^\dagger \hat{a}_\nu \hat{a}_\nu, \tag{3.42}$$

where  $J$  is the hopping energy from a site to its nearest neighbour,  $\hat{a}_\nu^\dagger$  (resp.  $\hat{a}_\nu$ ) is the creation (resp. annihilation) operator at site  $\nu$ ,  $V_\nu$  is the value of the potential at site  $\nu$  and  $U_\nu$  is the interaction term at site  $\nu$ . This Hamiltonian is very typical from scenarios involving quantum transport of interacting ultracold atoms through disorder potentials, as we study in this manuscript. More generally, it describes interacting systems that can be defined on a grid with possibly sophisticated links like in small-world networks [252, 253] that find applications in a wide array of domains that extend beyond the scope of ultracold atoms physics.

The von Neumann equation explicitly reads in this case

$$i\hbar \frac{\partial \hat{\rho}}{\partial t} = -\frac{J}{2} \sum_{\nu=0}^N \left( [\hat{a}_\nu^\dagger \hat{a}_{\nu+1}, \hat{\rho}] + [\hat{a}_{\nu+1}^\dagger \hat{a}_\nu, \hat{\rho}] \right) + \sum_{\nu=0}^N V_\nu [\hat{a}_\nu^\dagger \hat{a}_\nu, \hat{\rho}] + \frac{1}{2} \sum_{\nu=0}^N U_\nu [\hat{a}_\nu^\dagger \hat{a}_\nu^\dagger \hat{a}_\nu \hat{a}_\nu, \hat{\rho}].$$

We use the correspondence rules in Eqs. (3.38–3.41) for computing the equivalence in terms of  $W^{(\hat{\rho})}(\boldsymbol{\alpha}, \boldsymbol{\alpha}^*)$  of the Wigner functions associated to the commutators appearing in the above equation, such as  $W^{([\hat{a}_\nu^\dagger \hat{a}_\nu, \hat{\rho}])(\boldsymbol{\alpha}, \boldsymbol{\alpha}^*)}$ , and have the following motion equation for the Wigner



function<sup>4</sup>

$$\begin{aligned}
i\hbar \frac{\partial}{\partial t} W^{(\hat{\rho})}(\boldsymbol{\alpha}, \boldsymbol{\alpha}^*) = \sum_{\nu=0}^N \left[ -J \left( \frac{\partial}{\partial \alpha_{\nu}} \alpha_{\nu+1} - \frac{\partial}{\partial \alpha_{\nu}^*} \alpha_{\nu+1}^* \right) + V_{\nu} \left( \frac{\partial}{\partial \alpha_{\nu}} \alpha_{\nu} - \frac{\partial}{\partial \alpha_{\nu}^*} \alpha_{\nu}^* \right) \right. \\
\left. - U_{\nu} \left( \frac{\partial}{\partial \alpha_{\nu}} \alpha_{\nu} - \frac{\partial}{\partial \alpha_{\nu}^*} \alpha_{\nu}^* \right) (|\alpha_{\nu}|^2 - 1) \right. \\
\left. + \frac{U_{\nu}}{4} \left( \frac{\partial^2}{\partial \alpha_{\nu}^2} \frac{\partial}{\partial \alpha_{\nu}^*} \alpha_{\nu} - \frac{\partial}{\partial \alpha_{\nu}} \frac{\partial^2}{\partial \alpha_{\nu}^{*2}} \alpha_{\nu}^* \right) \right] W^{(\hat{\rho})}(\boldsymbol{\alpha}, \boldsymbol{\alpha}^*). \quad (3.43)
\end{aligned}$$

This partial differential equation provides the time evolution of  $W^{(\hat{\rho})}(\boldsymbol{\alpha}, \boldsymbol{\alpha}^*)$ . As such, it contains the same information as the von Neumann equation (3.35) for the density operator  $\hat{\rho}$  and reproduces the exact evolution of the system. One faces however the very high difficulty, not to say impossibility, to numerically integrate it owing to the excessively large dimension of the underlying phase space considered in realistic configurations such as those we study. An approximation is usually performed at this stage, which leads to the truncated Wigner method.

### 3.2.4 Truncated Wigner method

As is formally shown in Ref. [254], if the on–site density  $|\alpha_{\nu}|^2 \gg 1$  is high enough and the interaction term  $U_{\nu}$  is small enough, one can safely neglect the third order derivative terms appearing in (3.43) and thereby truncate it, giving its name to the method. One is then left with a Fokker–Planck equation

$$\begin{aligned}
i\hbar \frac{\partial}{\partial t} W^{(\hat{\rho})}(\boldsymbol{\alpha}, \boldsymbol{\alpha}^*) = \sum_{\nu=0}^N \left[ -J \left( \frac{\partial}{\partial \alpha_{\nu}} \alpha_{\nu+1} - \frac{\partial}{\partial \alpha_{\nu}^*} \alpha_{\nu+1}^* \right) + V_{\nu} \left( \frac{\partial}{\partial \alpha_{\nu}} \alpha_{\nu} - \frac{\partial}{\partial \alpha_{\nu}^*} \alpha_{\nu}^* \right) \right. \\
\left. - U_{\nu} \left( \frac{\partial}{\partial \alpha_{\nu}} \alpha_{\nu} - \frac{\partial}{\partial \alpha_{\nu}^*} \alpha_{\nu}^* \right) (|\alpha_{\nu}|^2 - 1) \right], \quad (3.44)
\end{aligned}$$

with only a drift term and no diffusion term. This Fokker–Planck equation can be mapped to a set of coupled Langevin equations for the canonically conjugated variables  $\alpha_{\nu}(t)$  and  $\alpha_{\nu}^*(t)$  which become now time–dependent. The solution of those coupled Langevin equations provide trajectories along which the Wigner function remains constant. Omitting the explicit time–dependence of  $\alpha_{\nu}(t)$  and  $\alpha_{\nu}^*(t)$  for compactness, this infinite set of Langevin equations reads

$$i\hbar \frac{\partial \alpha_{\nu}}{\partial t} = -J(\alpha_{\nu+1} + \alpha_{\nu-1}) + V_{\nu} \alpha_{\nu} + U_{\nu} (|\alpha_{\nu}|^2 - 1) \alpha_{\nu} \quad (3.45)$$

and represents an evolution equation for each site  $\nu$  considered in the Hamiltonian (3.42), very similarly to the discretised evolution equation one would obtain in a mean–field framework by replacing quantum operators by classical fields. An analogous equation is obtained for  $\alpha_{\nu}^*$ . These evolution equations may be used to compute the expectation values of an observable,

---

<sup>4</sup>The whole derivation of this equation can be found in App. D.

as was already stated in Eq. (3.16),

$$\begin{aligned}
\left\langle \left( \prod_{\nu=0}^N \hat{a}_{\nu}^{\dagger n_{\nu}} \hat{a}_{\nu}^{m_{\nu}} \right)_{\mathcal{W}} \right\rangle_t &= \prod_{\nu=0}^N \iint \alpha_{\nu}^{*n_{\nu}} \alpha_{\nu}^{m_{\nu}} W^{(\hat{\rho})}(\boldsymbol{\alpha}, \boldsymbol{\alpha}^*; t) d^{2N} \alpha \\
&= \prod_{\nu=0}^N \iint \alpha_{\nu}^{*n_{\nu}} \alpha_{\nu}^{m_{\nu}} W^{(\hat{\rho})}(\boldsymbol{\alpha}, \boldsymbol{\alpha}^*; t_0) d^{2N} \alpha, \\
&= \prod_{\nu=0}^N \lim_{N_t \rightarrow \infty} \frac{1}{N_t} \sum_{k=1}^{N_t} \alpha_{\nu,k}^{*n_{\nu}}(t) \alpha_{\nu,k}^{m_{\nu}}(t) \equiv \prod_{\nu=0}^N \overline{\alpha_{\nu}^{*n_{\nu}}(t) \alpha_{\nu}^{m_{\nu}}(t)}, \quad (3.46)
\end{aligned}$$

where we have used that along the trajectories which are solution of Eq. (3.45), the Wigner function is conserved (conservation of phase-space volumes) [255]. Quantum observables are then obtained by writing the Wigner function related to the initial system state and using it as a probability distribution to sample  $N_t$  independent trajectories that are evolved along the mean-field trajectories solutions of Eq. (3.45). This sampling of the initial state constitutes the main difference with a mean-field approach, where an initial empty system involves that all the classical amplitudes are initially set to zero. In contrast with this approach, the truncated Wigner method specifies that those classical fields acquire random values prescribed by the related Wigner function, which accounts for the presence of initial vacuum fluctuations [238].

In summary, one computes random initial conditions sampled by the Wigner function of the system at initial time  $t_0$ , each realisation of those initial conditions giving rise to a distinct mean-field trajectory in the phase space explored by the system. The evolution equation is provided by the mean-field Langevin equation (3.45) for the mode  $\nu$ . Owing to its resemblance with the Gross-Pitaevskii equation, it is sometimes called a stochastic Gross-Pitaevskii equation. Even though it explicitly contains no stochastic terms, we are fully entitled to qualify it as stochastic. Indeed, the initial sampling according to the Wigner function related to the initial state of the system introduces the presence of quantum noise, as we explicitly show in the following for atom lasers. The expectation value of an observable expressed in terms of Weyl ordered operators is then finally performed by means of an average over all mean-field trajectories, as is prescribed by Eq. (3.46). This procedure is summed up and sketched in FIG. 3.4.

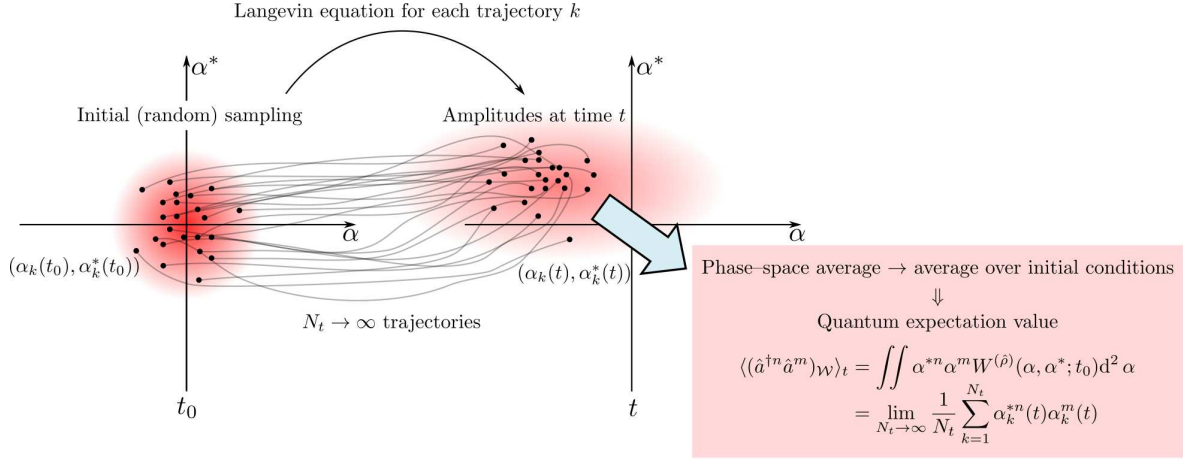


Figure 3.4 – Principle of the truncated Wigner method. A large number  $N_t$  of classical field amplitudes  $\alpha_k$  and  $\alpha_k^*$  are sampled according to the Wigner function associated to the density operator  $\hat{\rho}$  describing the state of the system at initial time  $t_0$ . This sampling accounts for the presence of initial quantum fluctuations. Those  $N_t$  amplitudes are each evolved according to a Langevin equation whose solution describes a trajectory in the underlying phase space. Quantum expectation values of symmetrically ordered, in terms of creation and annihilation operators, observables are computed through phase-space average that boils down to computing an average over the initial conditions of the classical amplitudes  $\alpha_k$  and  $\alpha_k^*$  at time  $t$ .

### 3.3 Truncated Wigner method applied to open quantum systems

In the following subsections, we first explain how to sample the initial quantum state related to an atom laser system and then apply the procedure previously described to derive an evolution equation for the sampling points in this context. We finally specify how to compute observables based on an average over the trajectories evolved along the evolution equation.

#### 3.3.1 Sampling of the initial quantum state

The Wigner function related to the whole system can be written as

$$\mathcal{W}(\{\psi_\alpha, \psi_\alpha^*\}, t_0) = \mathcal{W}_{SR}(\{\psi_\alpha, \psi_\alpha^*\}, t_0) \times \mathcal{W}_{\mathcal{S}}(\phi_{\mathcal{S}}, \phi_{\mathcal{S}}^*, t_0), \quad (3.47)$$

where  $\mathcal{W}_{SR}(\{\psi_\alpha, \psi_\alpha^*\}, t_0)$  is the Wigner function related to the scattering region ( $SR$ ) and  $\mathcal{W}_{\mathcal{S}}(\phi_{\mathcal{S}}, \phi_{\mathcal{S}}^*, t_0)$  is the Wigner function related to the reservoir ( $\mathcal{S}$ ) of bosonic atoms.

On the one hand, the scattering region is assumed to be initially totally empty at  $t = t_0$ , leading to a Wigner function obtained as the product of vacuum Wigner functions

$$\mathcal{W}_{SR}(\{\psi_\alpha, \psi_\alpha^*\}, t_0) = \prod_{\alpha} \left( \frac{2}{\pi} \right) e^{-2|\psi_\alpha|^2}, \quad (3.48)$$

which are coherent states  $|\alpha_0 = 0\rangle$  whose Wigner function is given in Eq. (3.26) and sketched in FIG. 3.1(a). The initial state is thus sampled by complex Gaussian random variables and the classical field amplitudes are consequently determined as

$$\psi_\alpha(t = t_0) = \frac{1}{2} (\mathcal{A}_\alpha + i\mathcal{B}_\alpha) \quad (3.49)$$

where  $\mathcal{A}_\alpha$  and  $\mathcal{B}_\alpha$  are real and independent Gaussian random variables fulfilling

$$\overline{\mathcal{A}_\alpha} = \overline{\mathcal{B}_\alpha} = 0, \quad (3.50)$$

$$\overline{\mathcal{A}_{\alpha'} \mathcal{A}_\alpha} = \overline{\mathcal{B}_{\alpha'} \mathcal{B}_\alpha} = \delta_{\alpha'\alpha}, \quad (3.51)$$

$$\overline{\mathcal{A}_{\alpha'} \mathcal{B}_\alpha} = 0, \quad (3.52)$$

where the overline notation  $\overline{\cdot}$  denotes an average over the random variables. This sampling implies a zero average for the field amplitudes  $\overline{\psi_\alpha} = 0$  but also, in great contrast with a mean-field treatment, a finite variance  $\overline{|\psi_\alpha|^2} = 1/2$ , as is illustrated in FIG. 3.1(a). This finite variance can be understood in terms of a half pseudo particle initially present on each site. This interpretation of the finite variance for the field amplitudes in terms of a half fictitious particle widely prevails in the literature, although it is formally valid only in the context of the vacuum Wigner function [256].

On the other hand, the reservoir of bosonic particles is populated with a large number  $\mathcal{N} \rightarrow \infty$  of bosonic atoms which allows us to safely model it as a coherent state  $|\alpha_0 = \phi_S^0\rangle$  whose Wigner function is given in Eq. (3.26) and an illustration in FIG. 3.1(b) and (c). It explicitly reads here

$$\mathcal{W}_S(\phi_S, \phi_S^*, t_0) = \left(\frac{2}{\pi}\right) e^{-2|\phi_S - \phi_S^0|^2}. \quad (3.53)$$

Owing to the very large number of particles contained in the reservoir, we describe the source term classically by setting  $\phi_S^0 = \sqrt{\mathcal{N}}$ , because both the amplitude and the phase of the source display a negligible relative uncertainties.

### 3.3.2 Evolution equation

The evolution equation is obtained by applying the aforescribed procedure to atom lasers, which amounts to solving

$$\begin{aligned} i\hbar \frac{\partial \psi_\alpha}{\partial t} = & (E_\delta/q_\alpha + V_\alpha - \mu q_\alpha) \psi_\alpha - \frac{E_\delta}{2} [J_{\alpha-} \psi_{\alpha-1} + J_{\alpha+} \psi_{\alpha+1}] + g_\alpha (|\psi_\alpha|^2 - 1) \psi_\alpha \\ & + \sqrt{\mathcal{N}} \kappa(t) \delta_{\alpha, \alpha_S} + \delta_{\alpha, 0} \chi_0(t) + \delta_{\alpha, N} \chi_N(t), \end{aligned} \quad (3.54)$$

where the field operators have been replaced by classical field amplitudes. The effective hopping term

$$J_{\alpha\pm} = \left( \frac{1}{q_{\alpha\pm 1}} - \frac{\delta q'_{\alpha\pm 1}}{2 q_{\alpha\pm 1}^2} \right) \quad (3.55)$$

and  $q_\alpha$  are introduced to implement smooth exterior complex scaling, in accordance with the procedure detailed in Chapter 2. Eq. (3.54) also contains the terms  $\chi_0(t)$  and  $\chi_N(t)$  that naturally arise when converting the spatially infinite atom-laser system to a finite extension system by imposing transparent boundary conditions, as described in Chapter 2. Those

terms represent particles that are initially contained in the left or right lead and penetrate the scattering region after some finite time. Contrarily to the mean-field approach followed in Chapter 2, where we initially set all amplitudes to zero, corresponding to an initially empty scattering region, the sampling by the Wigner function is such that those amplitudes initially acquire random values. Consequently, the presence of initial random values for the field amplitudes yields a non vanishing contribution for  $\chi_0(t)$  and  $\chi_N(t)$  that is interpreted as a quantum noise that penetrates into the scattering region at some finite time  $t$ . This quantum noise<sup>5</sup> is yielded as

$$\chi_0(t) = E_\delta \sum_{\alpha'=-\infty}^{-1} M_{\alpha'}(t-t_0)\psi_{\alpha'}(t_0) \quad (3.56)$$

$$\chi_N(t) = -E_\delta \sum_{\alpha'=N}^{\infty} M_{\alpha'-N}(t-t_0)\psi_{\alpha'}(t_0), \quad (3.57)$$

with

$$M_\alpha(\tau) = \frac{i^\alpha}{2} \left[ J_{\alpha-1} \left( \frac{E_\delta \tau}{\hbar} \right) + J_{\alpha+1} \left( \frac{E_\delta \tau}{\hbar} \right) \right] e^{-i(E_\delta - \mu)\tau/\hbar}, \quad (3.58)$$

where  $J_\alpha$  is the Bessel function of the first kind and order  $\alpha$ . The related autocorrelation function is provided by [216]

$$\overline{\chi_0^*(t)\chi_0(t+\tau)} = \overline{\chi_N^*(t)\chi_N(t+\tau)} = -iM_0(\tau). \quad (3.59)$$

### 3.3.3 Computation of observables

As is prescribed by Eq. (3.46), quantum expectation values related to observables are obtained through phase-space averages. In the case of the total on-site density, it reads

$$n_\alpha(t) = \langle \hat{n}_\alpha(t) \rangle = \langle \hat{a}_\alpha^\dagger(t)\hat{a}_\alpha(t) \rangle = \overline{|\psi_\alpha(t)|^2} - \frac{1}{2}, \quad (3.60)$$

where the subtraction of  $1/2$  in the density that naturally emerges from the expression of the density operator in terms of a Weyl ordered operator (see Eq. (3.20)) compensates for the initial half pseudo particle present on each site, as a result of the sampling of the initial state by complex random numbers. The total on-site current is given by

$$\begin{aligned} j_\alpha(t) &= \frac{iE_\delta}{2\hbar} \langle \hat{a}_{\alpha+1}^\dagger(t)\hat{a}_\alpha(t) - \hat{a}_\alpha^\dagger(t)\hat{a}_{\alpha+1}(t) \rangle \\ &= \frac{iE_\delta}{2\hbar} \overline{\psi_{\alpha+1}^*(t)\psi_\alpha(t) - \psi_\alpha^*(t)\psi_{\alpha+1}(t)}. \end{aligned} \quad (3.61)$$

Those contributions are referred to as total because they contain both the coherent and incoherent contributions. As we already highlighted earlier, this coherence is to be understood in terms of the ability for the several wave components of the incident atomic beam to display interference effects that result from a phase-coherence relation, which may be compromised by inelastic scattering that scrambles such a phase-coherence relation. This coherence is explicitly defined below for instance for the on-site density

$$n_\alpha^{\text{coh}}(t) = |\langle \hat{a}_\alpha(t) \rangle|^2 = \left| \overline{\psi_\alpha(t)} \right|^2, \quad (3.62)$$

---

<sup>5</sup>Its explicit expression is derived in Appendix C.

and the on-site current

$$\begin{aligned} j_\alpha^{\text{coh}}(t) &= \frac{iE_\delta}{2\hbar} \left( \langle \hat{a}_{\alpha+1}^\dagger(t) \rangle \langle \hat{a}_\alpha(t) \rangle - \langle \hat{a}_\alpha^\dagger(t) \rangle \langle \hat{a}_{\alpha+1}(t) \rangle \right) \\ &= \frac{iE_\delta}{2\hbar} \left( \overline{\psi_{\alpha+1}^*(t) \psi_\alpha(t)} - \overline{\psi_\alpha^*(t) \psi_{\alpha+1}(t)} \right). \end{aligned} \quad (3.63)$$

The notion of coherence is now clarified, because the averages in Eqs. (3.62) and (3.63) preserve an existing phase coherence relation, whilst the averages performed in Eqs. (3.60) and (3.61) do not. This is best understood when comparing Eq. (3.60) where the square modulus, that kills the overall phase related to each trajectory in the phase space, is performed before the average, in great contrast to Eq. (3.62) where the average is performed before the square modulus.

The incoherent contribution is identified as the difference between the total and the coherent contribution. In the case of the on-site current and density, it is explicitly yielded as

$$n_\alpha^{\text{incoh}} = n_\alpha - n_\alpha^{\text{coh}}, \quad (3.64)$$

$$j_\alpha^{\text{incoh}} = j_\alpha - j_\alpha^{\text{coh}}. \quad (3.65)$$

In the absence of atom-atom interaction, both the mean field approximation and the evolution equation in the framework of the truncated Wigner method boil down to the traditional Schrödinger equation. In this case, predictions of the truncated Wigner method reduce to the mean-field predictions, and the total contribution is identical to the coherent one, as is illustrated in FIG. 3.5.

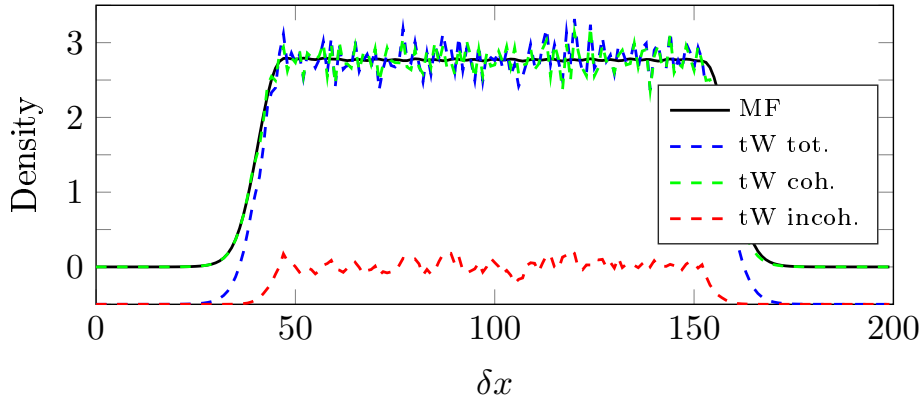


Figure 3.5 – Mean-field and truncated Wigner simulations performed in the absence of disorder and atom-atom interaction. Apart from the fluctuations related to the finite number of trajectories in the phase space, both the total and coherent contributions are equal to the mean-field prediction. The negative density in the complex scaling region is an artefact of the method. Numerical parameters:  $\mu/E_\delta = 0.2$ ,  $\rho^\varnothing \delta \simeq 2.77$ ,  $\sqrt{N}|\kappa|/E_\delta = 1$  and 100 trajectories.

We note that the negative density encountered for  $\delta x < 50$  or  $\delta x > 150$  is an artefact of the method. Indeed, as prescribed in Eq. (3.60), one has to subtract  $1/2$  from the total density when computing it. However, smooth exterior complex scaling that is implemented in spatial

regions characterised by  $\delta x < 50$  or  $\delta x > 150$  absorbs every outgoing wave and damps the density to zero, resulting in a negative quantity when computing the total density (3.60). This region is however not of interest for the simulations.

Owing to the finite number of phase-space trajectories, truncated Wigner curves however display oscillations around the mean-field prediction whose amplitude decreases with a higher number of trajectories. In practice, a compromise must be made between the numerical effort required to compute a higher number of trajectories and the accuracy of the predictions. Fortunately, it has been shown [257] that the truncated Wigner method provides a reliable description of disorder averaged quantities that shall be of primal relevance in the context of our work. This shall be leveraged to reduce the number of required truncated Wigner trajectories to obtain accurate predictions of quantities of relevance in a context of quantum transport towards disorder.

### 3.3.4 Validity of the truncated Wigner method

We could not end this chapter by eluding the primordial discussion about the validity of the truncated Wigner method. Until the truncation of the motion equation (3.43), the phase-space dynamics of the system described by a density operator  $\hat{\rho}$  was formulated in an exact manner. The omission of those third order derivatives in Eq. (3.43), necessary for numerical integration purposes, is perfectly justified in the limit of large on-site populations and weak interaction strength, as is formally shown in Ref. [254]. This regime corresponds to the mean-field regime which we precisely want to emancipate from.

This seek of a universal validity criterion for the truncated Wigner method still nowadays remains, to the best of our knowledge, an open question. A path integral formulation of the truncated Wigner method by Polkovnikov [258,259] provides corrections to the quantum dynamics that go one order beyond the truncation and which can be exploited as a validity criterion for a truncated Wigner simulation, thereby providing a controlled environment of simulation. Whereas it is in principle possible to evaluate those corrections explicitly, it is in general very demanding to do so for systems represented by Wigner functions containing a large number of modes.

Owing to the complexity of the aforescribed evaluation, the validity of a simulation generally remains an issue. With the starting point that the truncated Wigner method is asymptotically exact for short-time evolutions [258], it emanates from the literature that two classes of regimes of validity related to short and long times dynamics are usually assessed [256].

If the Wigner function can be written as a product of Gaussian Wigner functions, the method is granted valid for short times if the system exhibit a sufficiently high spatial density [239,260]. This validity criterion is less restrictive than the usual expectation that all modes display a large population, because it is not necessary that all modes be widely populated to reach a spatially high density, which extends the validity domain of the method. Other studies indicate that the truncated Wigner method is not reliable when the number of atoms contained in the system becomes overshadowed by quantum noise issued from the sampling of the initial state [254]. A criterion for the long time evolution is supplied by the same paper that provides a maximal temperature for the system beyond which the validity

is not granted [254].

Those criteria, which at least have the merit of existing, do not inform about the validity limitations that come in the presence of an atom–atom interaction. A possibility to circumvent that issue is to compare the findings of the truncated Wigner method with findings of other methods, such as for instance those related to the use of the positive–P representation method [261]. Another possibility is to confront the results to those of a genuine quantum method such as matrix product state (MPS) [262–264] that is based on the density matrix renormalisation group (DMRG) [265] or tensor product states [266]. Those methods are in principle exact, even for finite interaction, but are numerically very inefficient as soon as the number of atoms involved in the computation becomes large. A qualitative picture of the regime of validity for the truncated Wigner method in the presence of an atom–atom interaction is sketched in FIG. 3.6.

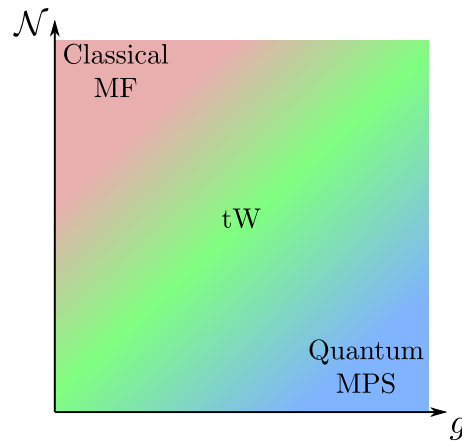


Figure 3.6 – Qualitative scheme of the validity regime of the truncated Wigner (tW) method that bridges the gap between the classical mean-field (MF) regime of large number of atoms and very weak interaction strength, and the quantum regime of low number of atoms and finite interaction strength, where genuine quantum methods such as the matrix product state (MPS) method work the best.

FIG. 3.6 shows the two opposite mean-field and quantum regimes. When the number of atoms is very large and the atom–atom interaction strength very low, a mean-field description provides reliable results. At the opposite limit of few atoms contained in the system and a finite atom–atom interaction strength, a fully-fledged quantum method is usually applied. Truncated Wigner method bridges the gap between those two regimes, whose boundaries, as well the regime of application of the truncated Wigner method are not accurately defined.



## Chapter 4

# Transport of Bose-Einstein condensate through Aharonov–Bohm rings

This chapter is devoted to the study of the 1D transport of Bose–Einstein condensates across a two–arm interferometer subject to an artificial gauge flux, which is referred to as an Aharonov–Bohm ring, owing to the analogy with the eponymous effect. The Aharonov–Bohm effect and the related oscillations, routinely encountered in solid–state physics, are first theoretically presented as a manifestation of wave coherence in a macroscopic transport related observable. In the presence of disorder, those Aharonov–Bohm rings are known to yield Al’tshuler–Aronov–Spivak oscillations in the ensemble averaged transmission, which shall be the subject of the next chapter.

This is what we highlight with Bose–Einstein condensates. To that purpose, we present the geometry that we study in this chapter and the following, and derive the related field equations that we numerically implement. We then show how Aharonov–Bohm oscillations arise in the transmission of particles across the ring. Since many–body interaction effects are a central thematic of this work, we study Aharonov–Bohm oscillations in the presence of finite interaction. This is also an opportunity to perform truncated Wigner simulations, as presented in Chapter 3, to investigate many–body effects beyond the mean–field approximation. We shall then be in a position to introduce the presence of disorder and examine its competition with interaction effects, which is the subject of the next chapter.

### 4.1 Aharonov–Bohm effect

In classical electromagnetism, the vector potential  $\mathbf{A}$  and the scalar potential  $\varphi$  are mathematical artefacts introduced to reformulate Maxwell equations in a more convenient and practical form. This reformulation implies two coupled second–order partial differential equations for the potentials  $\mathbf{A}$  and  $\varphi$ , also referred to as gauge fields, instead of the four coupled Maxwell equations for the electric field  $\mathbf{E}$  and the induction magnetic field  $\mathbf{B}$ . They are related to

each other through

$$\mathbf{B} = \nabla \times \mathbf{A} \quad (4.1)$$

$$\mathbf{E} = -\nabla\varphi - \frac{\partial\mathbf{A}}{\partial t}. \quad (4.2)$$

This appealing formulation of electrodynamics in terms of potentials, that by definition solves two of the Maxwell equations, is commonly used to express motion equations in Hamiltonian or Lagrangian form. It however remains artificial in the framework of classical mechanics because the potentials are ambiguous and even not measurable, contrarily to the fields  $\mathbf{E}$  and  $\mathbf{B}$ . Indeed, a gauge transformation of those gauge fields

$$\mathbf{A} \rightarrow \mathbf{A}' = \mathbf{A} + \nabla\chi \quad (4.3)$$

$$\varphi \rightarrow \varphi' = \varphi - \frac{\partial\chi}{\partial t}, \quad (4.4)$$

where  $\chi \equiv \chi(\mathbf{r}, t)$  is a scalar field referred to as gauge function, has absolutely no physical effect and yields the same  $\mathbf{E}$  and  $\mathbf{B}$  fields, which is known as gauge invariance. Therefore, any couple  $(\varphi', \mathbf{A}')$  is physically equivalent to the couple  $(\varphi, \mathbf{A})$ , provided there exists a gauge function  $\chi(\mathbf{r}, t)$  such that they are gauge transforms of each other. A gauge condition, such as Lorenz or Coulomb gauge, enforcing a relation between  $\varphi$  and  $\mathbf{A}$ , is frequently employed to deal with the ambiguous nature of the potentials.

In quantum mechanics however, as Aharonov and Bohm have shown in their famous article *Significance of Electromagnetic Potentials in the Quantum Theory* [41], the potentials are of more fundamental nature than in classical mechanics, since the vector potential can affect the behaviour of a particle moving a region where both  $\mathbf{E}$  and  $\mathbf{B}$  are absent. To illustrate it, we start from the time-dependent Schrödinger equation

$$i\hbar\frac{\partial\psi(\mathbf{r}, t)}{\partial t} = \frac{1}{2m} \left( \frac{\hbar}{i}\nabla - q\mathbf{A} \right)^2 \psi(\mathbf{r}, t) + q\varphi\psi(\mathbf{r}, t) \quad (4.5)$$

that describes a free particle of charge  $q$  and mass  $m$  in the presence of non-zero vector potential  $\mathbf{A}$  and scalar potential  $\varphi$ . Under a gauge transformation of the potentials  $(\varphi, \mathbf{A})$  to  $(\varphi', \mathbf{A}')$  following Eqs. (4.3) and (4.4), the Schrödinger equation (4.5) transforms according to

$$i\hbar\frac{\partial\psi'(\mathbf{r}, t)}{\partial t} = \frac{1}{2m} \left( \frac{\hbar}{i}\nabla - q\mathbf{A}' \right)^2 \psi'(\mathbf{r}, t) + q\varphi'\psi(\mathbf{r}, t) \quad (4.6)$$

with the gauge transformed wavefunction  $\psi \rightarrow \psi' = U\psi$ , with  $U = e^{iq\chi(\mathbf{r}, t)/\hbar}$ . Therefore, gauge transforming the potentials affects the wavefunction too, namely through a global phase factor [267–269] related to the scalar field  $\chi$  appearing in the gauge transformation (4.3) and (4.4). Thus, a local rotation of the phase of the wavefunction is equivalent to transforming the potentials acting on the charged particles. A multiplication of the wavefunction by a global phase factor  $e^{i\theta}$ , with  $\theta \in \mathbb{R}$ , yields a state indistinguishable from the original one, the same probability density, the same probability current and the same expectation values, as this phase factor cancels out in the related computations. Such a transformation is a global  $U(1)$  gauge transformation. When this phase factor related to the gauge function  $\chi$  additionally depends on the spatial coordinate  $\mathbf{r}$ , the gauge invariance of  $\psi(\mathbf{r}, t)$  is a local  $U(1)$

gauge invariance. The Hamiltonian of the system appearing in Eq. (4.5) is also left invariant under a transformation with the local gauge  $\chi(\mathbf{r}, t)$ , which implies that the Schrödinger equation (4.5) is gauge invariant under transformations (4.3), (4.4) and that  $\psi \rightarrow \psi' = e^{iq\chi(\mathbf{r}, t)/\hbar}\psi$ .

This local phase factor related to the gauge transformation parametrised by the gauge function  $\chi(\mathbf{r}, t)$  is of peculiar relevance for the Aharonov–Bohm effect. Indeed, Aharonov and Bohm have imagined a situation where the induction field  $\mathbf{B} = \nabla \times \mathbf{A} = \mathbf{0}$  vanishes, whereas the vector potential does not. This happens for a particular choice of the gauge function<sup>1</sup> such that  $\mathbf{A} = -\nabla\chi$ , which yields  $\mathbf{A}' = 0$  when using the gauge transformation (4.3). Experimentally, this may be realised by an infinite solenoid that produces a net magnetic flux  $\phi$ , but no induction field outside. The gauge function  $\chi(\mathbf{r}, t)$  is then written as

$$\chi(\mathbf{r}, t) = - \int_{\Gamma} \mathbf{A}(\mathbf{r}, t) \cdot d\mathbf{r}, \quad (4.7)$$

where  $\Gamma$  is the path followed by the particle. This gauge function yields the gauge transformed wavefunction as

$$\psi(\mathbf{r}, t) \rightarrow \psi'(\mathbf{r}, t) = \psi(\mathbf{r}, t) \exp\left(-i\frac{q}{\hbar} \int_{\Gamma} \mathbf{A}(\mathbf{r}, t) \cdot d\mathbf{r}\right), \quad (4.8)$$

as well as the gauge transformed Schrödinger equation

$$i\hbar \frac{\partial \psi'(\mathbf{r}, t)}{\partial t} = \frac{-\hbar^2}{2m} \Delta \psi'(\mathbf{r}, t), \quad (4.9)$$

which is nothing less than the Schrödinger equation for a free particle in the absence of vector potential. Therefore, the presence of a non-vanishing vector potential  $\mathbf{A}$  amounts to multiplying the wavefunction of a free particle by a local phase factor  $\exp[(iq/\hbar) \int_{\Gamma} \mathbf{A}(\mathbf{r}, t) \cdot d\mathbf{r}]$ .

#### 4.1.1 Aharonov–Bohm Gedankenexperiment

The idea of Aharonov and Bohm is to highlight the physical relevance of this phase factor through a double slit interference setup. An electron beam is split into two parts that follow interfering paths that go on both sides of the encircled magnetic flux produced by an infinite solenoid, before interfering downstream on a screen, as is sketched in FIG. 4.1.

---

<sup>1</sup>We note that this choice fulfils  $\mathbf{B} = \mathbf{0}$ .

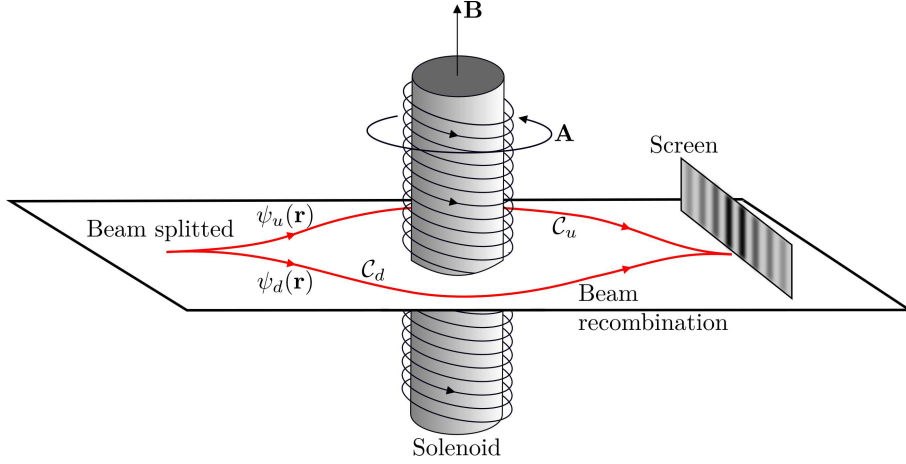


Figure 4.1 – Gedankenexperiment of Aharonov and Bohm. An electron beam is split into two parts that travel around each side of an infinite solenoid and that interfere downstream on a screen. Although the two beams experience no magnetic field along their trip, a phase is acquired due to a non vanishing vector potential  $\mathbf{A}$ . This phase is experimentally highlighted by a flux dependent interference pattern at the recombination of the beams. Figure adapted from [268].

The electronic wavefunctions along each path,  $\psi_u(\mathbf{r}, t)$  and  $\psi_d(\mathbf{r}, t)$ , are related through the wavefunction  $\psi'(\mathbf{r}, t)$  for a free particle through

$$\psi_u(\mathbf{r}, t) = \psi'(\mathbf{r}, t) \exp\left(\frac{iq}{\hbar} \int_{\mathcal{C}_u} \mathbf{A} \cdot d\mathbf{r}\right) \quad (4.10)$$

$$\psi_d(\mathbf{r}, t) = \psi'(\mathbf{r}, t) \exp\left(\frac{iq}{\hbar} \int_{\mathcal{C}_d} \mathbf{A} \cdot d\mathbf{r}\right). \quad (4.11)$$

Owing to the superposition principle, the total wavefunction at a point  $P$  of the screen is given by  $\psi(\mathbf{r}_P, t) = \psi_u(\mathbf{r}_P, t) + \psi_d(\mathbf{r}_P, t)$  so that the intensity at that point is given by

$$\begin{aligned} |\psi(\mathbf{r}_P, t)|^2 &= |\psi_u(\mathbf{r}_P, t) + \psi_d(\mathbf{r}_P, t)|^2 \\ &= |\psi_u(\mathbf{r}_P, t)|^2 + |\psi_d(\mathbf{r}_P, t)|^2 + 2 \operatorname{Re} \left( \psi_u(\mathbf{r}_P, t) \psi_d^*(\mathbf{r}_P, t) e^{iq[\chi_u(\mathbf{r}_P, t) - \chi_d(\mathbf{r}_P, t)]/\hbar} \right). \end{aligned} \quad (4.12)$$

Thanks to Stokes theorem, we can rewrite the phase difference as

$$\delta \equiv \chi_u(\mathbf{r}_P, t) - \chi_d(\mathbf{r}_P, t) = \int_{\mathcal{C}_u} \mathbf{A} \cdot d\mathbf{r} - \int_{\mathcal{C}_d} \mathbf{A} \cdot d\mathbf{r} = \oint_{\mathcal{C}} \mathbf{A} \cdot d\mathbf{r} = \iint \mathbf{B} \cdot d\mathbf{S} = \phi, \quad (4.13)$$

because  $\mathcal{C}_u - \mathcal{C}_d \equiv \mathcal{C}$  is a closed contour that encircles the solenoid. The phase shift between the two interfering trajectories is thus related to the magnetic flux  $\phi$  traversing the solenoid and the intensity at point  $P$  finally reads

$$|\psi(\mathbf{r}_P, t)|^2 = |\psi_u(\mathbf{r}_P, t)|^2 + |\psi_d(\mathbf{r}_P, t)|^2 + 2 \operatorname{Re} \left( \psi_u(\mathbf{r}_P, t) \psi_d^*(\mathbf{r}_P, t) e^{iq\phi/\hbar} \right). \quad (4.14)$$

A flux dependence is consequently encountered on the interference pattern, although particles did not penetrate the solenoid and never experienced any induction field  $\mathbf{B}$ , in great contrast with the classical intuition.

### 4.1.2 Aharonov–Bohm effect in condensed–matter physics

This effect was first discovered in 1949 by Ehrenberg and Siday [270] who derived, in a paper that then widely went under the radar of the scientific community [271], a relation between the phase shift of interfering electron beams and the magnetic flux enclosed in a long solenoid disposed close to the beams. They also established the optical significance of the gauge freedom on  $\mathbf{A}$ . Aharonov and Bohm rediscovered the effect<sup>2</sup>, that nowadays bears their names<sup>3</sup>, ten years later and published their seminal paper [41] that shook the scientific community and gave rise to an abundant literature dedicated to the observation of the effect and its fundamental implications. Probably because of its conclusion that is counterintuitive with respect to classical mechanics and because it has important implications at the very fundamental level [273–275], this effect was the object of a vast controversy: it generated more than three hundreds of papers until 1989 [276].

A first early experimental confirmation was brought by Chambers [277] and other similar experiments that were conducted at that epoch. Nevertheless, some authors [278–283] questioned the validity of those results, arguing that owing to the finiteness of the solenoid or to the imperfectly shielded magnets that are used in practice, any effect on the charged particles is due to a leakage of induction field rather than to the vector potential itself<sup>4</sup>. In 1986, Tonomura and colleagues [284] found a way to deal with those side effects. They developed a toroidal magnet which, exploiting the Meißner effect, they covered with niobium, which is superconductor under  $T = 9$  K and perfectly shields the magnet below that temperature. They sent a collimated electron beam across a Fresnel biprism to separate the beam into two and placed the aforementioned shielded magnet perpendicularly along one of the two paths. They observed a shift of the interference pattern between particles that have crossed the torus by the inside and those that have crossed it by the outside, providing robust evidence for the existence of Aharonov–Bohm effect and putting an end to the controversy.

Since then, the Aharonov–Bohm effect has become a central thematic of study in mesoscopic physics [285, 286] and is even predicted [287] and observed [288] with neutral particles that carry a non zero magnetic moment. Webb *et. al.* [42, 44] have also detected Aharonov–Bohm oscillations in the conductance of ordinary metal rings penetrated by a magnetic flux  $\phi$  and crossed by an electron beam, forming a matter wave interferometer that provides another experimental observation of Aharonov–Bohm oscillations which can be used as a probe to investigate phase coherence effects in electronic systems [289]. Until nowadays,  $\approx 70$  years after the publication of the paper of Ehrenberg and Siday, Aharonov–Bohm oscillations remain an active field of research [290–292] and shall probably remain so in the foreseeable future.

---

<sup>2</sup>Aharonov and Bohm learned about the work of Ehrenberg and Siday after the publication of [41] and acknowledged it in their subsequent article [272]: *Further Considerations on Electromagnetic Potentials in the Quantum Theory*.

<sup>3</sup>In a sense, one could think it would be much fairer to speak about the Ehrenberg–Siday–Aharonov–Bohm effect rather than referring to Aharonov and Bohm alone. We however stick to the latter denomination in conformity with the usage in the literature.

<sup>4</sup>See Ref. [271] for an instructional review of the criticism brought at that time to the experiments and how it helped Tonomura to design an experiment that brought a solid evidence of the existence and observation of the effect.

Stimulated by the advent of ultracold atoms that have become a real tool for quantum simulation, as they provide a flexible framework to emulate various quantum effects (see [27] for a recent review of the state of the art), Aharonov–Bohm oscillations have also been experimentally observed with ultracold atoms [293–295] and widely used as a probe in various studies [291, 296–302]. In the following, we describe the geometry we study to highlight those oscillations with Bose–Einstein condensates.

## 4.2 Description of the scattering region and Aharonov–Bohm rings

Following the principle of the setup used in the experimental observation of the effect [42], we study so-called Aharonov–Bohm rings. Those rings simply consist in a two-arm structure that is pierced by a flux  $\Phi$ , forming a matter wave interferometer. This system is connected to two waveguides, as is sketched in Fig. 4.2.

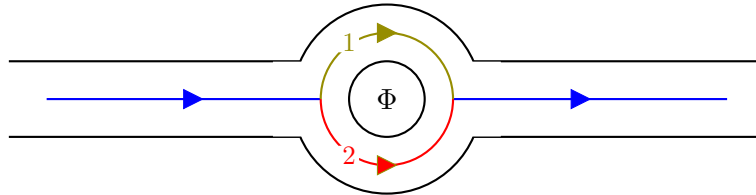


Figure 4.2 – Schematic description of a transport experiment of ultracold atoms through an Aharonov–Bohm ring penetrated by a flux  $\Phi = 2\pi q\phi/h$ . The ring is connected to two semi-infinite waveguides, which forms a two-arm interferometer. The flux  $\Phi$  breaks the time-reversal symmetry of the ring and is responsible for a phase difference between interfering trajectories related to any injected beam propagating towards the ring. This results in periodic oscillations in the transport properties, such as the transmission of particles.

Experimentally, a ring-shaped optical lattice can be produced by interfering two red-detuned lasers: a plane wave with a Laguerre–Gauss lasing mode whose rotational symmetry is leveraged, resulting in a series of traps arranged along a ring [303, 304]. That optical lattice can be connected to two semi-infinite leads to experimentally implement the scheme depicted in FIG. 4.2. This is achieved by engineering a horizontal atomic matter wave guide in an arbitrary direction. This is obtained by utilising a far-detuned laser beam, as is done in Ref. [212]. Owing to the neutral nature of the ultracold atoms that are used in such experiment, the role of the magnetic flux  $\Phi$  is played by a light-induced synthetic gauge flux. This artificial flux can be for instance produced by coupling two internal atomic states by means of a close-to-resonance laser beam, which produces a geometrical phase [305], similar to what would be implemented by a magnetic field [306, 307]. Indeed, this light-induced coupling confers to the atomic wavefunction a phase shift similar to that a vector potential would yield on a charged particle. Moreover, owing to the Zeeman effect, in the presence of an authentic magnetic field, the coupled energy levels acquire a spatial dependence that renders the artificial field space-dependent too. Of course, there also exists more sophisticated schemes for producing

light-induced synthetic gauge fields, as is reported in Refs. [30, 31].

This kind of toroidal lattices are suitable candidates for the study of the Aharonov–Bohm effect. For example, in the context of electronic transport, this geometry leads to Aharonov–Bohm oscillations in the current when the ring is exposed to a magnetic field [308]. Indeed, in the presence of a flux  $\Phi$  that breaks the time-reversal symmetry down, any particle beam injected upstream of the ring gets separated into partial waves that interfere, as a result of the phase they acquire during their traversal of the ring. This interference is responsible for periodic oscillations in the transport properties of the ring, such as the transmission of particles which can be defined as the ratio between the outgoing current and the injected current of particles.

The injection of particles towards Aharonov–Bohm rings is performed following the working principle of atom lasers that we extensively described in Chapter 2. They indeed produce matter plane waves with a well-defined energy that are well suited for the study of coherent effects. The injection of a wavepacket instead of a plane wave produced by atom lasers would introduce a more complicated treatment of the scattering processes without adding necessarily useful ingredients to the discussion.

#### 4.2.1 Description of the scattering region

The geometry previously described is depicted in FIG. 4.3(a) and takes the form of an atom laser injecting particles towards an Aharonov–Bohm ring connected to two semi-infinite matter wave guides.

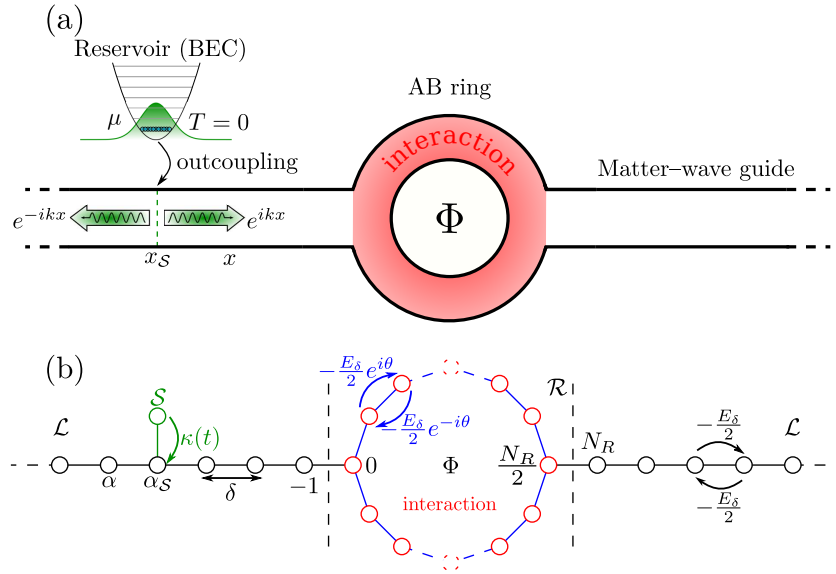


Figure 4.3 – (a) Injection of a Bose–Einstein condensate in the left matter wave guide towards the Aharonov–Bohm ring, following the working principle of an atom laser. (b) Discretisation of the continuous geometry depicted in (a) in a series of equidistant sites.

The reservoir containing  $\mathcal{N} \rightarrow \infty$  atoms is maintained at the temperature  $T = 0$  K and the chemical potential  $\mu$ . It injects plane waves  $e^{\pm ikx}$  of wavevector  $k$  into the left matter wave guide, those waves propagating both in the direction of increasing and decreasing  $x$ . This guide is connected to the left side of an Aharonov–Bohm ring with tunable artificial gauge flux  $\Phi$ . A second matter wave guide is connected to the right side of the ring. Particles crossing the ring acquire a path–dependent overall phase that yields, as previously described, interferences that are responsible for Aharonov–Bohm oscillations. A many–body model for this setup can be derived, very similarly to the approach we followed in Chapter 2.

In view of numerically integrating this model, we proceed to the discretisation of the 1D space, as is shown in FIG. 4.3(b), which results in a series of sites separated by the constant spacing  $\delta$  and labelled by  $\alpha$ . Consequently, this system is governed by a discrete Hamiltonian split into several contributions that we discuss in the following.

The two semi–infinite matter wave guide are described by the discrete Hamiltonian

$$\hat{H}_{\mathcal{L}_L} = \sum_{\alpha=-\infty}^{-1} \left[ E_\delta \hat{a}_\alpha^\dagger \hat{a}_\alpha - \frac{E_\delta}{2} (\hat{a}_{\alpha-1}^\dagger \hat{a}_\alpha + \hat{a}_\alpha^\dagger \hat{a}_{\alpha-1}) \right] \quad (4.15)$$

$$\hat{H}_{\mathcal{L}_R} = \sum_{\alpha=N_R}^{\infty} \left[ E_\delta \hat{a}_\alpha^\dagger \hat{a}_\alpha - \frac{E_\delta}{2} (\hat{a}_{\alpha+1}^\dagger \hat{a}_\alpha + \hat{a}_\alpha^\dagger \hat{a}_{\alpha+1}) \right], \quad (4.16)$$

where we have introduced  $\hat{a}_\alpha^\dagger$  (resp.  $\hat{a}_\alpha$ ) the bosonic creation (resp. annihilation) operator at site  $\alpha$ . The discretisation procedure gives birth to an on–site energy  $E_\delta = \hbar^2/(m\delta^2)$  and to nearest neighbours hopping terms  $-E_\delta/2$  that express the tunnelling from one site to its nearest neighbours. Indices in the interval  $[0, N_R - 1]$  are excluded from the summations in Eqs. (4.15) and (4.16) because they refer to ring sites, whilst the rest of indices stand either for the left lead ( $]-\infty, -1]$ ) or for the right lead ( $[N_R, \infty[$ ). As is explained in Chapter 2, smooth exterior complex scaling [222–227, 231, 309] shall be implemented according to Ref. [216] for absorption at both ends of the leads, as we show later on in the mean–field equations.

Following the atom–laser approach developed in Chapter 2, the reservoir of  $\mathcal{N} \rightarrow \infty$  atoms maintained at chemical potential  $\mu$  is modelled by a coherent and point–like source whose discretised Hamiltonian reads

$$\hat{H}_{\mathcal{S}} = \mu \hat{b}^\dagger \hat{b}, \quad (4.17)$$

where  $\hat{b}^\dagger$  (resp.  $\hat{b}$ ) denotes the bosonic creation (resp. annihilation) operator of particles in the source  $\mathcal{S}$ . For the sake of simplicity, we make the Ansatz of a strongly localised source that injects atoms at one single site labelled  $\alpha_{\mathcal{S}}$ . This is described by the coupling Hamiltonian

$$\hat{H}_{\mathcal{S}\mathcal{L}_L} = \kappa(t) \hat{a}_{\alpha_{\mathcal{S}}}^\dagger \hat{b} + \kappa^*(t) \hat{b}^\dagger \hat{a}_{\alpha_{\mathcal{S}}}. \quad (4.18)$$

This idealised coupling gives rise to injected particles propagating in both directions of decreasing and increasing  $\alpha$ . Particles propagating in the direction of increasing  $\alpha$  face the ring on their trip, yielding back–reflected (either by direct reflection or after a trip inside the ring) and transmitted waves.

The ring symmetry is broken by the presence of an artificial gauge flux  $\Phi$ , responsible for an Aharonov–Bohm phase  $\theta = \Phi/N_R$ , with  $N_R$  the number of ring sites. This is reflected



as an additional a Peierls [310, 311] phase factor  $e^{\pm i\theta}$  in the related hopping terms that are depicted in blue in FIG. 4.3(b). A positive (resp. negative) sign is associated to a hopping in the clockwise (resp. counterclockwise) direction. Because we want to investigate many–body interaction effects on the transport properties of the system, interaction is brought in the system via the effective 1D interaction parameter  $g = 2\hbar\omega_{\perp}a_S/\delta$  [312]. In the presence of an interaction that is spatially restricted inside the ring, the ring Hamiltonian is formulated as

$$\hat{H}_{\mathcal{R}} = \sum_{\alpha=0}^{N_R-1} \left[ E_{\delta} \hat{a}_{\alpha}^{\dagger} \hat{a}_{\alpha} - \frac{E_{\delta}}{2} \left( \hat{a}_{\alpha-1}^{\dagger} \hat{a}_{\alpha} e^{i\theta} + \hat{a}_{\alpha+1}^{\dagger} \hat{a}_{\alpha} e^{-i\theta} \right) + \frac{g}{2} \hat{a}_{\alpha}^{\dagger} \hat{a}_{\alpha}^{\dagger} \hat{a}_{\alpha} \hat{a}_{\alpha} \right]. \quad (4.19)$$

The ring is finally coupled to each lead through the Hamiltonian

$$\hat{H}_{\mathcal{LR}} = -\frac{E_{\delta}}{2} \left( \hat{a}_{-1}^{\dagger} \hat{a}_0 + \hat{a}_0^{\dagger} \hat{a}_{-1} + \hat{a}_{N_R/2}^{\dagger} \hat{a}_{N_R} + \hat{a}_{N_R}^{\dagger} \hat{a}_{N_R/2} \right) \quad (4.20)$$

that expresses the coupling between the left lead to the ring through the hopping from site  $-1$  to site  $0$  and vice–versa, as well as between the ring and the right lead through the hopping from site  $N_R/2$  to site  $N_R$  and vice–versa.

All together, these Hamiltonians form the total Hamiltonian describing the system under study

$$\hat{H} = \hat{H}_{\mathcal{L}_L} + \hat{H}_{\mathcal{L}_R} + \hat{H}_S + \hat{H}_{S\mathcal{L}_L} + \hat{H}_{\mathcal{R}} + \hat{H}_{\mathcal{LR}}, \quad (4.21)$$

which we can write in a more compact and concise form

$$\hat{H} = \sum_{\alpha=-\infty}^{\infty} \left( E_{\delta} \hat{a}_{\alpha}^{\dagger} \hat{a}_{\alpha} + \frac{g}{2} \hat{a}_{\alpha}^{\dagger} \hat{a}_{\alpha}^{\dagger} \hat{a}_{\alpha} \hat{a}_{\alpha} \right) + \sum_{\alpha, \alpha'} J_{\alpha\alpha'} \hat{a}_{\alpha}^{\dagger} \hat{a}_{\alpha'} + \kappa(t) \hat{a}_{\alpha_S}^{\dagger} \hat{b} + \kappa^*(t) \hat{b}^{\dagger} \hat{a}_{\alpha_S} + \mu \hat{b}^{\dagger} \hat{b}, \quad (4.22)$$

where  $J_{\alpha\alpha'}$  is the matrix element encoding the hopping from site  $\alpha$  to site  $\alpha'$ , possibly including the proper phase factor if  $\alpha$  and  $\alpha'$  are ring sites. More precisely, those matrix elements read

$$J_{\alpha\alpha'} = -\frac{E_{\delta}}{2} \begin{cases} 1 & \text{if } |\alpha - \alpha'| = 1 \text{ and } \alpha, \alpha' \notin \mathcal{R} \\ 1 & \text{if } \alpha, \alpha' \rightarrow \text{junction} \\ e^{i\theta} & \text{if } \alpha' = \alpha + 1 \text{ and } \alpha, \alpha' \in \mathcal{R} \\ e^{-i\theta} & \text{if } \alpha' = \alpha - 1 \text{ and } \alpha, \alpha' \in \mathcal{R} \\ 0 & \text{otherwise} \end{cases}, \quad (4.23)$$

where the notation  $\mathcal{R}$  stands for the ring.

### 4.3 Mean–field equations of the system

Starting from Hamiltonian (4.22), we want to find the evolution equation of the annihilation operators, which, in the Heisenberg picture, is provided by the Heisenberg equations

$$\begin{aligned} i\hbar \frac{\partial \hat{a}_\alpha(t)}{\partial t} &= -[\hat{H}, \hat{a}_\alpha(t)] \\ &= E_\delta \hat{a}_\alpha(t) + \sum_{\alpha'} J_{\alpha\alpha'} \hat{a}_{\alpha'}(t) + g_\alpha \hat{a}_\alpha^\dagger(t) \hat{a}_\alpha(t) \psi_\alpha(t) + \kappa(t) \delta_{\alpha, \alpha_S} \hat{b}(t) \end{aligned} \quad (4.24)$$

$$\begin{aligned} i\hbar \frac{\partial \hat{b}(t)}{\partial t} &= -[\hat{H}, \hat{b}(t)] \\ &= \mu \hat{b}(t) + \kappa^*(t) \hat{a}_{\alpha_S}(t). \end{aligned} \quad (4.25)$$

Following the principle of the mean–field approximation, in the limit of large on–site densities and very weak interactions, quantum field operators are replaced by complex scalar fields

$$\hat{a}_\alpha(t) \mapsto \psi_\alpha(t) = \langle \hat{a}_\alpha(t) \rangle e^{-i\mu t/\hbar} \quad (4.26)$$

$$\hat{b}(t) \mapsto \chi(t) = \langle \hat{b}(t) \rangle e^{-i\mu t/\hbar}, \quad (4.27)$$

related to their expectation values. With this substitution, the mean–field equations governing the dynamics of the system read

$$i\hbar \frac{\partial \psi_\alpha(t)}{\partial t} = (E_\delta - \mu) \psi_\alpha(t) + \sum_{\alpha'} J_{\alpha\alpha'} \psi_{\alpha'}(t) + g_\alpha |\psi_\alpha(t)|^2 \psi_\alpha(t) + \kappa(t) \delta_{\alpha, \alpha_S} \chi(t) \quad (4.28)$$

$$i\hbar \frac{\partial \chi(t)}{\partial t} = \kappa^*(t) \psi_{\alpha_S}(t), \quad (4.29)$$

with initial conditions  $\psi_\alpha(t_0) = 0$  and  $\chi(t_0) = \sqrt{\mathcal{N}}$ , corresponding to empty waveguides, an empty ring, and a source consisting in a coherent Bose–Einstein condensate made of  $\mathcal{N}$  atoms. The mean–field approximation consists in casting the initial many–body problem into an effective one–body problem that is formalised by the nonlinear equation (4.28), where the nonlinearity describes an effective potential experienced by an atom as a result of the presence of the other ones.

Following exactly the same approach as for atom lasers in Chapter 2, we set that  $\chi(t) \simeq \sqrt{\mathcal{N}}$  for all finite  $t$ , and we solely focus on the evolution of  $\psi_\alpha$ , which is described by a nonlinear Schrödinger equation with a source term [215, 313, 314]

$$i\hbar \frac{\partial \psi_\alpha(t)}{\partial t} = (E_\alpha - \mu) \psi_\alpha(t) + \sum_{\alpha'} J_{\alpha\alpha'} \psi_{\alpha'}(t) + g_\alpha |\psi_\alpha|^2 \psi_\alpha(t) + \sqrt{\mathcal{N}} \kappa \delta_{\alpha, \alpha_S}, \quad (4.30)$$

the last term of which being a constant in time. Before we apply smooth exterior complex scaling and numerically integrate this equation in Section 4.5, we derive an expression for the reflection and transmission in a steady regime.

### 4.4 Reflection and transmission across an Aharonov–Bohm ring

In order to obtain an expression for the stationary reflection and transmission, we start by rederiving the injected mean density and probability current. For that purpose, we consider

the mean–field equation describing an infinite lead into which a source injects particles. This equation is given by

$$(E_\delta - \mu)\psi_\alpha - \frac{E_\delta}{2}(\psi_{\alpha+1} + \psi_{\alpha-1}) + \sqrt{\mathcal{N}}\kappa(t)\delta_{\alpha\alpha_S} = 0, \quad (4.31)$$

that is, a discretised version of Eq. (2.65), where the mean–field prescription (4.26) and (4.27) are performed. We first solve it for  $\alpha \neq \alpha_S$ , in which case it reduces to

$$(E_\delta - \mu)\psi_\alpha - \frac{E_\delta}{2}(\psi_{\alpha+1} + \psi_{\alpha-1}) = 0, \quad (4.32)$$

which is a discretised version of the wave equation

$$-\frac{\hbar^2}{2m} \frac{\partial^2}{\partial x^2} \psi(x) = \mu \psi(x) \quad (4.33)$$

that describes the propagation of plane waves with energy  $\mu$ . Consequently, we make the usual plane wave Ansatz, consisting in finding a solution of the form

$$\psi_\alpha = A e^{ik\delta\alpha} + B e^{-ik\delta\alpha} \quad (4.34)$$

in Eq. (4.32), where  $A$  and  $B$  are the amplitudes related to the plane waves propagating in directions of increasing and decreasing  $\alpha$ . This Ansatz, when injected in Eq. (4.32), gives back the dispersion relation of the lattice

$$\mu = E_\delta[1 - \cos(k\delta)] \quad \Leftrightarrow \quad k\delta = \arccos\left(1 - \frac{\mu}{E_\delta}\right). \quad (4.35)$$

Computing the related one–dimensional probability current, given by

$$j(x, t) = \frac{\hbar}{2mi} \left( \psi^*(x, t) \frac{\partial \psi(x, t)}{\partial x} - \psi(x, t) \frac{\partial \psi^*(x, t)}{\partial x} \right), \quad (4.36)$$

and which discretised version, obtained by means of a finite–difference scheme, reads

$$j_\alpha = \frac{E_\delta}{2i\hbar} (\psi_\alpha^* \psi_{\alpha+1} - \psi_{\alpha+1} \psi_\alpha^*), \quad (4.37)$$

we find that

$$\begin{aligned} j_\alpha &= \frac{E_\delta}{2i\hbar} \left[ |A|^2 (e^{ik\delta} - e^{-ik\delta}) + |B|^2 (e^{-ik\delta} - e^{ik\delta}) \right] \\ &= \frac{E_\delta}{\hbar} \sin(k\delta) (|A|^2 - |B|^2). \end{aligned} \quad (4.38)$$

Therefore, the plane wave corresponding to the amplitude  $A$  describes a plane wave with current in the direction of increasing  $\alpha$ , whilst the component related to the amplitude  $B$  emits in the direction of decreasing  $\alpha$ .

Including the treatment of the source amounts to modifying our plane wave Ansatz (4.34) into

$$\psi_\alpha = \begin{cases} A_1 e^{-ik\delta\alpha} & \alpha \leq \alpha_S \\ A_2 e^{ik\delta\alpha} & \alpha \geq \alpha_S, \end{cases} \quad (4.39)$$

as we assume that the reservoir is the only source of emitted waves and that upstream and downstream of the source, the solution is a plane wave given by (4.34), as it solves the finite–difference equation (4.32). When  $\alpha = \alpha_S$ , both amplitudes have to coincide

$$\psi_{\alpha_S} = A_1 e^{-ik\delta\alpha_S} = A_2 e^{ik\delta\alpha_S} \equiv \mathcal{A}. \quad (4.40)$$

This new amplitude  $\mathcal{A}$  allows us to rewrite our Ansatz (4.39) in a more compact form

$$\psi_\alpha = \begin{cases} \mathcal{A} e^{-ik\delta(\alpha-\alpha_S)} & \alpha \leq \alpha_S \\ \mathcal{A} e^{ik\delta(\alpha-\alpha_S)} & \alpha \geq \alpha_S, \end{cases} \Leftrightarrow \psi_\alpha = \mathcal{A} e^{ik\delta|\alpha-\alpha_S|} \quad (4.41)$$

The identification of the amplitude  $\mathcal{A}$  is performed by inserting (4.41) into Eq. (4.31) for  $\alpha = \alpha_S$ , yielding for the amplitude

$$\mathcal{A} = \frac{\kappa\sqrt{\mathcal{N}}}{\mu - E_\delta(1 - e^{ik\delta})} = \frac{\kappa\sqrt{\mathcal{N}}}{i\sqrt{\mu(2E_\delta - \mu)}} = \frac{\kappa\sqrt{\mathcal{N}}}{iE_\delta \sin(k\delta)} \quad (4.42)$$

and for the on–site wavefunction

$$\psi_\alpha = \frac{\kappa\sqrt{\mathcal{N}}}{iE_\delta \sin(k\delta)} e^{ik\delta|\alpha-\alpha_S|}, \quad (4.43)$$

where we have exploited the dispersion relation (4.35) and  $E_\delta \sin(k\delta) = \sqrt{\mu(2E_\delta - \mu)}$  to transform amplitude  $\mathcal{A}$ . The square modulus of this amplitude gives the mean density of particles that the source injects in the waveguide

$$\rho^\varnothing \delta = |\psi_\alpha|^2 = |\mathcal{A}|^2 = \frac{|\kappa|^2 \mathcal{N}}{E_\delta^2 \sin^2(k\delta)} = \frac{|\kappa|^2 \mathcal{N}}{\mu(2E_\delta - \mu)} \quad (4.44)$$

whilst the stationary injected current is given by Eq. (4.37) that finally yields

$$j^\varnothing = \frac{E_\delta}{\hbar} |\mathcal{A}|^2 \sin(k\delta) = \frac{1}{\hbar} \frac{|\kappa|^2 \mathcal{N}}{E_\delta \sin(k\delta)} = \frac{1}{\hbar} \frac{|\kappa|^2 \mathcal{N}}{\sqrt{\mu(2E_\delta - \mu)}}, \quad (4.45)$$

that is, the density and current given in Eqs. (2.69) and (2.70).

With those expressions established, we are now in a position to derive the steady reflection and transmission across the ring. In the limit of large propagation times and very weak nonlinearity, Eq. (4.30) is indeed expected to produce a stationary solution, which is found by solving the steady mean–field equation

$$(E_\alpha - \mu)\psi_\alpha + \sum_{\alpha'} J_{\alpha\alpha'} \psi_{\alpha'} + g_\alpha |\psi_\alpha|^2 \psi_\alpha + \sqrt{\mathcal{N}} \kappa \delta_{\alpha,\alpha_S} = 0. \quad (4.46)$$

This equation will allow us to derive an expression for the reflection and the transmission of particles across the ring. The scattering state that is realised in stationary regime admits the form

$$\psi_\alpha = \frac{\kappa\sqrt{\mathcal{N}}}{iE_\delta \sin(k\delta)} \left( e^{ik\delta\alpha} + R(\Phi) e^{-ik\delta\alpha} \right) \equiv \psi_{\alpha,k}^{\mathcal{L}} + \psi_{\alpha,-k}^{\mathcal{L}}, \quad (4.47)$$

in the region upstream from the ring, where  $\alpha_S < \alpha < 0$ , as well as

$$\psi_\alpha = \frac{\kappa\sqrt{\mathcal{N}}}{iE_\delta \sin(k\delta)} T(\Phi) e^{ik\delta(\alpha - N_R + 1)} \equiv \psi_{\alpha,k}^{\mathcal{L}_R}, \quad (4.48)$$

in the region downstream from the ring, when  $\alpha \geq N_R$ .

In the upstream region, this scattering state consists in a superposition of the incoming plane wave (with wavenumber  $k$ ) and a reflected plane wave (with wavenumber  $-k$ ). The related amplitude is multiplied by the reflection probability amplitude  $R(\Phi)$  that accounts for the possible reflection by the ring (either a direct reflection or after an exploration of the ring) in the upstream matter wave guide. In the right matter wave guide however, only the transmitted plane wave, obtained by multiplying the incident plane wave by the transmission probability amplitude  $T(\Phi)$ , is propagating.

The reflection  $R(\Phi)$  and transmission  $T(\Phi)$  probability amplitudes parametrise in which extent the incident wave is split into a reflected and a transmitted wave. They depend not only on the Aharonov–Bohm flux  $\Phi$ , through which they include interference phenomena, but also on the interaction, on the presence of disorder<sup>5</sup> within the ring and upon the on-site energy at the junction sites. Their square modulus,  $|R(\Phi)|^2$  and  $|T(\Phi)|^2$ , are called the reflection and transmission probabilities and are of central importance in the study of transport across Aharonov–Bohm rings since they inform about the interferences taking place within such rings.

The current associated to the scattering state in the downstream region (where  $\alpha_S < \alpha < 0$ ) reads

$$j_\alpha = \frac{E_\delta}{\hbar} \frac{|\kappa|^2 \mathcal{N}}{\mu(2E_\delta - \mu)} \sin(k\delta) (1 - |R(\Phi)|^2) \equiv j_{\alpha,k}^{\mathcal{L}_L} - j_{\alpha,-k}^{\mathcal{L}_L}, \quad (4.49)$$

whilst the current in the upstream region (where  $\alpha \geq N_R$ ) reads

$$j_\alpha = \frac{E_\delta}{\hbar} \frac{|\kappa|^2 \mathcal{N}}{\mu(2E_\delta - \mu)} |T(\Phi)|^2 \sin(k\delta) \equiv j_{\alpha,k}^{\mathcal{L}_R}, \quad (4.50)$$

where the incoming (resp. reflected) current  $j_{\alpha,k}^{\mathcal{L}_L}$  (resp.  $j_{\alpha,-k}^{\mathcal{L}_L}$ ) with wavenumber  $k$  (resp.  $-k$ ) in the left matter wave guide, as well as the transmitted current  $j_{\alpha,k}^{\mathcal{L}_R}$  in the right matter wave guide, were calculated using the discretised expression (4.37) for the current, with  $\psi_\alpha$  given by Eqs. (4.47) and (4.48). This current must be conserved, as particles are conserved, implying that  $j_{\alpha,k}^{\mathcal{L}_L} = j_{\alpha,-k}^{\mathcal{L}_L} + j_{\alpha,k}^{\mathcal{L}_R}$ .

The reflection and the transmission, that can be respectively interpreted as the reflected and transmitted currents divided by the injected current, are given

$$|R(\Phi)|^2 = j_{\alpha,-k}^{\mathcal{L}_L} / j_{\alpha,k}^{\mathcal{L}_L} \quad (4.51)$$

$$|T(\Phi)|^2 = j_{\alpha,k}^{\mathcal{L}_R} / j_{\alpha,k}^{\mathcal{L}_L}, \quad (4.52)$$

with  $|R(\Phi)|^2 + |T(\Phi)|^2 = 1$ , as is deduced from current conservation.

---

<sup>5</sup>See the next chapter dedicated to the inversion of Al'tshuler–Aronov–Spivak oscillations.

## 4.5 Aharonov–Bohm oscillations in the transmission

In this section, we present numerical results that are obtained by numerically integrating Eq. (4.30) to which we apply smooth exterior complex scaling. This amounts to integrating

$$i\hbar \frac{\partial \psi_\alpha(t)}{\partial t} = \left( \frac{E_\delta}{q_\alpha} - \mu q_\alpha \right) \psi_\alpha(t) + \sum_{\alpha'} J_{\alpha\alpha'} \psi_{\alpha'}(t) + g_\alpha |\psi_\alpha(t)|^2 \psi_\alpha(t) + \sqrt{\mathcal{N}} \kappa \delta_{\alpha, \alpha_S}, \quad (4.53)$$

with  $q_\alpha$  being introduced for implementing smooth exterior complex scaling (see Section 2.6.2). We also note that non-zero matrix elements  $J_{\alpha\alpha'}$ , that encode neighbourly relations between sites, are also subject to complex scaling following the shape indicated in Eq. (2.102). As initial conditions, we choose  $\psi_\alpha = 0$  at initial time  $t = t_0$  which corresponds to an initially empty scattering region.

As we have already mentioned, interferences due to the artificial gauge field are responsible for oscillations of period  $2\pi$  in the transport properties, such as the transmission. FIG. 4.4 shows, in the absence of interaction, a typical oscillation in the transmission resulting from the phase difference between interfering paths. The flux dependence of the transmission is a clear signature of the Aharonov–Bohm effect. The typical shape of the oscillations in the transmission depicted FIG. 4.4 is frequently encountered in the dedicated literature, in great accordance with the results of Ref. [315] or with the conductance oscillations in Aharonov–Bohm rings [316] for electrons, in nanowires [317] or in graphene rings [318].

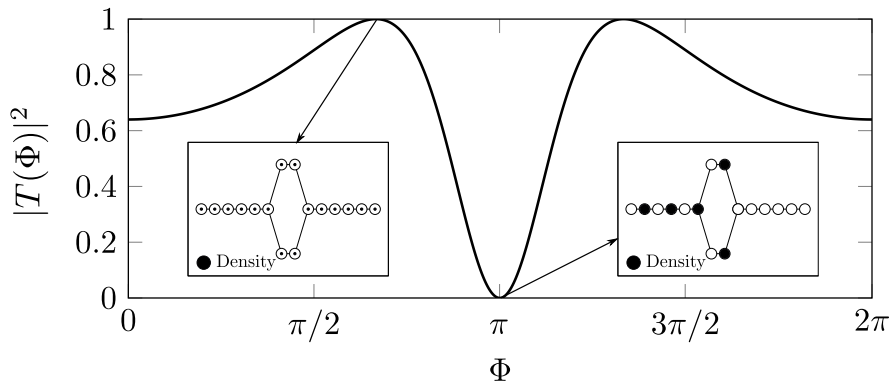


Figure 4.4 – Transmission as a function of the artificial gauge flux  $\Phi$  penetrating the ring in the absence of interaction. Because of the breaking of the ring symmetry due to the artificial gauge flux  $\Phi$ , flux-dependent interferences occur. They can be tuned from constructive to destructive and vice-versa by varying  $\Phi$ : Aharonov–Bohm oscillations are encountered. Inset: circles whose filling is proportional to the on-site density. Depending on the value of  $\Phi$ , the sites are approximately equivalently populated or display, on the contrary, a large density imbalance from a site to its nearest neighbour. When  $\Phi = \pi$ , a transmission blockade is encountered as a result of destructive interferences. Numerical parameters:  $\mu/E_\delta = 1$  and  $\rho^\otimes \delta \simeq 2.77$ .

The inset of FIG. 4.4 shows circles whose filling is proportional to the on-site density. As a result of the flux-dependent interferences, discrepancies in the on-site density are found de-

pending on the value for  $\Phi$ . At a maximum of the transmission, all sites display approximately the same density, whilst at the minimum of transmission, a significant density imbalance is found from one site to its nearest neighbours: some sites are densely populated whereas their neighbour exhibit zero density. As the flux is modulated, it can turn interferences from constructive to destructive and vice-versa. This can even induce a transmission blockade characterised by a zero density at the exit and all downstream sites, as is encountered when  $\Phi = \pi$ .

#### 4.5.1 Interaction effects

While the literature contains several studies about interaction effects for electrons [319–322], the subject is less documented for bosonic particles. Many-body interaction effects on the transmission are investigated both in the mean-field regime and by means of the truncated Wigner method that we described in details in Chapter 2 and that we implement accordingly. For that purpose, we numerically integrate Eq. (3.54) in the absence of disorder potential and with hopping terms particularised to the specific geometry we study, which yields the following equation

$$i\hbar \frac{\partial \psi_\alpha(t)}{\partial t} = \left( \frac{E_\delta}{q_\alpha} - \mu q_\alpha \right) \psi_\alpha(t) + \sum_{\alpha'} J_{\alpha\alpha'} \psi_{\alpha'}(t) + g_\alpha (|\psi_\alpha(t)|^2 - 1) \psi_\alpha(t) + \sqrt{\mathcal{N}} \kappa \delta_{\alpha, \alpha_S} + \delta_{\alpha, 0} \chi_0(t) + \delta_{\alpha, N} \chi_N(t), \quad (4.54)$$

where, for convenience sake, we repeat here some part of the explanation coming after Eq. (3.54) about the meaning of the various terms appearing in the numerically integrated equation. The noise terms  $\chi_0(t)$  and  $\chi_N(t)$  are given by

$$\chi_0(t) = E_\delta \sum_{\alpha'=-\infty}^{-1} M_{\alpha'}(t-t_0) \psi_{\alpha'}(t_0) \quad (4.55)$$

$$\chi_N(t) = -E_\delta \sum_{\alpha'=N}^{\infty} M_{\alpha'-N}(t-t_0) \psi_{\alpha'}(t_0), \quad (4.56)$$

with

$$M_\alpha(\tau) = \frac{i^\alpha}{2} \left[ J_{\alpha-1} \left( \frac{E_\delta \tau}{\hbar} \right) + J_{\alpha+1} \left( \frac{E_\delta \tau}{\hbar} \right) \right] e^{-i(E_\delta - \mu)\tau/\hbar}, \quad (4.57)$$

where  $J_\alpha$  is the Bessel function of the first kind and order  $\alpha$ . They represent the quantum noise entering the scattering region at time  $t$  owing to the sampling of the initial state. The truncated Wigner method allows to take into account the incoherent contribution to the transmission, which is defined as

$$T^{\text{incoh}} = T^{\text{tot}} - T^{\text{coh}}. \quad (4.58)$$

The total and coherent contributions are defined according to the procedure detailed in Chapter 3, namely

$$T^{\text{tot}} = \langle j^{\text{tot}} \rangle / j^\emptyset \quad (4.59)$$

$$T^{\text{coh}} = \langle j^{\text{coh}} \rangle / j^\emptyset. \quad (4.60)$$

The total current is given in Eq. (3.61), that is,

$$j^{\text{tot}} = \frac{iE_\delta}{2\hbar} \overline{\psi_{\alpha+1}^*(t)\psi_\alpha(t) - \psi_\alpha^*(t)\psi_{\alpha+1}(t)}, \quad (4.61)$$

the coherent contribution is provided by Eq. (3.63), that is,

$$j^{\text{coh}} = \frac{iE_\delta}{2\hbar} \left( \overline{\psi_{\alpha+1}^*(t)\psi_\alpha(t)} - \overline{\psi_\alpha^*(t)\psi_{\alpha+1}(t)} \right), \quad (4.62)$$

and the expression of the injected current  $j^\varnothing$  is recalled in Eq. (4.45).

The presence of finite interaction is accounted for and controlled by the interaction strength  $g$  in the mean–field equation (4.30). Interaction is spatially restricted only inside the ring, in accordance with an experimental situation where, due to the transverse confinement, collisions are much more likely to occur within the ring than outside. A mean–field simulation (solid black curve of FIG. 4.5) for  $g/E_\delta = 0.1$  shows that, in comparison with the mean–field simulation of FIG. 4.4 performed in the absence of interaction, the maxima of transmission are slightly displaced and the transmission blockade is preserved.

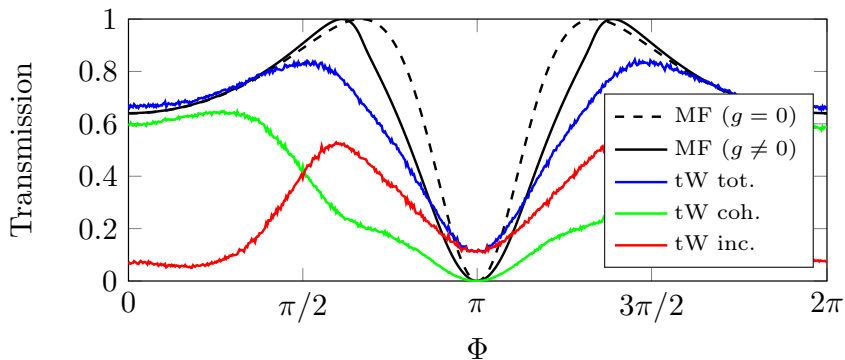


Figure 4.5 – Mean–field (MF) and truncated Wigner (tW) simulations of the transmission as a function of the artificial gauge flux  $\Phi$  penetrating the ring. The truncated Wigner results show that, owing to the presence of interaction, the perfect transmission occurring in the mean–field regime is inhibited and become only maxima. In addition, those maxima of transmission are displaced away from  $\Phi = \pi$ . The transmission blockade at  $\Phi = \pi$  is also removed, as a result of the creation of incoherent particles, resulting from inelastic scattering, within the ring that do not interfere. Numerical parameters:  $\mu/E_\delta = 1$ ,  $\rho^\varnothing\delta \simeq 2.77$ ,  $g/E_\delta = 0.1$  and 20000 trajectories.

The blue curve, that shows the total transmission in the truncated Wigner framework, indicates that, compared to the mean–field simulation depicted in solid black, the perfect transmission in the mean–field regime is inhibited and the related maxima of transmission are displaced away from  $\Phi = \pi$ . Resonant transmission peaks move further away from  $\Phi = \pi$  as  $g$  increases and can even disappear if  $g$  is strong enough, as is shown in FIG. 4.7. This decrease of the transmission with increasing interaction strength is in qualitative agreement with the related decrease of conductance observed in Ref. [319] for interacting electrons.



The comparison stops here, because the underlying mechanism is very different owing to the electron–electron interaction which is of long–range nature, in contrast to the contact interaction we consider in our work and, most importantly, because we are dealing with a bosonic type of particle.

Truncated Wigner simulations also reveal an incoherent transmission that suspends the transmission blockade at  $\Phi = \pi$ . This suspension is entirely due to incoherent particles because the coherent transmission at  $\Phi = \pi$  remains perfectly blocked. Indeed, this blockade is due to the destructive interference between incoming coherent waves interfering together inside the ring. The creation of incoherent particles inside the ring is a result of inelastic scattering processes taking place only within the ring and partially destroys interference effects, as incoherent waves are dephased and mostly do not interfere.

A further investigation about the competition between the interference effects due to coherent waves and the creation of incoherent particles is performed in FIG. 4.6. It displays the on–site density in the ring and in the upstream and downstream matter wave guides for particular values of the artificial gauge flux associated to maxima and a minimum of transmission. The density is represented by circles whose radius is proportional to the local value of the density.

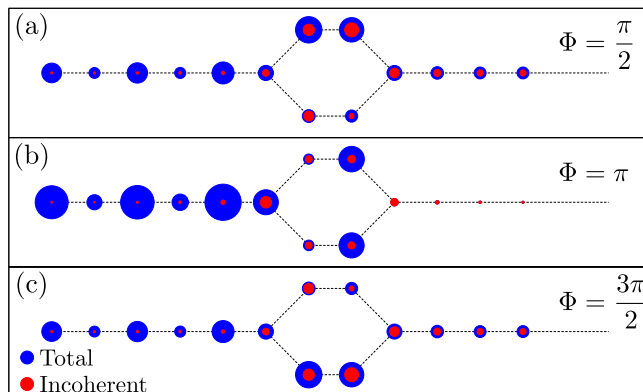


Figure 4.6 – Truncated Wigner simulations of the on–site density within the ring and both in the upstream and downstream leads, in the neighbourhood of the ring for particular values of the artificial gauge flux. The density is represented by circles whose radius is proportional to the local value of the density. Panels (a) and (c) correspond to maxima of the total truncated Wigner transmission, at  $\Phi \simeq \pi/2$  and  $\Phi \simeq 3\pi/2$ . For those values of  $\Phi$ , transmitted particles are nearly equivalently distributed between coherent and incoherent particles. Panel (b) shows on the other hand the on–site density for a minimum of transmission encountered when  $\Phi = \pi$ . Destructive interferences suppress the coherent transmission, but a small on–site density nevertheless prevails downstream, due to incoherent particles. Numerical parameters:  $\mu/E_\delta = 1$ ,  $\rho^\varnothing \delta \simeq 2.77$  and  $g/E_\delta = 0.1$ .

FIGS. 4.6(a) and 4.6(c) show the on–site density for respectively  $\Phi \simeq \pi/2$  and  $\Phi \simeq 3\pi/2$ , which are the values of the artificial gauge flux for which the truncated Wigner total trans-

mission is maximal. They indicate that a branch of the ring is clearly privileged in terms of coherent density, the choice of the branch depending on the value taken by  $\Phi$ . For  $\Phi \simeq \pi/2$ , the upper branch displays a large on-site coherent density whereas the lower branch displays a weak coherent density, the role of the branches being inverted for  $\Phi \simeq 3\pi/2$ . Downstream of the ring, the on-site density does not vary appreciably from one site to its neighbour, which is not surprising because the only particle flux in that region is directed in the direction of increasing  $\alpha$  and no interference mechanism is present outside the ring. In that region of space, although a coherent contribution is still present, the incoherent contribution dominates the density.

FIG. 4.6(b) shows the on-site density for  $\Phi = \pi$  which corresponds to the minimum of the transmission. For that particular flux, both arms are populated with approximately the same density which is sometimes mainly coherent, sometimes mainly incoherent because of the spatially varying profile of the coherent density. Since incoherent particles display energies ranging within a certain energy spectrum, they mostly do not interfere and populate both arms nearly similarly. In the downstream region, in contrast with panels (a) and (c), the density is found totally incoherent because coherent particles interfere destructively at the exit junction and cause a coherent transmission blockade, as was found both in mean-field (black curves) and truncated Wigner (green curve) simulations, shown in FIG. 4.5. As a result of particle conservation and due to the transmission blockade, a higher density is found upstream compared to the panels (a) and (c). The relatively low incoherent on-site density encountered in the upstream lead confirms that the incoherent particles are created inside the ring, which is not surprising insofar interaction, and the related inelastic scattering processes that generate those incoherent particles, is only present inside the ring.

As the interaction strength is increased, the contribution of incoherent particles becomes more and more prominent and modifies the transmission profile, as FIG. 4.7 indicates.

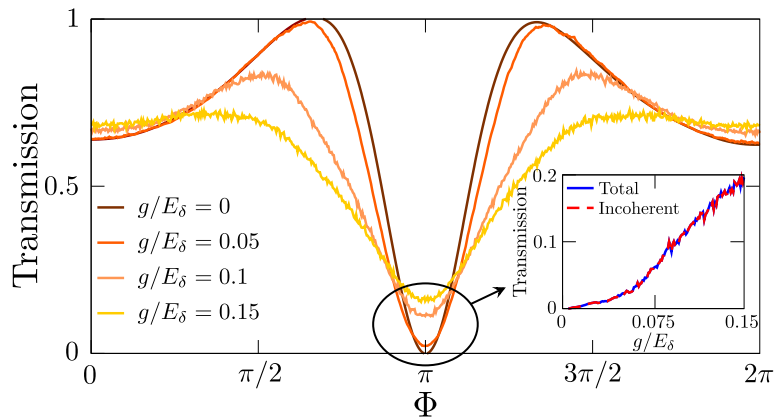


Figure 4.7 – Truncated Wigner simulations of the total transmission as a function of the artificial gauge flux  $\Phi$  penetrating the ring for an increasing interaction strength controlled by  $g/E_\delta \in [0; 0.05; 0.1; 0.15]$ . As the interaction strength is increased, maxima are progressively displaced, flattened and even removed for higher interaction strengths, as well as the transmission blockade at  $\Phi = \pi$  that gets suspended. Incoherent particles, whose density increases with the interaction strength, overshadow the interference pattern carried by coherent particles as they dominate the total transmission. Inset: total and incoherent transmission at  $\Phi = \pi$ . The transmission for this particular flux is entirely due to the incoherent contribution that suspends the coherent transmission blockade. Numerical parameters:  $\mu/E_\delta = 1$  and  $\rho^\phi \delta \simeq 2.77$ .

Maxima are first progressively displaced and lowered before being suppressed. The transmission blockade at  $\Phi = \pi$  is also progressively removed by dephased incoherent trajectories, which is the only underlying mechanism responsible for the blockade suspension. The interference pattern carried by coherent particles is progressively drowned and dominated by a flatter, incoherent, transmission profile that results from dephasing. Refs. [323–325] indicate that, in great contrast with their fermionic counterpart for which they persist in the presence of interaction, Aharonov–Bohm oscillations are washed out for sufficiently strongly interacting bosons, which looks in qualitative accordance with our numerical findings. The statistics of the particles, as well as the interparticle interaction nature, have a marked influence on the Aharonov–Bohm oscillations [36].

Destruction of the Aharonov–Bohm oscillations for higher values of the interaction strength is illustrated by mean–field simulations, as is depicted in FIG. 4.8 for  $g/E_\delta = 0.2$ , revealing oscillations that are an artefact of the mean–field approach. That curve indeed features bistability and indicates that the overall matter wave coherence is destroyed, as is stated in Refs. [216, 313, 314, 326]. This is not surprising since the very existence of a reachable steady scattering state is only ensured for small nonlinearities in the Gross–Pitaevskii equation [190]. For higher nonlinearities, dynamical instabilities generally occur [191, 192] and the convergence towards a steady scattering state is not guaranteed, rendering the process abidingly time–dependent [327].

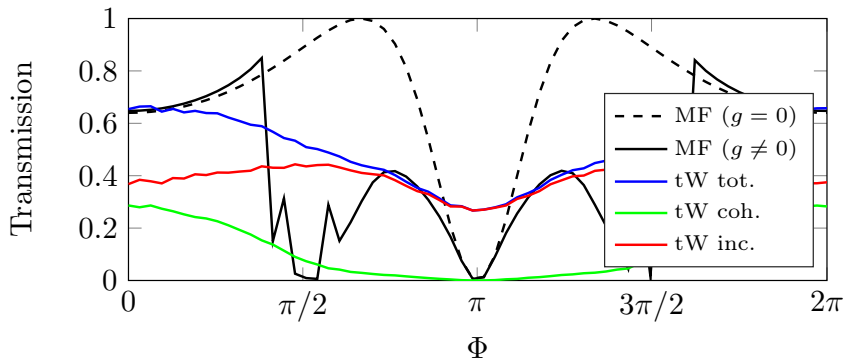


Figure 4.8 – Mean–field (MF) and truncated Wigner (tW) simulations of the transmission as a function of the artificial gauge flux  $\Phi$  penetrating the ring. Owing to dynamical instabilities arising for finite nonlinearities, artificial oscillations are encountered in the mean–field transmission, indicating a breakdown of matter wave coherence. Truncated Wigner simulations corroborate this observation, as the incoherent contribution is the most prominent one, confirming a dephasing of quantum interference effects, as a result of inelastic scattering. Numerical parameters:  $\mu/E_\delta = 1$  and  $\rho^\varrho\delta \simeq 2.77$  and  $g/E_\delta = 0.2$ .

Truncated Wigner simulations supplied in FIG. 4.8 show and confirm that phase coherence is destroyed. The related quantum interference effects are dephased for  $g/E_\delta = 0.2$  and stronger interaction, as the incoherent contribution due to inelastic scattering governs the total transmission. Aharonov–Bohm oscillations are washed out by dephasing and confirm the accordance of our numerical findings with Refs. [323–325]. However, owing to significant remnants of coherent components of the atomic cloud near  $\Phi = 0$  and  $\Phi = 2\pi$ , oscillations that look like Aharonov–Bohm oscillations are still encountered. They are nevertheless also expected to be washed out for stronger interactions.

## Chapter 5

# Al'tshuler–Aronov–Spivak oscillations of bosonic matter wave beams in the presence of interaction

This chapter is dedicated to the study of matter wave transport across disordered Aharonov–Bohm rings in the presence of atom–atom interaction. As we first discuss from an experimental point of view, the presence of a smooth and weak disorder converts Aharonov–Bohm oscillations in the ensemble averaged transmission of particles across the ring into Al'tshuler–Aronov–Spivak oscillations that have twice the frequency of the latter.

Based on the Green's function of the system we study, and that we introduced in Chapter 4, we theoretically demonstrate the advent of Al'tshuler–Aronov–Spivak oscillations in the ensemble averaged transmission by highlighting the crucial role of robust pairings of time–reversed partners in the averaging process.

Those oscillations are then studied numerically, especially in the presence of weak atom–atom interaction. Mean–field simulations show a crossover from constructive to destructive interferences: Al'tshuler–Aronov–Spivak oscillations are reverted due to weak interaction. This antilocalisation scenario is then investigated beyond the mean–field regime by means of the truncated Wigner method. Those simulations are then leveraged to address the question of the experimental observability of the inversion of Al'tshuler–Aronov–Spivak oscillations.

### 5.1 From Webb to Sharvin–Sharvin experiment

Most early experimental evidences of the Aharonov–Bohm effect were performed in the vacuum [277, 284, 328], following the Gedankenexperiment presented in the seminal paper of Aharonov and Bohm [41]. In this Gedankenexperiment, electrons travel in the vacuum around an infinitely long solenoid and can be described in terms of a wavefunction that propagates following a plane wave motion. In contrast with this idealised propagation for the electrons, in the experiment of Webb that highlights Aharonov–Bohm oscillations in the magnetoresistance of a gold ring [42], electrons propagate diffusively in a disordered medium, as they do

in every non superconducting metal.

Some static defects of the underlying lattice-like structure, such as impurities, vacancies or dislocations of atoms cause elastic scattering<sup>1</sup> of the wavefunction related to the electron. For that reason, the conduction process in normal metals is diffusive and can be described in terms of a random walk for the electrons with an elastic scattering mean free path that depends on the degree of disorder (which is proportional to the density of scatterers) of the metal. As a consequence, the electronic motion turns from ballistic in the vacuum to very diffusive in normal metals since, in practice, the size of the sample is large compared to the scattering mean free path<sup>2</sup>, so that an electron propagating in this random medium is scattered many times [44].

Because of the presence of disorder and the related elastic scattering events, the question to know whether the phase coherence is preserved or destroyed after the traversal of such a disordered medium in the diffusive regime of multiple scattering was open until 1981. According to Washburn and Webb [44], the most dominant opinion was that Aharonov–Bohm oscillations would be destroyed. The culprit for this loss of coherence would be elastic scattering, as Ref. [329] indicates. On the other hand, theoretical physicists [330] claimed that Aharonov–Bohm oscillations are preserved by disorder and the related elastic scattering, the responsible for the destruction of the Aharonov–Bohm oscillations actually being inelastic scattering.

A theoretical answer to that question was brought in 1981 by Al'tshuler, Aronov and Spivak, who theoretically studied weak localisation in doubly connected disordered conductors [95,96] and predicted oscillations, with half the period of Aharonov–Bohm oscillations, that nowadays bear their names<sup>3</sup>. Its experimental counterpart was brought a few months later by Sharvin and Sharvin, who performed measurements of the magnetoresistance of long and hollow, thin-walled, Mg cylinders [94] and observed the oscillations predicted by Al'tshuler, Aronov and Spivak, indicating that phase coherence is not affected by elastic scattering. This has been confirmed by Büttiker [331], who indicates that the phase shift resulting from the elastic scattering by impurities does not suppress phase coherence nor introduces any irreversibility [39], in contrast with inelastic scattering which introduces dephasing in the oscillations. This was also later confirmed by the Webb experiment [42] and by other experiments [332,333]. Elastic scattering indeed modifies the phase of the electron wavefunction in a deterministic manner<sup>4</sup> and does not randomise it.

The measurements by Sharvin and Sharvin are characterised not only by the presence of

---

<sup>1</sup>Because the mass of the scattering centre – which often happens to be that of an ion – in such scattering events is large compared to that of an electron, the scattering can be considered as elastic.

<sup>2</sup>In the experiment of Webb and colleagues, the characteristic size of the gold ring is  $\sim$  mm [42] while the mean free path is typically several nanometers.

<sup>3</sup>Al'tshuler–Aronov–Spivak oscillations are in the literature frequently referred to as  $h/2e$  oscillations, sometimes as Sharvin–Sharvin effect or seldom as disordered Aharonov–Bohm effect.

<sup>4</sup>All the electrons that traverse the same series of elastic, reversible, scattering events possess the same relative phase one with respect to the others, both at the beginning and at the end of the traversal. Their phase coherence relation is thus maintained during such a traversal punctuated by the same elastic scattering events.

Al'tshuler–Aronov–Spivak oscillations, but also by the absence of Aharonov–Bohm oscillations. Similar experiments have been reproduced by other research groups, either with cylinders [334] or arrays of loops [335–337] and all confirmed both the presence of Al'tshuler–Aronov–Spivak oscillations and the absence of Aharonov–Bohm oscillations. At the temperature they worked, Sharvin and Sharvin estimated that the phase coherence length  $L_\phi$  of the electrons is of the same order of magnitude as the circumference of the cylinder. Because this cylinder is much longer than  $L_\phi$  in this experiment<sup>5</sup>, it can be thought as a stack of many non-correlated Aharonov–Bohm rings of circumference  $\sim L_\phi$  along which phase coherence should be maintained, each of which with its own disorder landscape. The magnetoresistance of such a cylinder is then obtained as the ensemble average over the rings, or equivalently, over the disorder configurations.

Trajectories similar to the paths depicted in FIG. 5.1(a) interfere with a relative phase that is a signature of the experienced disorder configuration. Owing to the specificity of this relative phase at zero flux to the disorder realisation, such pairs that carry an Aharonov–Bohm contribution do not survive ensemble averaging because the individual relative phases they carry are not correlated and the related oscillations consequently average out in the cylinder of Sharvin and Sharvin.

On the contrary, pairings of trajectories similar to those depicted in FIG. 5.1(b), which are time-reversed counterpart of each other and experience the same sequence of elastic scattering events in the reversed order, all display the same relative phase (which is zero because those paths consists in the same scattering events in the reversed order) at zero flux. They thus survive ensemble averaging to give rise to Al'tshuler–Aronov–Spivak oscillations, confirming that phase coherence is preserved by disorder [44]. Such pairs of paths, referred to as Cooperons in analogy with Cooper pairs in superconductivity, significantly enhance the probability to return to the origin and the underlying backscattering.

This enhancement reveals the intimate connection between Al'tshuler–Aronov–Spivak oscillations, weak localisation and coherent backscattering which are discussed in Chapter 1. The doubling of frequency (or halving of period) of Al'tshuler–Aronov–Spivak oscillations compared to Aharonov–Bohm oscillations is best explained with FIG. 5.1, because the flux encircled by trajectories such as those depicted in FIG. 5.1(b) is double the flux encircled by trajectories such as those depicted in FIG. 5.1(a).

---

<sup>5</sup>In practice, Sharvin and Sharvin have estimated that at the working temperature of their experiment, electrons could maintain a phase coherence relation over a length of the order of magnitude of the circumference of the cylinder. In order to have an insight, the cylinder has a diameter of  $1.5 \mu\text{m}$  and a length of  $L = 1 \text{ cm}$ , which gives  $L/L_\phi \simeq 2100$ .

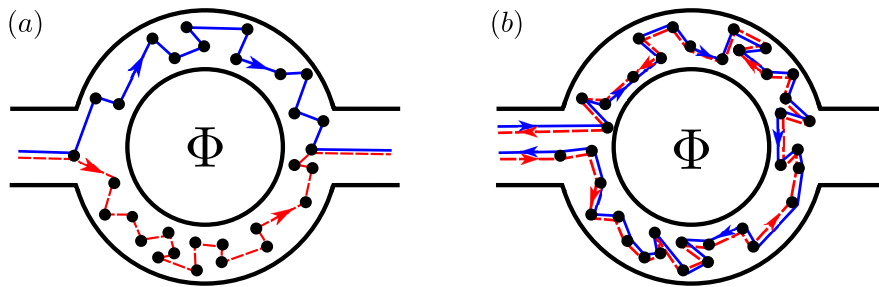


Figure 5.1 – (a) Example of a pair of paths that interfere to give rise to Aharonov–Bohm oscillations with a random relative phase at zero flux, depending on the disorder landscape. Those contributions vanish out after ensemble averaging. (b) Example of a pairing between a path and its time–reversed counterpart, made of the same series of scattering events in the reversed order. Those pairings exhibit the same relative phase at zero flux and survive the ensemble average to generate Al’tshuler–Aronov–Spivak oscillations.

The Sharvin–Sharvin experiment demonstrates that some interference effects survive ensemble averaging. This ensemble averaging process is nevertheless not a necessary condition to observe Al’tshuler–Aronov–Spivak oscillations, since they are also present for a single realisation of the disorder potential, namely for instance for a single ring as in Webb experiment<sup>6</sup> [42]. Indeed, the magnetoresistance of the gold ring shows the typical Aharonov–Bohm oscillations due to pairings similar to that depicted in FIG. 5.1(a), but also displays weaker, half–period oscillations, as Fourier power spectrum reveals [42]. Although in such a configuration both oscillations coexist, Al’tshuler–Aronov–Spivak oscillations are hidden by the stronger amplitude Aharonov–Bohm oscillations and ensemble averaging provides a way to highlight Al’tshuler–Aronov–Spivak oscillations by destroying Aharonov–Bohm oscillations.

Since their experimental observation, Al’tshuler–Aronov–Spivak oscillations have been investigated in details in the context of disordered mesoscopic physics of which they have become a central thematic. They have indeed been encountered with cylinders [334], with arrays of loops [335–337], with mesoscopic disordered rings [43, 338–341] made of normal metals, in ballistic Aharonov–Bohm billiards [342], in semiconductors [343], in superconductors [344] in nanoscale topological insulators [345] and even in optics [346].

## 5.2 Theory of Al’tshuler-Aronov-Spivak oscillations

Aharonov–Bohm rings, studied in Chapter 4 and whose main ingredients are briefly recalled in FIG. 5.2 for the sake of convenience, are excellent candidates to observe Al’tshuler–Aronov–Spivak oscillations with ultracold bosons, provided a disorder potential is present inside the ring. However, in order to observe Al’tshuler–Aronov–Spivak oscillations in a more convincing

<sup>6</sup>Webb and colleagues indeed designed a ring of characteristic length smaller than  $L_\phi$  which can be seen as an individual realisation of one of Sharvin–Sharvin rings. Because phase coherence is preserved along this gold ring, it can be referred to as a coherent conductor.



manner, we shall average the relevant observables over many disorder configurations to cancel Aharonov–Bohm contributions.

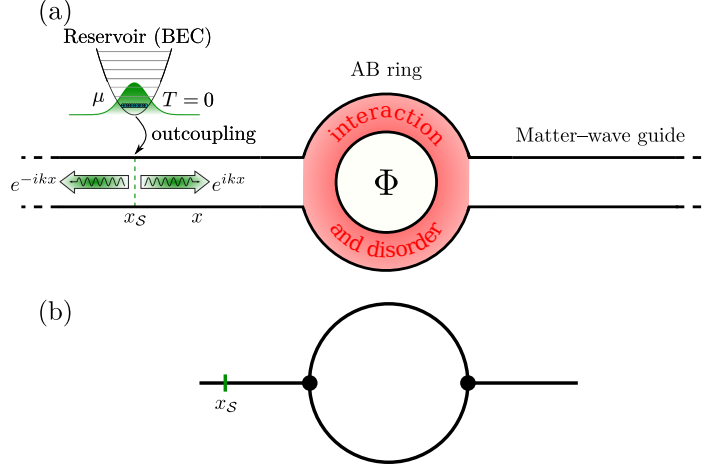


Figure 5.2 – (a) A reservoir, made of a trapped Bose–Einstein condensate at zero temperature and maintained at the chemical potential  $\mu$ , is connected to a matter wave guide in which it injects plane waves going both in the direction of increasing and decreasing  $x$ . This guide is connected to an Aharonov–Bohm ring with tunable artificial gauge flux  $\Phi$ . A second matter wave guide is connected to the other side of the Aharonov–Bohm ring. (b) Modelling of the system sketched in the panel (a) in terms of a quantum graph with two vertices, two internal bonds of finite length and two external bonds of infinite extension.

We first theoretically demonstrate the advent of Al'tshuler–Aronov–Spivak oscillations in this context of ensemble averaging over disorder configurations within Aharonov–Bohm rings. We model the ring as a quantum graph [347–349] with two vertices at the ring junctions, two internal bonds of finite length representing the arms of the ring and two external bonds of infinite extension standing for the two semi–infinite matter wave guides.

### 5.2.1 Formulation of the scattering problem in terms of Green's functions

Our first goal in this section is to derive a theory explaining the appearance of Al'tshuler–Aronov–Spivak oscillations based on the Green's function of the system, following a scattering matrix approach with two leads. This amounts to solving [326]

$$\hat{G}^{-1}(\mu)\psi = \psi_S, \quad (5.1)$$

where we have introduced the (retarded) Green's function of the system

$$\hat{G}(\mu) = \frac{1}{\mu - \hat{H} + i\epsilon}. \quad (5.2)$$

Without the source, the Hamiltonian describing the system we study can be split into sub-Hamiltonians describing each region of the system and cast into the form

$$\begin{aligned}\hat{H} &= \hat{H}_{\mathcal{L}_L} + \hat{H}_{\mathcal{R}} + \hat{H}_{\mathcal{L}_R} + \hat{H}_{\mathcal{L}_L\mathcal{R}} + \hat{H}_{\mathcal{L}_R\mathcal{R}} \\ &= \hat{P}_{\mathcal{L}_L}\hat{H}\hat{P}_{\mathcal{L}_L} + \hat{P}_{\mathcal{R}}\hat{H}\hat{P}_{\mathcal{R}} + \hat{P}_{\mathcal{L}_R}\hat{H}\hat{P}_{\mathcal{L}_R} + \left(\hat{P}_{\mathcal{L}_L}\hat{W}\hat{P}_{\mathcal{R}} + \hat{P}_{\mathcal{R}}\hat{W}\hat{P}_{\mathcal{L}_L}\right) + \left(\hat{P}_{\mathcal{R}_R}\hat{W}\hat{P}_{\mathcal{R}} + \hat{P}_{\mathcal{R}}\hat{W}\hat{P}_{\mathcal{L}_R}\right) \\ &= \hat{H}_{\mathcal{L}_L} + \hat{H}_{\mathcal{R}} + \hat{H}_{\mathcal{L}_R} + \left(\hat{W}_{\mathcal{L}_L\mathcal{R}} + \hat{W}_{\mathcal{R}\mathcal{L}_L}\right) + \left(\hat{W}_{\mathcal{L}_R\mathcal{R}} + \hat{W}_{\mathcal{R}\mathcal{L}_R}\right),\end{aligned}\quad (5.3)$$

following the principle of the Feshbach projection operator formalism [184,185], as in Chapter 2. In Eq. (5.3), we have introduced the projectors  $\hat{P}_X$  which satisfy

$$\hat{P}_X\hat{P}_Y = \delta_{XY}\hat{P}_X, \quad \forall X, Y = \mathcal{L}_L, \mathcal{R}, \mathcal{L}_R \quad (5.4)$$

and project a state  $|\psi\rangle$  onto either the left lead ( $\mathcal{L}_L$ ), the ring ( $\mathcal{R}$ ) or the right lead ( $\mathcal{L}_R$ ). The compact notation  $\hat{H}_X = \hat{P}_X\hat{H}\hat{P}_X$  has been employed for the sub-Hamiltonians and  $\hat{W}_{X\mathcal{R}} = \hat{P}_X\hat{W}\hat{P}_{\mathcal{R}} = \hat{W}_{\mathcal{R}X}^\dagger$  for the junctions Hamiltonians. Eq. (5.3) consequently allows us to write the wavefunction of the scattering system as

$$|\psi\rangle = \hat{P}_{\mathcal{L}_L}|\psi\rangle + \hat{P}_{\mathcal{R}}|\psi\rangle + \hat{P}_{\mathcal{L}_R}|\psi\rangle = |\psi_{\mathcal{L}_L}\rangle + |\psi_{\mathcal{R}}\rangle + |\psi_{\mathcal{L}_R}\rangle, \quad (5.5)$$

that is, as a sum of the wavefunction in each lead and the wavefunction of the ring. By introducing the retarded Green's function at energy  $\mu$

$$\hat{G}_X(\mu) = \frac{1}{\mu - \hat{H}_X + i\epsilon}, \quad (5.6)$$

still with the notation  $X = \mathcal{L}_L, \mathcal{R}, \mathcal{L}_R$ , we can write the Schrödinger equation in each region, following a scattering matrix formalism, as

$$\hat{G}_{\mathcal{L}_L}^{-1}(\mu)|\psi_{\mathcal{L}_L}\rangle + \hat{W}_{\mathcal{L}_L\mathcal{R}}|\psi_{\mathcal{R}}\rangle = \hat{P}_{\mathcal{L}_L}|\psi_S\rangle \quad (5.7)$$

$$\hat{G}_{\mathcal{L}_R}^{-1}(\mu)|\psi_{\mathcal{L}_R}\rangle + \hat{W}_{\mathcal{L}_R\mathcal{R}}|\psi_{\mathcal{R}}\rangle = 0 \quad (5.8)$$

$$\hat{G}_{\mathcal{R}}^{-1}(\mu)|\psi_{\mathcal{R}}\rangle + \hat{W}_{\mathcal{R}\mathcal{L}_L}|\psi_{\mathcal{L}_L}\rangle + \hat{W}_{\mathcal{R}\mathcal{L}_R}|\psi_{\mathcal{L}_R}\rangle = 0. \quad (5.9)$$

Injecting Eqs. (5.7) and (5.8) into (5.9), we arrive at the following expression for the ring wavefunction

$$|\psi_{\mathcal{R}}\rangle = -\left[\hat{G}_{\mathcal{R}}^{-1}(\mu) - \hat{\Sigma}_{\mathcal{L}_L}(\mu) - \hat{\Sigma}_{\mathcal{L}_R}(\mu)\right]^{-1}\hat{W}_{\mathcal{R}\mathcal{L}_L}\hat{G}_{\mathcal{L}_L}(\mu)|\psi_S\rangle, \quad (5.10)$$

where we have introduced the so-called self-energy

$$\hat{\Sigma}_X(\mu) = \hat{W}_{\mathcal{R}X}\hat{G}_X(\mu)\hat{W}_{X\mathcal{R}}, \quad \forall X = \mathcal{L}_L, \mathcal{L}_R. \quad (5.11)$$

This finally allows us to write the wavefunction in the leads

$$|\psi_{\mathcal{L}_L}\rangle = \hat{G}_{\mathcal{L}_L}(\mu)|\psi_S\rangle + \hat{G}_{\mathcal{L}_L}(\mu)\hat{W}_{\mathcal{L}_L\mathcal{R}}\left(\hat{G}_{\mathcal{R}}^{-1}(\mu) - \hat{\Sigma}_{\mathcal{L}_L}(\mu) - \hat{\Sigma}_{\mathcal{L}_R}(\mu)\right)^{-1}\hat{W}_{\mathcal{R}\mathcal{L}_L}\hat{G}_{\mathcal{L}_L}(\mu)|\psi_S\rangle \quad (5.12)$$

$$|\psi_{\mathcal{L}_R}\rangle = \hat{G}_{\mathcal{L}_R}(\mu)\hat{W}_{\mathcal{L}_R\mathcal{R}}\left(\hat{G}_{\mathcal{R}}^{-1}(\mu) - \hat{\Sigma}_{\mathcal{L}_L}(\mu) - \hat{\Sigma}_{\mathcal{L}_R}(\mu)\right)^{-1}\hat{W}_{\mathcal{R}\mathcal{L}_L}\hat{G}_{\mathcal{L}_L}(\mu)|\psi_S\rangle. \quad (5.13)$$

In these expressions, the junctions Hamiltonians explicitly read

$$\hat{W}_{\mathcal{L}_L\mathcal{R}} = -\frac{E_\delta}{2} |-1\rangle \langle 0|, \quad (5.14)$$

$$\hat{W}_{\mathcal{L}_R\mathcal{R}} = -\frac{E_\delta}{2} |N_R\rangle \langle \frac{N_R}{2}|, \quad (5.15)$$

where, for the sake of clarity, we recall that the ring extends from site  $|0\rangle$  to site  $|N_R - 1\rangle$ . One still has to find an expression for the Green's functions of the ring and leads. The latter is quite simple to obtain but the former is a little bit more tedious.

### 5.2.2 Green's function of a 1D infinite lattice

The discretised Hamiltonian of an infinite extension lead is provided, in the local lattice sites basis  $|\alpha\rangle$ , by

$$\hat{H} = \sum_{\alpha=-\infty}^{\infty} E_\delta \left( |\alpha\rangle \langle \alpha| - \frac{1}{2} |\alpha\rangle \langle \alpha+1| - \frac{1}{2} |\alpha+1\rangle \langle \alpha| \right) = \int_{-\pi}^{\pi} E_k |k\rangle \langle k| dk, \quad (5.16)$$

with  $E_\delta = \hbar^2/(m\delta^2)$  the on-site energy,  $E_k = (1 - \cos k\delta)E_\delta$  and  $\langle \alpha|k\rangle = e^{i\alpha k}/\sqrt{2\pi}$ . The related Green's function is then written as

$$\hat{G}(\mu) = \lim_{\epsilon \rightarrow 0^+} \frac{1}{\mu - \hat{H} + i\epsilon} = \lim_{\epsilon \rightarrow 0^+} \int_{-\pi}^{\pi} \frac{1}{\mu - E_k + i\epsilon} |k\rangle \langle k| dk, \quad (5.17)$$

which yields, in the lattice sites representation  $|\alpha\rangle$ ,

$$\langle \alpha| \hat{G}(\mu) |\alpha'\rangle = \lim_{\epsilon \rightarrow 0^+} \frac{1}{2\pi} \int_{-\pi}^{\pi} \frac{e^{i(\alpha-\alpha')k}}{\mu - (1 - \cos k\delta)E_\delta + i\epsilon} dk. \quad (5.18)$$

Using the fact that for  $|\epsilon| \ll 1$ , we have the identity

$$\frac{1}{2\pi} \int_{-\pi}^{\pi} \frac{e^{il\varphi}}{\cos \varphi + x + i\epsilon} d\varphi = \frac{[-(x + i\epsilon) + i\sqrt{1 - (x + i\epsilon)^2}]^{|l|}}{i\sqrt{1 - (x + i\epsilon)^2}}, \quad (5.19)$$

we can rewrite Eq. (5.18) as

$$\langle \alpha| \hat{G}(\mu) |\alpha'\rangle = \lim_{\epsilon \rightarrow 0^+} \frac{[E_\delta - \mu - i\epsilon + i\sqrt{(\mu + i\epsilon)(2E_\delta - \mu - i\epsilon)}]^{|\alpha-\alpha'|}}{iE_\delta^{|\alpha-\alpha'|} \sqrt{(\mu + i\epsilon)(2E_\delta - \mu - i\epsilon)}}, \quad (5.20)$$

which ultimately yields, for  $0 < \mu < 2E_\delta$ ,

$$\langle \alpha| \hat{G}(\mu) |\alpha'\rangle = \frac{e^{i|\alpha-\alpha'|k}}{i\sqrt{\mu(2E_\delta - \mu)}} = \frac{e^{i|\alpha-\alpha'|k}}{iE_\delta \sin(k\delta)}, \quad (5.21)$$

that is the expression of Green's function of an infinite extension lead in the basis  $|\alpha\rangle$ .

### 5.2.3 Green's function of the ring

In the following, we first derive the one-dimensional Green's function of a closed clean ring. We then explain how this Green's function can be modified to take into account the presence of a smooth and weak disorder. Finally, we describe how the Green's function describing such a disordered ring can be modified to model an open ring, connected to the two semi-infinite leads.

### Green's function of a closed clean ring

In the absence of disorder and interaction, the discretised Hamiltonian related to a closed Aharonov–Bohm ring of  $N_R$  sites is given in the local lattice sites basis  $|\alpha\rangle$ , by

$$\hat{H}_{\mathcal{R}} = \sum_{\alpha=0}^{N_R-1} E_{\delta} \left( |\alpha\rangle \langle \alpha| - \frac{e^{-i\Phi}}{2} |\alpha\rangle \langle \alpha+1| - \frac{e^{i\Phi}}{2} |\alpha+1\rangle \langle \alpha| \right). \quad (5.22)$$

Its eigenvalues are  $E_n = E_{\delta} [1 - \cos(2n\pi/N_R - \Phi)]$  and its eigenstates are given by

$$|n\rangle = \frac{1}{\sqrt{N_R}} \sum_{\nu=0}^{N_R-1} e^{2i\pi n\nu/N_R} |\nu\rangle, \quad (5.23)$$

with  $\nu = 0, \dots, N_R - 1$ . With the eigenvalues and eigenvectors at our disposal, we are now in a position to express the Green's function of the closed ring

$$\hat{G}_{\mathcal{R}}(\mu) = \frac{1}{\mu - \hat{H}_{\mathcal{R}} + i\epsilon} = \sum_{n=0}^{N_R-1} \frac{1}{\mu - E_n + i\epsilon} |n\rangle \langle n|, \quad (5.24)$$

which, in site representation  $|\alpha\rangle$ , reads

$$G_{\alpha\alpha'} = \langle \alpha | \hat{G}_{\mathcal{R}} | \alpha' \rangle = \frac{1}{N_R} \sum_{n=0}^{N_R-1} \frac{e^{2i\pi(\alpha-\alpha')n/N_R}}{\mu - [1 - \cos(2n\pi/N_R - \Phi)] E_{\delta} + i\epsilon} \quad (5.25)$$

$$= \frac{e^{i(|\alpha-\alpha'|-L)\tilde{\Phi}} \sin(|\alpha-\alpha'|k\delta) - e^{i|\alpha-\alpha'|\tilde{\Phi}} \sin((|\alpha-\alpha'|-L)k\delta)}{E_{\delta}[\cos L\tilde{\Phi} - \cos(Lk\delta)] \sin k\delta} \quad (5.26)$$

$$= \frac{1}{iE_{\delta} \sin k\delta} \left[ e^{i|\alpha-\alpha'|(k\delta+\tilde{\Phi})} \sum_{n=0}^{\infty} e^{inL(k\delta+\tilde{\Phi})} + e^{i(L-|\alpha-\alpha'|)(k\delta-\tilde{\Phi})} \sum_{n=0}^{\infty} e^{inL(k\delta-\tilde{\Phi})} \right], \quad (5.27)$$

with  $\tilde{\Phi} = \Phi \text{sign}(\alpha - \alpha')$  and where we have used an application of the geometric series and applied Liouville's theorem to compute the second and third above lines [326]. Therefore, the free one-dimensional Green's function between sites  $\alpha$  and  $\alpha'$  consists in a sum over each possible path going from  $\alpha$  to  $\alpha'$ . Amongst those paths and depending on the sites location, some paths may visit the junctions many times, thus consisting of many explorations of the ring arms.

### Green's function of a closed smoothly and weakly disordered ring

In the case of a ring containing smooth and weak disorder, some factors appearing in the Green's function of the clean ring have to be replaced, namely

$$e^{iLk\delta} \rightarrow e^{i(\Phi_u+\Phi_d)}, \quad (5.28)$$

with  $\Phi_u$  and  $\Phi_d$  the phases due to the disorder in the upper and lower arms, which phases are given by

$$\Phi_u = \sum_{\alpha=0}^{N_R/2-1} k_{\alpha}, \quad (5.29)$$

$$\Phi_d = \sum_{\alpha=N_R/2}^{N_R-1} k_{\alpha}, \quad (5.30)$$

where  $k_\alpha \delta = \arccos(1 - (\mu - V_\alpha)/E_\delta)$  is the disorder-dependent local wavevector. Due to the presence of disorder within the ring, we must also make the following substitution

$$e^{i|\alpha - \alpha'|k} \rightarrow \exp\left(i \operatorname{sign}(\alpha - \alpha') \sum_{\alpha''=\alpha'}^{\alpha-1} k_{\alpha''}\right), \quad (5.31)$$

which ultimately gives the Green's function of a smoothly and weakly disordered ring

$$G_{\alpha\alpha'}^{\text{dis}} = \frac{1}{iE_\delta \sin k\delta} \left\{ \exp\left(i\delta\tilde{\Phi} \operatorname{sign}(\alpha - \alpha') \sum_{\alpha''=\alpha'}^{\alpha-1} k_{\alpha''}\right) \sum_{n=0}^{\infty} e^{in(\Phi_u + \Phi_d + L\tilde{\Phi})} \right. \\ \left. + \exp\left[i\left(\Phi_u + \Phi_d - L\tilde{\Phi} - \delta \operatorname{sign}(\alpha - \alpha') \sum_{\alpha''=\alpha'}^{\alpha-1} k_{\alpha''} + |\alpha - \alpha'| \tilde{\Phi}\right)\right] \sum_{n=0}^{\infty} e^{in(\Phi_u + \Phi_d - L\tilde{\Phi})} \right\} \quad (5.32)$$

that still needs to be connected to the two leads.

### Green's function of the coupled ring

Finally, the last missing ingredient in the description of the problem is to connect the closed disordered ring described by its Green's function (5.32) to the semi-infinite leads whose Green's function is provided in Eq. (5.18). In this case, we are left with the calculation of  $(\hat{G}_{\mathcal{R}}^{-1} - (\hat{\Sigma}_{\mathcal{L}_L} + \hat{\Sigma}_{\mathcal{L}_R}))^{-1}$  that can be expanded in a perturbative series of the self-energies, hence giving rise to a Dyson series

$$(\hat{G}_{\mathcal{R}}^{-1} - (\hat{\Sigma}_{\mathcal{L}_L} + \hat{\Sigma}_{\mathcal{L}_R}))^{-1} = \hat{G}_{\mathcal{R}} + \hat{G}_{\mathcal{R}}(\hat{\Sigma}_{\mathcal{L}_L} + \hat{\Sigma}_{\mathcal{L}_R})\hat{G}_{\mathcal{R}} \\ + \hat{G}_{\mathcal{R}}(\hat{\Sigma}_L + \hat{\Sigma}_R)\hat{G}_{\mathcal{R}}(\hat{\Sigma}_{\mathcal{L}_L} + \hat{\Sigma}_{\mathcal{L}_R})\hat{G}_{\mathcal{R}} + \dots \quad (5.33)$$

The total Green's function of the system is then expressed as a sum over scattering paths within the ring, with the possibility of reflection, transmission or exit each time a junction is visited. Adopting a quantum graph view of our system, the ring and the leads can be represented in this formalism as a graph with two vertices, two internal bonds of finite length and two external bonds of infinite extension. On this graph, the total Green's function may be written in a more compact form

$$G(\alpha, \alpha', \mu) = \frac{1}{iE_\delta \sin(k\delta)} \sum_{\gamma} A_{\gamma} e^{iS_{\gamma}/\hbar}, \quad (5.34)$$

that is, a sum over all possible scattering paths  $\gamma$  linking two given points  $\alpha', \alpha$  at the chemical potential  $\mu$  on the graph, with multiple scattering events occurring at the junctions and plane wave propagation in between, as is described in the Dyson series (5.33). In the above equation,  $S_{\gamma} = k\delta n_{\gamma}$  is the accumulated action integral along the path  $\gamma$  going from  $\alpha'$  to  $\alpha$  at chemical potential  $\mu$ , with  $n_{\gamma}$  giving the number of sites visited in the related path. This action integral is weighted by the amplitude  $A_{\gamma} = r^{n_r} t^{n_t}$ , which is obtained by multiplying the reflection and transmission matrix elements at each junction encountered by the path  $\gamma$ , where  $n_r$  (resp.  $n_t$ ) is the number of reflections (resp. transmissions) at each junction along that path. Our task is now to derive those matrix elements by solving the scattering across a symmetric Y-junction problem, in order to gain more insight in those amplitudes.

### Scattering across a symmetric Y-junction

A symmetric Y-junction consists in three identical semi-infinite leads that are connected to a central junction, as is depicted in FIG. 5.3. Sites in the leads are labelled by the index  $\alpha$ , with  $\alpha \in ]-\infty, -1]$  for the left lead,  $\alpha \in [1_u, \infty[$  for the upper right lead and  $\alpha \in [1_l, \infty[$  for the lower right lead. Those sites possess an energy  $E_\delta$  and a nearest neighbour hopping term  $-E_\delta/2$ , whilst the junction at  $\alpha = 0$  possesses the energy  $E_Y$ .

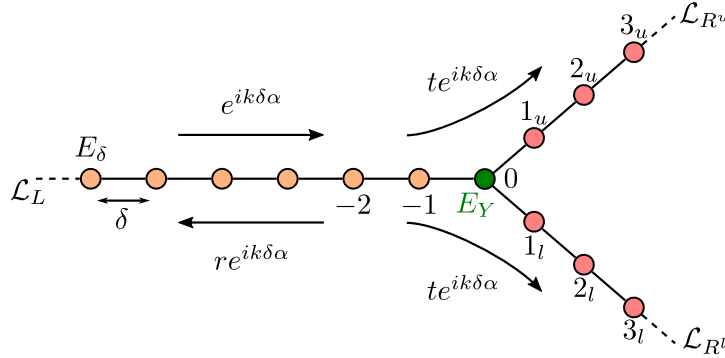


Figure 5.3 – The symmetric Y-junction is made of three semi-infinite leads with sites labelled by  $\alpha$  (with  $\alpha \in ]-\infty, -1]$  for the left lead  $\mathcal{L}_L$ ,  $\alpha \in [1_u, \infty[$  for the upper right lead  $\mathcal{L}_{R^u}$  and  $\alpha \in [1_l, \infty[$  for the lower right lead  $\mathcal{L}_{R^l}$ ), with the energy  $E_\delta$  and the nearest neighbour hopping term  $-E_\delta/2$  that are connected to site  $\alpha = 0$  with energy  $E_Y$ . An incoming plane wave  $e^{ik\delta\alpha}$  can either be transmitted, resulting in an outgoing plane wave  $te^{ik\delta\alpha}$  or either backreflected, resulting in  $re^{ik\delta\alpha}$ .

The Hamiltonian describing the leads reads

$$\hat{H}_{\mathcal{L}_X} = \sum_{\alpha} \left( E_\delta |\alpha\rangle \langle \alpha| - \frac{E_\delta}{2} |\alpha+1\rangle \langle \alpha| - \frac{E_\delta}{2} |\alpha\rangle \langle \alpha+1| \right), \quad (5.35)$$

with  $X = L, R^u, R^l$  denoting either the left lead or the upper/lower right lead, with  $\alpha$  laying in the previously mentioned intervals. The Hamiltonian of the junction, as well as those of the connections to the junction read

$$\hat{H}_Y = E_Y |0\rangle \langle 0| \quad (5.36)$$

$$\hat{H}_{Y \leftrightarrow \mathcal{L}_L} = -\frac{E_\delta}{2} (|-1\rangle \langle 0| + |0\rangle \langle -1|) \quad (5.37)$$

$$\hat{H}_{Y \leftrightarrow \mathcal{L}_{R^u}} = -\frac{E_\delta}{2} (|0\rangle \langle 1^u| + |1^u\rangle \langle 0|) \quad (5.38)$$

$$\hat{H}_{Y \leftrightarrow \mathcal{L}_{R^l}} = -\frac{E_\delta}{2} (|0\rangle \langle 1^l| + |1^l\rangle \langle 0|), \quad (5.39)$$

and the total Hamiltonian describing that system is finally provided by

$$\hat{H} = \hat{H}_{\mathcal{L}_L} + \hat{H}_{\mathcal{L}_{R^u}} + \hat{H}_{\mathcal{L}_{R^l}} + \hat{H}_Y + \hat{H}_{Y \leftrightarrow \mathcal{L}_L} + \hat{H}_{Y \leftrightarrow \mathcal{L}_{R^u}} + \hat{H}_{Y \leftrightarrow \mathcal{L}_{R^l}}. \quad (5.40)$$

The related stationary Schrödinger equation to solve reads

$$\hat{H} |\psi\rangle = \mu |\psi\rangle, \quad (5.41)$$

with  $\mu = E_\delta(1 - \cos(k\delta))$ . We once again assume that there is only one contribution: the contribution incoming from the source, travelling from the left towards the ring. Therefore, the left lead contains both an incident ( $e^{ik\delta\alpha}$ ) and a reflected ( $re^{-ik\delta\alpha}$ ) plane waves, whilst the two right leads contain only those waves that were transmitted across the junction, namely  $te^{ik\delta\alpha}$ . An Ansatz to solve the Schrödinger equation is thus found to be

$$\psi_\alpha = \begin{cases} e^{ik\delta\alpha} + re^{-ik\delta\alpha} & \text{for } \alpha = -\infty, \dots, -2, -1, \\ 1 + r = t & \text{for } \alpha = 0, \\ te^{ik\delta\alpha} & \text{for } \alpha = 1^u, 1^l, 2^u, 2^l, \dots \end{cases} \quad (5.42)$$

and it will allow one to determine the values of  $r$  and  $t$  by solving

$$E_Y\psi_0 - \frac{E_\delta}{2}(\psi_{-1} + \psi_{1^u} + \psi_{1^l}) = \mu\psi_0, \quad (5.43)$$

the Schrödinger equation at the junction site  $\alpha = 0$ . Inserting Ansatz (5.42) into Eq. (5.43), we finally find

$$r = -\frac{1 - E_Y/E_\delta + \frac{1}{2}e^{ik\delta}}{1 - E_Y/E_\delta + e^{ik\delta} - \frac{1}{2}e^{-ik\delta}}, \quad (5.44)$$

$$t = \frac{i \sin k\delta}{1 - E_Y/E_\delta + e^{ik\delta} - \frac{1}{2}e^{-ik\delta}}. \quad (5.45)$$

Those probability amplitudes satisfy the continuity and conservation of current equations

$$1 + r = t \quad (5.46)$$

$$|r|^2 + 2|t|^2 = 1. \quad (5.47)$$

In the continuous limit where the spacing  $\delta \rightarrow 0$  vanishes, a nonvanishing transmission is obtained only for  $E_Y = \frac{3}{2}E_\delta$ , which yields

$$r = -\frac{e^{ik\delta} - 1}{2e^{ik\delta} - 1 - e^{-ik\delta}} \xrightarrow{k\delta \rightarrow 0} -\frac{1}{3}, \quad (5.48)$$

$$t = \frac{e^{ik\delta} - e^{-ik\delta}}{2e^{ik\delta} - 1 - e^{-ik\delta}} \xrightarrow{k\delta \rightarrow 0} \frac{2}{3}. \quad (5.49)$$

Here, we choose  $E_Y = E_\delta$ , which corresponds to the case of a nearly closed ring (actually, with nearly disconnected arms) that is weakly connected to the waveguides, as well as  $\mu = 0.2E_\delta$ . This choice yields the following expressions for  $r$  and  $t$ :

$$r = -\frac{e^{ik\delta}}{2e^{ik\delta} - e^{-ik\delta}} = -\frac{43}{97} + \frac{24}{97}i \quad (5.50)$$

$$t = \frac{e^{ik\delta} - e^{-ik\delta}}{2e^{ik\delta} - e^{-ik\delta}} = \frac{54}{97} + \frac{24}{97}i, \quad (5.51)$$

which are the values that we further use in the simulations and in the development of the diagrammatic theory in Chapter 6.

### 5.2.4 Theory of Al'tshuler–Aronov–Spivak oscillations

#### Smooth and weak disorder

As we have explained earlier, disorder is a key ingredient in obtaining Al'tshuler–Aronov–Spivak oscillations: it thus needs to be carefully chosen. The disorder we use to derive the theory of Al'tshuler–Aronov–Spivak oscillations and that we shall use in the numerical simulations is, in the continuous space, generated by the following convolution product

$$V(x) = \bar{V}_0 \int \frac{1}{\sqrt{\sigma\sqrt{\pi}}} \exp\left[-\frac{(x-y)^2}{2\sigma^2}\right] \eta(y) dy, \quad (5.52)$$

where  $\bar{V}_0$  is the amplitude of the disorder and  $\sigma$  its correlation length [257,350]. The correlator  $\eta(y)$  is a Gaussian random white noise with zero mean and unit variance, *i.e.*  $\langle \eta(x)\eta(y) \rangle = \delta(x-y)$ , with  $\langle \cdot \rangle$  denoting the ensemble average. We have written this disorder potential in such a manner that the probability to obtain a particular value for  $V$  follows a Gaussian distribution

$$P(V) = \frac{1}{\sqrt{2\pi\bar{V}_0}} e^{-V^2/(2\bar{V}_0)^2}. \quad (5.53)$$

This choice for the disorder potential in Eq. (5.52) implies a vanishing ensemble averaged value  $\langle V(x) \rangle = 0$ , as well as a correlation length  $\sigma$  defined through the Gaussian two-point correlation function

$$\langle V(x)V(x') \rangle = \bar{V}_0^2 \exp\left(\frac{-|x-x'|^2}{4\sigma^2}\right). \quad (5.54)$$

Following the discretisation scheme introduced in Chapter 2, we have to discretise the  $\delta$  distribution appearing in the two-point correlation function of the correlator  $\eta(y)$ . This boils down to drawing complex random numbers  $\eta_\alpha$  following a Gaussian distribution and fulfilling  $\langle \eta_\alpha \eta_{\alpha'} \rangle = \delta_{\alpha,\alpha'}$ . The discretised disorder potential is then obtained by taking the convolution product of those random numbers with a Gaussian envelope, which gives birth to the following on-site energies

$$V_\alpha = \bar{V}_0 \sum_{\alpha'=0}^{N_R} \frac{1}{\sqrt{\sigma\sqrt{\pi}}} \exp\left[-\frac{\delta^2}{2\sigma^2}(\alpha-\alpha')^2\right] \eta_{\alpha'}, \quad (5.55)$$

The random values generated for  $V_\alpha$  must be correlated by the discrete convolution over a correlation length  $\sigma \gg \delta$  (in order that the discretisation scheme captures the details of the disorder). The resulting disorder potential varies slowly and smoothly over the correlation length  $\sigma$ .

The disorder has been chosen such that the ensemble averaged mean of  $V_\alpha$  is zero and the ensemble averaged standard deviation is  $\bar{V}_0$ . In order to render a semiclassical treatment of the disorder potential possible, the disorder strength  $\bar{V}_0$  has to be weak compared to the chemical potential  $\mu$ , yielding  $\bar{V}_0 \ll \mu$ . We must also impose that the correlation length  $\sigma$  be large compared to the wavelength  $\lambda$ , yielding  $\sigma \gg \lambda$ . The length of each arm should moreover contain at least several times the correlation length  $\sigma$  but also remain much smaller than the localisation length  $l_{\text{loc}}$  in order to avoid the localised regime. In the case of a Gaussian



disorder potential, the localisation length is given by  $\xi_{\text{loc}} \propto \exp(4k^2\sigma^2)$  [350]. It is finally possible to combine all length scales requirements on disorder related lengths in the compact form

$$\delta \ll \lambda \ll \sigma \ll L \ll \xi_{\text{loc}}, \quad (5.56)$$

where all conditions must simultaneously be enforced, as well as the condition  $\bar{V}_0 \ll \mu$  on the disorder strength.

### Semiclassical treatment of the disorder potential

The Green's function of the whole system is, as we have shown earlier, given by

$$G(\alpha, \alpha', \mu) = \frac{1}{iE_\delta \sin(k\delta)} \sum_{\gamma} A_{\gamma} e^{iS_{\gamma}/\hbar}. \quad (5.57)$$

Because the disorder present within the ring is assumed to be weak and smooth, we are allowed to safely neglect reflections that could possibly occur within the arms of the ring. Indeed, we assumed that the disorder amplitude is such that  $\bar{V}_0 \ll \mu$  and its correlation length  $\sigma$  is such that  $k\sigma \gg 1$ , implying a slow variation of the disorder over a length scale given by the wavelength  $\lambda$ . Under those assumptions, the action integral in the upper (resp. lower) arm consequently takes on the form

$$S_u = \hbar \sum_{\alpha=0}^{\frac{N_R}{2}-1} \arccos \left( 1 - \frac{\mu - V_{\alpha}}{E_{\delta}} \right) \quad (5.58)$$

$$\simeq \hbar \sum_{\alpha=0}^{\frac{N_R}{2}} \left[ \arccos \left( 1 - \frac{\mu}{E_{\delta}} \right) - \frac{V_{\alpha}}{\sqrt{\mu(E_{\delta} - \mu)}} \right] \quad (5.59)$$

$$= \hbar \frac{N_R}{2} k\delta - \frac{\hbar}{E_{\delta} \sin(k\delta)} \sum_{\alpha=0}^{\frac{N_R}{2}} V_{\alpha}, \quad (5.60)$$

where one has to replace  $u$  by  $l$  and adapt the summation indices to obtain  $S_l$ . This allows us to treat the phase factors  $e^{iS_u/\hbar}$  and  $e^{iS_l/\hbar}$  as random complex numbers following a uniform distribution over the complex circle with unit radius provided that

$$\left\langle \frac{1}{E_{\delta} \sin(k\delta)} \sum_{\alpha=0}^{\frac{N_R}{2}} V_{\alpha} \right\rangle = \frac{1}{E_{\delta} \sin(k\delta)} \sum_{\alpha=0}^{\frac{N_R}{2}} \langle V_{\alpha} \rangle = 0 \quad (5.61)$$

and

$$\left\langle \left[ \frac{1}{E_{\delta} \sin(k\delta)} \sum_{\alpha=0}^{\frac{N_R}{2}} V_{\alpha} \right]^2 \right\rangle - \left[ \left\langle \frac{1}{E_{\delta} \sin(k\delta)} \sum_{\alpha=0}^{\frac{N_R}{2}} V_{\alpha} \right\rangle \right]^2 \gg \pi^2. \quad (5.62)$$

The average value of the disorder is zero by construction, so that the condition expressed in Eq. (5.61) is automatically fulfilled. To enforce the second condition, expressed in Eq. (5.62), we need to choose the length  $L$  of the arms large enough, depending upon the disorder strength  $\bar{V}_0$ , in order for the variance of the accumulated phase to satisfy Eq. (5.62).

In the additional presence of an Aharonov–Bohm flux  $\Phi$ , the phase factors become

$$\exp\left(\frac{i}{\hbar}S_u\right) = \exp\left[i\left(\Phi_u \pm \frac{\Phi}{2}\right)\right] \quad (5.63)$$

and

$$\exp\left(\frac{i}{\hbar}S_d\right) = \exp\left[i\left(\Phi_d \mp \frac{\Phi}{2}\right)\right], \quad (5.64)$$

where  $\Phi_u$  and  $\Phi_d$  are real random numbers following a uniform distribution law taking values in  $[0, 2\pi[$ , as previously explained. The presence of the Aharonov–Bohm phase is responsible for an additional phase  $\pm\Phi/2$  acquired each time an arm is crossed from a junction to the other one, the + (resp. –) sign corresponding to the clockwise (resp. counterclockwise) direction. It is remarkable that the effects of both the disorder potential and the flux  $\Phi$  are encoded in the phase factors  $\exp\left(\frac{i}{\hbar}S_u\right)$  and  $\exp\left(\frac{i}{\hbar}S_d\right)$  with expressions as simple as those in Eqs. (5.63) and (5.64).

The goal is to compute both the reflection and transmission probability amplitudes across the ring. They are obtained from the Green’s function  $G(\alpha, \alpha_S, \mu)$  provided in Eq. (5.57), where the site  $\alpha$  is chosen downstream (resp. upstream) of the ring for the transmission (resp. the reflection). We are now in a position to give some concrete example of what the Green’s function looks like. As we said, in the semiclassical context, the Green’s function consists in a sum over interfering classical paths linking two sites of the unperturbed system with a path-specific phase taking into account the disorder and the Aharonov–Bohm flux along each path.

In the example of the path provided in Fig. 5.4 that shows a global outgoing path consisting in two visits of the upper branch and one of the lower, we have

$$\begin{aligned} A_\gamma &= t^3 r \\ S_\gamma &= 2S_u + S_d - \Phi/2 = 2\Phi_u + \Phi_d - \Phi/2, \end{aligned}$$

that is, a product of transmission and reflection probability amplitudes and a sum of phases resulting from the multiple visits of each arm and where  $r$  and  $t$  are given by Eqs. (5.44) and (5.45).

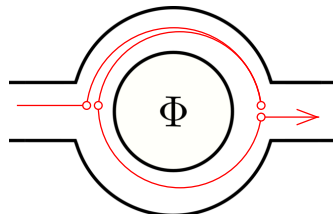


Figure 5.4 – Example of a possible classical path consisting in two explorations of the upper branch and one of the lower, with three transmission events and one reflection event in between.

All classical paths considered in the semiclassical Green’s function are sequences of explorations of ring arms with reflection or transmission scattering events at the junctions. It

implies that the amplitude  $A_\gamma$  is computed as a product of  $r$  and  $t$  at each reflection or transmission event and that the reduced action  $S_\gamma$  is obtained by summing the phases due to disorder, depending upon the number of visits of each arm and the overall net phase resulting from the Aharonov–Bohm flux  $\Phi$ . The shape of the paths allows for a diagrammatic and more visual representation of the Green's function, as is seen in Fig. 5.5.

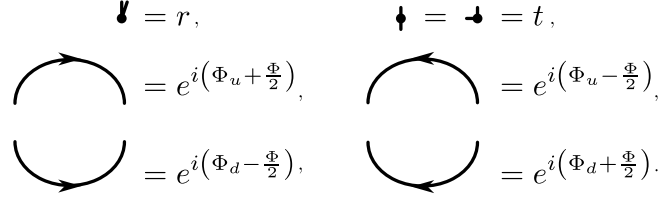


Figure 5.5 – Diagrammatic representation of reflection and transmission scattering events as well as paths consisting in the single exploration of the upper or lower arm of the ring, either in the forward or backward direction.

These are the building blocks for the diagrammatic theory that we shall develop in Chapter 6. They allow us to express any journey within the ring, as complicated as it can be, as a combination of arbitrary explorations of both arms separated by reflection or transmission events. This representation allows for a concise form for the Green's function of the system that can be written as

$$\begin{aligned}
 G(\alpha, \alpha_S, \mu) &= \frac{1}{iE_\delta \sin(k\delta)} \left( \begin{array}{c} \text{Diagram 1} \\ \text{Diagram 2} \\ \text{Diagram 3} \\ \text{Diagram 4} \\ \text{Diagram 5} \\ \dots \end{array} \right) \\
 &= \frac{e^{i|\alpha_S|k\delta}}{iE_\delta \sin(k\delta)} \left\{ t \exp [iS(\alpha, 0, \mu) + i\alpha\theta] \right. \\
 &\quad + tr \exp \left[ i \left( \Phi_u + \frac{\Phi}{2} \right) \right] \exp \left[ iS \left( \alpha, \frac{N_R}{2}, \mu \right) - i \left( \frac{N_R}{2} - \alpha \right) \theta \right] \\
 &\quad + t^2 \exp \left[ i \left( \Phi_d - \frac{\Phi}{2} \right) \right] \exp \left[ iS \left( \alpha, \frac{N_R}{2}, \mu \right) - i \left( \frac{N_R}{2} - \alpha \right) \theta \right] \\
 &\quad + tr^2 \exp (2i\Phi_u) \exp [iS(\alpha, 0, \mu) + i\alpha\theta] \\
 &\quad \left. + tr^2 \exp (2i\Phi_d) \exp [iS(\alpha, 0, \mu) - i\alpha\theta] + \dots \right\}.
 \end{aligned} \tag{5.65}$$

As we see, a diagrammatic representation is much easier to deal with and also paves the way for a more physical interpretation when computing the reflection or transmission, which are given by

$$|R(\Phi_u, \Phi_d, \Phi)|^2 = E_\delta^2 \sin^2(k\delta) |G(\alpha_S, \alpha_S, \mu)|^2 = \sum_{\gamma, \gamma': \alpha_S \rightarrow \alpha_S} A_\gamma A_{\gamma'}^* \exp \left( \frac{i}{\hbar} (S_\gamma - S_{\gamma'}) \right) \tag{5.66}$$

$$|T(\Phi_u, \Phi_d, \Phi)|^2 = E_\delta^2 \sin^2(k\delta) |G(\alpha, \alpha_S, \mu)|^2 = \sum_{\gamma, \gamma': \alpha_S \rightarrow \alpha} A_\gamma A_{\gamma'}^* \exp \left( \frac{i}{\hbar} (S_\gamma - S_{\gamma'}) \right), \tag{5.67}$$

which is diagrammatically represented, in the case of the reflection, by

$$\begin{aligned}
|R(\Phi_u, \Phi_d, \Phi)|^2 &= \left| \begin{array}{c} \text{↔} \bullet + \text{↔} \text{↺} \text{↻} + \text{↔} \text{↻} \text{↺} + \text{↔} \text{↻} \text{↻} + \text{↔} \text{↻} \text{↺} + \mathcal{O}((r, t)^5) \end{array} \right|^2 \\
&= \left| r + t^2 r (e^{2i\Phi_u} + e^{2i\Phi_d}) + t^3 e^{i(\Phi_u + \Phi_d)} (e^{i\Phi} + e^{-i\Phi}) + \mathcal{O}((r, t)^5) \right|^2. \quad (5.68)
\end{aligned}$$

This diagrammatic representation shall be of particular relevance and clarity when computing the disorder average of the reflection and the transmission. Thanks to the fact that  $\Phi_u$  and  $\Phi_d$  can be safely considered as real random numbers uniformly distributed in  $[0, 2\pi[$ , the ensemble average over the disorder configurations can be mapped to an average over  $\Phi_u$  and  $\Phi_d$ . In the case of the reflection, this for instance yields

$$\langle |R(\Phi_u, \Phi_d, \Phi)|^2 \rangle = \frac{1}{4\pi^2} \int_0^{2\pi} \int_0^{2\pi} |R(\Phi_u, \Phi_d, \Phi)|^2 d\Phi_u d\Phi_d, \quad (5.69)$$

where  $R(\Phi_u, \Phi_d, \Phi)$  is the reflection amplitude related to the specific disorder realisation that generates the phases  $\Phi_u$  and  $\Phi_d$ . Outside the ring, each path acquires the same phase so that no phase difference between two particular paths is due to the exploration of the leads. Therefore, the overall phase difference between two particular paths results only from the exploration of the ring.

Using the following identity from the distribution theory

$$\frac{1}{(2\pi)^2} \int_0^{2\pi} \int_0^{2\pi} e^{i(n_u - n'_u)\Phi_u + i(n_d - n'_d)\Phi_d} d\Phi_u d\Phi_d = \delta_{n_u n'_u} \delta_{n_d n'_d} \quad (5.70)$$

for  $n_u, n'_u, n_d, n'_d \in \mathbb{N}_0$  representing the number of comprehensive visits of each arm associated to  $\gamma$  and  $\gamma'$ , we observe that only pairs of paths  $(\gamma, \gamma')$  with the same number of visits of the upper arm  $n_u = n'_u$  and of the lower arm  $n_d = n'_d$  survive the disorder average. The physical interpretation results from this statement but is best explained using the diagrammatic representation of the disorder averaged reflection

$$\begin{aligned}
\langle |R(\Phi)|^2 \rangle &= \left| \text{↔} \bullet \right|^2 + \left| \text{↔} \text{↺} \text{↻} \right|^2 + \left| \text{↔} \text{↻} \text{↺} \right|^2 + \left| \text{↔} \text{↻} \text{↻} + \text{↔} \text{↻} \text{↺} \right|^2 + \mathcal{O}((r, t)^{10}) \\
&= |r|^2 + 2|t|^4 |r|^2 + 2|t|^6 (1 + \cos 2\Phi) + \mathcal{O}((r, t)^{10}) \quad (5.71)
\end{aligned}$$

which, in addition to the classical contribution of paths interfering with themselves, as the three first terms above, also contains interferences between time-reversed partners. Keeping only the dominant contributions, the disorder averaged reflection and transmission read

$$\langle |R(\Phi)|^2 \rangle = |r|^2 + 2|t|^4 |r|^2 + 2|t|^6 (1 + \cos 2\Phi) + \mathcal{O}((r, t)^{10}) \quad (5.72)$$

$$\langle |T(\Phi)|^2 \rangle = 2|t|^4 + 2|t|^4 |r|^4 + 8|t|^6 |r|^2 + 2|t|^8 - 1.6|t|^6 \cos 2\Phi + \mathcal{O}((r, t)^{12}). \quad (5.73)$$

All terms contributing to a  $\cos \Phi$  oscillation display a nonzero net power of the complex random numbers  $e^{i\Phi_u}$  and  $e^{i\Phi_d}$  and are therefore washed out by the averaging process, hence suppressing the Aharonov–Bohm contribution.

Compared to Aharonov–Bohm oscillations, we observe here a doubling of the frequency, that can be explained because the relevant trajectories for Al’tshuler–Aronov–Spivak oscillations are twice longer than those relevant for Aharonov–Bohm oscillations, therefore accumulating twice more flux. Indeed, reflecting trajectories necessarily accumulate a phase which is a multiple of  $\Phi$ , since they contain an odd number of individual explorations of the ring arms, each of which contributing for an additional phase  $\pm\Phi/2$ , depending upon the direction the trip is performed. Such interfering trajectories thus exhibit a phase difference which is a multiple of  $2\Phi$ , hence doubling the frequency of the oscillations compared to Aharonov–Bohm oscillations.

The mechanism behind Al’tshuler–Aronov–Spivak oscillations is the following: in addition to the classical contribution of paths interfering with themselves, only paths which are time-reversed of each other lead to interferences that survive the ensemble averaging process. This particular feature highlights the intimate connection between Al’tshuler–Aronov–Spivak oscillations, weak localisation and coherent backscattering. Indeed, exactly as in weak localisation and coherent backscattering, this mechanism leads to a time-reversed sensitive increase of the reflection probability associated with a concomitant drop in the transmission, as the dependence in the artificial gauge field  $\Phi$  in Eqs. (5.72) and (5.73) demonstrates.

### 5.3 From Aharonov–Bohm to Al’tshuler–Aronov–Spivak oscillations

As we have seen in the previous sections, the presence of smooth disorder destroys Aharonov–Bohm oscillations after ensemble averaging but preserves Al’tshuler–Aronov–Spivak oscillations. We illustrate those observations with the numerical integration of Eq. (4.53) in the presence of the on-site disorder potential described in Eq. (5.55). This amounts to numerically integrating

$$i\hbar \frac{\partial \psi_\alpha(t)}{\partial t} = \left( \frac{E_\delta}{q_\alpha} + V_\alpha - \mu q_\alpha \right) \psi_\alpha(t) + \sum_{\alpha'} J_{\alpha\alpha'} \psi_{\alpha'}(t) + g_\alpha |\psi_\alpha(t)|^2 \psi_\alpha(t) + \sqrt{N} \kappa \delta_{\alpha,\alpha_S}, \quad (5.74)$$

for increasing values  $\bar{V}_0$  of the disorder strength and with initial conditions corresponding to an initially empty scattering region, that is  $\psi_\alpha = 0$  at initial time  $t = t_0$ . For the sake of convenience, we repeat here some of the explanations previously given about some of the terms appearing in the above equation. The factor  $q_\alpha$  has been introduced to implement smooth exterior complex scaling, as explained in Section 2.6.2. Neighbourly relations are encoded by the matrix elements  $J_{\alpha\alpha'}$  whose shape is given in Eq. (4.23) and are also subject to complex scaling, following the shape indicated in Eq. (2.102).

We compute the transmission of particles across the ring, which is defined as

$$\langle |T(\Phi)|^2 \rangle = \frac{\langle j_\alpha \rangle}{j_\emptyset}, \quad (5.75)$$

where  $\langle \cdot \rangle$  stands for the ensemble averaging process, where the on-site current is defined by

$$j_\alpha = \frac{iE_\delta}{2\hbar} [\psi_{\alpha+1}^* \psi_\alpha - \psi_\alpha^* \psi_{\alpha+1}] \quad (5.76)$$

and the injected current  $j^\varnothing$  is defined in Eq. (2.70), that is,

$$j^\varnothing = \frac{1}{\hbar} \frac{\mathcal{N}|\kappa|^2}{\mu(2E_\delta - \mu)}. \quad (5.77)$$

The results regarding the ensemble averaged transmission for several values of the disorder strength are shown in FIG. 5.6.

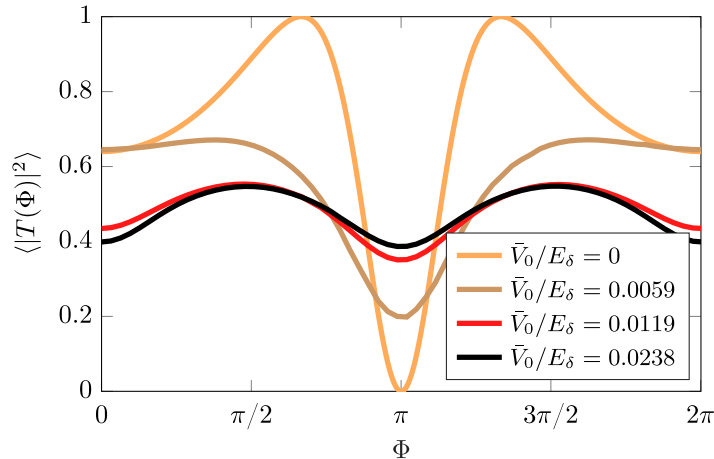


Figure 5.6 – Ensemble averaged transmission across the Aharonov–Bohm ring versus the enclosed artificial flux  $\Phi$  for several disorder amplitudes  $\bar{V}_0$  in the absence of interaction. The transmission is averaged over 20000 realisations of a Gaussian correlated disorder of correlation length  $\sigma = 20\delta$ . Owing to the increase of the disorder amplitude, Aharonov–Bohm oscillations (orange curve) of period  $2\pi$  are progressively damped out and let emerge Al’tshuler–Aronov–Spivak oscillations (black curve) of period  $\pi$ . Numerical parameters:  $\mu/E_\delta = 0.2$  and  $N_R = 200$  sites and  $\sqrt{\mathcal{N}}|\kappa|/E_\delta = 1$ .

As is expected from the theory developed earlier, a progressive increase of the disorder amplitude  $\bar{V}_0$  induces a decay of the Aharonov–Bohm contribution in the ensemble averaged transmission. We observe that for  $\bar{V}_0/E_\delta = 0.0238$ , those oscillations have completely vanished and give way to oscillations of half period  $\pi$  which are identified to as Al’tshuler–Aronov–Spivak oscillations. The oscillations for  $\bar{V}_0/E_\delta = 0.0238$  have a shape nearly identical to that encountered in the disorder averaged conductance of a normal metal ring [351]. In the following studies, we work with the disorder amplitude  $\bar{V}_0/E_\delta = 0.0238$  that yields a regime where the assumption to treat the phase factors due to disorder as complex random numbers of modulus equal to one is valid.

The underlying interferences can be illustrated with the ensemble averaged on-site density, as is shown in FIG. 5.7.

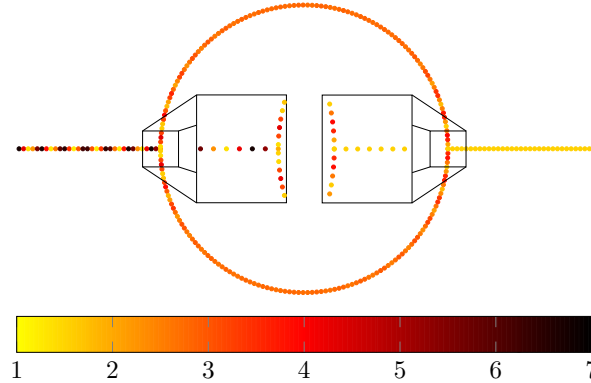


Figure 5.7 – Ensemble averaged on-site density of atoms for the particular value of the enclosed flux  $\Phi = \pi/2$  in the absence of interaction. The on-site density is averaged over realisations of a Gaussian correlated disorder taking random values in  $[-0.0119, 0.0119]$  with correlation length  $\sigma = 20\delta$ . The entrance and exit of the ring are the seat of systematic interferences between particles. Numerical parameters:  $\mu/E_\delta = 0.2$  and  $N_R = 200$  sites and  $\sqrt{N}|\kappa|/E_\delta = 1$ .

FIG. 5.7 highlights that close to the entrance and exit junctions of the ring, robust interferences between particles take place. A quite homogeneous mean on-site density is however encountered deep inside the ring as well as in the downstream region where only particles going to the right are travelling.

## 5.4 Interplay between disorder and interaction effects: inversion of Al'tshuler–Aronov–Spivak oscillations

In this section, we investigate the effects of the presence of interaction whose strength is progressively increased. FIG. 5.8 shows the results of mean-field simulations displaying the ensemble averaged transmission as a function of the flux  $\Phi$  penetrating the ring for different values of the interaction strength  $g$ .

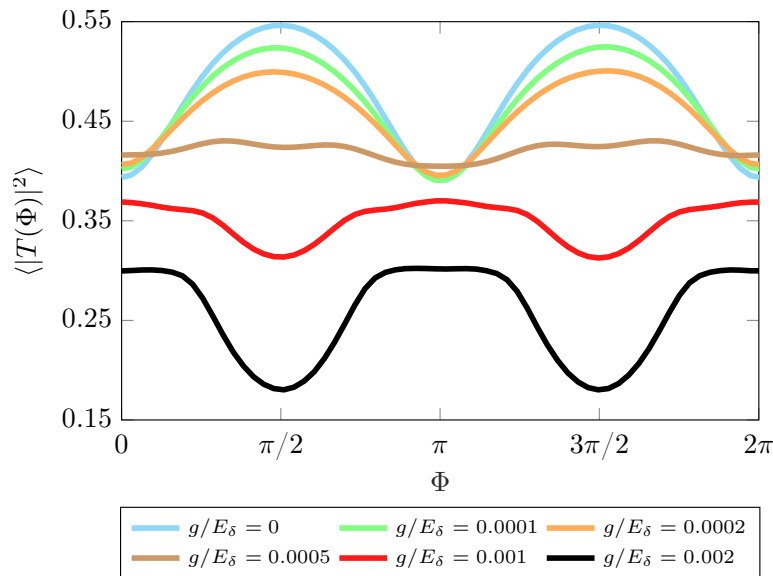


Figure 5.8 – Mean-field simulations of the ensemble averaged transmission versus the enclosed artificial flux  $\Phi$  in the presence of interaction for  $\mathcal{N}|\kappa|^2 = E_\delta^2 \Leftrightarrow \langle \hat{a}_\alpha^\dagger \hat{a}_\alpha \rangle \simeq 2.77$ . The transmission is averaged over 20000 realisations of a Gaussian correlated disorder taking random values in  $[-0.0119, 0.0119]$  with correlation length  $\sigma = 20\delta$ . As the interaction strength is increased, the oscillations are first flattened and then inverted: the maxima at  $\Phi = \pi/2$  and  $3\pi/2$  become minima and the minima at  $\Phi = 0, \pi$  and  $2\pi$  become maxima. Numerical parameters:  $\mu/E_\delta = 0.2$  and  $N_R = 200$  sites.

In a first regime that ranges from  $g/E_\delta = 0$  to  $g/E_\delta = 0.0005$ , we observe that the presence of interaction yields a reduction of the oscillations amplitude, resulting in a flattening of the Al'tshuler–Aronov–Spivak oscillations. For interaction strengths larger than  $g/E_\delta = 0.0005$ , Al'tshuler–Aronov–Spivak oscillations are progressively inverted and the minimum at  $\Phi = \pi/2$  turns to a maximum, in qualitative agreement with the coherent backscattering inversion [60, 352].

Indeed, the minima in the ensemble averaged transmission which are located at  $\Phi = 0, \pi, 2\pi$  can be interpreted as maxima of reflection whilst the maxima located around  $\Phi = \pi/2$  and  $3\pi/2$  can be interpreted as minima. We expect that this inversion remains quantitatively the same in a large range of parameters defining the disorder potential, provided the disorder remains in the regime giving rise to Al'tshuler–Aronov–Spivak oscillations. This regime is on



the one hand characterised by a disorder that is sufficiently strong to allow the phase factors  $e^{i\Phi_u}$  and  $e^{i\Phi_d}$  to be treated as complex random numbers lying on a circle of unit radius in the complex plane. On the other hand, that regime is also such that the disorder remains sufficiently weak and smooth, in order to prevent any partial or even total reflection inside the arms of the ring. In order to assess whether this effect is observable experimentally, we must have access to the coherent and incoherent contributions to the ensemble averaged transmission, which is not reachable by means of a mean-field approximation that only models elastic scattering.

#### 5.4.1 Al'tshuler–Aronov–Spivak oscillations beyond the mean-field regime

In order to implement the truncated Wigner for the system described in Section 5.2, we once again follow the procedure detailed in Chapter 3. This amounts to numerically integrating

$$i\hbar \frac{\partial \psi_\alpha(t)}{\partial t} = \left( \frac{E_\delta}{q_\alpha} + V_\alpha - \mu q_\alpha \right) \psi_\alpha(t) + \sum_{\alpha'} J_{\alpha\alpha'} \psi_{\alpha'}(t) + g_\alpha (|\psi_\alpha(t)|^2 - 1) \psi_\alpha(t) + \sqrt{\mathcal{N}} \kappa \delta_{\alpha,\alpha_S} + \delta_{\alpha,0} \chi_0(t) + \delta_{\alpha,N} \chi_N(t), \quad (5.78)$$

where, for the sake of convenience, we once again give some explanation about some of the terms appearing in that equation. The noise terms  $\chi_0(t)$  and  $\chi_N(t)$  are given by

$$\chi_0(t) = E_\delta \sum_{\alpha'=-\infty}^{-1} M_{\alpha'}(t-t_0) \psi_{\alpha'}(t_0) \quad (5.79)$$

$$\chi_N(t) = -E_\delta \sum_{\alpha'=N}^{\infty} M_{\alpha'-N}(t-t_0) \psi_{\alpha'}(t_0), \quad (5.80)$$

with

$$M_\alpha(\tau) = \frac{i^\alpha}{2} \left[ J_{\alpha-1} \left( \frac{E_\delta \tau}{\hbar} \right) + J_{\alpha+1} \left( \frac{E_\delta \tau}{\hbar} \right) \right] e^{-i(E_\delta - \mu)\tau/\hbar}, \quad (5.81)$$

where  $J_\alpha$  is the Bessel function of the first kind and order  $\alpha$ . They represent the quantum noise entering the scattering region at time  $t$  owing to the sampling of the initial state. The truncated Wigner method allows to take into account the incoherent contribution to the transmission, which is defined as

$$T^{\text{incoh}} = T^{\text{tot}} - T^{\text{coh}}. \quad (5.82)$$

The total and coherent contributions are defined according to the procedure detailed in Chapter 3, namely

$$T^{\text{tot}} = \langle j^{\text{tot}} \rangle / j^\emptyset \quad (5.83)$$

$$T^{\text{coh}} = \langle j^{\text{coh}} \rangle / j^\emptyset. \quad (5.84)$$

The total current is given in Eq. (3.61), that is,

$$j^{\text{tot}} = \frac{iE_\delta}{2\hbar} \overline{\psi_{\alpha+1}^*(t) \psi_\alpha(t) - \psi_\alpha^*(t) \psi_{\alpha+1}(t)} \quad (5.85)$$

the coherent contribution is provided by Eq. (3.63), that is,

$$j^{\text{coh}} = \frac{iE_\delta}{2\hbar} \left( \overline{\psi_{\alpha+1}^*(t) \psi_\alpha(t)} - \overline{\psi_\alpha^*(t) \psi_{\alpha+1}(t)} \right), \quad (5.86)$$

and the expression of the injected current  $j^\varnothing$  is recalled in Eq. (5.77).

We evaluate the transmission (total, coherent and incoherent) in two different regimes. The first context is related to an interaction strength for which no inversion is found, corresponding to parameters yielding the orange curve in FIG. 5.8 (mean-field simulation with  $g/E_\delta = 0.0002$ ). We have performed 6 sets of simulations, with different values for both  $\delta\rho^\varnothing$  and  $g$ , their product being kept constant and equal to  $g\rho^\varnothing = 0.0002E_\delta$ . Those panels are shown in FIG. 5.9.

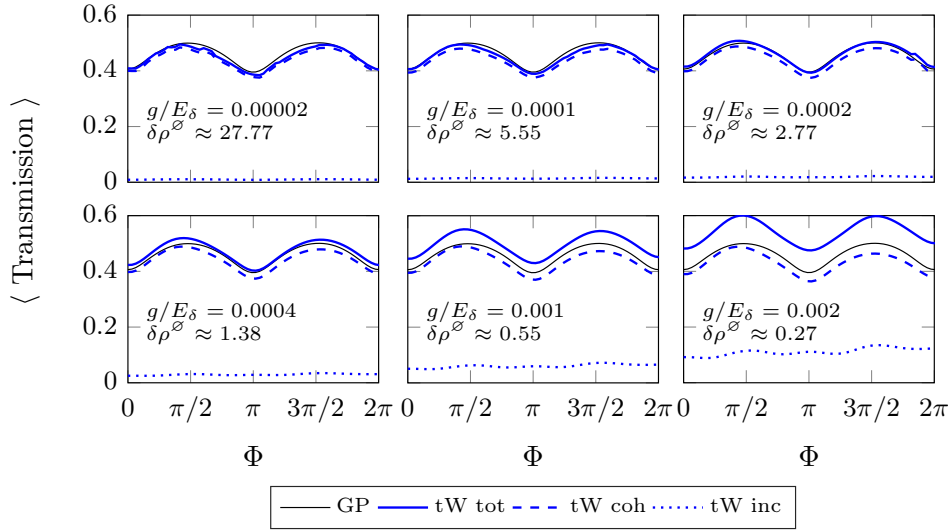


Figure 5.9 – Truncated Wigner simulations of the ensemble averaged transmission as a function of the enclosed artificial flux  $\Phi$  for different interaction strengths  $g$  and injected densities  $\delta\rho^\varnothing$ , the product  $\delta\rho^\varnothing g = 0.0002$  being kept constant. This scenario corresponds to a mean-field regime where no inversion of the oscillations is obtained. The transmission is averaged over 1000 realisations of a Gaussian correlated disorder taking random values in  $[-0.0119, 0.0119]$  with the correlation length  $\sigma = 20\delta$ , each of which performed with an average of 100 realisations over the initial conditions. In this regime of very weak nonlinearity, the oscillations keep an AAS structure and the transmission remains mostly coherent, even for high interaction strength and low injected density. Numerical parameters:  $\mu/E_\delta = 0.2$  and  $N_R = 200$  sites.

As is seen in FIG. 5.9, the structure of the oscillations that emerged from the mean-field approach is preserved, even for high interaction strengths and very low injected densities, the most important contribution remaining the coherent one. However, inelastic scattering becomes more prominent as  $g$  is increased and  $\delta\rho^\varnothing$  decreased. Those inelastic processes are responsible for a dephasing between interfering trajectories that can yield a structureless curve, owing to the shape of the incoherent contribution. This dephasing effect must

be carefully assessed in order to evaluate whether the effect under study is experimentally observable or hidden behind dephasing. The goal is to give a threshold beyond which the incoherent contribution becomes the most important one. Based upon that threshold, we aim at choosing an atomic species for which an experimental observation of the effect should be possible.

We now investigate in which extent the inversion remains observable as the interaction strength is increased and the injected density decreased. To this end, we realise truncated Wigner simulations in a context where the inversion is completely developed, which is obtained for  $g/E_\delta = 0.002$  in the mean-field simulations, as the black curve of FIG. 5.8 shows. We have also performed 6 sets of simulations, with different values for both  $\delta\rho^\varnothing$  and  $g$ , their product being kept constant and equal to  $g\rho^\varnothing = 0.002E_\delta$ . Those results are shown in FIG. 5.10.

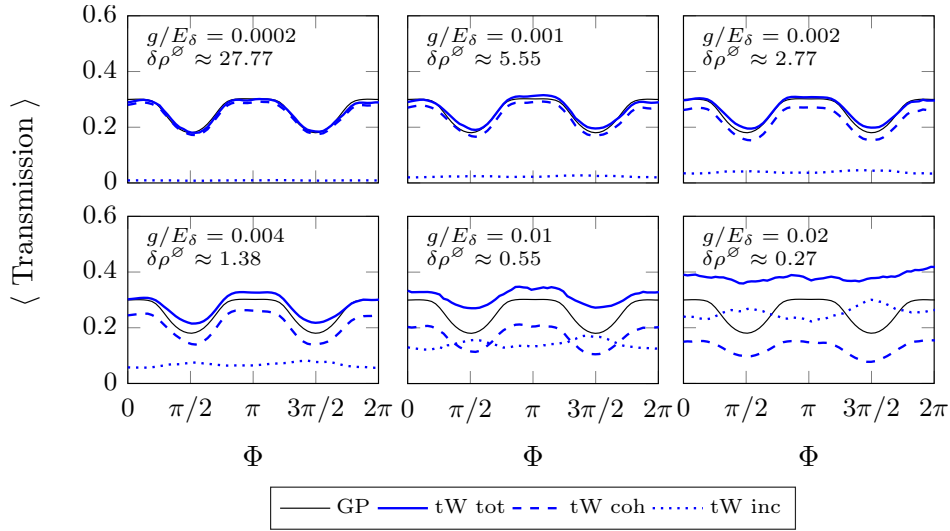


Figure 5.10 – Truncated Wigner simulations of the ensemble averaged transmission as a function of the enclosed artificial flux  $\Phi$  for different interaction strengths  $g$  and injected densities  $\delta\rho^\varnothing$ , the product  $\delta\rho^\varnothing g = 0.002$  being kept constant. This scenario corresponds to a mean-field regime where an inversion of the oscillations is fully developed. The transmission is averaged over 1000 realisations of a Gaussian correlated disorder taking random values in  $[-0.0119, 0.0119]$  with correlation length  $\sigma = 20\delta$ , each of which performed with an average of 100 realisations over the initial conditions. In this regime of fully developed inversion of AAS oscillations, the coherent part carries all the inverted structure whilst incoherent scattering processes take more and more importance as the interaction strength is increased and the injected density decreases. Far away from the mean-field limit, this coherent contribution is hidden by a large incoherent part which dominates, indicating the presence of dephasing for strong interaction. Numerical parameters:  $\mu/E_\delta = 0.2$  and  $N_R = 200$  sites.

FIG. 5.10 indicates that the inverted structure revealed by the mean-field simulations is formally due to a coherent contribution, which confirms that the inversion of the minimum in

the ensemble averaged transmission at  $\Phi = \pi$  and the coherent backscattering inversion have the same origin. As the interaction strength is increased and the injected density decreased, the simulations indicate that the inversion is not strictly restricted to a mean-field regime and extends beyond. However, the structure related to the inversion gets progressively hidden by a flat and structureless incoherent contribution originating from inelastic scattering. For stronger interaction, this incoherent contribution completely dominates and indicates the presence of dephasing, as is expected from many-body diagrammatic techniques [62].

#### 5.4.2 Experimental observability of the inversion of Al'tshuler–Aronov–Spivak oscillations

The challenge is to assess in which regime of injected density a realisation of a quantum transport experiment that is designed to observe the inversion of AAS oscillations would lie. Atoms of  $^{87}\text{Rb}$  are good candidates for such experiments since they are the most frequent atomic species used to produce a Bose–Einstein condensate. Such a species is indeed relatively easy to evaporatively cool due to its cooling-compliant atomic structure [353] and also possesses a positive s-wave scattering length that generates a repulsive interaction which prevents a condensate made of  $^{87}\text{Rb}$  atoms from collapsing. We thus evaluate whether the inversion of AAS oscillations is observable with  $^{87}\text{Rb}$  atoms for realistic experimental parameters. As indicated in Eq. (2.62), the effective one-dimension interaction strength is controlled by

$$g = \frac{2\hbar\omega_{\perp}a_S}{\delta}, \quad (5.87)$$

and the injected density  $\rho^{\varnothing}$  is related to the density per unit length  $\bar{\rho}(x)$  through  $\rho^{\varnothing} = \delta\bar{\rho}(x)$ . Therefore, the nonlinearity we chose in the simulations takes on the form

$$g\rho^{\varnothing} = 2\hbar\omega_{\perp}a_S\bar{\rho}(x) = 0.0055E_{\delta}. \quad (5.88)$$

Owing to the chemical potential chosen in the simulations, we can write that  $E_{\delta} = 5\mu = 5mv^2/2$  which in turn allows to rewrite the density per unit length from Eq. (5.88) as

$$\bar{\rho}(x) = \frac{0.0275}{4} \frac{mv^2}{\hbar\omega_{\perp}a_S}. \quad (5.89)$$

Considering that  $E_{\delta} = \hbar^2/(m\delta^2)$  and  $E_{\delta} = 5mv^2/2$ , we write the spacing as

$$\delta^2 = \frac{2}{5} \frac{\hbar^2}{m^2v^2}, \quad (5.90)$$

which finally yields the injected density

$$\rho^{\varnothing} = \delta\bar{\rho}(x) = \frac{0.0275}{4} \sqrt{0.4} \frac{v}{\omega_{\perp}a_S}. \quad (5.91)$$

For a source that injects  $^{87}\text{Rb}$  atoms in the waveguide with speed of  $v = 1$  mm/s and whose s-wave scattering length is  $a_S = 5.313 \times 10^{-9}$  m, we find that for a confinement frequency  $\omega_{\perp} = 2\pi \times 1$  kHz, the injected atomic density would correspond to the value  $\delta\rho^{\varnothing} \simeq 0.0826$ . Those realistic experimental parameters correspond to a situation where the inversion of Al'tshuler–Aronov–Spivak oscillations occurs in a regime where dephasing

---

is dominant and overshadows the effect, as FIG. 5.10 indicates. We thus do not expect the effect to be observable with  $^{87}\text{Rb}$  atoms. Other species, such as  $^{39}\text{K}$  atoms whose  $s$ -wave scattering length may be tuned to very low values by means of Feshbach tuning [136] are probably more appropriate candidates for an experimental observation of the inversion of Al'tshuler–Aronov–Spivak oscillations. Indeed,  $^{39}\text{K}$  atoms possess a very broad Feshbach resonance width  $\Delta B$  [354] that allows for a very fine tuning of the interaction strength of Bose–Einstein condensate of  $^{39}\text{K}$  atoms, whereas the resonance width related to  $^{87}\text{Rb}$  atoms is narrower [355].



## Chapter 6

# Diagrammatic theory for Al'tshuler–Aronov–Spivak oscillations in the presence of interaction

This chapter is devoted to a semiclassical diagrammatic mean-field theory of Al'tshuler–Aronov–Spivak oscillations in the presence of interaction. This theory has been mostly developed by our collaborator, Dr. Josef Rammensee, from the university of Regensburg. We explain in this chapter the main steps of his analytical theory that led to a joint publication [326].

The purpose of the diagrammatic theory is to solve the steady mean-field equation describing transport of matter waves towards the scattering region studied in Chapter 5 by means of Green's functions, and to develop a perturbative theory of the non-interacting Green's function by treating the atom–atom interaction as a small perturbation. We already initiated this diagrammatic treatment by deriving a semiclassical expression for the noninteracting Green's function of a disordered Aharonov–Bohm ring connected to two semi-infinite leads in the absence of atom–atom interaction. This Green's function consists in a summation of all the scattering paths that begin at one point and end at another one. This expression for the Green's function allows the calculation of the reflection (resp. transmission) probability, provided the starting point is located in the left lead and the ending point in the left (resp. right) lead. In the presence of a smooth and weak disorder, this approach has revealed dominant Al'tshuler–Aronov–Spivak oscillations in the ensemble averaged transmission.

The first step in this diagrammatic theory is to perform an exact and genuine resummation of the scattering paths involved in the semiclassical Green's function instead of deriving only the leading order terms, as in Chapter 5. More specifically, we focus on resumming the part of the scattering paths that describe the motion within the ring, made of sequences of explorations of both arms. After that, the next step is to perform a perturbative expansion in the nonlinear parameter  $g$ . We do so until the first order in  $g$ , that allows to show a linear effect in the interaction parameter on the ensemble averaged transmission, in good agreement

with the numerical results. This agreement is however restricted to a regime that is limited to a very weak interaction strength.

### 6.1 Fundamental building blocks of the diagrammatic theory

As we already explained in Chapter 5, the noninteracting Green’s function describing the system can be expressed as a summation over all paths joining the two points of interest,  $\alpha$  and  $\alpha'$ . Specifically, it reads

$$G(\alpha, \alpha', \mu) = \frac{1}{iE_\delta \sin(k\delta)} \sum_{\gamma} A_{\gamma} e^{iS_{\gamma}/\hbar}. \tag{6.1}$$

The idea behind the diagrammatic theory is to represent those scattering paths by diagrams and to find a way to perform their full summation. We first observe that each scattering path is built on the same skeleton: a trivial exploration of the leads and multiple visits of each arms, with reflection and transmission events at the junctions. An example is shown for instance for the following path

$$\text{Diagram of path } \alpha_S \rightarrow \alpha = \text{Diagram of } \alpha_S \rightarrow 0 \times \left[ \text{Diagram of reflection at } 0 \times \text{Diagram of loop visit} \times \text{Diagram of reflection at } \frac{N_R}{2} \times \text{Diagram of reflection at } \alpha \right] \times \text{Diagram of } \alpha \rightarrow \frac{N_R}{2} \tag{6.2}$$

that goes from  $\alpha_S$  to  $\alpha$ , by describing a free propagation from the source  $\alpha_S$  to the entrance of the ring at site 0, followed by a clockwise visit of the upper arm of the ring and finally a reflection at the site  $N_R/2$ , *i.e.* the right junction, back to the point  $\alpha$  located in the upper arm. The bracketed factors represent the intermediate path followed inside the ring, which we have separated from the direct trajectory between the departure/arrival and the junctions, since the former can be of infinite complexity whilst the latter are quite simple.

All the building blocks appearing in Eq. (6.2) contribute as multiplicative factors, allowing us to factor out the trivial explorations of the leads that are common to all paths from the traversal of the ring. In the following, we focus on resumming the segments of path describing the traversal of the ring, which are precisely those that generate Al’tshuler–Aronov–Spivak oscillations in the ensemble averaged transmission. Fundamental building blocks have already been introduced in this context, and we recall them from Chapter 5

$$\begin{aligned} \text{Diagram of reflection } r &= r, & \text{Diagram of transmission } t &= t, \\ \text{Diagram of clockwise loop} &= e^{i(\Phi_u + \frac{\Phi}{2})}, & \text{Diagram of counter-clockwise loop} &= e^{i(\Phi_u - \frac{\Phi}{2})}, \\ \text{Diagram of counter-clockwise loop} &= e^{i(\Phi_d - \frac{\Phi}{2})}, & \text{Diagram of clockwise loop} &= e^{i(\Phi_d + \frac{\Phi}{2})}. \end{aligned} \tag{6.3}$$

Every time a junction is visited, a reflection or transmission event occurs, and the overall amplitude  $A_{\gamma}$  of the path  $\gamma$  is multiplied by either  $r$  or  $t$ , thus highlighting that the longer a path, the smaller its contribution, since  $|r| < 1$  and  $|t| < 1$ . Every visit of an arm provides a phase that depends both upon the direction of visit and the visited arm. A full exploration of the ring yields a phase  $\pm\Phi$  so that a branch only yields a phase  $\pm\Phi/2$ , with the  $+$  sign associated with the clockwise rotation and the  $-$  sign with the opposite (counterclockwise) direction of rotation. Irrespective of the direction of rotation, a phase  $\Phi_u$  is also acquired



at each full traversal of the upper arm of the ring, and a phase  $\Phi_d$  is obtained at each full traversal of the lower arm.

Those building blocks – multiplicative amplitudes and phase factors – can be combined together to generate any sequence of explorations of the arms, and then combined to diagrams representing the exploration of the leads or partial exploration of an arm to obtain a diagrammatic representation of the Green’s function (6.1). Equipped with this arsenal, our goal is to perform a coherent resummation up to infinite order of all back and forth trajectories which are comprised inside the ring.

## 6.2 Resummation of diagrams in the noninteracting case

The idea we follow in deriving a resummation of the diagrams is to group similar diagrams together into families of diagrams sharing the same structure. For instance, a family containing all diagrams that traverse a given junction in a given direction: a member of this family is shown in Eq. (6.4). It displays diagrams traversing the left junction from the bottom to the top. The various families we shall present and their composing members are actually intimately related one to each other, certain directly through particular symmetry rules, others through a self-consistent equation. Those families of diagrams finally allow to formulate a compact expression for the reflection and transmission probability amplitudes that yield the related probabilities through square modulation and ensemble averaging.

### 6.2.1 Families of diagrams related to effective reflection and transmission at a junction

We can separate the diagrams representing back and forth trajectories into different families, depending upon how they visit the junctions. A first family of diagrams is found, namely the family that encompasses trajectories that enter and exit a junction the same way. With two possible directions by junction, this family contains four members, namely

$$\color{red}{\downarrow} = \downarrow + \text{[diagram 1]} + \text{[diagram 2]} + \text{[diagram 3]} + \text{[diagram 4]} + \dots \quad (6.4)$$

$$\color{red}{\downarrow} = \downarrow + \text{[diagram 1]} + \text{[diagram 2]} + \text{[diagram 3]} + \text{[diagram 4]} + \dots \quad (6.5)$$

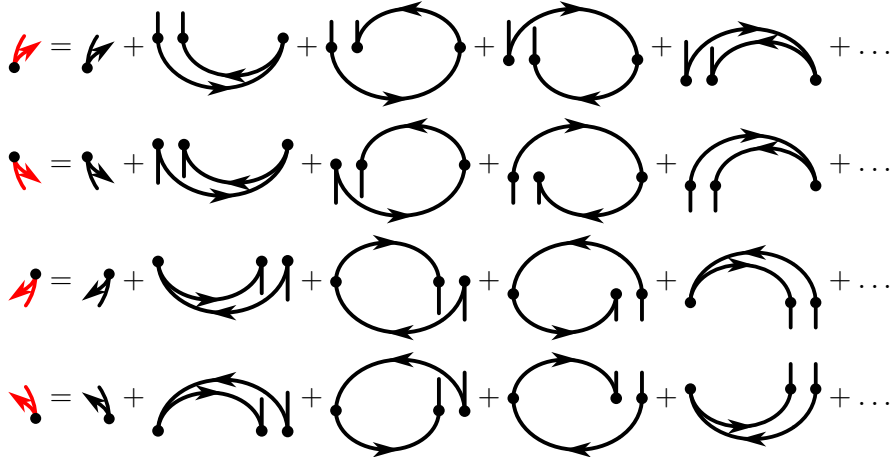
$$\color{red}{\downarrow} = \downarrow + \text{[diagram 1]} + \text{[diagram 2]} + \text{[diagram 3]} + \text{[diagram 4]} + \dots \quad (6.6)$$

$$\color{red}{\downarrow} = \downarrow + \text{[diagram 1]} + \text{[diagram 2]} + \text{[diagram 3]} + \text{[diagram 4]} + \dots \quad (6.7)$$

The direction pointed by the arrow and its curvature indicate which junction is traversed and how. For instance, the red diagram appearing in Eq. (6.4) encompasses all trajectories arriving from the lower branch to the left junction and, after a possible long and intricate

trip, exit it to the upper arm, following the clockwise direction.

A second family of diagrams is found and contains diagrams that are, again after a possible long and complicated trip, reflected at the same junction. It also contains four members which are



The direction pointed by the arrow and its curvature also obviously indicate which kind of resummed reflection we are dealing with.

We can couple those two families of diagrams, portraying effective resummed reflection and transmission at a junction, to express it as self-consistent equations, exploiting the fact that after an even number of explorations of the ring branches, the final junction is the same as the initial one. This is diagrammatically expressed as

$$\begin{matrix} \uparrow \\ \leftarrow \\ \uparrow \end{matrix} = \begin{matrix} \uparrow \\ \leftarrow \\ \uparrow \end{matrix} + \begin{matrix} \uparrow \\ \leftarrow \\ \uparrow \\ \leftarrow \\ \uparrow \end{matrix} + \begin{matrix} \uparrow \\ \leftarrow \\ \uparrow \\ \leftarrow \\ \uparrow \\ \leftarrow \\ \uparrow \end{matrix} + \begin{matrix} \uparrow \\ \leftarrow \\ \uparrow \\ \leftarrow \\ \uparrow \\ \leftarrow \\ \uparrow \\ \leftarrow \\ \uparrow \end{matrix} + \begin{matrix} \uparrow \\ \leftarrow \\ \uparrow \\ \leftarrow \\ \uparrow \end{matrix}, \tag{6.8}$$

$$\begin{matrix} \uparrow \\ \leftarrow \\ \uparrow \\ \leftarrow \\ \uparrow \end{matrix} = \begin{matrix} \uparrow \\ \leftarrow \\ \uparrow \end{matrix} + \begin{matrix} \uparrow \\ \leftarrow \\ \uparrow \\ \leftarrow \\ \uparrow \\ \leftarrow \\ \uparrow \end{matrix} + \begin{matrix} \uparrow \\ \leftarrow \\ \uparrow \\ \leftarrow \\ \uparrow \\ \leftarrow \\ \uparrow \\ \leftarrow \\ \uparrow \end{matrix} + \begin{matrix} \uparrow \\ \leftarrow \\ \uparrow \\ \leftarrow \\ \uparrow \\ \leftarrow \\ \uparrow \\ \leftarrow \\ \uparrow \\ \leftarrow \\ \uparrow \end{matrix}, \tag{6.9}$$

which is best understood in matrix form

$$\begin{bmatrix} \uparrow \\ \leftarrow \\ \uparrow \\ \leftarrow \\ \uparrow \end{bmatrix} = \begin{bmatrix} \uparrow \\ \leftarrow \\ \uparrow \end{bmatrix} + \underbrace{\begin{bmatrix} \begin{matrix} \uparrow \\ \leftarrow \\ \uparrow \\ \leftarrow \\ \uparrow \end{matrix} + \begin{matrix} \uparrow \\ \leftarrow \\ \uparrow \\ \leftarrow \\ \uparrow \\ \leftarrow \\ \uparrow \end{matrix} & \begin{matrix} \uparrow \\ \leftarrow \\ \uparrow \\ \leftarrow \\ \uparrow \\ \leftarrow \\ \uparrow \end{matrix} + \begin{matrix} \uparrow \\ \leftarrow \\ \uparrow \\ \leftarrow \\ \uparrow \\ \leftarrow \\ \uparrow \\ \leftarrow \\ \uparrow \end{matrix} \\ \begin{matrix} \uparrow \\ \leftarrow \\ \uparrow \\ \leftarrow \\ \uparrow \end{matrix} + \begin{matrix} \uparrow \\ \leftarrow \\ \uparrow \\ \leftarrow \\ \uparrow \\ \leftarrow \\ \uparrow \end{matrix} & \begin{matrix} \uparrow \\ \leftarrow \\ \uparrow \\ \leftarrow \\ \uparrow \\ \leftarrow \\ \uparrow \\ \leftarrow \\ \uparrow \end{matrix} + \begin{matrix} \uparrow \\ \leftarrow \\ \uparrow \\ \leftarrow \\ \uparrow \\ \leftarrow \\ \uparrow \\ \leftarrow \\ \uparrow \end{matrix} \end{bmatrix} \begin{bmatrix} \uparrow \\ \leftarrow \\ \uparrow \\ \leftarrow \\ \uparrow \end{bmatrix}. \tag{6.10}$$

$= \mathcal{A}(\Phi_u, \Phi_d, \Phi)$

The solution of this equation is obtained by matrix inversion



$$\begin{bmatrix} \uparrow \\ \leftarrow \\ \uparrow \\ \leftarrow \\ \uparrow \end{bmatrix} = \underbrace{[\mathbb{I} - \mathcal{A}(\Phi_u, \Phi_d, \Phi)]^{-1}}_{=\mathcal{A}(\Phi_u, \Phi_d, \Phi)} \begin{bmatrix} \uparrow \\ \leftarrow \\ \uparrow \end{bmatrix} = \mathcal{A}(\Phi_u, \Phi_d, \Phi)^{-1} \begin{bmatrix} t \\ r \end{bmatrix}. \tag{6.11}$$

In terms of the fundamental building blocks introduced in Eq. (6.3), we can express the matrix  $\mathcal{A}(\Phi_u, \Phi_d, \Phi) = \mathbb{I} - A(\Phi_u, \Phi_d, \Phi)$  as

$$\mathcal{A}(\Phi_u, \Phi_d, \Phi) = \begin{bmatrix} 1 - \text{diag} & - \text{circ} & - \text{circ} & - \text{diag} \\ - \text{diag} & - \text{circ} & 1 - \text{circ} & - \text{diag} \end{bmatrix} = \begin{bmatrix} 1 - r^2 e^{2i\Phi_u} - t^2 e^{i(\Phi_u + \Phi_d + \Phi)} & -rte^{i(\Phi_u + \Phi_d - \Phi)} - rte^{2i\Phi_d} \\ -rte^{2i\Phi_u} - rte^{i(\Phi_u + \Phi_d + \Phi)} & 1 - t^2 e^{i(\Phi_u + \Phi_d - \Phi)} - r^2 e^{2i\Phi_d} \end{bmatrix} \quad (6.12)$$

In order to invert the matrix  $\mathcal{A}$ , we must compute

$$\begin{aligned} \det[\mathcal{A}(\Phi_u, \Phi_d, \Phi)] &= \left(1 - r^2 e^{2i\Phi_u} - t^2 e^{i(\Phi_u + \Phi_d + \Phi)}\right) \left(1 - r^2 e^{2i\Phi_d} - t^2 e^{i(\Phi_u + \Phi_d - \Phi)}\right) \\ &\quad - r^2 t^2 \left(e^{2i\Phi_d} + e^{i(\Phi_u + \Phi_d - \Phi)}\right) \left(e^{2i\Phi_u} + e^{i(\Phi_u + \Phi_d + \Phi)}\right) \\ &= 1 + r^4 e^{2i(\Phi_u + \Phi_d)} + t^4 e^{2i(\Phi_u + \Phi_d)} - r^2 \left(e^{2i\Phi_u} + e^{2i\Phi_d}\right) - 2t^2 e^{i(\Phi_u + \Phi_d)} \cos(\Phi) \\ &\quad + r^2 t^2 e^{i(\Phi_u + \Phi_d)} \left(e^{i(2\Phi_u - \Phi)} + e^{i(2\Phi_d + \Phi)}\right) \\ &\quad - r^2 t^2 e^{i(\Phi_u + \Phi_d)} \left(e^{i(2\Phi_d + \Phi)} + e^{i(2\Phi_u - \Phi)}\right) - 2r^2 t^2 e^{2i(\Phi_u + \Phi_d)} \\ &= 1 - r^2 \left(e^{2i\Phi_u} + e^{2i\Phi_d}\right) - 2t^2 e^{i(\Phi_u + \Phi_d)} \cos(\Phi) + \left(r^2 - t^2\right)^2 e^{2i(\Phi_u + \Phi_d)}, \end{aligned} \quad (6.13)$$


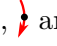
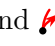
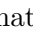
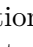
that must be different from zero for the matrix inversion to be possible. Due to the parity of  $\cos \Phi$ , we observe that the determinant is left unchanged after a sign permutation of  $\Phi$ , which would for instance result from a horizontal mirroring of the ring, or a trip in the other direction of rotation. Vertical mirroring also leaves the determinant unchanged, as this would imply exchanging  $\Phi_u$  and  $\Phi_d$  which are perfectly symmetric in Eq. (6.13). Those symmetries may be leveraged to derive resummed diagrams similar to  and . Since our system is open, the determinant is nonzero [356] and we obtain in this case

$$\mathcal{A}(\Phi_u, \Phi_d, \Phi)^{-1} = \frac{1}{\det[\mathcal{A}(\Phi_u, \Phi_d, \Phi)]} \begin{bmatrix} 1 - r^2 e^{2i\Phi_d} - t^2 e^{i(\Phi_u + \Phi_d - \Phi)} & rt \left(e^{2i\Phi_d} + e^{i(\Phi_u + \Phi_d - \Phi)}\right) \\ rt \left(e^{2i\Phi_u} + e^{i(\Phi_u + \Phi_d + \Phi)}\right) & 1 - r^2 e^{2i\Phi_u} - t^2 e^{i(\Phi_u + \Phi_d + \Phi)} \end{bmatrix}. \quad (6.14)$$

In other contexts, the zeros of the denominator would indicate sets of parameters for which the ring exhibit bound states at particular values of the artificial flux  $\Phi$  [356]. We are now in a position to compute the resummed diagrams, which are found to be

$$\text{red arrow up} = t \frac{1 + (r^2 - t^2) e^{i(\Phi_u + \Phi_d - \Phi)}}{1 - r^2 (e^{2i\Phi_u} + e^{2i\Phi_d}) - 2t^2 e^{i(\Phi_u + \Phi_d)} \cos(\Phi) + (r^2 - t^2)^2 e^{2i(\Phi_u + \Phi_d)}} \quad (6.15)$$

$$\text{red arrow down} = r \frac{1 - (r^2 - t^2) e^{2i\Phi_u}}{1 - r^2 (e^{2i\Phi_u} + e^{2i\Phi_d}) - 2t^2 e^{i(\Phi_u + \Phi_d)} \cos(\Phi) + (r^2 - t^2)^2 e^{2i(\Phi_u + \Phi_d)}}. \quad (6.16)$$

Amongst the four members of each of the two families of the resummed diagrams, we are still left with the determination of three members of each, that are ,  and . This determination could be tediously achieved, similarly as for  and , but we can also exploit the symmetry properties of the determinant to obtain the diagrams under study by simply modifying the numerator properly.

For instance, a modification of the direction pointed by an arrow of a resummed diagram leads to a modification of the sign of  $\Phi$  only, since the same branches are crossed but a clockwise rotation becomes counterclockwise and vice-versa. On the other hand, one can also flip vertically a resummed diagram, leading to an exchange of roles between  $\Phi_u$  and  $\Phi_d$ , as well as to a sign inversion in front of  $\Phi$ . Finally, a diagram can also be flipped horizontally, which does not change the branches that are crossed, but is responsible for another sign inversion in front of  $\Phi$ , since it once again inverts the direction of rotation.

All together, those observations allow us to write the complete set of resummed diagrams for the effective reflection and transmission at a single junction as

$$\begin{array}{c} \text{Diagram 1} = t \frac{1 + (r^2 - t^2) e^{i(\Phi_u + \Phi_d - \Phi)}}{D(\Phi_u, \Phi_d, \Phi)} = \text{Diagram 2} \end{array} \quad (6.17)$$

$$\begin{array}{c} \text{Diagram 3} = r \frac{1 - (r^2 - t^2) e^{i2\Phi_u}}{D(\Phi_u, \Phi_d, \Phi)} = \text{Diagram 4} \end{array} \quad (6.18)$$

$$\begin{array}{c} \text{Diagram 5} = t \frac{1 + (r^2 - t^2) e^{i(\Phi_u + \Phi_d + \Phi)}}{D(\Phi_u, \Phi_d, \Phi)} = \text{Diagram 6} \end{array} \quad (6.19)$$


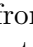
$$\begin{array}{c} \text{Diagram 7} = r \frac{1 - (r^2 - t^2) e^{i2\Phi_d}}{D(\Phi_u, \Phi_d, \Phi)} = \text{Diagram 8} \end{array} \quad (6.20)$$



Those resummed diagrams will be of particular relevance as building blocks to construct diagrams that join a junction to the other one.

### 6.2.2 Families of diagrams that join the junctions

It is possible to discriminate diagrams connecting the two junctions depending upon where they start and end, but also upon the way each junction is crossed. A first example consists in the resummed diagram that encompasses all diagrams representing paths that join the left to the right junction by starting and ending their trip in the lower branch. Such a resummed diagram is obtained as



translating that this resummed diagram combines two scenarios. A first case consists in an effective transmission described by  at the left junction from the lower to the upper branch, followed by a direct traversal of the upper branch to the right junction, which is exited by the bottom, after a last transmission event. A second possibility is an effective reflection described by  at the left junction from the lower branch to the same branch, followed by a direct traversal of the lower branch to the right junction, on which a last reflection event

occurs. Finally, the resummed diagram under study is obtained by summing  and  after multiplying each of those by the proper factors

$$\begin{aligned}
\text{---}\text{---}\text{---} &= t \frac{1 + (r^2 - t^2) e^{i(\Phi_u + \Phi_d - \Phi)}}{D(\Phi_u, \Phi_d, \Phi)} e^{i(\Phi_u + \frac{\Phi}{2})} t + r \frac{1 - (r^2 - t^2) e^{i2\Phi_u}}{D(\Phi_u, \Phi_d, \Phi)} e^{i(\Phi_d - \frac{\Phi}{2})} r \\
&= \frac{r^2 e^{i(\Phi_d - \frac{\Phi}{2})} + t^2 e^{i(\Phi_u + \frac{\Phi}{2})} - (r^2 - t^2)^2 e^{i(2\Phi_u + \Phi_d - \frac{\Phi}{2})}}{D(\Phi_u, \Phi_d, \Phi)} \\
&= e^{-i(\Phi_d + \frac{\Phi}{2})} \frac{r^2 e^{2i\Phi_d} + t^2 e^{i(\Phi_u + \Phi_d + \Phi)} - (r^2 - t^2)^2 e^{2i(\Phi_u + \Phi_d)}}{D(\Phi_u, \Phi_d, \Phi)} \\
&= e^{-i(\Phi_d + \frac{\Phi}{2})} \left( \frac{1 - r^2 e^{2i\Phi_u} - t^2 e^{i(\Phi_u + \Phi_d - \Phi)}}{D(\Phi_u, \Phi_d, \Phi)} - 1 \right), \tag{6.21}
\end{aligned}$$

where we have brought the phase factor  $e^{-i(\Phi_d + \frac{\Phi}{2})}$  out to exploit the symmetry rules detailed earlier in order to obtain the other diagrams. A second example of resummed diagram is a diagram that encompasses all diagrams representing paths that join the left junction to the right one by starting their trip in the lower branch and ending it in the upper branch. Such a resummed diagram is obtained as

$$\begin{aligned}
\text{---}\text{---}\text{---} &= \text{---}\text{---}\text{---} + \text{---}\text{---}\text{---} \\
&= t \frac{1 + (r^2 - t^2) e^{i(\Phi_u + \Phi_d - \Phi)}}{D(\Phi_u, \Phi_d, \Phi)} e^{i(\Phi_u + \frac{\Phi}{2})} r + r \frac{1 - (r^2 - t^2) e^{i2\Phi_u}}{D(\Phi_u, \Phi_d, \Phi)} e^{i(\Phi_d - \frac{\Phi}{2})} t \\
&= \frac{rt \left( e^{i(\Phi_u + \frac{\Phi}{2})} + e^{i(\Phi_d - \frac{\Phi}{2})} \right)}{D(\Phi_u, \Phi_d, \Phi)} \\
&= e^{-i(\Phi_u - \frac{\Phi}{2})} \frac{rt \left( e^{2i\Phi_u} + e^{i(\Phi_u + \Phi_d - \Phi)} \right)}{D(\Phi_u, \Phi_d, \Phi)}. \tag{6.22}
\end{aligned}$$

Thanks to the diagrams in Eqs. (6.21), (6.22) and to the symmetry rules of the system, we can derive the other ones. For instance, inverting the arrow whilst keeping the starting and ending branches invariant, which is equivalent to switching from a clockwise to a counterclockwise exploration of the ring, or vice-versa, altogether results in a sign inversion in front of  $\Phi$ . A second example consists in keeping the arrow invariant, but modifying both the starting and ending branches. Such an operation amounts to exchanging the roles of  $\Phi_u$  and  $\Phi_d$ . Those symmetry rules applied to Eq. (6.21) allow us to write

$$\text{---}\text{---}\text{---} = e^{-i(\Phi_d + \frac{\Phi}{2})} \left( \frac{1 - r^2 e^{i2\Phi_u} - t^2 e^{i(\Phi_u + \Phi_d - \Phi)}}{D(\Phi_u, \Phi_d, \Phi)} - 1 \right), \tag{6.23}$$

$$\text{---}\text{---}\text{---} = e^{-i(\Phi_d - \frac{\Phi}{2})} \left( \frac{1 - r^2 e^{i2\Phi_u} - t^2 e^{i(\Phi_u + \Phi_d + \Phi)}}{D(\Phi_u, \Phi_d, \Phi)} - 1 \right), \tag{6.24}$$

$$\text{---}\text{---}\text{---} = e^{-i(\Phi_u - \frac{\Phi}{2})} \left( \frac{1 - r^2 e^{i2\Phi_d} - t^2 e^{i(\Phi_u + \Phi_d + \Phi)}}{D(\Phi_u, \Phi_d, \Phi)} - 1 \right), \tag{6.25}$$

$$\text{---}\text{---}\text{---} = e^{-i(\Phi_u + \frac{\Phi}{2})} \left( \frac{1 - r^2 e^{i2\Phi_d} - t^2 e^{i(\Phi_u + \Phi_d - \Phi)}}{D(\Phi_u, \Phi_d, \Phi)} - 1 \right). \tag{6.26}$$

The symmetry rules can also be applied to Eq. (6.22) in order to write

$$\begin{array}{c} \text{---} \bullet \text{---} \bullet \text{---} \\ \text{---} \bullet \text{---} \end{array} = e^{-i(\Phi_u - \frac{\Phi}{2})} \frac{rt \left( e^{2i\Phi_u} + e^{i(\Phi_u + \Phi_d - \Phi)} \right)}{D(\Phi_u, \Phi_d, \Phi)} \quad (6.27)$$

$$= e^{-i(\Phi_d + \frac{\Phi}{2})} \frac{rt \left( e^{2i\Phi_d} + e^{i(\Phi_u + \Phi_d + \Phi)} \right)}{D(\Phi_u, \Phi_d, \Phi)} = \begin{array}{c} \text{---} \bullet \text{---} \bullet \text{---} \\ \text{---} \bullet \text{---} \end{array}, \quad (6.28)$$

$$\begin{array}{c} \text{---} \bullet \text{---} \bullet \text{---} \\ \text{---} \bullet \text{---} \end{array} = e^{-i(\Phi_u + \frac{\Phi}{2})} \frac{rt \left( e^{2i\Phi_u} + e^{i(\Phi_u + \Phi_d + \Phi)} \right)}{D(\Phi_u, \Phi_d, \Phi)} \quad (6.29)$$

$$= e^{-i(\Phi_d - \frac{\Phi}{2})} \frac{rt \left( e^{2i\Phi_d} + e^{i(\Phi_u + \Phi_d - \Phi)} \right)}{D(\Phi_u, \Phi_d, \Phi)} = \begin{array}{c} \text{---} \bullet \text{---} \bullet \text{---} \\ \text{---} \bullet \text{---} \end{array}. \quad (6.30)$$

The equivalence between  $\begin{array}{c} \text{---} \bullet \text{---} \bullet \text{---} \\ \text{---} \bullet \text{---} \end{array}$  and  $\begin{array}{c} \text{---} \bullet \text{---} \bullet \text{---} \\ \text{---} \bullet \text{---} \end{array}$ , as well as for  $\begin{array}{c} \text{---} \bullet \text{---} \bullet \text{---} \\ \text{---} \bullet \text{---} \end{array}$  and  $\begin{array}{c} \text{---} \bullet \text{---} \bullet \text{---} \\ \text{---} \bullet \text{---} \end{array}$  naturally results from the symmetry rules. Indeed, they are obtained one from another by inverting the direction of the arrow and the starting and ending junctions, which leaves the diagram invariant since it results in a double sign inversion in front of  $\Phi$ .

### 6.2.3 Family of diagrams connecting the ring to the leads

Another family of diagrams is found and encompasses all diagrams that connect the ring to the junction, either the left lead to the left junction, or the right junction to the right lead. That family contains only six members instead of eight, because there is no trajectory associated with paths consisting in entering the right junction from the right lead, since there is no injection of particles in the right lead. A first diagram, namely  $\begin{array}{c} \text{---} \bullet \text{---} \bullet \text{---} \\ \text{---} \bullet \text{---} \end{array}$ , encompasses all diagrams whose starting point is in the left lead and that effectively penetrates the ring by the upper arm. This resummed diagram is provided by

$$\begin{aligned} \begin{array}{c} \text{---} \bullet \text{---} \bullet \text{---} \\ \text{---} \bullet \text{---} \end{array} &= \begin{array}{c} \text{---} \bullet \text{---} \bullet \text{---} \\ \text{---} \bullet \text{---} \end{array} + \begin{array}{c} \text{---} \bullet \text{---} \bullet \text{---} \\ \text{---} \bullet \text{---} \end{array} + \begin{array}{c} \text{---} \bullet \text{---} \bullet \text{---} \\ \text{---} \bullet \text{---} \end{array} \\ &= t + t \left( \frac{1 - r^2 e^{i2\Phi_d} - t^2 e^{i(\Phi_u + \Phi_d - \Phi)}}{D(\Phi_u, \Phi_d, \Phi)} - 1 \right) + t \frac{rt \left( e^{2i\Phi_d} + e^{i(\Phi_u + \Phi_d - \Phi)} \right)}{D(\Phi_u, \Phi_d, \Phi)} \\ &= t \frac{1 - r^2 e^{i2\Phi_d} - t^2 e^{i(\Phi_u + \Phi_d - \Phi)} + r t e^{2i\Phi_d} + r t e^{i(\Phi_u + \Phi_d - \Phi)}}{D(\Phi_u, \Phi_d, \Phi)} \\ &= t \frac{1 - (r - t) \left( r e^{i2\Phi_d} - t e^{i(\Phi_u + \Phi_d - \Phi)} \right)}{D(\Phi_u, \Phi_d, \Phi)}. \end{aligned}$$

The same symmetry rules can be exploited once again to obtain the five remaining diagrams and mainly consists in inverting the sign in front of  $\Phi$  properly and exchanging  $\Phi_u$  with  $\Phi_d$

when needed. Those rules allow us to write

$$\begin{array}{c} \text{---} \bullet \text{---} \uparrow \\ \text{---} \bullet \text{---} \uparrow \end{array} = t \frac{1 - (r - t) \left( r e^{i2\Phi_d} - t e^{i(\Phi_u + \Phi_d - \Phi)} \right)}{D(\Phi_u, \Phi_d, \Phi)} = \begin{array}{c} \text{---} \bullet \text{---} \uparrow \\ \text{---} \bullet \text{---} \uparrow \end{array}, \quad (6.31)$$

$$\begin{array}{c} \text{---} \bullet \text{---} \downarrow \\ \text{---} \bullet \text{---} \downarrow \end{array} = t \frac{1 - (r - t) \left( r e^{i2\Phi_u} - t e^{i(\Phi_u + \Phi_d + \Phi)} \right)}{D(\Phi_u, \Phi_d, \Phi)} = \begin{array}{c} \text{---} \bullet \text{---} \downarrow \\ \text{---} \bullet \text{---} \downarrow \end{array}, \quad (6.32)$$

$$\begin{array}{c} \text{---} \bullet \text{---} \uparrow \\ \text{---} \bullet \text{---} \downarrow \end{array} = t \frac{1 - (r - t) \left( r e^{i2\Phi_d} - t e^{i(\Phi_u + \Phi_d + \Phi)} \right)}{D(\Phi_u, \Phi_d, \Phi)}, \quad (6.33)$$

$$\begin{array}{c} \text{---} \bullet \text{---} \downarrow \\ \text{---} \bullet \text{---} \uparrow \end{array} = t \frac{1 - (r - t) \left( r e^{i2\Phi_u} - t e^{i(\Phi_u + \Phi_d - \Phi)} \right)}{D(\Phi_u, \Phi_d, \Phi)}. \quad (6.34)$$

A second (and last) family of resummed diagrams encompasses diagrams representing paths consisting in the effective traversal of the ring from one junction to the other. Such an effective traversal consists either in paths starting in one lead and ending in one branch at the opposite junction, or either in paths starting in a branch and ending in the lead connected to the junction opposite to the first encountered. A concrete example of such diagrams is the one representing a path whose starting point is located in the left lead, and the ending point is in the upper arm, after a visit of the ring. This diagram is represented by the following analytical expression

$$\begin{aligned} \begin{array}{c} \text{---} \bullet \text{---} \uparrow \\ \text{---} \bullet \text{---} \uparrow \end{array} &= \begin{array}{c} \text{---} \bullet \text{---} \uparrow \\ \text{---} \bullet \text{---} \uparrow \end{array} + \begin{array}{c} \text{---} \bullet \text{---} \uparrow \\ \text{---} \bullet \text{---} \uparrow \end{array} \\ &= t \frac{1 - (r - t) \left( r e^{i2\Phi_d} - t e^{i(\Phi_u + \Phi_d - \Phi)} \right)}{D(\Phi_u, \Phi_d, \Phi)} e^{i(\Phi_u + \frac{\Phi}{2})} r \\ &\quad + t \frac{1 - (r - t) \left( r e^{i2\Phi_u} - t e^{i(\Phi_u + \Phi_d + \Phi)} \right)}{D(\Phi_u, \Phi_d, \Phi)} e^{i(\Phi_d - \frac{\Phi}{2})} t \\ &= t \frac{r e^{i(\Phi_u + \frac{\Phi}{2})} - r(r - t) \left( r e^{i(\Phi_u + 2\Phi_d + \frac{\Phi}{2})} - t e^{i(2\Phi_u + \Phi_d - \frac{\Phi}{2})} \right)}{D(\Phi_u, \Phi_d, \Phi)} \\ &\quad + t \frac{t e^{i(\Phi_d - \frac{\Phi}{2})} - t(r - t) \left( r e^{i(2\Phi_u + \Phi_d - \frac{\Phi}{2})} - t e^{i(\Phi_u + 2\Phi_d + \frac{\Phi}{2})} \right)}{D(\Phi_u, \Phi_d, \Phi)} \\ &= e^{-i(\Phi_u - \frac{\Phi}{2})} t \frac{r e^{i2\Phi_u} - r(r - t) \left( r e^{i2(\Phi_u + \Phi_d)} - t e^{i(3\Phi_u + \Phi_d - \Phi)} \right)}{D(\Phi_u, \Phi_d, \Phi)} \\ &\quad + e^{-i(\Phi_u - \frac{\Phi}{2})} t \frac{t e^{i(\Phi_u + \Phi_d - \Phi)} - t(r - t) \left( r e^{i(3\Phi_u + \Phi_d - \Phi)} - t e^{i2(\Phi_u + \Phi_d)} \right)}{D(\Phi_u, \Phi_d, \Phi)} \\ &= e^{-i(\Phi_u - \frac{\Phi}{2})} t \frac{r e^{i2\Phi_u} + t e^{i(\Phi_u + \Phi_d - \Phi)} - (r - t) (r^2 - t^2) e^{i2(\Phi_u + \Phi_d)}}{D(\Phi_u, \Phi_d, \Phi)}. \quad (6.35) \end{aligned}$$

As usual, we can use the symmetry properties of the ring to derive the other members of this family of resummed diagrams, which are given by

$$\begin{array}{c} \bullet \xrightarrow{\text{red}} \uparrow \\ \bullet \end{array} = e^{-i(\Phi_u - \frac{\Phi}{2})t} \frac{r e^{i2\Phi_u} + t e^{i(\Phi_u + \Phi_d - \Phi)} - (r-t)(r^2 - t^2) e^{i2(\Phi_u + \Phi_d)}}{D(\Phi_u, \Phi_d, \Phi)} = \begin{array}{c} \bullet \xrightarrow{\text{red}} \\ \bullet \end{array} \quad (6.36)$$

$$\begin{array}{c} \bullet \xrightarrow{\text{red}} \downarrow \\ \bullet \end{array} = e^{-i(\Phi_d + \frac{\Phi}{2})t} \frac{r e^{i2\Phi_d} + t e^{i(\Phi_u + \Phi_d + \Phi)} - (r-t)(r^2 - t^2) e^{i2(\Phi_u + \Phi_d)}}{D(\Phi_u, \Phi_d, \Phi)} = \begin{array}{c} \bullet \xrightarrow{\text{red}} \\ \bullet \end{array} \quad (6.37)$$

$$\begin{array}{c} \bullet \xleftarrow{\text{red}} \uparrow \\ \bullet \end{array} = e^{-i(\Phi_u + \frac{\Phi}{2})t} \frac{r e^{i2\Phi_u} + t e^{i(\Phi_u + \Phi_d + \Phi)} - (r-t)(r^2 - t^2) e^{i2(\Phi_u + \Phi_d)}}{D(\Phi_u, \Phi_d, \Phi)} \quad (6.38)$$

$$\begin{array}{c} \bullet \xleftarrow{\text{red}} \downarrow \\ \bullet \end{array} = e^{-i(\Phi_d - \frac{\Phi}{2})t} \frac{r e^{i2\Phi_d} + t e^{i(\Phi_u + \Phi_d - \Phi)} - (r-t)(r^2 - t^2) e^{i2(\Phi_u + \Phi_d)}}{D(\Phi_u, \Phi_d, \Phi)}. \quad (6.39)$$

As for the previous family, only six diagrams populate this family, because diagrams associated with a path coming from the right junction are not related to a physical situation, since no particles are injected from the right lead. Our toolbox is now complete and we are in a position to express the noninteracting Green's function in terms of resummed diagrams. This formulation of the problem not only allows for a visual expression of the reflection and transmission probability amplitudes, but also provides an elegant and concise manner to compute them.

#### 6.2.4 Total reflection and transmission amplitudes in the noninteracting case

We have everything relevant at our disposal to write a diagrammatic expression for the noninteracting Green's function, no matter the location of sites  $\alpha$  and  $\alpha'$ . For instance, if we choose the sites  $\alpha$  and  $\alpha'$  both in the upper branch, the Green's function takes on the following form

$$\begin{aligned} G(\alpha, \alpha', E) = \frac{1}{iE\delta \sin(k\delta)} & \left[ \left( \Theta(\alpha - \alpha') \begin{array}{c} \alpha \quad \alpha' \\ \bullet \xrightarrow{\text{red}} \bullet \end{array} \right) \right. \\ & \left. + \left( \Theta(\alpha' - \alpha) \begin{array}{c} \alpha' \quad \alpha \\ \bullet \xrightarrow{\text{red}} \bullet \end{array} \right) + \begin{array}{c} \alpha' \\ \bullet \xrightarrow{\text{red}} \bullet \end{array} + \begin{array}{c} \alpha \\ \bullet \xrightarrow{\text{red}} \bullet \end{array} \right] \quad (6.40) \end{aligned}$$

where we have introduced the Heaviside step function  $\Theta(\cdot)$  to distinguish whether the site  $\alpha$  is located to the left ( $\alpha < \alpha'$ ) or to the right ( $\alpha > \alpha'$ ) of the site  $\alpha'$ . In the particular case of this example, the exact details of the disorder are required to compute the phase correctly, since the latter diagrams include incomplete traversals of the branches. Fortunately, the calculation of the reflection and transmission amplitudes implies only full explorations of the branches. Phases outside the ring, which are those of a plane wave motion, appear by pairs cancelling each other in the action difference in Eqs. (5.66) and (5.67), due to complex conjugation of the Green's function. Our diagrammatic toolbox allows us to write the total reflection amplitude  $R^{(0)}(\Phi_u, \Phi_d, \Phi)$  for a particular disorder configuration characterised by



$\Phi_u$  and  $\Phi_d$  and the gauge field  $\Phi$ . This reflection amplitude is computed according to

$$\begin{aligned}
R^{(0)}(\Phi_u, \Phi_d, \Phi) &= [iE_\delta \sin(k\delta)G(\alpha_S, \alpha_S, \mu) - 1] e^{-2i|\alpha|k\delta} \\
&= \text{diagram 1} + \text{diagram 2} + \text{diagram 3} \\
&= r + t^2 \frac{re^{2i\Phi_u} + te^{i(\Phi_u+\Phi_d-\Phi)} - (r-t)(r^2-t^2)e^{2i(\Phi_u+\Phi_d)}}{D(\Phi_u, \Phi_d, \Phi)} \\
&\quad + t^2 \frac{re^{2i\Phi_d} + te^{i(\Phi_u+\Phi_d+\Phi)} - (r-t)(r^2-t^2)e^{2i(\Phi_u+\Phi_d)}}{D(\Phi_u, \Phi_d, \Phi)} \\
&= r + t^2 \frac{r(e^{2i\Phi_u} + e^{2i\Phi_d}) + 2te^{i(\Phi_u+\Phi_d)} \cos(\Phi) - 2(r-t)(r^2-t^2)e^{2i(\Phi_u+\Phi_d)}}{D(\Phi_u, \Phi_d, \Phi)},
\end{aligned}$$

where we have introduced the phase factor  $e^{-2i|\alpha|k\delta}$  to compensate the phase acquired from the source to the left junction back and forth and subtracted one in order to exclude the incoming wave from the treatment of the reflection amplitude. Very similarly, the transmission amplitude  $T^{(0)}(\Phi_u, \Phi_d, \Phi)$  is obtained thanks to the Green's function linking the source to any site  $\alpha$  located after the ring

$$\begin{aligned}
T^{(0)}(\Phi_u, \Phi_d, \Phi) &= [iE_\delta \sin(k\delta)G(\alpha_S, \alpha, \mu)] e^{-i(|\alpha_S|+\alpha-N_{\mathcal{R}})k\delta} \\
&= \text{diagram 4} + \text{diagram 5} \\
&= t \frac{1 - (r-t)(re^{i2\Phi_d} - te^{i(\Phi_u+\Phi_d-\Phi)})}{D(\Phi_u, \Phi_d, \Phi)} e^{i(\Phi_u+\frac{\Phi}{2})t} \\
&\quad + t \frac{1 - (r-t)(re^{i2\Phi_u} - te^{i(\Phi_u+\Phi_d+\Phi)})}{D(\Phi_u, \Phi_d, \Phi)} e^{i(\Phi_d-\frac{\Phi}{2})t} \\
&= t^2 \frac{e^{i(\Phi_u+\frac{\Phi}{2})} - (r-t)(re^{i(\Phi_u+2\Phi_d+\frac{\Phi}{2})} - te^{i(2\Phi_u+\Phi_d-\frac{\Phi}{2})})}{D(\Phi_u, \Phi_d, \Phi)} \\
&\quad + t^2 \frac{e^{i(\Phi_u+\frac{\Phi}{2})} - (r-t)(re^{i(2\Phi_u+\Phi_d-\frac{\Phi}{2})} - te^{i(\Phi_u+2\Phi_d+\frac{\Phi}{2})})}{D(\Phi_u, \Phi_d, \Phi)} \\
&= t^2 \frac{e^{i(\Phi_u+\frac{\Phi}{2})} + e^{i(\Phi_d-\frac{\Phi}{2})} - (r-t)^2 e^{i(\Phi_u+\Phi_d)} (e^{i(\Phi_u-\frac{\Phi}{2})} + e^{i(\Phi_d+\frac{\Phi}{2})})}{D(\Phi_u, \Phi_d, \Phi)},
\end{aligned}$$

where we have once again introduced the phase factor  $e^{-i(|\alpha_S|+\alpha-N_{\mathcal{R}})k\delta}$  to compensate the phase acquired as plane wave motion between the source located at  $\alpha_S$  and the left junction at 0 as well as between the right junction and the point  $\alpha$  located after the ring.

Our noninteracting diagrammatic theory will be complete as soon as we take the square modulus of  $R^{(0)}(\Phi_u, \Phi_d, \Phi)$  and  $T^{(0)}(\Phi_u, \Phi_d, \Phi)$  and perform the average over all disorder phases  $\Phi_u$  and  $\Phi_d$  uniformly lying in  $[0, 2\pi]$

$$\langle |R^{(0)}(\Phi_u, \Phi_d, \Phi)|^2 \rangle = \frac{1}{4\pi^2} \int_0^{2\pi} \int_0^{2\pi} |R^{(0)}(\Phi_u, \Phi_d, \Phi)|^2 d\Phi_u d\Phi_d \quad (6.41)$$

$$\langle |T^{(0)}(\Phi_u, \Phi_d, \Phi)|^2 \rangle = \frac{1}{4\pi^2} \int_0^{2\pi} \int_0^{2\pi} |T^{(0)}(\Phi_u, \Phi_d, \Phi)|^2 d\Phi_u d\Phi_d. \quad (6.42)$$

Those integrations are numerically performed by means of a Monte–Carlo integration scheme and shall be confronted to the numerical results obtained in Chapter 5.

### 6.3 Resummation of diagrams in the interacting case

Our goal here is to make use of the principles introduced in the noninteracting case to derive a similar approach taking interaction into account. We discriminate the scattering paths where interaction is taken into account depending upon their ending point  $\alpha$  is located in the lower or in the upper branch of the ring, and upon it is approached from the left or from the right. The wavefunction  $\psi_\alpha$  is, following the approach developed until here, written as a sum of diagrams that share the same meaning as in the noninteracting case<sup>1</sup>. If, for instance, the ending point  $\alpha$  is located in the upper branch, we can write

$$\psi_\alpha = \frac{\sqrt{\mathcal{N}}\kappa(t)}{iE_\delta \sin(k\delta)} \left( \text{---} \overset{\alpha}{\curvearrowright} + \text{---} \overset{\alpha}{\curvearrowleft} \right), \tag{6.43}$$

and the interpretation of such diagrams is immediate in the framework detailed in the noninteracting case. A horizontal flip of such diagrams also directly provides  $\psi_\alpha$  in case the final point  $\alpha$  is located in the lower branch. Although the interpretation is quite simple, the calculation of those green diagrams requires great care and to introduce more tools. Following the approach of Refs. [61, 90], we represent by a black box



the intermediate site  $\alpha'$ , where the wave interacts with itself nonlinearly through the density  $|\psi_{\alpha'}|^2$ , as is suggested by the mean–field Gross–Pitaevskii equation. We also need a diagrammatic representation of  $\psi_\alpha^*$ , as the density implies a complex conjugation of the wavefunction, which we present below

$$\psi_\alpha^* = -\frac{\sqrt{\mathcal{N}}\kappa(t)}{iE_\delta \sin(k\delta)} \left( \text{---} \overset{\alpha}{\curvearrowright} + \text{---} \overset{\alpha}{\curvearrowleft} \right), \tag{6.44}$$

and where dotted lines, in contrast to solid lines, indicate complex conjugation. As we already stated, the wavefunction at site  $\alpha$  follows a self–consistent equation

$$\psi_\alpha = \sqrt{\mathcal{N}}\kappa(t)G(\alpha, \alpha_S, \mu) + \sum_{\alpha'} G(\alpha, \alpha_S, \mu)g_{\alpha'}|\psi_{\alpha'}|^2\psi_{\alpha'}, \tag{6.45}$$

---

<sup>1</sup>We employ the green colour to differentiate interacting diagrams from noninteracting ones.

which takes the form of a set of four diagrammatic coupled equations that we have to solve. The first one is given by

$$\begin{aligned}
 \text{Diagram 1} = \text{Diagram 2} - ig_{\text{eff}} \left[ \sum_{\text{upper branch}} dx' \left( \text{Diagram 3} + \text{Diagram 4} \right)^2 \left( \text{Diagram 5} + \text{Diagram 6} \right) \right. \\
 \left. \times \left( \theta(\alpha - \alpha') \text{Diagram 7} + \text{Diagram 8} + \text{Diagram 9} \right) \right. \\
 \left. + \sum_{\text{lower branch}} \left( \text{Diagram 10} + \text{Diagram 11} \right)^2 \left( \text{Diagram 12} + \text{Diagram 13} \right) \left( \text{Diagram 14} + \text{Diagram 15} \right) \right].
 \end{aligned}
 \tag{6.46}$$

The second equation is provided by

$$\begin{aligned}
 \text{Diagram 16} = \text{Diagram 17} - ig_{\text{eff}} \left[ \sum_{\text{upper branch}} \left( \text{Diagram 18} + \text{Diagram 19} \right)^2 \left( \text{Diagram 20} + \text{Diagram 21} \right) \right. \\
 \left. \times \left( \theta(\alpha - \alpha') \text{Diagram 22} + \text{Diagram 23} + \text{Diagram 24} \right) \right. \\
 \left. + \sum_{\text{lower branch}} \left( \text{Diagram 25} + \text{Diagram 26} \right)^2 \left( \text{Diagram 27} + \text{Diagram 28} \right) \left( \text{Diagram 29} + \text{Diagram 30} \right) \right].
 \end{aligned}
 \tag{6.47}$$

The third equation reads

$$\begin{aligned}
 \text{Diagram 31} = \text{Diagram 32} - ig_{\text{eff}} \left[ \sum_{\text{upper branch}} dx' \left( \text{Diagram 33} + \text{Diagram 34} \right)^2 \left( \text{Diagram 35} + \text{Diagram 36} \right) \right. \\
 \left. \times \left( \text{Diagram 37} + \text{Diagram 38} \right) \right. \\
 \left. + \sum_{\text{lower branch}} \left( \text{Diagram 39} + \text{Diagram 40} \right)^2 \left( \text{Diagram 41} + \text{Diagram 42} \right) \right. \\
 \left. \times \left( \theta(\alpha - \alpha') \text{Diagram 43} + \text{Diagram 44} + \text{Diagram 45} \right) \right].
 \end{aligned}
 \tag{6.48}$$

The fourth and last equation reads

$$\begin{aligned}
 \text{Diagram} &= \text{Diagram} - ig_{\text{eff}} \left[ \sum_{\text{upper branch}}^{\alpha'} \left( \text{Diagram} + \text{Diagram} \right)^2 \left( \text{Diagram} + \text{Diagram} \right) \left( \text{Diagram} + \text{Diagram} \right) \right. \\
 &\quad + \sum_{\text{lower branch}}^{\alpha'} \left( \text{Diagram} + \text{Diagram} \right)^2 \left( \text{Diagram} + \text{Diagram} \right) \\
 &\quad \left. \times \left( \theta(\alpha - \alpha') \text{Diagram} + \text{Diagram} + \text{Diagram} \right) \right].
 \end{aligned} \tag{6.49}$$

In the four equations above, we have defined

$$g_{\text{eff}} = \frac{g\mathcal{N} |\kappa(t)|^2}{[E_\delta \sin(k\delta)]^3} = \frac{g}{E_\delta} \frac{\rho^\varnothing \delta}{\sin(k\delta)}, \tag{6.50}$$

the effective interaction strength. It depends not only on the true interaction strength  $g$ , but also on the mean density  $\rho^\varnothing$  of particles that are injected in the ring from the source. This is understood in terms of scattering processes that become more likely and more significant in case of a high density of particles. It also finally depends upon the wavevector through the  $1/\sin k\delta \simeq 1/k\delta$  dependence, indicating interaction effects that are more important for small wavevectors. As is usual with self-consistent equations such as Eqs. (6.46), (6.47), (6.48) and (6.49), the insertion of the left-hand-side into the right-hand-side produces a formal power series in the perturbation parameter  $g_{\text{eff}}$ .

In accordance with the noninteracting case, the reflection (resp. transmission) amplitude is obtained by choosing the final site  $\alpha$  in the wavefunction (6.43) either in the left (resp. right) waveguide, which is diagrammatically written as

$$\begin{aligned}
 R^{(\text{coh})} &= \text{Diagram} = \text{Diagram} + \text{Diagram} + \text{Diagram}, \\
 T^{(\text{coh})} &= \text{Diagram} = \text{Diagram} + \text{Diagram}.
 \end{aligned} \tag{6.51}$$

Those expressions can in principle be computed up to the desired order in  $g_{\text{eff}}$  but require for this purpose the exact disorder potential at each visited site to be able to evaluate the phase resulting from the incomplete traversal of one arm of the ring, due to the occurrence of an interaction event within the explored arm.

However, as in the noninteracting case, a large number of diagrams do not survive the disorder averaging and only pairs of diagrams that share the same number of full explorations of branches do. Consequently, only diagrams which, after pairing, show no phase due to an incomplete traversal of an arm have a chance to contribute to disorder averaged quantities. This can be either due to a net extension to a phase corresponding to a full exploration

of an arm or either due to the cancellation by a net phase with an opposite sign resulting from an incomplete traversal in the other direction. This observation allows us to select the interaction events based upon the structure they display. Interaction events displaying the following structure

$$\begin{array}{c} \leftarrow \leftarrow \leftarrow \blacksquare \leftarrow \\ \leftarrow \leftarrow \leftarrow \blacksquare \leftarrow \end{array}, \quad (6.52)$$

as well as similar structures obtained by symmetry operations around the horizontal and vertical axes or complex conjugation, produce only phases resulting from total explorations of branches. Indeed, an arrow is paired with its complex conjugate  $\rightleftarrows$ , thereby cancelling the phase produced by each other, whilst the two arrows left  $\rightarrow \blacksquare \rightarrow$  add their phase up, to produce a global phase that results from full traversals of branches, consequently removing the  $\alpha'$  dependence. On the contrary, structures like the following

$$\begin{array}{c} \leftarrow \leftarrow \leftarrow \blacksquare \leftarrow \\ \leftarrow \leftarrow \leftarrow \blacksquare \leftarrow \end{array}, \quad (6.53)$$

as well as similar structures obtained by symmetry operations around the horizontal and vertical axes or complex conjugation, produce a phase, resulting from a partial exploration of branches, because the arrows implied in such structures do not cancel or extend each other. As such, structures appearing in (6.53) and those obtained by symmetry or complex conjugation, produce a non-compensated phase that will be responsible for the damp out in the averaging process.

This observation allows us to exclude interaction events that display a structure depicted in (6.53) or similar ones, not that they do not contribute to individual realisations of the reflection and transmission amplitudes (which we are not interested in), but they vanish when computing the disorder averaged reflection and transmission probabilities. Keeping only structures depicted in (6.52) is achieved by introducing a new wavefunction, which differs from the true wavefunction appearing in Eq. (6.43) in the extent that scattering paths involving structures which we excluded are not considered. This amounts to redefining the diagrams by explicitly excluding forbidden paths. Such a definition, of course, will not yield the true wavefunction for an individual disorder realisation but produces the same results when transport quantities are averaged over a large number of disorder realisations. Such a substitution amounts to replacing Eq. (6.46) by

$$\begin{aligned} \text{---} \bullet \xrightarrow{\alpha} \bullet \text{---} &= \text{---} \bullet \xrightarrow{\alpha} \bullet \text{---} - ig_{\text{eff}} \left\{ \sum_{\substack{\alpha' \\ \text{upper} \\ \text{branch}}} \left[ \text{---} \bullet \xrightarrow{\alpha'} \bullet \left( \text{---} \bullet \xrightarrow{\alpha'} \blacksquare \xrightarrow{\alpha'} \bullet + 2\theta(\alpha - \alpha') \text{---} \bullet \xrightarrow{\alpha'} \blacksquare \xrightarrow{\alpha'} \bullet + 2 \text{---} \bullet \xrightarrow{\alpha'} \blacksquare \xrightarrow{\alpha'} \bullet \right) \right. \right. \\ &+ \left. \text{---} \bullet \xrightarrow{\alpha'} \bullet \left( 2 \text{---} \bullet \xrightarrow{\alpha'} \blacksquare \xrightarrow{\alpha'} \bullet + \theta(\alpha - \alpha') \text{---} \bullet \xrightarrow{\alpha'} \blacksquare \xrightarrow{\alpha'} \bullet + \text{---} \bullet \xrightarrow{\alpha'} \blacksquare \xrightarrow{\alpha'} \bullet \right) \right] \\ &+ \sum_{\substack{\alpha' \\ \text{lower} \\ \text{branch}}} \left[ \text{---} \bullet \xrightarrow{\alpha'} \bullet \left( \text{---} \bullet \xrightarrow{\alpha'} \blacksquare \xrightarrow{\alpha'} \bullet + 2 \text{---} \bullet \xrightarrow{\alpha'} \blacksquare \xrightarrow{\alpha'} \bullet \right) \right. \\ &\left. \left. + \text{---} \bullet \xrightarrow{\alpha'} \bullet \left( 2 \text{---} \bullet \xrightarrow{\alpha'} \blacksquare \xrightarrow{\alpha'} \bullet + \text{---} \bullet \xrightarrow{\alpha'} \blacksquare \xrightarrow{\alpha'} \bullet \right) \right] \right\}, \quad (6.54) \end{aligned}$$

where the presence of the factor 2 in the above expression results from the square that appears in Eq. (6.46) and expresses the two possibilities one has when one wants to build such a diagram from the diagram at disposal in Eq. (6.46). A more compact version of (6.54) is found and reads

$$\begin{aligned}
 \text{Diagram 1} &= \text{Diagram 2} - ig_{\text{eff}} \left\{ \sum_{\text{upper branch}} \left[ \text{Diagram 3} \right] \begin{bmatrix} 1 & 2 \\ 2 & 1 \end{bmatrix} \left[ \theta(\alpha - \alpha') \text{Diagram 4} + \text{Diagram 5} \right] \right. \\
 &\quad \left. + \sum_{\text{lower branch}} \left[ \text{Diagram 6} \right] \begin{bmatrix} 1 & 2 \\ 2 & 1 \end{bmatrix} \left[ \text{Diagram 7} \right] \right\}
 \end{aligned} \tag{6.55}$$

as well as for the second interacting diagrams

$$\begin{aligned}
 \text{Diagram 8} &= \text{Diagram 9} - ig_{\text{eff}} \left\{ \sum_{\text{upper branch}} \left[ \text{Diagram 10} \right] \begin{bmatrix} 1 & 2 \\ 2 & 1 \end{bmatrix} \left[ \theta(\alpha - \alpha') \text{Diagram 11} + \text{Diagram 12} \right] \right. \\
 &\quad \left. + \sum_{\text{lower branch}} \left[ \text{Diagram 13} \right] \begin{bmatrix} 1 & 2 \\ 2 & 1 \end{bmatrix} \left[ \text{Diagram 14} \right] \right\},
 \end{aligned} \tag{6.56}$$

but also the third

$$\begin{aligned}
 \text{Diagram 15} &= \text{Diagram 16} - ig_{\text{eff}} \left\{ \sum_{\text{upper branch}} \left[ \text{Diagram 17} \right] \begin{bmatrix} 1 & 2 \\ 2 & 1 \end{bmatrix} \left[ \text{Diagram 18} \right] \right. \\
 &\quad \left. + \sum_{\text{lower branch}} \left[ \text{Diagram 19} \right] \begin{bmatrix} 1 & 2 \\ 2 & 1 \end{bmatrix} \left[ \theta(\alpha - \alpha') \text{Diagram 20} + \text{Diagram 21} \right] \right\},
 \end{aligned} \tag{6.57}$$

and finally the fourth and last diagram

$$\begin{aligned}
 \text{Diagram 22} &= \text{Diagram 23} - ig_{\text{eff}} \left\{ \sum_{\text{upper branch}} \left[ \text{Diagram 24} \right] \begin{bmatrix} 1 & 2 \\ 2 & 1 \end{bmatrix} \left[ \text{Diagram 25} \right] \right. \\
 &\quad \left. + \sum_{\text{lower branch}} \left[ \text{Diagram 26} \right] \begin{bmatrix} 1 & 2 \\ 2 & 1 \end{bmatrix} \left[ \theta(\alpha - \alpha') \text{Diagram 27} + \text{Diagram 28} \right] \right\}.
 \end{aligned} \tag{6.58}$$

Finally, with the help of those resummed diagrams, we are in a position to formulate the effective reflection amplitude as

$$\begin{aligned}
R^{(\text{coh, eff})}(\Phi_u, \Phi_d, \Phi) &= \text{diagram 1} + \text{diagram 2} \\
&= \text{diagram 3} + \text{diagram 4} \\
&\quad - ig_{\text{eff}} \sum_{\alpha'}^{\text{upper branch}} \left[ \text{diagram 5} \right] \begin{bmatrix} 1 & 2 \\ 2 & 1 \end{bmatrix} \left[ \text{diagram 6} \right] \\
&\quad - ig_{\text{eff}} \sum_{\alpha'}^{\text{lower branch}} \left[ \text{diagram 7} \right] \begin{bmatrix} 1 & 2 \\ 2 & 1 \end{bmatrix} \left[ \text{diagram 8} \right], \tag{6.59}
\end{aligned}$$

and the effective transmission amplitude as

$$\begin{aligned}
T^{(\text{coh, eff})}(\Phi_u, \Phi_d, \Phi) &= \text{diagram 9} + \text{diagram 10} \\
&= \text{diagram 11} + \text{diagram 12} \\
&\quad - ig_{\text{eff}} \sum_{\alpha'}^{\text{upper branch}} \left[ \text{diagram 13} \right] \begin{bmatrix} 1 & 2 \\ 2 & 1 \end{bmatrix} \left[ \text{diagram 14} \right] \\
&\quad - ig_{\text{eff}} \sum_{\alpha'}^{\text{lower branch}} \left[ \text{diagram 15} \right] \begin{bmatrix} 1 & 2 \\ 2 & 1 \end{bmatrix} \left[ \text{diagram 16} \right]. \tag{6.60}
\end{aligned}$$

Whilst the above expressions in Eqs. (6.59) and (6.60) theoretically permit to compute the exact ensemble averaged reflection and transmission probabilities, we restrict in the following to a first-order, linear, correction in the effective interaction  $g_{\text{eff}}$ .

### 6.3.1 First-order correction to the noninteracting reflection and transmission amplitudes

The first-order correction is simply obtained by replacing each interacting resummed diagram by its noninteracting counterpart, which amounts to replacing the green parts by equivalent red parts, followed by a partial traversal of the arm, in Eqs. (6.59) and (6.60). In this approximation, the  $\alpha'$  dependence in the summations carried out in Eqs. (6.59) and (6.60) vanishes, the sum is performed immediately and simply yields an additional  $N_R/2$  factor. In the case of reflection, the diagrammatic correction in the first-order to the noninteracting

reflection amplitude is obtained as

$$\begin{aligned}
 \Delta R^{(1)}(\Phi_u, \Phi_d, \Phi) &= R^{(\text{coh}, \text{eff}, 1)}(\Phi_u, \Phi_d, \Phi) - R^{(0)}(\Phi_u, \Phi_d, \Phi) \\
 &= -ig_{\text{eff}} \frac{N_R}{2} \left[ \left[ \text{Diagram 1} \right] \begin{bmatrix} 1 & 2 \\ 2 & 1 \end{bmatrix} \left[ \text{Diagram 2} \right] \right. \\
 &\quad \left. + \left[ \text{Diagram 3} \right] \begin{bmatrix} 1 & 2 \\ 2 & 1 \end{bmatrix} \left[ \text{Diagram 4} \right] \right]. \quad (6.61)
 \end{aligned}$$

We once again want to stress that this correction is meaningless and useless on its own, since some diagrams have been arbitrarily excluded. It is only when averaged over  $\Phi_u$  and  $\Phi_d$  that this correction makes sense, in the context of the first-order approximation. Eq. (6.61) shows that the linear correction to the ensemble averaged probability of reflection is obtained due to the set of scattering paths that penetrate the ring and interact at some point in one of the arms with the density  $|\psi|^2$  (which is diagrammatically represented by paired diagrams of a path depicted in solid lines and combined with its complex conjugate in dashed lines). After this interaction event took place, those paths continue their traversal of the arm to reach the opposite junction and the ring is finally exited back to the incident lead.

The first-order correction to the transmission is obtained similarly, that is, by replacing each interacting resummed diagram by its noninteracting counterpart, which once again amounts to replacing green parts of the diagrams by a red resummed diagram followed by the partial exploration of the arm. The  $\alpha'$  dependence also disappears in the summations carried out in Eqs. (6.59) and (6.60) which only leaves a  $N_R/2$  factor. The correction in the first-order to the noninteracting transmission amplitude is diagrammatically written as

$$\begin{aligned}
 \Delta T^{(1)}(\Phi_u, \Phi_d, \Phi) &= T^{(\text{coh}, \text{eff}, 1)}(\Phi_u, \Phi_d, \Phi) - T^{(0)}(\Phi_u, \Phi_d, \Phi) \\
 &= -ig_{\text{eff}} \frac{N_R}{2} \left[ \left[ \text{Diagram 1} \right] \begin{bmatrix} 1 & 2 \\ 2 & 1 \end{bmatrix} \left[ \text{Diagram 2} \right] \right. \\
 &\quad \left. + \left[ \text{Diagram 3} \right] \begin{bmatrix} 1 & 2 \\ 2 & 1 \end{bmatrix} \left[ \text{Diagram 4} \right] \right]. \quad (6.62)
 \end{aligned}$$

The physical interpretation is almost identical compared to that of the reflection. The correction is indeed obtained due to the set of scattering paths that penetrate the ring, interact with the density  $|\psi|^2$  at some point in one of the branches, pursue their exploration of the arm to the opposite junction and exit the ring by the downstream lead. An analytical formula for Eqs. (6.61) and (6.62) can be found by replacing the diagrams by their analytical counterpart but is rather cumbersome. Since it brings no added value to the discussion, we do not provide this lengthy expression.



### 6.3.2 Ensemble average of the reflection and transmission probabilities

The ensemble average is performed exactly as in the noninteracting case, which in the case of reflection provides

$$\begin{aligned} \langle |R(\Phi)|^2 \rangle &= \frac{1}{4\pi^2} \int_0^{2\pi} \int_0^{2\pi} |R(\Phi_u, \Phi_d, \Phi)|^2 d\Phi_u d\Phi_d \\ &= \frac{1}{4\pi^2} \int_0^{2\pi} \int_0^{2\pi} |R^{(0)}(\Phi_u, \Phi_d, \Phi) + \Delta R^{(1)}(\Phi_u, \Phi_d, \Phi) + \mathcal{O}(g^2)|^2 d\Phi_u d\Phi_d \\ &= \langle |R^{(0)}(\Phi)|^2 \rangle + \Delta \langle |R^{(1)}(\Phi)|^2 \rangle + \mathcal{O}(g^2), \end{aligned} \quad (6.63)$$

with

$$\langle |R^{(0)}(\Phi)|^2 \rangle = \frac{1}{4\pi^2} \int_0^{2\pi} \int_0^{2\pi} |R^{(0)}(\Phi_u, \Phi_d, \Phi)|^2 d\Phi_u d\Phi_d. \quad (6.64)$$

The first-order correction to the ensemble averaged reflection is found to be

$$\Delta \langle |R^{(1)}(\Phi)|^2 \rangle = \frac{1}{4\pi^2} \int_0^{2\pi} \int_0^{2\pi} 2\text{Re} \left[ R^{(0)*}(\Phi_u, \Phi_d, \Phi) \Delta R^{(1)}(\Phi_u, \Phi_d, \Phi) \right] d\Phi_u d\Phi_d. \quad (6.65)$$

This is once again best written and understood under diagrammatical form

$$\begin{aligned} \Delta \langle |R^{(1)}(\Phi)|^2 \rangle &= \frac{g_{\text{eff}} N_R}{4\pi^2} \int_0^{2\pi} \int_0^{2\pi} \text{Im} \left\{ \left( \begin{array}{c} \text{---} \bullet \text{---} \\ \text{---} \bullet \text{---} \\ \text{---} \bullet \text{---} \end{array} + \begin{array}{c} \text{---} \bullet \text{---} \\ \text{---} \bullet \text{---} \\ \text{---} \bullet \text{---} \end{array} + \begin{array}{c} \text{---} \bullet \text{---} \\ \text{---} \bullet \text{---} \\ \text{---} \bullet \text{---} \end{array} \right) \\ &\quad \left[ \begin{array}{c} \text{---} \bullet \text{---} \\ \text{---} \bullet \text{---} \\ \text{---} \bullet \text{---} \end{array} \right] \begin{bmatrix} 1 & 2 \\ 2 & 1 \end{bmatrix} \left[ \begin{array}{c} \text{---} \bullet \text{---} \\ \text{---} \bullet \text{---} \\ \text{---} \bullet \text{---} \end{array} \right] \\ &\quad + \left[ \begin{array}{c} \text{---} \bullet \text{---} \\ \text{---} \bullet \text{---} \\ \text{---} \bullet \text{---} \end{array} \right] \begin{bmatrix} 1 & 2 \\ 2 & 1 \end{bmatrix} \left[ \begin{array}{c} \text{---} \bullet \text{---} \\ \text{---} \bullet \text{---} \\ \text{---} \bullet \text{---} \end{array} \right] \right\} d\Phi_u d\Phi_d. \end{aligned} \quad (6.66)$$

Also, we note the following identity

$$\begin{aligned} &\int_0^{2\pi} \int_0^{2\pi} \left( \begin{array}{c} \text{---} \bullet \text{---} \\ \text{---} \bullet \text{---} \\ \text{---} \bullet \text{---} \end{array} + \begin{array}{c} \text{---} \bullet \text{---} \\ \text{---} \bullet \text{---} \\ \text{---} \bullet \text{---} \end{array} + \begin{array}{c} \text{---} \bullet \text{---} \\ \text{---} \bullet \text{---} \\ \text{---} \bullet \text{---} \end{array} \right) \left[ \begin{array}{c} \text{---} \bullet \text{---} \\ \text{---} \bullet \text{---} \\ \text{---} \bullet \text{---} \end{array} \right] \begin{bmatrix} 1 & 2 \\ 2 & 1 \end{bmatrix} \left[ \begin{array}{c} \text{---} \bullet \text{---} \\ \text{---} \bullet \text{---} \\ \text{---} \bullet \text{---} \end{array} \right] d\Phi_u d\Phi_d \\ &= \int_0^{2\pi} \int_0^{2\pi} \left( \begin{array}{c} \text{---} \bullet \text{---} \\ \text{---} \bullet \text{---} \\ \text{---} \bullet \text{---} \end{array} + \begin{array}{c} \text{---} \bullet \text{---} \\ \text{---} \bullet \text{---} \\ \text{---} \bullet \text{---} \end{array} + \begin{array}{c} \text{---} \bullet \text{---} \\ \text{---} \bullet \text{---} \\ \text{---} \bullet \text{---} \end{array} \right) \left[ \begin{array}{c} \text{---} \bullet \text{---} \\ \text{---} \bullet \text{---} \\ \text{---} \bullet \text{---} \end{array} \right] \begin{bmatrix} 1 & 2 \\ 2 & 1 \end{bmatrix} \left[ \begin{array}{c} \text{---} \bullet \text{---} \\ \text{---} \bullet \text{---} \\ \text{---} \bullet \text{---} \end{array} \right] d\Phi_u d\Phi_d \\ &= \int_0^{2\pi} \int_0^{2\pi} \left( \begin{array}{c} \text{---} \bullet \text{---} \\ \text{---} \bullet \text{---} \\ \text{---} \bullet \text{---} \end{array} + \begin{array}{c} \text{---} \bullet \text{---} \\ \text{---} \bullet \text{---} \\ \text{---} \bullet \text{---} \end{array} + \begin{array}{c} \text{---} \bullet \text{---} \\ \text{---} \bullet \text{---} \\ \text{---} \bullet \text{---} \end{array} \right) \left[ \begin{array}{c} \text{---} \bullet \text{---} \\ \text{---} \bullet \text{---} \\ \text{---} \bullet \text{---} \end{array} \right] \begin{bmatrix} 1 & 2 \\ 2 & 1 \end{bmatrix} \left[ \begin{array}{c} \text{---} \bullet \text{---} \\ \text{---} \bullet \text{---} \\ \text{---} \bullet \text{---} \end{array} \right] d\Phi_u d\Phi_d, \end{aligned} \quad (6.67)$$

that results from the symmetry that exists when one flips a diagram around the horizontal axis, which simply amounts to swapping  $\Phi_u$  and  $\Phi_d$ . Eq. (6.67) is used to bring Eq. (6.65)

under a more compact and concise form

$$\Delta \left\langle \left| R^{(1)}(\Phi) \right|^2 \right\rangle = \frac{g_{\text{eff}} N_R}{4\pi^2} \int_0^{2\pi} \int_0^{2\pi} \text{Im} \left\{ \left( \begin{array}{c} \text{---} \bullet \text{---} + \text{---} \bullet \text{---} + \text{---} \bullet \text{---} \\ \text{---} \bullet \text{---} + \text{---} \bullet \text{---} + \text{---} \bullet \text{---} \end{array} \right) \right. \\ \left. \left[ \begin{array}{c} \text{---} \bullet \text{---} + \text{---} \bullet \text{---} \\ \text{---} \bullet \text{---} + \text{---} \bullet \text{---} \end{array} \right] \right. \\ \left. \left[ \begin{array}{c} 1 & 2 \\ 2 & 1 \end{array} \right] \left[ \begin{array}{c} \text{---} \bullet \text{---} \\ \text{---} \bullet \text{---} \end{array} \right] \right] \left. \right\} d\Phi_u d\Phi_d. \quad (6.68)$$

A very similar result is obtained for the first-order correction to the transmission probability and is diagrammatically written as

$$\Delta \left\langle \left| T^{(1)}(\Phi) \right|^2 \right\rangle = \frac{g_{\text{eff}} N_R}{4\pi^2} \int_0^{2\pi} \int_0^{2\pi} \text{Im} \left\{ \left( \begin{array}{c} \text{---} \bullet \text{---} + \text{---} \bullet \text{---} \\ \text{---} \bullet \text{---} + \text{---} \bullet \text{---} \end{array} \right) \right. \\ \left[ \begin{array}{c} \text{---} \bullet \text{---} + \text{---} \bullet \text{---} \\ \text{---} \bullet \text{---} + \text{---} \bullet \text{---} \end{array} \right] \left[ \begin{array}{c} 1 & 2 \\ 2 & 1 \end{array} \right] \left[ \begin{array}{c} \text{---} \bullet \text{---} \\ \text{---} \bullet \text{---} \end{array} \right] \\ \left. + \left[ \begin{array}{c} \text{---} \bullet \text{---} + \text{---} \bullet \text{---} \\ \text{---} \bullet \text{---} + \text{---} \bullet \text{---} \end{array} \right] \left[ \begin{array}{c} 1 & 2 \\ 2 & 1 \end{array} \right] \left[ \begin{array}{c} \text{---} \bullet \text{---} \\ \text{---} \bullet \text{---} \end{array} \right] \right\} d\Phi_u d\Phi_d. \quad (6.69)$$

Those expressions are numerically integrated and compared with our numerical findings of Chapter 5.

## 6.4 Confrontation of the diagrammatic theory to the numerical results

In this section, we confront the results obtained by the numerical integration of the equations related to mean-field and truncated Wigner simulations to the diagrammatic predictions. That comparison is shown in FIG. 6.1. An excellent, almost perfect, agreement is found between the mean-field results and the diagrammatic predictions in the absence of interaction: both approaches benchmark each other.

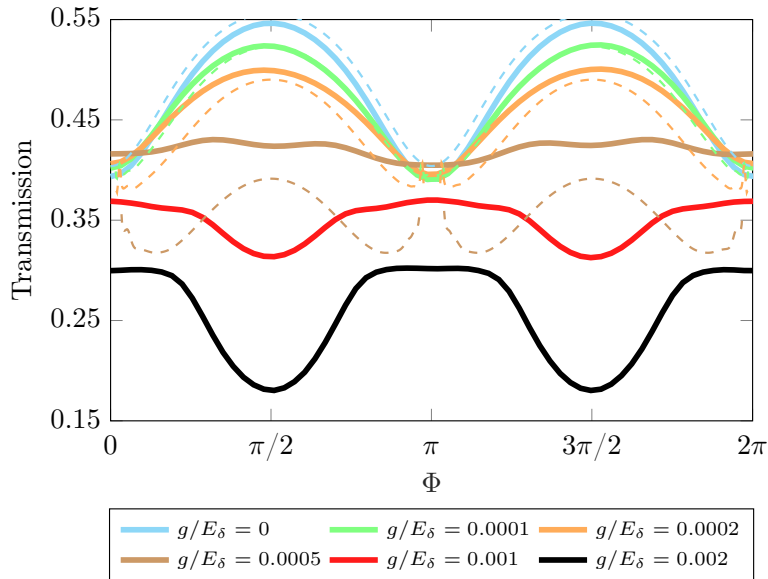


Figure 6.1 – Mean–field simulations of the ensemble averaged transmission versus the enclosed artificial flux  $\Phi$  in the presence of interaction for  $\mathcal{N}|\kappa|^2 = E_\delta^2 \Leftrightarrow \langle \hat{a}^\dagger \hat{a} \rangle \simeq 2.77$ . The transmission is averaged over 20000 realisations of a Gaussian correlated disorder taking random values in  $[-0.0119, 0.0119]$  with correlation length  $\sigma = 20\delta$ . Diagrammatic theory predictions are represented in dashed lines of the same colour as the corresponding mean–field simulation. Diagrammatic predictions at  $\Phi = 0, \pi$  and  $2\pi$  are excluded owing to the presence of divergences. Numerical parameters:  $\mu/E_\delta = 0.2$  and  $N_R = 200$  sites.

In the presence of interaction, a good qualitative and quantitative agreement is first found, for weak values of the interaction strength, that is for  $g$  such that  $g/E_\delta \lesssim 0.0002$ . For larger values of the interaction strength however, significant deviations are encountered. This is not surprising since, as FIG. 6.2 indicates, the inversion shows a nonlinear dependence in the interaction strength. Those deviations indicate that our first–order diagrammatic model underfits the inversion, as quadratic and higher order corrections become more and more prominent at higher interaction strength.

Not shown in FIG. 6.1 are numerical divergences at  $\Phi = 0, \pi$  and  $2\pi$  that arise in the Monte–Carlo method that we use to numerically perform the disorder average of the transmission. A possible explanation for the origin of those divergences could be inferred from the determinant (6.13) that vanishes for  $\Phi = 0, \pi$  and  $2\pi$  when  $\Phi_u \simeq \Phi_d$ , which is not accompanied by a concomitant drop out of the numerator [356].

Away from those particular values of the gauge flux  $\Phi$ , the Monte–Carlo integration fortunately converges. FIG. 6.2 is dedicated to the study of the ensemble averaged transmission probability as a function of the interaction strength  $g$  for  $\Phi = \pi/2$  and serves as a comparison of the diagrammatic results with the numerical ones.

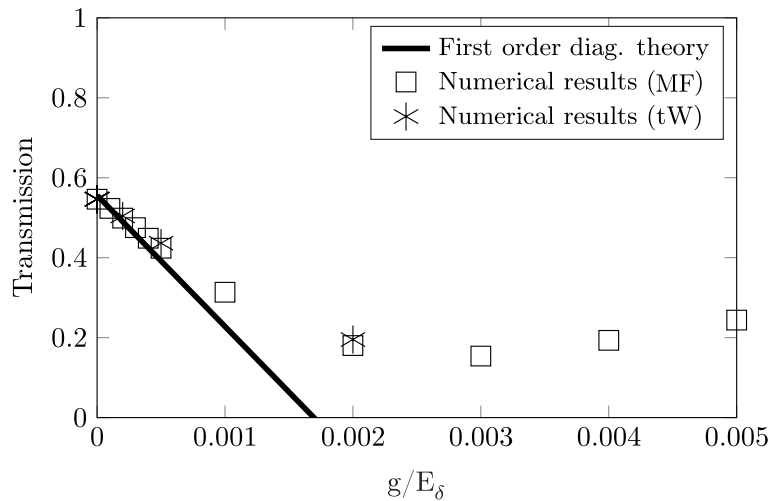


Figure 6.2 – Comparison between the numerical, mean–field and truncated Wigner, ensemble averaged transmission at  $\Phi = \pi/2$  and the first–order diagrammatic theory predictions. The transmission is averaged over 20000 realisations of a Gaussian correlated disorder taking random values in  $[-0.0119, 0.0119]$  with correlation length  $\sigma = 20\delta$ . Good agreement is found for weak interaction strength where the transmission decreases approximately linearly with  $g$ . Numerical parameters:  $\mu/E_\delta = 0.2$  and  $N_R = 200$  sites.

As expected from a first–order perturbative theory, a linear transmission is found, with negative slope. An excellent agreement between diagrammatic and numerical results is encountered for weak interaction strengths, as was already highlighted. However, the slope of the linear predictions from the diagrammatic theory is steeper than the slope of the numerical results, highlighting that the diagrammatic theory seems to (slightly) overestimate interaction effects in that regime of parameters.

The disagreement between the curves is probably due to a lack of the diagrammatic theory itself, as higher order terms might correct this overestimation and are clearly missing for high interaction strengths. Indeed, for higher interaction strengths, the significant deviations already observed in FIG. 6.1 are also present. The parabolic–like shape of the mean–field results seems to indicate that quadratic corrections to the ensemble averaged transmission would describe the inversion much more accurately. Whilst it is almost certain that quadratic corrections would yield better predictions, it might be that higher order terms are nevertheless also required because FIG. 6.2 is drawn for  $\Phi = \pi/2$  only.

We also note that in the formulation of the diagrammatic theory, the junction energies have been treated as constant, whereas they are also subject to the disorder potential. This dependence in the disorder potential is not accounted for in the theory, and the reflection and transmission probability amplitudes at a junction,  $r$  and  $t$ , should acquire a dependence in the specific disorder landscape. This dependence could possibly soften the slope of the linear decrease of the transmission, but also fill the slight gap that exists in FIG. 6.1 in the absence of interaction.



where we use the following values

$$\begin{aligned} r &= -\frac{43}{97} + \frac{24}{97}i \\ t &= \frac{54}{97} + \frac{24}{97}i, \end{aligned} \tag{6.72}$$

in accordance with the values used in the numerical simulations. Eq. (6.71) indicates an expected increase in the reflection probability for  $\Phi = \pi/2$  and a corresponding drop in the transmission probability [356]. We also note that Eq. (6.71) sort of a posteriori justifies our choice of a weakly connected ring yielding expressions for  $r$  and  $t$  in Eq. (6.72), because the real-valued expressions for  $r$  and  $t$  that would result from a fully connected ring obviously bring no contribution in Eq. (6.70).

## Chapter 7

# Inversion of coherent backscattering with interacting ultracold bosons: a truncated Wigner approach

The recent observation of coherent backscattering with Bose–Einstein condensates in the momentum space by the group of A. Aspect in Palaiseau [57] as well in the laboratory of G. Labeyrie in Nice [58] in the absence of interaction raises some questions related to the effects of such atom–atom interaction which are most naturally present within Bose–Einstein condensates. To shed more light on this issue, we propose to study coherent backscattering in the presence of atom–atom interaction in the idealised framework of a plane wave propagation towards a two–dimensional disordered slab instead of a wavepacket of finite extent [57, 58]. Atom lasers appear in this context as the ideal candidate to produce such plane waves of matter that allow us to put aside additional complexity, for instance related to the width of the wavepacket, which would result in more complicated scattering processes (for instance due to the superposition of the various energy components).

In this chapter, we begin by describing the two–dimensional scattering geometry we study and formulate the many–body model we use in this context. This many–body model is discretised and the resulting discretised equations are then numerically integrated in the mean–field approximation. A number of length scales related to transport processes that naturally emerge in this context are then discussed, as well as the occurrence of coherent backscattering in the momentum space. The effect of an atom–atom interaction in the mean–field approximation is then investigated. We find that the coherent backscattering peak is inverted in the presence of non–vanishing interaction, which indicates a crossover from constructive to destructive interferences around the backward direction. Truncated Wigner simulations that allow to go beyond the mean–field limit and to model inelastic scattering processes indicate that a dephasing of interference effects is expected far beyond the mean–field limit. However, those simulations also predict that for realistic experimental atomic and waveguide parameters, the antilocalisation scenario appearing in the mean–field approximation prevails, despite a partial dephasing.

## 7.1 Description of the scattering geometry

We study the coherent transport of a Bose–Einstein condensate which contains  $\mathcal{N} \rightarrow \infty$  particles and which is maintained at the temperature  $T = 0$  and the chemical potential  $\mu$ . This Bose–Einstein condensate propagates towards a two–dimensional disorder potential which can be, in the case of ultracold atoms, created by optical speckle fields [357–360]. The restriction to a planar motion can be experimentally realised by superposing two counter-propagating lasers to form a standing wave from which results a one–dimensional optical lattice, as is sketched on FIG. 7.1. The particles injected towards this lattice are squeezed in a stack of two–dimensional layers, leading to quasi two–dimensional motion between two adjacent layers of the lattice. At this location, an effective quasi two–dimensional waveguide of transverse extension  $a_{\perp}(x) = \sqrt{\hbar/m\omega_{\perp}(x)}$  is formed, where  $\hbar = h/2\pi$  is the reduced Planck constant,  $m$  is the mass of the injected atoms and  $\omega_{\perp}(x)$  is the angular frequency of the trap that produces the confinement. The transverse extension  $a_{\perp}(x)$  is called the oscillator length and is related to the transverse confinement whose longitudinal profile it characterises.

The situation under study is sketched in FIG. 7.1, where a condensate is outcoupled from a reservoir and injected in a quasi 2D effective waveguide, similarly to the principle of an atom laser [202, 212–214, 361–363].

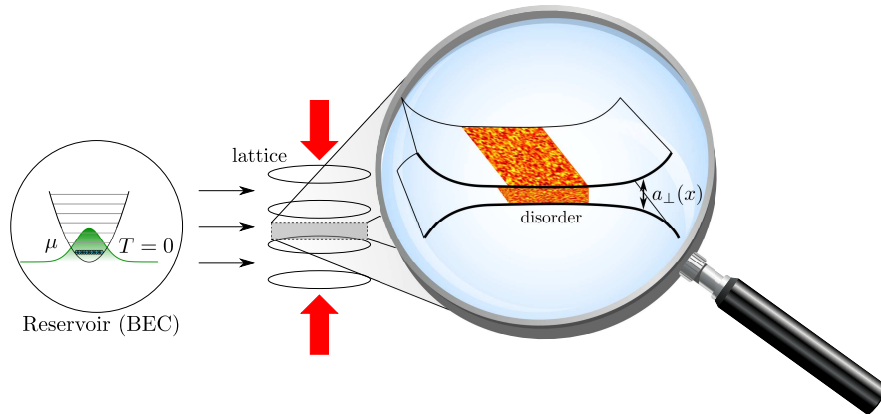


Figure 7.1 – A Bose–Einstein condensate maintained at the temperature  $T = 0$  and the chemical potential  $\mu$  is injected into a quasi two–dimensional waveguide of transverse extension  $a_{\perp}(x) = \sqrt{\hbar/m\omega_{\perp}(x)}$  realised between two adjacent layers of a 1D optical lattice within which it encounters a disorder potential.

To describe this quantum transport problem, we use a many–body model consisting in evolution equations for the field operator  $\hat{\psi}(\mathbf{r}, t)$  of the bosonic particles in the scattering region, where  $\mathbf{r} \equiv (x, y)$  is the spatial position, and for the particle annihilation operator of the



source  $\hat{\phi}_S(t)$ . These evolution equations are yielded as [215, 326]

$$i\hbar \frac{\partial \hat{\psi}(\mathbf{r}, t)}{\partial t} = \left( -\frac{\hbar^2}{2m} \Delta + V(\mathbf{r}) \right) \hat{\psi}(\mathbf{r}, t) + \tilde{g}(\mathbf{r}) \hat{\psi}^\dagger(\mathbf{r}, t) \hat{\psi}(\mathbf{r}, t) \hat{\psi}(\mathbf{r}, t) + K(\mathbf{r}, t) \hat{\phi}_S(0) e^{-i\mu t/\hbar} \hat{\phi}_S(t) \quad (7.1)$$

$$i\hbar \frac{\partial \hat{\phi}_S(t)}{\partial t} = \mu \hat{\phi}_S(t) + \int d\mathbf{r} K^*(\mathbf{r}, t) \hat{\psi}(\mathbf{r}, t), \quad (7.2)$$

with  $V(\mathbf{r})$  the disorder potential and  $K(\mathbf{r}, t)$  the position-dependent coupling strength that describes the outcoupling process of atoms issued from the reservoir and injected towards the scattering region. In Eqs. (7.2), we have introduced the 2D effective interaction strength  $\tilde{g}(\mathbf{r})$ . In the presence of a two-dimensional confinement whose transverse extension is given by the position dependent oscillator length  $a_\perp(x)$ , it is yielded as  $\tilde{g}(\mathbf{r}) \equiv \hbar^2 g(x)/m$ , with the 2D effective dimensionless interaction strength

$$g(x) = 2\sqrt{2} \frac{a_S}{a_\perp(x)}, \quad (7.3)$$

and  $a_S$  the s-wave scattering length of the particles. Owing to the spatial profile of the confinement potential, the dimensionless interaction strength possesses a spatial dependence that is encoded in the oscillator length  $a_\perp(x)$ . In accordance with the profile sketched in the zoom in FIG. 7.1, we model the dimensionless interaction strength as a constant equal to  $g_{\max}$  along the longitudinal extension of the disorder. It is smoothly and adiabatically ramped on from zero at position  $x_{L_b}$  to a finite value  $g_{\max}$  at position  $x_{L_e} = x_{L_b} + \Delta x$  and then ramped off from  $g_{\max}$  at position  $x_{R_b}$  to zero at position  $x_{R_e} = x_{R_b} + \Delta x$ , as is depicted in FIG. 7.2.

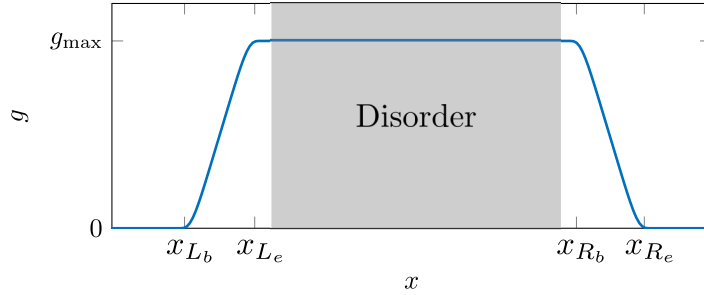


Figure 7.2 – Spatial profile of the dimensionless interaction strength  $g(x)$  along the  $x$ -direction. It is smoothly and adiabatically ramped on from zero at position  $x_{L_b}$  to a finite value  $g_{\max}$  at position  $x_{L_e} = x_{L_b} + \Delta x$  and then ramped off from  $g_{\max}$  at position  $x_{R_b}$  to zero at position  $x_{R_e} = x_{R_b} + \Delta x$  following the smooth switching function profile for the ramps.

An obvious choice for the interaction is obtained as a subtraction of spatially shifted hyperbolic tangents. The drawback with such a profile is that the interaction never reaches perfectly 0 far away from the disordered region nor reaches  $g_{\max}$  within. To circumvent this major disadvantage and to ramp the interaction strength as smoothly as possible, we use Hartmann's smooth switching function [364] for the ramps and we set the interaction

strength to a constant between the ramps. It is analytically yielded as

$$g(x) = g_{\max} \begin{cases} 0 & \text{for } x \leq x_{L_b} \\ f\left(\frac{x-x_{L_e}}{x_{L_b}-x_{L_e}}\right) & \text{for } x_{L_b} < x \leq x_{L_e} \\ 1 & \text{for } x_{L_e} < x \leq x_{R_b} \\ f\left(\frac{x-x_{R_b}}{x_{R_e}-x_{R_b}}\right) & \text{for } x_{R_b} < x \leq x_{R_e} \\ 0 & \text{for } x_{R_e} < x \end{cases}, \quad (7.4)$$

where we have used the function  $f : [0, 1] \rightarrow \mathbb{R}$  which is defined as

$$f(x) = \frac{t(x)}{t(x-1) + t(x)}, \quad (7.5)$$

with the test function

$$t(x) = \begin{cases} \exp\left[-b\left(ax^2 + \frac{1}{1-x^2}\right)\right] & \text{for } |x| < 1 \\ 0 & \text{for } |x| \geq 1 \end{cases}, \quad (7.6)$$

where  $a = 0.557747$  and  $b = 1.364054$  are numerical parameters optimised by Hartmann [364] so that  $t(x)$  is as smooth as possible.

The injection of a monochromatic and coherent (in contrast to a finite-width wavepacket that would display a certain energy spectrum) beam of particles is described by the idealised Ansatz of a strongly localised coupling

$$K(\mathbf{r}, t) = \kappa(t)\delta(x - x_S)\phi(y), \quad (7.7)$$

that acts as a point-like source of particles with wavenumber  $k = \sqrt{2m\mu}/\hbar$ , localised at position  $x_S$  with a temporal profile specified by  $\kappa(t)$  and transverse profile  $\phi(y) = 1$ . We assume this profile to be homogeneous, unless explicit mention of the contrary. In order to prevent the possible advent of dynamical instabilities during the propagation and to favour numerical convergence towards a stationary scattering state, the coupling intensity  $\kappa(t)$  is smoothly and adiabatically ramped from zero to a constant value  $\kappa_{\max}$  following Hartmann's smooth switching function [364]. It is analytically explicitly provided by

$$\kappa(t) = \kappa_{\max} \begin{cases} 0 & \text{for } t \leq 0 \\ f\left(\frac{t_s - t}{t_s}\right) & \text{for } 0 < t \leq t_s \\ 1 & \text{for } t_s < t \end{cases}, \quad (7.8)$$

with the function  $f$  defined in Eq. (7.5) and  $t_s$  is the switching time of the source that must be considered large enough in order to prevent oscillations in the density that delay the convergence towards a steady scattering state.

Experimentally, this time-dependent coupling can be for instance realised by means of a radio-frequency knife [212] whose intensity is varied according to the desired temporal profile. The existence of a quasi stationary scattering state is only ensured for small nonlinearities in

the Gross–Pitaevskii equation [190]. For higher nonlinearities, dynamical instabilities generally occur [191, 192] and the convergence towards a steady scattering state is not guaranteed, rendering the process abidingly time-dependent [327]. In order to avoid any back-action of the nonlinearity with the source, we place the source sufficiently far upstream from the interacting region, so that  $x_S \ll x_L$ .

The disorder potential is controlled via

$$V(\mathbf{r}) = V_0 \int \frac{1}{\sqrt{\pi}\sigma} \exp\left(\frac{-|\mathbf{r} - \mathbf{r}'|^2}{2\sigma^2}\right) \eta(\mathbf{r}') d\mathbf{r}', \quad (7.9)$$

where  $V_0$  is the disorder strength,  $\sigma$  its correlation length and  $\eta(\mathbf{r})$  is a Gaussian white noise correlator satisfying  $\langle \eta(\mathbf{r}) \rangle = 0$  as well as  $\langle \eta(\mathbf{r})\eta(\mathbf{r}') \rangle = \delta(\mathbf{r} - \mathbf{r}')$ . This potential is such that its probability distribution to obtain a certain value for  $V$  is given by the Gaussian distribution.

$$P(V) = \frac{1}{\sqrt{2\pi V_0}} e^{-V^2/(2V_0)^2}. \quad (7.10)$$

This choice for the disorder leads to a vanishing average value  $\langle V(\mathbf{r}) \rangle = 0$  (where  $\langle \cdot \rangle$  denotes the random average) and to a Gaussian-shaped two-point correlation function

$$\langle V(\mathbf{r})V(\mathbf{r}') \rangle = V_0^2 \exp\left(\frac{-|\mathbf{r} - \mathbf{r}'|^2}{4\sigma^2}\right). \quad (7.11)$$

It may be argued that a Gaussian disorder potential is a quite primitive and “academic” approximation of the effective disorder potential that is experimentally generated by optical speckle fields. A more convincing speckle potential is obtained following its experimental realisation consisting of a laser beam shining a diffusive plate with a circular aperture [357–360]. The Gaussian potential remains nevertheless easier to deal with. Furthermore, predictions based on that choice for the disorder potential are expected to be very similar to those resulting from the choice of a speckle potential, provided both correlation lengths are equal and although the Gaussian two-point correlator is not identical to the one describing an optical speckle field [352, 365].

## 7.2 Numerical discretisation procedure

The aforementioned two-dimensional scattering region of length  $\mathcal{L}$  and width  $\mathcal{W}$  is sketched in FIG. 7.3(a). It basically consists in a disordered slab of length  $\mathcal{L}_D$  surrounded by two regions characterised by the absence of any disorder potential and towards which a coherent beam of matter wave is injected, following the working principle of an atom laser. This scattering region is discretised, giving birth to a regular grid of  $L \times W$  sites labelled by  $l$  and  $w$  and separated by the same spacing  $\delta$ , which we choose in the following such that  $k\delta = 1$ . A finite-difference scheme is used to discretise the kinetic energy operator

$$\frac{\partial^2 \hat{\psi}(x, y)}{\partial x^2} \simeq \frac{\hat{\psi}(x + \delta, y) + \hat{\psi}(x - \delta, y) - 2\hat{\psi}(x, y)}{\delta^2}, \quad (7.12)$$

$$\frac{\partial^2 \hat{\psi}(x, y)}{\partial y^2} \simeq \frac{\hat{\psi}(x, y + \delta) + \hat{\psi}(x, y - \delta) - 2\hat{\psi}(x, y)}{\delta^2}. \quad (7.13)$$

This choice of a finite-difference scheme for the discretisation of the kinetic operator on the two-dimensional grid leads to the on-site energy  $E_\delta = \hbar^2/m\delta^2$  and the nearest-neighbour hopping term  $-E_\delta/2$ . The numerical discretisation grid we use is sketched in FIG. 7.3(b).

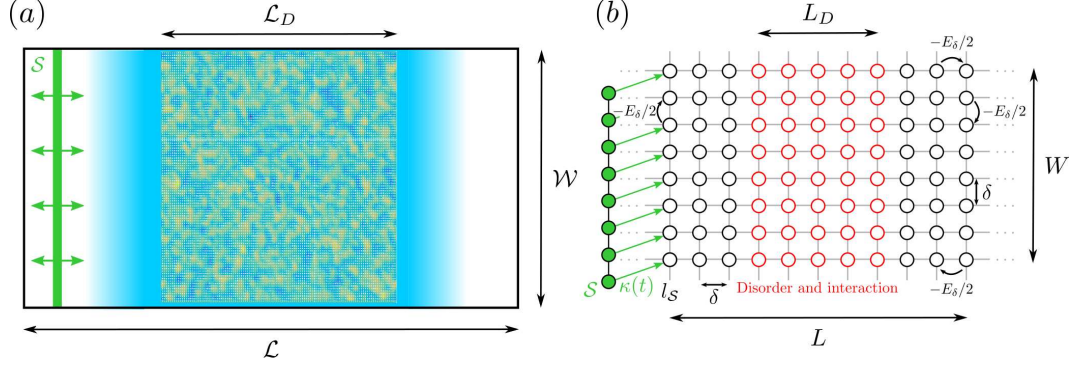


Figure 7.3 – Panel (a): scattering region of length  $\mathcal{L}$  and width  $\mathcal{W}$  containing a source injecting particles towards a disordered slab of length  $\mathcal{L}_D$  and width  $\mathcal{W}$ . Panel (b): regular grid resulting from the discretisation of the scattering region resulting in  $L \times W$  sites equally spaced by  $\delta$ , of on-site energy  $E_\delta$  and nearest-neighbour hopping term  $-E_\delta/2$ . The source is treated as being strongly localised and injects particles at site  $l_S$  towards the disordered slab containing  $L_D \times W$  sites. Smooth exterior complex scaling is applied in the longitudinal direction and periodic boundary conditions are applied in the transverse direction.

Following this discretisation procedure, the field operators are written on each site as a function of  $\delta$  as  $\hat{\psi}_{l,w}(t) \equiv \delta^2 \hat{\psi}(x = l\delta, y = w\delta, t)$ , whilst the on-site disorder potential is written as  $V_{l,w} \equiv V(x = l\delta, y = w\delta)$  and the interaction strength as  $g_l \equiv g(x = l\delta) / \delta^2$ .

The discrete Hamiltonian describing our system is expressed as

$$\begin{aligned} \hat{H} = & \sum_{l=1}^L \sum_{w=1}^W \left[ 2E_\delta \hat{a}_{l,w}^\dagger \hat{a}_{l,w} + V_{l,w} \hat{a}_{l,w}^\dagger \hat{a}_{l,w} - \frac{E_\delta}{2} \left( \hat{a}_{l+1,w}^\dagger \hat{a}_{l,w} + \hat{a}_{l,w}^\dagger \hat{a}_{l+1,w} \right) \right. \\ & \left. - \frac{E_\delta}{2} \left( \hat{a}_{l,w+1}^\dagger \hat{a}_{l,w} + \hat{a}_{l,w}^\dagger \hat{a}_{l,w+1} \right) + E_\delta g_l \hat{a}_{l,w}^\dagger \hat{a}_{l,w} \hat{a}_{l,w} \right] \\ & + \sum_{j=1}^W \left[ \kappa(t) \hat{a}_{l_S,j}^\dagger \hat{b} + \kappa^*(t) \hat{b}^\dagger \hat{a}_{l_S,j} \right] + \mu \hat{b}^\dagger \hat{b}, \end{aligned} \quad (7.14)$$

with  $\hat{a}_{l,w}^\dagger$  (resp.  $\hat{a}_{l,w}$ ) the creation (resp. annihilation) operator at site  $(l, w)$  and  $\hat{b}^\dagger$  (resp.  $\hat{b}$ ) is the creation (resp. annihilation) operator of the source which is maintained at the chemical potential  $\mu$  and the vanishing temperature  $T = 0$ . In the longitudinal direction, we use smooth exterior complex scaling to absorb outgoing waves [216, 222–227, 231, 232, 309, 326, 366] and we apply periodic boundary conditions in the transverse direction.

The Gaussian disorder potential is created within a slab of spatial extension  $\mathcal{L}_D \times \mathcal{W}$ . It is explicitly generated by drawing complex Gaussian random numbers  $\xi_{l,w}$  fulfilling

$$\langle \xi_{l,w} \xi_{l',w'} \rangle = \delta_{l,l'} \delta_{w,w'} \quad (7.15)$$

at each site within the disordered slab. Those complex Gaussian random numbers are then convoluted with a Gaussian envelope, giving rise to the following expression for the disorder at the point  $(l, w)$  of the disordered slab

$$V_{l,w} = \sum_{l'=-l_{\text{start}}}^{l_{\text{end}}} \sum_{w'=-\infty}^{\infty} A_{l,l'} A_{w,w'} \xi_{l',w'}, \quad (7.16)$$

with the Gaussian weight

$$A_{j,j'} = \sqrt{\frac{V_0 \delta}{\sqrt{\pi} \sigma}} \exp \left[ -\frac{\delta^2}{2\sigma^2} (j - j')^2 \right], \quad (7.17)$$

where  $V_0$  is the disorder strength and  $\sigma$  its correlation length. At the boundaries of the domain along the transverse direction, periodic boundary conditions are applied, which must also be enforced for the disorder potential. In practice, this is obtained by multiplying the on-site disorder potential in Eq. (7.16) by  $\Theta_{l,w-n\sigma}$  and  $\Theta_{l,w+n\sigma}$ , where

$$\Theta_{k,k'} = \begin{cases} 1 & \text{if } k \geq k' \\ 0 & \text{otherwise} \end{cases} \quad (7.18)$$

is the Heaviside step function, with  $n \in \mathbb{N}$  sufficiently large (in practice, we have chosen  $n = 5$ ), in order to safely neglect the value of the Gaussian weight at the point. The on-site disorder, compliant with the periodic boundary conditions, finally reads

$$V_{l,w} = \sum_{l'=l_{\text{start}}}^{l_{\text{end}}} \sum_{w'=w-n\sigma}^{w+n\sigma} A_{l,l'} A_{w,w'} \xi_{l',w' \bmod W}, \quad (7.19)$$

where  $W$  is the number of sites of the disordered slab along the transverse direction.

The on-site interaction parameter is defined as

$$U(x) = \tilde{g}/\delta^2 = gE_\delta = \frac{4\pi\hbar^2 a_S}{\sqrt{2\pi} m \delta^2 a_\perp(x)} \quad (7.20)$$

and is modulated by the dimensionless interaction strength  $g(x) = 2\sqrt{2\pi} a_S/a_\perp(x)$ . This choice for the interaction parameter may however be problematic in the continuous limit  $\delta \rightarrow 0$ , as convergence issues arise in that context [367]. However, as is shown in Ref. [352], the correct scaling of the interaction parameter yields negligible corrections to the approximated scaling Eq. (7.20) far away from the continuous limit.

An equation of motion for the time evolution of the annihilation operators is obtained thanks to the Heisenberg equation which, for the Hamiltonian specified in Eq. (7.14), explicitly reads

$$\begin{aligned} i\hbar \frac{\partial \hat{a}_{l,w}(t)}{\partial t} &= (2E_\delta + V_{l,w}) \hat{a}_{l,w}(t) - \frac{E_\delta}{2} [\hat{a}_{l-1,w}(t) + \hat{a}_{l+1,w}(t)] - \frac{E_\delta}{2} [\hat{a}_{l,w-1}(t) + \hat{a}_{l,w+1}(t)] \\ &\quad + E_\delta g_l \hat{a}_{l,w}^\dagger(t) \hat{a}_{l,w}^2(t) + \kappa(t) \delta_{l,l_S} \hat{b}(t) \end{aligned} \quad (7.21)$$

$$i\hbar \frac{\partial \hat{b}(t)}{\partial t} = \mu \hat{b}(t) + \sum_{j=1}^W \kappa^*(t) \hat{a}_{l_S,j}(t). \quad (7.22)$$

In the absence of interaction and disorder, a steady many-body scattering state characterised by the stationary density and current

$$\rho^\varnothing = \frac{1}{\delta^2} \frac{\mathcal{N}|\kappa(t)|^2}{\mu(2E_\delta - \mu)} \quad (7.23)$$

$$j^\varnothing = \frac{1}{\hbar} \frac{\mathcal{N}|\kappa(t)|^2}{\sqrt{\mu(2E_\delta - \mu)}} \quad (7.24)$$

is obtained, as is specified in Refs. [216, 218, 326, 352].

The mean-field approximation consists in replacing the creation and annihilation operators by c-numbers in Eqs. (7.21) and (7.22), which maps the many-body problem into an effective one body problem with a nonlinear term describing the effective potential created by the  $N-1$  particles and experienced by the  $N^{\text{th}}$  particle. More specifically, we make the Ansatz

$$\hat{a}_{l,w} \rightarrow \psi_{l,w} = \langle \hat{a}_{l,w} \rangle e^{-i\mu t/\hbar} \quad (7.25)$$

$$\hat{a}_{l,w}^\dagger \rightarrow \psi_{l,w}^* = \langle \hat{a}_{l,w}^\dagger \rangle e^{i\mu t/\hbar} \quad (7.26)$$

$$\hat{b} \rightarrow \chi(t) = \sqrt{\mathcal{N}} e^{-i\mu t/\hbar}, \quad (7.27)$$

which yields the following mean-field equations

$$i\hbar \frac{\partial \psi_{l,w}(t)}{\partial t} = (2E_\delta + V_{l,w} - \mu)\psi_{l,w}(t) - \frac{E_\delta}{2} [\psi_{l-1,w}(t) + \psi_{l+1,w}(t)] - \frac{E_\delta}{2} [\psi_{l,w-1}(t) + \psi_{l,w+1}(t)] \\ + E_\delta g_l |\psi_{l,w}(t)|^2 \psi_{l,w}(t) + \kappa(t) \delta_{l,l_S} \chi(t) \quad (7.28)$$

$$i\hbar \frac{\partial \chi(t)}{\partial t} = \sum_{w=1}^W \kappa^*(t) \psi_{l_S,w}(t), \quad (7.29)$$

with the initial conditions  $\psi_{l,w}(t_0) = 0$  and  $\chi(t_0) = \sqrt{\mathcal{N}}$ , corresponding to an empty scattering region and a coherent Bose-Einstein condensate within the reservoir of atoms.

Following the approach we developed in Chapter 2, we consider that the source is populated with a very large number of atoms  $\mathcal{N} \rightarrow \infty$  (for instance  $10^5$  atoms) and is coupled to the waveguide by means of a small outcoupling amplitude (for instance  $\kappa \sim 10^{-2}$  in the natural units that we consider here). Therefore, since  $\chi(t) = \sqrt{\mathcal{N}} [1 + \mathcal{O}(|\kappa|^2)]$  for some finite time interval  $t-t_0$ , we can claim that in the formal limit where the coupling  $\kappa$  tends to zero in such a way that the product  $\mathcal{N}|\kappa|^2$  is maintained constant,  $\chi(t)$  is approximately also constant in time. This latter approximation allows us to solely focus on Eq. (7.28) which appears as a nonlinear Schrödinger equation with a source term [215, 313, 314] that explicitly reads

$$i\hbar \frac{\partial \psi_{l,w}(t)}{\partial t} = \left( \frac{2E_\delta}{q_{l,w}} - \mu q_{l,w} + V_{l,w} \right) \psi_{l,w}(t) - \frac{E_\delta}{2} [J_{l-} \psi_{l-1,w}(t) + J_{l+} \psi_{l+1,w}(t)] \\ - \frac{E_\delta}{2} [\psi_{l,w-1}(t) + \psi_{l,w+1}(t)] + E_\delta g_l |\psi_{l,w}(t)|^2 \psi_{l,w}(t) + \sqrt{\mathcal{N}} \kappa \delta_{l,l_S}. \quad (7.30)$$

We have introduced in Eq. (7.30) an effective hopping term

$$J_{l\pm} = \left( \frac{1}{q_{l\pm 1,w}} - \frac{\delta q'_{l\pm 1,w}}{2 q_{l\pm 1,w}^2} \right) \quad (7.31)$$

that models smooth exterior complex scaling. In accordance with this method, we take  $q_{l,w} = 1$  within the scattering region in order to preserve the Hamiltonian from any scaling in that region, whereas we enforce the absorption of outgoing waves by choosing  $q_{l,w}$  smoothly ramped to  $e^{i\theta}$  outside the scattering region which rotates the  $x$  coordinate in the complex plane according to  $x \mapsto z = xe^{i\theta}$ , with  $\theta > 0$  the rotation angle [216, 222–227, 231, 232, 309, 326, 366].

### 7.3 Coherent backscattering peak

We numerically integrate the mean–field equation (7.30) on the two–dimensional grid sketched in FIG. 7.3(b), with initial conditions corresponding to an empty scattering region, *i.e.*  $\psi_{l,w} = 0$  at  $t = t_0$ . The propagation described by Eq. (7.30) leads to a stationary and stable scattering state [190], provided the nonlinearity remains sufficiently small in the Gross–Pitaevskii equation (7.30). For higher nonlinearities, the existence of such a steady state is not granted since dynamical instabilities generally occur [191, 327] and prevent the convergence towards a stationary scattering state, because they render the scattering process abidingly time–dependent. Our intention is precisely to prevent the advent of this turbulent regime and to focus on quasi–steady scattering processes, which implies that we must restrict the interaction strength to very low values.

The propagation described by Eq. (7.30) is performed in the presence of many realisations of the discrete disorder potential described in Eq. (7.19). In the absence of non–linearity, each of those propagations yields a stationary scattering state related to the specific disorder landscape encountered during the propagation, one of which being represented in FIG. 7.4(a).

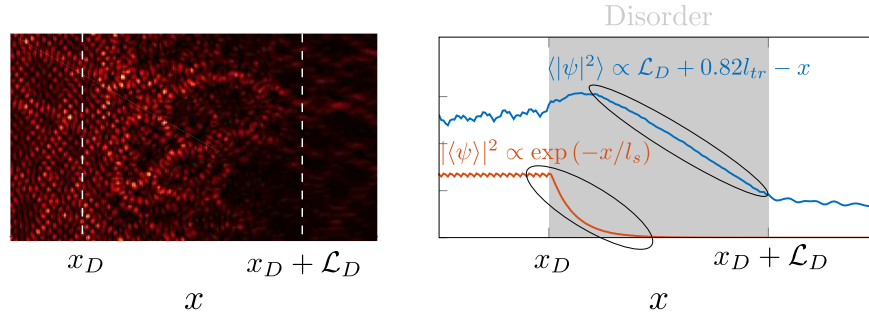


Figure 7.4 – Panel (a): the density  $|\psi_{l,w}|^2$  related to a scattering state that is reached in steady state regime for a single disorder realisation. The white dashed lines indicate the position of the disorder potential. Panel (b): Average along the transverse direction of the ensemble averaged coherent mode  $\langle |\psi_{l,w}\rangle|^2$  and of the density  $\langle |\psi|^2 \rangle$ . The exponential decay of the coherent mode allows us to extract the scattering mean free path  $l_s$  and the linear decrease of the density supplies the transport mean free path  $l_{tr}$ . The light grey square indicates the position of the disorder potential. Numerical parameters:  $k = \sqrt{2m\mu}/\hbar$ ,  $k\delta = 1$ ,  $\sqrt{N}|\kappa|^2 m/(\hbar^2 k^2) = 1$ , 1000 realisations of a Gaussian correlated disorder with disorder strength  $V_0 m/(\hbar^2 k^2) = 0.1$  and correlation length  $k\sigma = 1$ , length  $k\mathcal{L}_D = 100$  and width  $k\mathcal{W} = 120$ .

An ensemble average of those scattering states is then performed and, depending on whether the ensemble average is realised before or after taking the square modulus of the scattering states, the coherent mode  $|\langle\psi_{l,w}\rangle|^2$  or the on-site mean density  $\langle|\psi_{l,w}|^2\rangle$  are obtained. Averages over the transverse direction are shown for both quantities in FIG. 7.4(b).

As is expected from similar studies in the literature [60], the coherent mode follows an exponential decay  $|\langle\psi_{l,w}\rangle|^2 \propto \exp(-x/l_s)$  along the longitudinal direction whose exponential decay constant is given by the elastic scattering mean free path  $l_s$ . An exponential fit of the surrounded red curve of FIG. 7.4(b) yields  $kl_s \approx 11$ , which first indicates that the set of chosen numerical parameters lies in the so-called weak disorder regime for which  $kl_s \gg 1$ . Moreover, this value also specifies that  $l_s \ll \mathcal{L}_D$ , which corresponds to the diffusive regime, as is confirmed by the linear decrease of the density along the longitudinal direction.

The Boltzmann mean free path can be computed from the elastic scattering mean path, as it is yielded in the case of a Gaussian potential [39] by

$$\frac{l_s}{l_B} = 1 - \frac{I_1(2k^2\sigma^2)}{I_0(2k^2\sigma^2)}, \quad (7.32)$$

where  $I_\nu(z)$  is the modified Bessel function of order  $\nu$ , providing  $kl_B \approx 37$ . As is usually the case in two dimensions, this value yields a localisation length [368] provided by

$$\xi_{\text{loc}} = l_B \exp(\pi kl_B/2) \gg \mathcal{L}, \quad (7.33)$$

which is far larger than any dimension of the scattering region, indicating that transport occurs on a length scale much smaller than the localisation length  $\xi_{\text{loc}}$ .

The transport mean free path  $l_{tr}$  [369] can also be extracted from the linear decrease [39,370] in the longitudinal direction of the ensemble averaged density  $\langle|\psi_{l,w}|^2\rangle$  averaged along the transverse direction which decreases like  $\langle|\psi_{l,w}|^2\rangle \propto \mathcal{L}_D + 0.82l_{tr} - x$ . This linearly decaying law is obtained by a linear fit of the decrease that takes place within the disordered slab. The distance between the  $x$ -intercept of this linear fit and the boundary of the disordered slab corresponds to  $z_0 l_{tr}$ , where  $z_0$  is a numerical factor such that  $z_0 \approx 0.82$  in two dimensions [369]. Based on FIG. 7.4(b) and on the previous discussion, we find that  $kl_{tr} \approx 39$ , which essentially indicates that the disorder slab favours forward scattering. This is indeed expected for a correlation length  $k\sigma \gg 1$  that yields anisotropic scattering. An enhancement in the forward direction is found compared to other directions, deviating from the simplified case of point-like scatterers for which  $k\sigma \ll 1$  and that yields isotropic scattering.

The ensemble averaged momentum distribution in the two-dimensional space can be obtained by means of a discrete two-dimensional Fourier transform of the ensemble averaged wavefunction. With the purpose of relating the resulting various Fourier modes with spatial directions for the outgoing current, we take this discrete Fourier transform in an upstream region characterised by the absence of disorder and nonlinearity, so that the superposition principle is applicable. In that case, the different Fourier modes can safely be associated to outgoing waves which are characterised by the wavenumbers

$$\mathbf{k}_n = \sqrt{k^2 - \left(\frac{2\pi n}{\mathcal{W}}\right)^2} \mathbf{e}_x + \frac{2\pi n}{\mathcal{W}} \mathbf{e}_y, \quad (7.34)$$



describing the propagation in a spatial direction characterised by the angle  $\theta_n = \arcsin[2\pi n/(k\mathcal{W})]$ , with  $n = -W/2, -W/2 + 1, \dots, W/2$ . The resulting momentum distribution in the absence of interaction is displayed in FIG. 7.5.

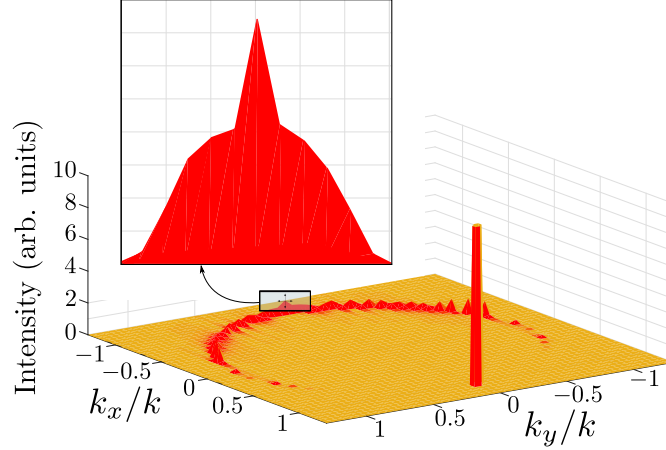


Figure 7.5 – Ensemble averaged momentum distribution in the two–dimensional space obtained as a 2D discrete Fourier transform of the wavefunction describing the reached quasi–steady scattering state in the absence of interaction. A signature of the incident plane matter wave is encountered in the form of a substantial population (height cut) of the  $(k_x, k_y)/k = (1, 0)$  mode. States of constant energy describing the circle  $k_x^2 + k_y^2 = k^2$  around the origin are almost equivalently populated, with a notable increase of the  $(k_x, k_y)/k = (-1, 0)$  mode related to the backscattered direction. Shown in inset is a zoom around this mode, which highlights the presence of coherent backscattering. Numerical parameters:  $k = \sqrt{2m\mu}/\hbar$ ,  $k\delta = 1$ ,  $\sqrt{\mathcal{N}}|\kappa|^2 m/\hbar^2 k^2 = 1$ , 1500 realisations of a gaussian correlated disorder with disorder strength  $V_0 m/\hbar^2 k^2 = 0.1$  and correlation length  $k\sigma = 1$ , length  $k\mathcal{L}_D = 100$  and width  $k\mathcal{W} = 120$ .

FIG. 7.5 shows a strong peak (whose height is cut) at the  $(k_x, k_y)/k = (1, 0)$  mode which most naturally results from the incident plane matter wave. As a result of elastic scattering processes, the entire space formed by constant energy states is filled out almost equivalently, which in two dimensions results in a ridge that follows the circle centred around the  $(0, 0)$  mode and such that  $k_x^2 + k_y^2 = k^2$ , indicating that all directions of reflection are nearly equivalent, as is expected from an incoherent classical theory of diffusive transport [39]. Artificial oscillations in the population of those states of constant energy are present for large angles owing to the finite spacing of the grid, as well as to the presence of periodic boundary conditions in the transverse direction. Amongst the states that form the ridge, the  $(k_x, k_y)/k = (-1, 0)$  mode stands out as it reveals a signature of coherent backscattering, owing to its high population compared to modes related to other scattering directions. This is best illustrated in the inset of FIG. 7.5 that shows a zoom around the  $(k_x, k_y)/k = (-1, 0)$  mode and which highlights a localised enhancement of population owing to coherent backscattering.

Compared to the semiclassical expectation that predicts a factor two enhancement compared to the incoherent background, the height of the coherent backscattering peak is here reduced. This reduction is explained by the presence of short-length self-retracing paths, mostly paths that consist in a single and immediate backreflection at the first scattering event that takes place in the disordered slab. An example of such paths is given in FIG. 7.6.



Figure 7.6 – Example of a self-retraced path. Those paths consist in paths that are backreflected at the first scattering event that takes place in the disorder potential. Obviously, such a path is identical to its time-reversed counterpart and hence do not enter in the Cooperon contribution that gives rise to coherent backscattering.

That kind of paths is obviously identical to its time-reversed counterpart and their pairing, consisting in a path paired with itself, therefore brings no contribution to coherent backscattering. In a diagrammatic language, such single scattering paths appear as doubly counted in the Diffuson and Cooperon contributions. It should therefore be excluded from the Cooperon contribution, thereby reducing the expected enhancement of an amount given by their relative weight in the summation over backreflected paths that together give rise to coherent backscattering. As is argued in Ref. [61], these self-retraced paths are further responsible for the formation of a dip that arises in the presence of a mean-field atom-atom interaction and whose depth should be quantitatively identical to the reduction of the peak height.

## 7.4 Angular resolved current

The previously described discrete two-dimensional Fourier transform certainly provides a manner to visualise coherent backscattering, but it requires a large number of simulation sites to produce an acceptable resolution. In order to limit the numerical effort, as well as to deliver a more detailed study of coherent backscattering, we detail below how we can extract the angular resolved current which relies on the reflected part of the wavefunction related to the stationary scattering state.

A possibility to extract this reflected part consists in performing a discrete partial Fourier transform  $\tilde{\psi}(x, k_y)$  of  $\psi(x, y)$  along the transverse direction. At this point, both the incident part and the reflected part are contained in  $\tilde{\psi}(x, k_y)$  and we must separate those two parts. We first make the general Ansatz that this wavefunction can be written as the superposition

$$\tilde{\psi}(x, k_y) = \alpha_+ \tilde{\psi}^{(+)}(x, k_y) + \alpha_- \tilde{\psi}^{(-)}(x, k_y), \quad (7.35)$$

with  $\alpha_+$  (resp.  $\alpha_-$ ) the amplitude of the incident (resp. reflected) wave and  $\tilde{\psi}^{(+)}(x, k_y)$  (resp.  $\tilde{\psi}^{(-)}(x, k_y)$ ) the related wavefunction. The separation is now achieved by evaluating  $\tilde{\psi}(x, k_y)$

at positions<sup>1</sup>  $x_0$  and  $x_0 + \Delta$  with  $\Delta > 0$ , and relating them thanks to the Ansatz in Eq. (7.35)

$$\alpha_+ \tilde{\psi}^{(+)}(x_0 + \Delta, k_y) + \alpha_- \tilde{\psi}^{(-)}(x_0 + \Delta, k_y) = \alpha_+ \tilde{\psi}^{(+)}(x_0, k_y) e^{ik_x \Delta} + \alpha_- \tilde{\psi}^{(-)}(x_0, k_y) e^{-ik_x \Delta}, \quad (7.36)$$

which finally renders the separation between the amplitude of the incident and reflected waves possible and accessible.

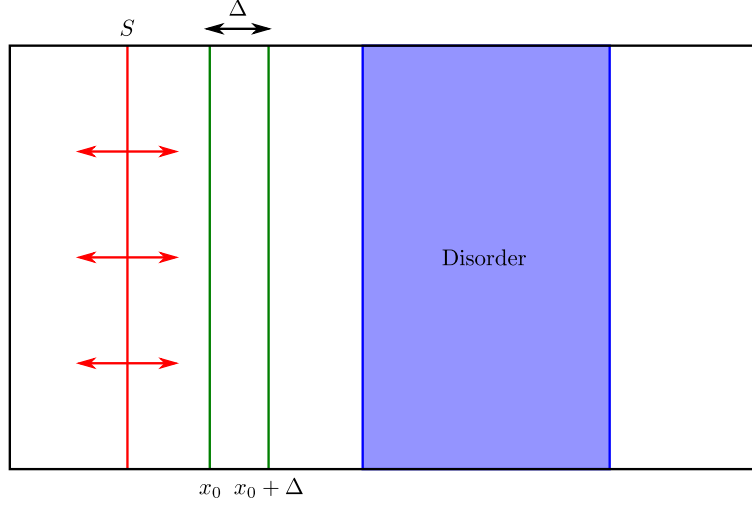


Figure 7.7 – The partial discrete Fourier transform  $\tilde{\psi}(x, k_y)$  of the wavefunction related to the reached scattering state is evaluated at positions  $x_0$  and  $x_0 + \Delta$  which are chosen in a region of space characterised by the absence of interaction and disorder potential.

Eq. (7.36) is best understood when rewritten under the form of a  $2 \times 2$  linear system of equations

$$\begin{pmatrix} \tilde{\psi}(x_0 + \Delta, k_y) \\ \tilde{\psi}(x_0, k_y) \end{pmatrix} = \begin{pmatrix} e^{ik_x \Delta} & e^{-ik_x \Delta} \\ 1 & 1 \end{pmatrix} \begin{pmatrix} \alpha_+ \tilde{\psi}^{(+)}(x_0, k_y) \\ \alpha_- \tilde{\psi}^{(-)}(x_0, k_y) \end{pmatrix}, \quad (7.37)$$

whose solution is yielded by matrix inversion as

$$\begin{pmatrix} \alpha_+ \tilde{\psi}^{(+)}(x_0, k_y) \\ \alpha_- \tilde{\psi}^{(-)}(x_0, k_y) \end{pmatrix} = \frac{1}{2i \sin(k_x \Delta)} \begin{pmatrix} 1 & -e^{-ik_x \Delta} \\ -1 & e^{ik_x \Delta} \end{pmatrix} \begin{pmatrix} \tilde{\psi}(x_0 + \Delta, k_y) \\ \tilde{\psi}(x_0, k_y) \end{pmatrix}. \quad (7.38)$$

The Fourier transformed wavefunction is thus separated into an incoming and reflected components at position  $x_0$ . The reflected part, related to the backscattered current, is explicitly provided by

$$\alpha_- \tilde{\psi}^{(-)}(x_0, k_y) = \frac{\tilde{\psi}(x_0, k_y) e^{ik_x \Delta} - \tilde{\psi}(x_0 + \Delta, k_y)}{2i \sin(k_x \Delta)}. \quad (7.39)$$

We are now in a position to compute the backscattered current based on  $|\tilde{\psi}_n|^2$ , where  $\tilde{\psi}_n \equiv \alpha_- \tilde{\psi}^{(-)}(x_0, k_y)$  is yielded by Eq. (7.39). Indeed, the periodic boundary conditions imposed

<sup>1</sup>In order for the superposition principle to be applicable, we must, as previously discussed, perform the Fourier transform and thus choose  $x_0$  and  $x_0 + \Delta$  in a region of space characterised by the absence of interaction and disorder potential.

in the transverse direction decompose the state under study into transverse eigenmodes to which we associate an outgoing plane wave with wavevector

$$\mathbf{k}_n = \begin{pmatrix} \sqrt{k^2 - \left(\frac{2\pi n}{W}\right)^2} \\ \frac{2\pi n}{W} \end{pmatrix} \quad \text{with} \quad n = -\frac{W}{2}, -\frac{W}{2} + 1, \dots, \frac{W}{2} - 1, \frac{W}{2}, \quad (7.40)$$

describing the propagation in a spatial direction characterised by the angle  $\theta_n = \arcsin[2\pi n/(kW)]$ , as is shown in FIG. 7.8.

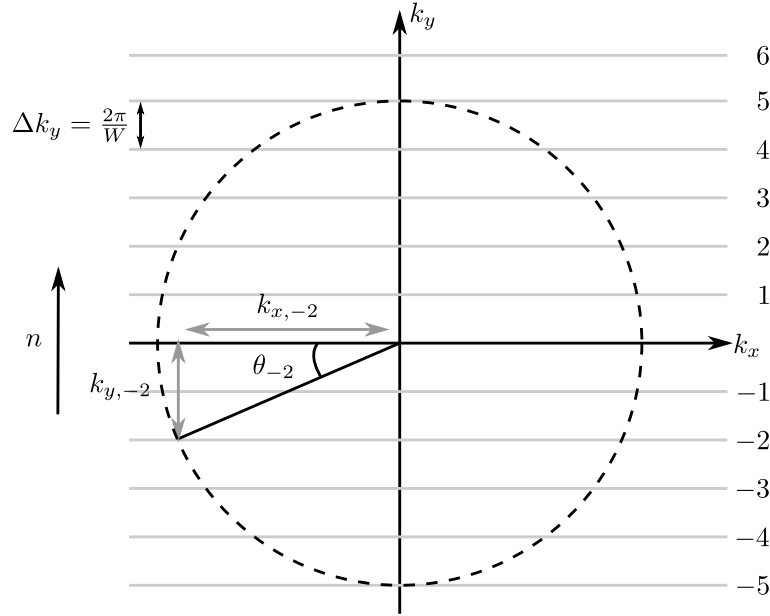


Figure 7.8 – Decomposition of the transverse wavevector  $k_y$  into discrete modes and the associated angles  $\theta_n = \arcsin[2\pi n/(kW)]$ . Figure adapted from [371].

The current density in the direction indicated by  $\theta_n$  is finally expressed as

$$j_n = 2\pi \frac{\hbar}{m} \sqrt{k^2 - k_y^2} |\tilde{\psi}_n|^2 \cos(\theta_n) \quad (7.41)$$

and allows us to closely monitor coherent backscattering with a lower number of grid sites.

The angular resolved current which features a strong peak around  $\theta = 0$ , corresponding to the backscattered direction and closely related to the population peak for the  $(k_x, k_y)/k = (-1, 0)$  mode in the momentum space displayed in FIG. 7.5, highlights the appearance of coherent backscattering in the absence of interaction, as is shown by the light orange curve of FIG. 7.9.

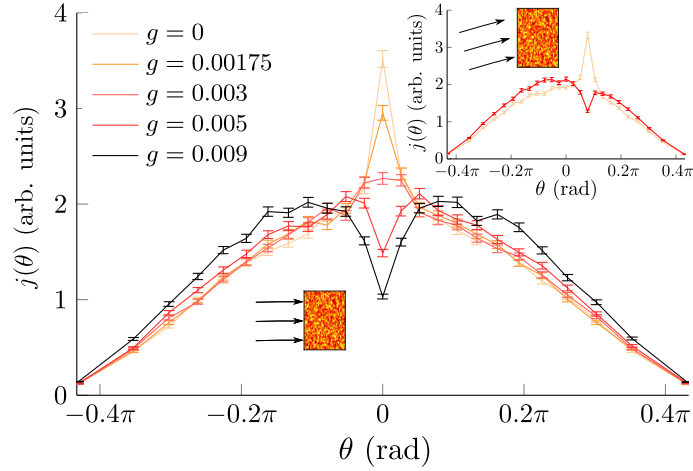


Figure 7.9 – Angular resolved current as a function of the backscattered angle  $\theta_n = \arcsin[2\pi n/(k\mathcal{W})]$  for increasing values of the interaction strength  $g$ , with error bars indicating the related standard deviation. The typical cone-shaped coherent backscattering peak around  $\theta = 0$  emerges in the absence of interaction. In the presence of interaction, this peak gets first mitigated and even vanishes for  $g = 0.003$ , as the related light brown curve illustrates. For higher interaction strengths, the peak is transformed into a pronounced dip. Inset: an incident wave tilted by the angle  $\phi_{-3} = \arcsin[2\pi(-3)/(k\mathcal{W})] \approx -0.16$  rad yields the same coherent backscattering peak and related inversion in the presence of interaction, in the direction opposite to the incident one. Numerical parameters:  $k = \sqrt{2m\mu}/\hbar$ ,  $k\delta = 1$ ,  $\sqrt{\mathcal{N}}|\kappa|^2 m/\hbar^2 k^2 = 1$ , 1500 realisations of a gaussian correlated disorder with disorder strength  $V_0 m/\hbar^2 k^2 = 0.1$  and correlation length  $k\sigma = 1$ , length  $k\mathcal{L}_D = 40$  and width  $k\mathcal{W} = 120$ .

In the presence of weak but finite interaction whose strength is increased step by step, the coherent backscattering peak is first mitigated before being completely flattened for  $g = 0.003$ . For higher interaction strength, namely for  $g = 0.009$ , the peak is inverted and becomes a pronounced dip, revealing a crossover from constructive to destructive interferences, in qualitative agreement with a nonlinear diagrammatic theory of coherent backscattering [59]. Our findings also turn out to be in excellent agreement with the numerical mean-field study of Ref. [60] dedicated to coherent backscattering in two-dimensional disorder potentials and upon which the present study is based.

In order to validate the mechanism behind this inversion as due to coherent backscattering and not, for instance, as due to an artificial effect resulting from the specific geometry of the disordered slab, we tilt the incident profile of the source by a finite angle

$$\phi_{-3} = \arcsin \left[ \frac{2\pi(-3)}{k\mathcal{W}} \right] \approx -0.16 \text{ rad} \quad (7.42)$$

which amounts to choosing the tilted transverse profile

$$\phi(y) = \exp \left[ \frac{2i\pi(-3)}{k\mathcal{W}} y \right] \quad (7.43)$$

in Eq. (7.7) instead of a constant profile. As is shown in the inset of FIG. 7.9, the coherent backscattering peak and the related dip that emerges in the presence of finite interaction are both realised in the exact opposite direction, with characteristics (height and width) very similar to those related to the peak appearing for a perpendicular incident wave characterised by  $\phi_0 = 0$  rad. We can thus conclude that this effect and the related inversion originate from interference effects appearing in the pairing of time-reversed scattering paths.

As was already highlighted earlier, one of the main drawbacks of the mean-field approximation is to model only elastic scattering events. We have indeed stressed that inelastic scattering events however play a major role in various situations, for instance in the case of Al'tshuler–Aronov–Spivak oscillations inversion discussed in Chapter 5. This role is exacerbated with increasing interaction strengths and poses a fundamental question regarding the emergence of dephasing of interfering trajectories which is precisely triggered by interaction. More specifically, the question to determine whether the peak inversion prevails beyond the mean-field regime or gets hidden behind dephasing remains open at this moment. In order to answer this question and the related question regarding the experimental observability of coherent backscattering inversion with the studied system, we use the truncated Wigner method.

## 7.5 Inversion of coherent backscattering beyond the mean-field regime

As we have explained in Chapter 3, the truncated Wigner method tries to mimic quantum fluctuations, that are neglected within the mean-field approximation, by sampling the initial quantum state, which offers a possibility to compute observables related to coherent as well as to incoherent contributions. This notion of coherence shall be explicitly defined below and refers to the ability of wave components of the bosonic matter wave beam to form coherent superpositions that together interfere, in accordance with the principle of atom lasers. This ability may be compromised by atom–atom interactions, that may give rise to a depletion of the condensate state that constitutes the atom laser, thus forming what we refer to as incoherent contributions that mostly do not interfere with each other and may yield to global dephasing. We stress that the loss of this matter wave coherence as a result of finite interaction must not be confused with environment-induced decoherence in the many-body Fock space that would arise if the system were coupled to a heat bath.

We start by sampling the initial quantum state with classical field amplitudes  $\{\psi_{l,w}\}$ . At initial time  $t_0$ , the scattering region ( $SR$ ) is empty and the related Wigner function can be written as a product of on-site vacuum Wigner functions

$$\mathcal{W}_{SR}(\{\psi_{l,w}, \psi_{l,w}^*\}, t_0) = \prod_l \prod_m \left( \frac{2}{\pi} e^{-2|\psi_{l,w}|^2} \right). \quad (7.44)$$

The reservoir ( $\mathcal{S}$ ) of atoms contains a large number  $|\chi|^2 = \mathcal{N} \gg 1$  of bosonic particles which motivates us to treat this reservoir as a coherent state. In this case, the related Wigner function is provided by

$$\mathcal{W}_{\mathcal{S}}(\chi, \chi^*, t_0) = \frac{2}{\pi} e^{-2|\chi - \sqrt{\mathcal{N}}|^2}. \quad (7.45)$$

The Wigner function for the whole system is then naturally obtained as the product of (7.44) and (7.45), which reads

$$\mathcal{W}(\{\psi_{l,w}, \psi_{l,w}^*\}, t_0) = \mathcal{W}_{SR}(\{\psi_{l,w}, \psi_{l,w}^*\}, t_0) \times \mathcal{W}_S(\chi, \chi^*, t_0). \quad (7.46)$$

Consequently, the classical field amplitudes are written as random complex Gaussian numbers

$$\psi_{l,w}(t = t_0) = \frac{1}{2} (\mathcal{A}_{l,w} + i\mathcal{B}_{l,w}), \quad (7.47)$$

that account for initial quantum fluctuations. The numbers  $\mathcal{A}_{l,w}$  and  $\mathcal{B}_{l,w}$  are real and independent Gaussian random variables fulfilling

$$\begin{aligned} \overline{\mathcal{A}_{l,w}} &= \overline{\mathcal{B}_{l,w}} = 0, \\ \overline{\mathcal{A}_{l',w'}\mathcal{A}_{l,w}} &= \overline{\mathcal{B}_{l',w'}\mathcal{B}_{l,w}} = \delta_{l,l'}\delta_{w,w'}, \\ \overline{\mathcal{A}_{l',w'}\mathcal{B}_{l,w}} &= 0, \end{aligned} \quad (7.48)$$

where  $\bar{\cdot}$  stands for an average over the random variables. In particular, Eqs. (7.48) imply that the classical amplitudes are such that

$$\overline{\psi_{l,w}}|_{t_0} = 0 \quad \text{and} \quad \overline{\psi_{l,w}^*\psi_{l',w'}}|_{t_0} = \frac{1}{2}\delta_{l,l'}\delta_{w,w'}. \quad (7.49)$$

This initial – non vanishing – one half variance may somehow be conceived as a half pseudo particle on each site which must be subtracted when computing the atomic density, as we already discussed in Chapters 3, 4 and 5. This subtraction appears most naturally in the Weyl-ordered representation of the total density.

We treat the source of atoms in a completely classical manner and set  $\chi(t = t_0) = \sqrt{\mathcal{N}}$  because of the large number of bosonic particles contained in the source that allows us to neglect the relative uncertainties of both the amplitude and the phase of the source. As in the mean-field treatment, we also choose  $\kappa(t) \rightarrow 0$  and concomitantly maintain  $\mathcal{N}|\kappa|^2$  finite and constant in order to neglect the source depletion or any back-action of the scattering region onto the source [216]. We can once again, in this formal limit, focus on the evolution within the scattering region which is prescribed by the evolution of the classical field amplitudes at each grid point.

In order to obtain this equation, we apply the formalism described in Chapter 3 for implementing the truncated Wigner method to the many-body model described in Eqs. (7.1) and (7.2). The following evolution equation for the classical field  $\psi_{l,w}$  at site  $(l, w)$  is then yielded as

$$\begin{aligned} i\hbar \frac{d}{dt} \psi_{l,w}(t) &= \left( \frac{2E_\delta}{q_{l,w}} - \mu q_{l,w} + V_{l,w} \right) \psi_{l,w}(t) + \sqrt{\mathcal{N}} \kappa \delta_{l,l_S} + E_\delta g_l (|\psi_{l,w}(t)|^2 - 1) \psi_{l,w}(t) \\ &\quad - \frac{E_\delta}{2} [J_{l+} \psi_{l+1,w}(t) + J_{l-} \psi_{l-1,w}(t)] - \frac{E_\delta}{2} [\psi_{l,w+1}(t) + \psi_{l,w-1}(t)] \\ &\quad + \chi_{L,w}(t) \delta_{l_L,w} + \chi_{R,w}(t) \delta_{l_R,w}, \end{aligned} \quad (7.50)$$

where  $q_{l,w}$  as well as the effective hopping term  $J_{l\pm}$  defined in Eq. (7.31) are introduced for the implementation of smooth exterior complex scaling, with the same meaning as in Eq. (7.30).

The main difference with the mean-field evolution equation (7.30) is the presence of quantum noise in the third line of Eq. (7.50). Due to the sampling of the initial quantum state by random numbers with vanishing mean but finite variance (as is shown in Eq. (7.49)) that accounts for initial quantum fluctuations, and owing to the necessity of spatially truncating the system into a finite simulation region, quantum noise originating from the left and from the right of the simulation region enters the system [216]. This quantum noise, whose exact shape is derived in Appendix C, is given by

$$\chi_{lL,w}(t) = E_\delta e^{-i(2E_\delta - \mu)\tau/\hbar} \sum_{l'=-\infty}^{-1} L_{l'}(\tau) \sum_{k=0}^{W-1} T_k(\tau) \eta_{l',k}(0) e^{2\pi i k w / W} \quad (7.51)$$

$$\chi_{lR,w}(t) = -E_\delta e^{-i(2E_\delta - \mu)\tau/\hbar} \sum_{l'=1}^{\infty} L_{l'}(\tau) \sum_{k=0}^{W-1} T_k(\tau) \eta_{l',k}(0) e^{2\pi i k w / W}, \quad (7.52)$$

with  $\tau = (t - t_0)$  and

$$L_l(t - t_0) = \frac{i^l}{2} \left[ J_{l+1} \left( \frac{E_\delta \tau}{\hbar} \right) + J_{l-1} \left( \frac{E_\delta \tau}{\hbar} \right) \right], \quad (7.53)$$

where  $J_\nu(\tau)$  are the Bessel functions of the first-kind of order  $\nu$  and

$$T_k(t - t_0) = \frac{1}{\sqrt{W}} e^{iE_\delta \tau \cos(2\pi k / W) / \hbar}. \quad (7.54)$$

Equipped with a proper sampling of the initial quantum state and with an evolution equation, we still have to define how we compute observables. They are obtained, as is explained in Chapter 3, by averages of the relevant observable over the initial many-body quantum state sampling. We show how to do so for the  $(k, n)$  mode density in the momentum space, which must be evaluated in a slab of  $\tilde{L} \times W$  sites that is localised upstream of the disordered slab and that should be, for the same reasons as in the mean-field treatment, characterised by the absence of nonlinearity or disorder. This mode density is explicitly given by

$$\tilde{n}_{k,n} = \frac{1}{\tilde{L}W} \left\langle \left| \sum_l \sum_w \psi_{l,w} e^{-2\pi i (kl/\tilde{L} + nw/W)} \right|^2 \right\rangle - \frac{1}{2}, \quad (7.55)$$

where the subtraction of  $1/2$  compensates the initial one half variance of the classical field amplitudes. The related coherent  $(k, n)$  mode density in the momentum space is given by

$$\tilde{n}_{k,n}^{\text{coh}} = \frac{1}{\tilde{L}W} \left| \left\langle \sum_l \sum_w \psi_{l,w} e^{-2\pi i (kl/\tilde{L} + nw/W)} \right\rangle \right|^2, \quad (7.56)$$

and the incoherent one is then obtained through

$$\tilde{n}_{k,n}^{\text{incoh}} = \tilde{n}_{k,n} - \tilde{n}_{k,n}^{\text{coh}}. \quad (7.57)$$

The main difference between the total and the coherent contribution is due to the order in which the square modulus and the averages (over the disorder and the initial conditions) are performed. The total contribution is obtained when the square modulus, that destroys any coherent effect, is performed first whilst the coherent contribution arises when the averages



are first performed. We stress again that this notion of coherence is to be understood in terms of the ability for the various wave components of the bosonic matter wave to yield interference effects.

Following the same principle, we can also define a total, coherent and incoherent backscattered current that are yielded as, in a very similar fashion as in the mean-field approximation,

$$j_n^{\text{tot}} = 2\pi \frac{\hbar}{m} \sqrt{k^2 - k_n^2} \left( \langle |\tilde{\psi}_n|^2 \rangle - \frac{1}{2} \right) \cos \theta_n \quad (7.58)$$

$$j_n^{\text{coh}} = 2\pi \frac{\hbar}{m} \sqrt{k^2 - k_n^2} |\langle \tilde{\psi}_n \rangle|^2 \cos \theta_n. \quad (7.59)$$

The incoherent part of the current is most naturally obtained as the subtraction of the coherent contribution from the total one

$$j_n^{\text{incoh}} = j_n^{\text{tot}} - j_n^{\text{coh}}. \quad (7.60)$$

This discrimination between the coherent and incoherent contribution to the backscattered current allows us to examine the prevalence of the coherent contribution that carries the dip structure in a regime that goes beyond the mean-field approximation, as well as to scrutinise in which extent inelastic scattering dephases interference effects. It has indeed been stressed in Chapter 5 that dephasing of interference effects is triggered by inelastic scattering that reduces the phase coherence length and, at some point, annihilates coherent effects. Both nonlinear diagrammatic theory [115] and numerical studies [372] indicate that far away from the mean-field regime, a total dephasing is expected, thereby yielding a structureless current, dominated by the incoherent contribution. Quantifying the advent of this regime of dominating dephasing is of crucial relevance in an experimental context since it provides indications whether the inversion of coherent backscattering should be observable or not. Indeed, despite a partial dephasing of coherence effects, a signature of the coherent backscattering inversion might prevail in an experimentally accessible regime of parameters.

To shed more light on this issue, interaction effects beyond the mean-field regime are explored within the parameter space begot by the on-site interaction strength  $g$  and the density per unit surface  $\rho^\varnothing$  with the constraint that their product yields a constant nonlinearity  $\rho^\varnothing g/k^2$ . Any increase of the interaction strength is then concomitantly accompanied by a decrease in the density per unit surface. We start by investigating the importance of inelastic scattering in a regime of mean-field parameters corresponding to the red curve of FIG. 7.9 for which  $\rho^\varnothing g/k^2 \simeq 0.00665$ . This curve shows a partial inversion of coherent backscattering and is used as a starting point in the investigation of the coherence prevalence.

FIGS. 7.10(b) and 7.10(c) indicate that within the mean-field regime, coherent effects dominate the backscattered current and the peak inversion consequently prevails.

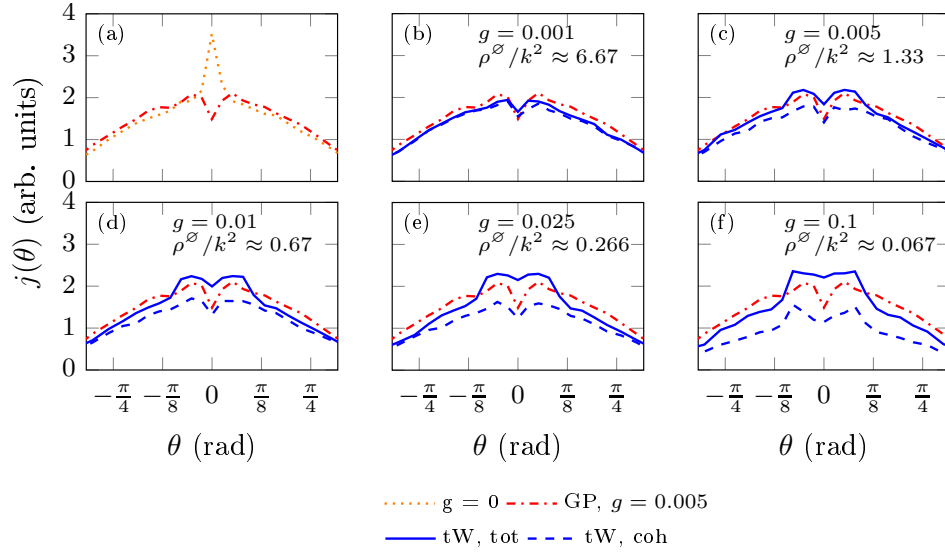


Figure 7.10 – Truncated Wigner simulations of the angular-resolved backscattered current. Panel (a) displays a mean-field simulation in the absence of interaction (dotted orange curve) and in the presence of interaction (dashed red curve) giving rise to CBS inversion. Panels (b)–(f) show truncated Wigner simulations of an increasing interaction strength  $g$  and a correspondingly decreasing average density  $\rho^\varnothing$ , the product  $g\rho^\varnothing/k^2 \simeq 0.00665$  being kept constant for all simulations. The mean-field peak inversion is preserved beyond the mean-field approximation in spite of an interaction-induced dephasing. Numerical parameters:  $k = \sqrt{2m\mu}/\hbar$ ,  $k\delta = 1$ , 500 realisations of a Gaussian correlated disorder with disorder strength  $V_0m/\hbar^2k^2 = 0.1$  and correlation length  $k\sigma = 1$ , length  $k\mathcal{L}_D = 40$  and width  $k\mathcal{W} = 120$ .

Panels (d)–(f) show that, despite a partial dephasing that mitigates the inversion of coherent backscattering, this effect is preserved, even for densities as low as  $\rho^\varnothing/k^2 \simeq 0.067$ .

We are in a position to examine the possible experimental observability with  $^{87}\text{Rb}$  atoms. As we already mentioned, this atomic species is routinely employed to produce Bose–Einstein condensates. The observability of the peak inversion with  $^{87}\text{Rb}$  atoms is hence of fundamental relevance.

The two-dimensional effective interaction strength is written as

$$\tilde{g}(x) = \frac{\hbar^2}{m}g(x) = 2\sqrt{2\pi}\frac{\hbar^2}{m} \frac{a_S}{a_\perp(x)}, \quad (7.61)$$

with  $a_\perp(x) = \sqrt{\hbar/m\omega_\perp(x)}$  the oscillator length associated to the confinement frequency  $\omega_\perp(x)$  of the trap. In the disordered slab, we can thus write the nonlinear parameter as

$$\tilde{g}(x)\frac{\rho^\varnothing}{k^2} = 2\sqrt{2\pi}\frac{\hbar^2}{m} \frac{a_S}{a_\perp(x)} \frac{\rho^\varnothing}{k^2}. \quad (7.62)$$

All the simulations were performed with a chemical potential equal to  $\mu = E_\delta/2 = mv^2/2$ , that yields the wavevector  $k = mv/\hbar$  with  $v$  the velocity of the injected matter wave. The nonlinear parameter is in the case of FIG. 7.10 chosen to  $\rho^\varnothing g(x)/k^2 = 0.00665$ , which yields the following injected density as

$$\rho^\varnothing = \frac{0.00665}{2\sqrt{2\pi}} \frac{a_\perp}{a_S}, \quad (7.63)$$

which scales as the s-wave scattering length divided by the oscillator length. In the case of  $^{87}\text{Rb}$  atoms of mass  $m = 1.443 \times 10^{-25}$  kg and s-wave scattering length  $a_S = 5.313 \times 10^{-9}$  m, Eq. (7.63) predicts that for a confinement frequency of  $\omega_\perp/2\pi = 75$  Hz, an injected density  $\rho^\varnothing/k^2 \approx 0.31$  is found. The regime of parameters corresponding to such an injected density lies between the (d) and (e) panels of FIG. 7.10, which indicates that despite a partial dephasing, as is found in those panels, the coherent backscattering inversion should be observable experimentally.

In order to comply with our hypothesis of a propagation in the transverse ground mode, we note that the velocity  $v$  of the injected particles related to the choice of parameters yields

$$v = \sqrt{\frac{\hbar\omega_\perp}{m}} = 0.00068 \text{ m/s}, \quad (7.64)$$

that enforces  $\frac{1}{2}mv^2 < \hbar\omega_\perp$  and allows a posteriori to have assumed a propagation in the transverse ground state, as the incident kinetic energy is not high enough to populate the transverse excited levels. We finally indicate that this velocity for the incident matter wave yields a propagation in the supersonic regime, as the speed of sound within the condensate is given by

$$v_c = \sqrt{\frac{\rho^\varnothing g_{3D}}{m\sqrt{\pi}a_\perp}}, \quad (7.65)$$

where the  $1/\sqrt{\pi}a_\perp$  factor comes from the transverse wavefunction in its ground state  $\phi(z) = e^{-z^2/2a_\perp^2}/\sqrt{\sqrt{\pi}a_\perp}$  evaluated for  $z = 0$  and where  $g_{3D} = 4\pi\hbar^2 a_S/m$  is the 3D interaction strength. The speed of sound in the condensate is then rewritten as

$$v_c = \sqrt{\frac{\sqrt{2}g\rho^\varnothing}{k^2}}v, \quad (7.66)$$

confirming the prevention of the advent of superfluidity since  $v_c \simeq 0.1v \ll v$ , for the parameters used in FIG. 7.10 as well as for those used in FIG. 7.11. It thereby confirms the possible experimental observability of coherent backscattering peak inversion in the presence of a finite interaction strength with  $^{87}\text{Rb}$  atoms.

We still have to determine which regime corresponds to a dominating incoherent contribution that induces dephasing. To that end, we investigate the regime related to the nonlinearity that yields a full inversion of coherent backscattering in the mean-field approximation for which we expect dephasing to be more pronounced, as is shown in FIG. 7.11.

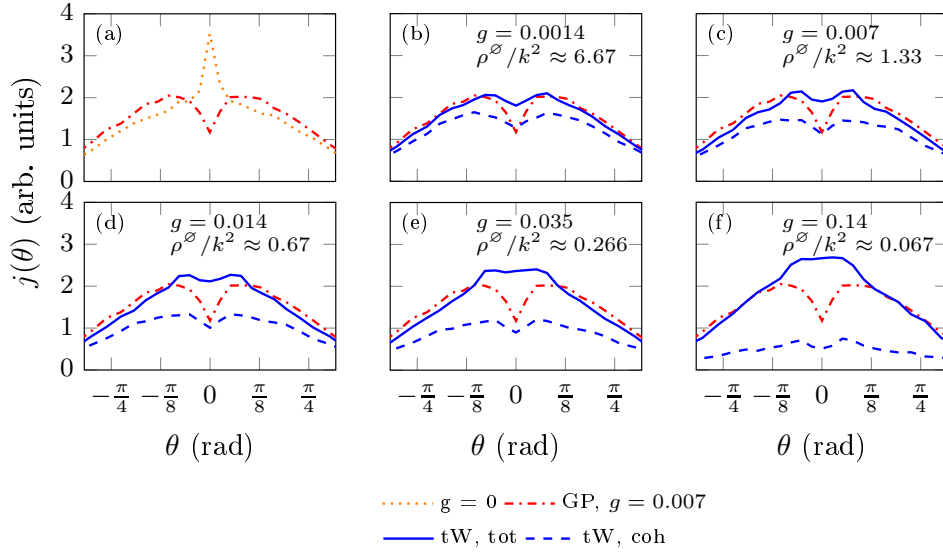


Figure 7.11 – Truncated Wigner simulations of the angular-resolved backscattered current. The panel (a) displays a mean-field simulation in the absence of interaction (dotted orange curve) and in the presence of interaction (dashed red curve) giving rise to CBS inversion. Panels (b)–(f) show truncated Wigner simulations of an increasing interaction strength  $g$  and a correspondingly decreasing average density  $\rho^\varnothing$ , the product  $g\rho^\varnothing/k^2 \simeq 0.00931$  being kept constant for all simulations. The deep dip that appears in the mean-field regime is little by little destroyed by dephasing but still prevails in the (b)–(d) panels, before getting hidden behind a structureless and mostly incoherent current in panels (e) and (f). Numerical parameters:  $k = \sqrt{2m\mu}/\hbar$ ,  $k\delta = 1$ , 500 realisations of a Gaussian correlated disorder with disorder strength  $V_0m/\hbar^2k^2 = 0.1$  and correlation length  $k\sigma = 1$ , length  $k\mathcal{L}_D = 40$  and width  $k\mathcal{W} = 120$ .

FIG. 7.10 indicates the presence of a certain dephasing far away from the mean-field limit. For a higher nonlinear parameter, namely  $g\rho^\varnothing/k^2 \simeq 0.00931$  for FIG. 7.11, dephasing is already present in a regime of parameters lying in the mean-field regime, as panels (b) and (c) show. Panel (d) shows that the prevalence of dephasing increases but also that the inversion remains observable beyond the mean-field regime. Panels (e) and (f) reveal the annihilation of coherent effects by dephasing far away from the mean-field limit: inelastic scattering processes have strongly reduced the phase coherence length and nearly completely destroyed the peak inversion. Panel (f) indeed shows a flat and structureless total profile mostly resulting from the incoherent current. However, we can conduct the same reasoning as for FIG. 7.10 regarding the experimental observability and conclude that with the nonlinear parameter  $g\rho^\varnothing/k^2 = 0.00931$  and the same experimental parameters, an injected density  $\rho^\varnothing/k^2 \approx 0.44$  is found, which situates somewhere between panels (d) and (e). This should still be observable although dephasing destroys the inversion in some extent. Nevertheless, other atomic species such as  $^{39}\text{K}$  whose s-wave scattering length can be easily tuned to very low values by means of Feshbach resonances, owing to their large resonance width, may represent a candidate for which the inversion is more easily experimentally realised.

# Conclusion and perspectives

The present manuscript deals with the quantum simulation of transport phenomena in random media with ultracold atoms and more specifically with Bose–Einstein condensates. As we addressed in the manuscript, ultracold atoms actually offer a versatile and efficient toolbox to emulate complex phenomena originating from condensed–matter physics. In particular, they supply a sensitive probe to explore coherent and many–body interaction effects in well–controlled scenarios, both from the theoretical and experimental point–of–view. In this manuscript, we leveraged this flexibility to study the intriguing competition between coherent and interaction effects in various contexts with Bose–Einstein condensates. This reveals a very rich physics where interference effects that naturally arise in the coherent transport of waves are strongly affected by the presence of many–body interaction effects, highlighting the crucial need of a fully–fledged understanding of this interplay in view, for instance, of designing atomtronics components.

We have studied this competition both in one– and two–dimensional situations, in contexts that are often encountered in solid–state physics. The traditional theoretical approach that is routinely employed is to account for interaction effects in the mean–field approximation. The principle of this approach is to cast the complicated many–body problem into a simpler one–body problem by replacing quantum field operators arising in the modelling of the related systems by their expectation values. This portrays the interaction experienced by a particle amongst the  $N$  particles constituting the atomic gas as an effective potential created by the remaining  $N - 1$  particles, which results in a nonlinear Schrödinger equation. This approach is restricted to very weak interaction strengths and suffers the lack of modelling of inelastic scattering that may compromise coherent effects. We went one step further by employing the truncated Wigner method that allows to model inelastic scattering and to address the related dephasing issues that can eclipse coherent effects. In particular, we used this approach in this manuscript to evaluate the experimental observability of coherent effects arising in the scenarios we studied.

The *first chapter* introduced the transport of coherent waves in random media in a very general context. It is written as a launching pad for the rest of the manuscript, as it paves the way for various ubiquitous concepts, such as the crucial role of disorder, the corresponding transport lengths or the mechanisms behind diverse interference–related effects. The discussion follows a path of ascending sophistication in the description of transport of waves, ranging from the classical and incoherent modelling of transport to Anderson localisation. Diffusive transport emerges from the classical approach, yielding famous successes, as for instance Ohm’s law that results from the Drude model or heat conduction. This intuitive

interpretation gets however compromised by interference effects, that give rise to weak localisation and coherent backscattering, which mitigate diffusive transport. The latter gets even completely suppressed, as strong localisation scenarios indicate.

In the *second chapter*, we introduced Bose–Einstein condensation – and the related condensates – that we recurrently used in this work. We followed a pedagogical approach and showed how condensation naturally results from statistical considerations. In particular, we detailed how it occurs in a trap and how to model it, including the atom–atom interaction amongst its constituting particles. We showed how in the framework of low energy scattering in the far–field limit, this atom–atom interaction can be reduced to a two–body interaction modelled by a contact potential which is encoded by the s–wave scattering length. This quantity may be tuned by means of Feshbach resonances which are used as a tool to adjust the interaction parameter. Finally, we also introduced atom lasers that are used in this work as a source producing coherent and monochromatic matter plane waves, the ideal candidate for studying interference effects in a disordered landscape. We adapted this scenario to a generic scattering configuration that we particularised in the following chapters to more specific contexts.

As we developed in Chapter 2, the drawbacks of the mean–field approximation restrict the study to very weak interaction strengths and prevent us from evaluating the prevalence of dephasing at stronger interaction, which is precisely one of the goals of this work. To this end, we employed and described in the *third chapter* the truncated Wigner method, an approximation method that goes beyond the mean–field approximation by emulating quantum fluctuations that are neglected in the mean–field approach. A pedagogical introduction of the Wigner function is performed, laying on familiar concepts associated with the phase–space formulation of classical mechanics. The extension to quantum mechanics is quite straightforward, but the price to pay is high: the Wigner function is not a genuine probability density. Notwithstanding this technical difficulty, this phase–space formulation of quantum mechanics delivers a framework where expectation values are obtained as phase–space averages with functions, not quantum operators. The motion equation for the Wigner function is however too complex to be solved as such: a truncation of high order terms is performed and gives its name to the method. The resulting motion equation has finally been adapted to the generic scattering configuration we study, so that it is more easily particularised to more specific configurations.

The *fourth chapter* was dedicated to Aharonov–Bohm oscillations in the transmission of particles across the eponymous rings. The Aharonov–Bohm effect, routinely encountered in solid–state physics, is widely discussed in the first part of the chapter. We then described the system we study, made of an atom laser injecting matter plane waves towards the scattering region consisting in two one–dimensional leads connected to an Aharonov–Bohm ring. This system exhibits Aharonov–Bohm oscillations in the transmission of particles across the ring, as a first demonstration of coherence effects. The interplay with many–body interaction effects has then been investigated, both in the mean–field approximation and with the truncated Wigner method, and already reveals a notable effect, as a transmission blockade due to destructive interferences is suspended in the presence of interaction. This blockade suspension is due to incoherent particles that are locally generated within the ring, owing to the presence of interaction at this location.

Adding disorder as a missing ingredient to the previous chapter brings a novel physics that was discussed in the *fifth chapter*. Indeed, in the presence of a smooth and weak correlated disorder in the ring, Aharonov–Bohm oscillations leave the room to half-period and double frequency oscillations referred to as Al’tshuler–Aronov–Spivak oscillations. Those oscillations are revealed in the ensemble average of the transmission, required to produce reliable predictions. A mean-field theory of those oscillations was first discussed, based on the semi-classical Green’s function of the system that is expressed as a sum over all classical scattering paths that join an arbitrary point to another one. Those paths are best understood with the diagrammatic representation that is introduced, paving the way for the full resummation performed in Chapter 6. This pictorial expression for the Green’s function brings to light the common mechanism between those oscillations, weak localisation and coherent backscattering. Then, the discretised field equations were numerically integrated in the presence of interaction, which revealed the advent of a subtle interplay between disorder and interaction: Al’tshuler–Aronov–Spivak oscillations are inverted. This inversion, and more specifically its prevalence, was investigated thanks to the truncated Wigner method in a regime that goes beyond mean-field. Those simulations indicated that the inversion is subject to dephasing and could be observed for instance with  $^{39}\text{K}$  atoms whose s-wave scattering length may be tuned to very low values.

The *sixth chapter* was devoted to the development of a diagrammatic theory of Al’tshuler–Aronov–Spivak oscillations in the ensemble averaged transmission. Based on the diagrammatic formulation of the noninteracting Green’s function in Chapter 5, we reported a full resummation of the scattering paths appearing in the Green’s function, as was performed by our collaborator, Dr. Josef Rammensee. The focus was brought on the diagrams describing oscillatory motion within the ring. They indeed contain all the ingredients that are necessary to obtain Al’tshuler–Aronov–Spivak oscillations. The full resummation was performed by regrouping similar diagrams into families which are related through symmetry operations and a self-consistent equation. A similar procedure was employed for deriving a perturbative expansion in the nonlinear parameter. Owing to the large number of diagrams involved in the computation, this expansion is limited to the first order in the nonlinearity. We have finally compared our numerical findings with the predictions of the interacting diagrammatic theory and they turned out to be in very good agreement in a regime of very weak interaction. At stronger interaction, significant deviations occurred, indicating missing ingredients in the theory, such as higher order terms in the perturbative expansion for example.

The *seventh chapter* focussed on the two-dimensional transport of ultracold bosonic atoms in a disorder potential and in the presence of atom–atom interaction. We clarified the scattering region we studied, which is very similar to the experimental configuration in Ref. [57]. Coherent backscattering was encountered both in the ensemble averaged momentum distribution and in the backscattered current. The presence of interaction in the disordered region yielded an inversion of coherent backscattering, in a fashion similar to what we encountered with Al’tshuler–Aronov–Spivak oscillations. This inversion and its prevalence were also investigated beyond the mean-field approximation by means of the truncated Wigner method. The prominence of dephasing resulting from inelastic scattering is indeed a crucial issue to address in view of guiding experimentalists towards an implementation of a scheme that can

reveal the above-mentioned inversion. We found that despite a partial dephasing, the inversion prevails in a regime that extends beyond mean-field. We also found that  $^{87}\text{Rb}$ , an atomic species routinely employed in ultracold experiments, would constitute a candidate for the observation of the inversion.

In conclusion, the work reported in this manuscript was mainly devoted to the study of matter waves transport in various configurations beyond the traditional mean-field approximation. More generally, this work brings a contribution in the understanding of many-body effects in transport processes in general. Besides a better understanding of mesoscopic physics and more specifically of interaction effects in that context, it also has a remote impact on the implementation of atomtronics devices [32–36]. In this context, the truncated Wigner method has revealed to be a very useful and versatile tool, particularly in the presence of finite interaction where significant deviations with the mean-field approximation were encountered. Other possibilities are also readily offered by this truncated Wigner method, as for instance the modelling of a finite temperature in the reservoir, as is discussed in the perspectives. Finally, we would like to conclude by saying that we would be very keen if our work initiated state-of-the-art transport experiments and stimulated continued research activities.

## Perspectives

A lot of prospects and open questions remain at this point unexplored. The first and most obvious perspective related to our work that is quite accessible in the foreseeable future concerns the study of coherent forward scattering. As is detailed in the end of Chapter 1, this interference effect and the related notable peak (whose structure is twin of the coherent backscattering peak) around the forward direction in the scattered current can be, in some contexts, understood as a signature of Anderson localisation in the momentum space [143]. As a matter of fact, the scattering region we studied in Chapter 7 is particularly well suited for this study. The researched peak is however, as such, completely hidden behind the large intensity peak related to the incident plane wave, as is for instance shown in FIG. 7.5. A solution to circumvent this issue is to compute the current<sup>2</sup> in Eq. (7.41) in a slab located downstream of the disorder potential, which result is provided in FIG. 2.

---

<sup>2</sup>This can be done by extracting  $\tilde{\psi}_n^{(+)} \equiv \alpha_+ \tilde{\psi}^{(+)}$  from Eq. (7.38) and plugging it into Eq. (7.41).



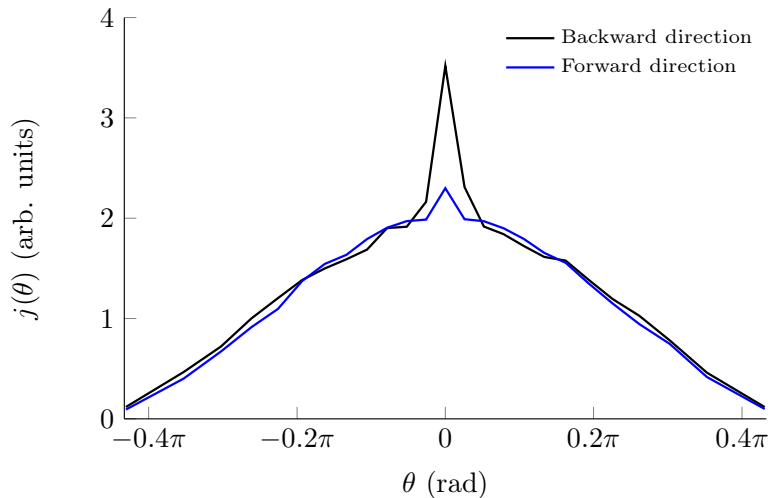


Figure 2 – Angular resolved current as a function of the back (black curve) and the forward scattered (blue curve) angles  $\theta_n = \arcsin[2\pi n/(k\mathcal{W})]$  in the absence of interaction. A low intensity peak appears in the direction related to forward scattering. Numerical parameters:  $k = \sqrt{2m\mu}/\hbar$ ,  $k\delta = 1$ ,  $\sqrt{\mathcal{N}}|\kappa|^2 m/\hbar^2 k^2 = 1$ , 1500 realisations of a gaussian correlated disorder with disorder strength  $V_0 m/\hbar^2 k^2 = 0.1$  and correlation length  $k\sigma = 1$ , length  $k\mathcal{L}_D = 40$  and width  $k\mathcal{W} = 120$ .

As FIG. 2 illustrates, a peak of amplitude smaller than the coherent backscattering peak appears in the forward direction. This result is certainly encouraging, but more investigation is still required to confirm that this peak is due to coherent forward scattering and not, for instance, to a remnant of the incident wave. Either way, the subsequent investigation of interaction effects on coherent forward scattering is an interesting and challenging task that our setup would probably allow to perform.

Other perspectives are still left aside, as for instance the generalisation to three dimensions and the related investigation of many-body effects. This does not pose any conceptual difficulty, but this is however a very demanding numerical task to implement the truncated Wigner method in three dimensions, in particular regarding the generation of quantum noise, that would have a shape similar to that in Eqs. (7.51) and (7.52), but even more challenging owing to the higher dimension of space. We could also refine the description of the source to emancipate from the simplifying hypothesis of an incident plane wave, in a situation closer to what is experimentally encountered. We however do not expect this extension of our study to bring something very different from the message we delivered.

Another exciting perspective consists in the implementation of transport configurations involving more than one reservoir and containing a finite number of atoms. In that context, the most obvious configuration is probably a source–drain scenario. It was already theoretically studied in Refs. [323,373], but also experimentally realised in the group of Tilman Esslinger with fermionic atoms [47] to generate a particle current resulting from a temperature imbalance between the reservoirs. The configuration in Ref. [47] consequently requires the treatment of a finite temperature reservoir, which can actually be quite straightforwardly

handled in the framework of the truncated Wigner method, as the Wigner function related to a thermal state is already derived in Eq. (3.34). It would be interesting to study such a heat engine with bosonic atoms instead, and more particularly to investigate many-body interaction effects in that context, which remains, to our best knowledge, an open issue.

In a much more advanced stage, the understanding of temperature effects, as well as source-drain scenarios, could be leveraged to study a source-drain configuration in the presence of a gate reservoir, (see FIG. 3), the truncated Wigner method providing the suitable framework for that purpose.

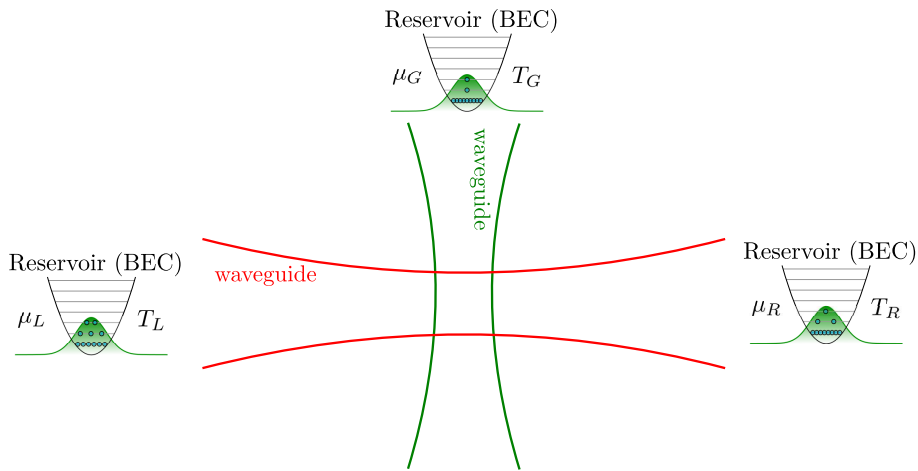


Figure 3 – Schematic theoretical prototype of an atomic transistor where the source consists in a reservoir at the temperature  $T_L$  and the chemical potential  $\mu_L$  and the drain is a reservoir at the temperature  $T_R$  and the chemical potential  $\mu_R$ . A third reservoir at the temperature  $T_G$  and the chemical potential  $\mu_G$  plays the role of the gate in a transistor and controls the current between the source and the drain.

The third reservoir, in a role totally analogous to the gate in an electronic transistor, would control the particle current resulting from a temperature gradient between the reservoirs and would therefore provide a configuration that mimics a transistor with ultracold atoms. This long-sought goal of atomtronics remains however nowadays distant because the challenges are considerable and numerous, but it would certainly be a tremendous progress in the route towards the implementation of a quantum computer.

# Appendix A

## Numerical integration routine

In this appendix, we present the home made numerical integration package we developed, inspired by Ref. [374], for integrating the ordinary differential equations that result from the discretisation of the continuous scattering regions envisaged in this manuscript in terms of regular grids. We first expose the general principle of our routine that relies on a Taylor's expansion of the solution that is propagated on a regular time grid from the initial to the final time.

This method is then readily particularised to the 1D mean-field equations we encountered in the manuscript, with a particular care brought to the nonlinear terms whose derivatives appearing in the Taylor's expansion can be very computation time-consuming if implemented naively. We then generalise this integration routine to the truncated Wigner method. The main challenge introduced by this implementation lies in an effective computation of the noise terms, especially in two dimensions, whose discussion constitutes the end of the appendix.

### A.1 Taylor's method for numerical integration

A Cauchy problem, sometimes referred to as an initial value problem, is formulated in two parts. The first part is an ordinary differential equation

$$\frac{dy}{dt} = \mathbf{f}[\mathbf{y}(t), t], \quad (\text{A.1})$$

where  $\mathbf{y} \equiv (y_1, \dots, y_n)$  is a vector containing the  $n \in \mathbb{N}$  components of the function under study  $\mathbf{f} : \Omega \subseteq (\mathbb{C}^n \times \mathbb{R}) \rightarrow \mathbb{C}^n$ ,  $[\mathbf{y}(t), t] \mapsto \mathbf{f}[\mathbf{y}(t), t]$ , with  $\Omega$  an open subset of  $\mathbb{C}^n \times \mathbb{R}$ . The second part is the initial condition  $\mathbf{y}(t_0) = \mathbf{y}_0$  of the problem<sup>1</sup> that Eq. (A.1) must initially verify.

---

<sup>1</sup>The formulation of an initial value problem expressed in Eq. (A.1) does not only reduce the treatment to first order differential equations. Indeed, the ordinary differential equation of order  $n$

$$\frac{d^n x}{dt^n} = g[x(t), \dot{x}(t), \dots, x^{(n-1)}(t), t] \quad (\text{A.2})$$

with  $g : \Omega' \subseteq (\mathbb{C}^n \times \mathbb{R}) \rightarrow \mathbb{C}^n$ ,  $[x(t), \dot{x}(t), \dots, x^{(n-1)}(t), t] \mapsto g[x(t), \dot{x}(t), \dots, x^{(n-1)}(t), t]$ , with  $\Omega'$  an open subset of  $\mathbb{C}^n \times \mathbb{R}$ , is perfectly equivalent to Eq. (A.1) provided the vector  $\mathbf{y}$  is defined according to  $\mathbf{y} \equiv [x(t), \dot{x}(t), \dots, x^{(n-1)}(t)]$  and  $f$  according to  $\mathbf{f}[\mathbf{y}(t), t] \equiv g[x(t), \dot{x}(t), \dots, x^{(n-1)}(t), t]$ . In this case, the  $n^{\text{th}}$  order ordinary differential equation is cast into a system of  $n$  coupled first order ordinary differential equations.

A solution of the Cauchy problem is a function  $\mathbf{y}(t)$  that is both solution of Eq. (A.1) and also fulfils the initial condition  $\mathbf{y}(t_0) = \mathbf{y}_0$ . The function  $\mathbf{f}$  appearing in Eq. (A.1) can be nonlinear, or in general even form a system of nonlinear coupled equations, rendering an analytical calculation hard, when feasible. Provided the function  $\mathbf{f}$  is continuous and satisfies the Lipschitz condition, the solution  $\mathbf{y}$  is granted to exist and to be unique thanks to the Picard–Lindelöf theorem.

A very general and systematic way to solve an ordinary differential equation consists in assuming that the solution is sufficiently differentiable to expand it in Taylor series around the initial condition  $t_0$ , which yields

$$\mathbf{y}(t) = \mathbf{y}(t_0) + (t - t_0) \left. \frac{d\mathbf{y}}{dt} \right|_{t_0} + \frac{(t - t_0)^2}{2!} \left. \frac{d^2\mathbf{y}}{dt^2} \right|_{t_0} + \dots \quad (\text{A.3})$$

A systematic and iterative procedure for obtaining  $\mathbf{y}(t)$  at final time  $t_f$  is to propagate the initial condition  $\mathbf{y}(t_0) = \mathbf{y}_0$  from the initial time  $t_0$  step by step to the final time  $t_f$  on a regular grid of  $N + 1$  points equally spaced by  $\delta t$  and labelled  $t_0, t_1, \dots, t_{N-1}, t_N \equiv t_f$ . The propagation is performed thanks to the Taylor expansion in Eq. (A.3) from one point to its nearest neighbour on the grid, in the direction of increasing time. This approach actually boils down to solving a succession of elementary initial value problems. More precisely, the determination of  $\mathbf{y}_{n+1}$ , which is the solution at time  $t \equiv t_0 + (n+1)\delta t$ , amounts to propagating  $\mathbf{y}_n$  from  $t_n \equiv t_0 + n\delta t$  to  $t_{n+1} \equiv t_0 + (n+1)\delta t$ . In other words, this amounts to solving the Cauchy problem between  $t_n$  and  $t_{n+1}$ , consisting in the ordinary differential equation

$$\frac{d\mathbf{y}}{dt} = \mathbf{f}[\mathbf{y}(t), t] \quad (\text{A.4})$$

together with the initial condition  $\mathbf{y}(t_n) = \mathbf{y}_n$ . This is achieved via Eq. (A.3) which specifically reads in this case

$$\mathbf{y}_{n+1} = \mathbf{y}_n + \delta t \frac{d\mathbf{y}_n}{dt} + \frac{1}{2}(\delta t)^2 \frac{d^2\mathbf{y}_n}{dt^2} + \dots \quad (\text{A.5})$$

and which is used repeatedly until reaching the final time  $t_f$ , as is sketched below

$$\mathbf{y}_{n+1} = \mathbf{y}_n + \delta t \dot{\mathbf{y}}_n + \frac{\delta t^2}{2!} \ddot{\mathbf{y}}_n + \dots$$

The explicit evaluation of the derivatives up to the desired order at each grid point is required to perform the propagation. The first order derivative is actually already provided by the ordinary differential equation (A.1) itself and takes on, at time  $t_n$ , the form  $\dot{\mathbf{y}}_n = \mathbf{f}[\mathbf{y}_n, t_n]$ . The second derivative at time  $t_n$  is obtained by using the chain rule

$$\frac{d^2\mathbf{y}_n}{dt^2} = \left( \frac{\partial \mathbf{f}}{\partial t} + (\nabla \mathbf{f}) \frac{\partial \mathbf{y}}{\partial t} \right) \Bigg|_{\mathbf{y}_n, t_n} = \left( \frac{\partial \mathbf{f}}{\partial t} + (\mathbf{f} \cdot \nabla) \mathbf{f} \right) \Bigg|_{\mathbf{y}_n, t_n}. \quad (\text{A.6})$$

Higher order derivatives are computed similarly, so that the  $n^{\text{th}}$  derivative is obtained iteratively from the  $(n - 1)^{\text{th}}$  derivative. The propagation equation therefore reads

$$\mathbf{y}_{n+1} = \mathbf{y}_n + \delta t f[\mathbf{y}_n, t_n] + \frac{1}{2}(\delta t)^2 \left( \frac{\partial \mathbf{f}}{\partial t} + (\mathbf{f} \cdot \nabla) \mathbf{f} \right) \Big|_{\mathbf{y}_n, t_n} + \dots \quad (\text{A.7})$$

The quality of the approximation provided by successive propagations of Eq. (A.7) can be quite good, particularly as the order of the derivative considered in the expansion is large and the timestep  $\delta t$  small (compared to the convergence radius of the expansion). Practically, a compromise between both is realised. One may for instance choose a rather large timestep and obtain accurate results if the expansion includes derivatives of sufficiently high order, which is particularly interesting when those derivatives are analytically known.

This is also one of the few limitations of Taylor's method (which a priori applies to any ordinary differential equation). It indeed requires the calculability of the derivatives up to the desired order, which is not always granted. Additionally, crossed terms appearing in the explicit computation of the derivatives may render the process tedious and inefficient. In some cases however, the structure of the ordinary differential equation allows to derive those derivatives analytically, as we show below. Automatic differentiation techniques [375–379] may also be applied to avoid this disadvantage.

## A.2 Numerical routine for integrating the one-dimensional field equations

The finite difference scheme we use to discretise the one-dimensional space results in a lattice of ordinary differential equations that we numerically integrate following the afore-explained procedure. The discrete wavefunction at site  $\alpha$  is expanded in Taylor series and is propagated from time  $t$  to time  $t + \delta t$  up to order  $N_{\text{max}}$  according to

$$\psi_\alpha(t + \delta t) = \psi_\alpha(t) + \delta t \frac{d\psi_\alpha}{dt}(t) + \frac{1}{2}(\delta t)^2 \frac{d^2\psi_\alpha}{dt^2}(t) + \dots \quad (\text{A.8})$$

$$= \sum_{n=0}^{N_{\text{max}}} \frac{1}{n!} (\delta t)^n \frac{d^n \psi_\alpha}{dt^n}(t) + \mathcal{O}[(\delta t)^{N_{\text{max}}+1}], \quad (\text{A.9})$$

which is repeatedly used to cross the time grid from initial time  $t_0$  to final time  $t$  step by step. The derivatives of the on-site wavefunction  $\psi_\alpha$  are found by successive differentiation of the field equation at site  $\alpha$ . This equation reads

$$i\hbar \frac{d}{dt} \psi_\alpha(t) = \left( \frac{E_\delta}{q_\alpha} - \mu q_\alpha + V_\alpha \right) \psi_\alpha(t) + g_\alpha |\psi_\alpha(t)|^2 \psi_\alpha(t) + \kappa(t) \sqrt{\mathcal{N}} \delta_{\alpha\beta} \\ - \frac{E_\delta}{2} \left[ \left( \frac{1}{q_{\alpha+1}} + \frac{\delta q'_{\alpha+1}}{2 q_{\alpha+1}^2} \right) \psi_{\alpha+1}(t) + \left( \frac{1}{q_{\alpha-1}} - \frac{\delta q'_{\alpha-1}}{2 q_{\alpha-1}^2} \right) \psi_{\alpha-1}(t) \right]. \quad (\text{A.10})$$

Higher order derivatives are then obtained by differentiating Eq. (A.10) as many times as requested. Omitting the explicit  $t$  dependence, this procedure gives, for instance for the

second and third derivatives,

$$i\hbar\ddot{\psi}_\alpha = \left(\frac{E_\delta}{q_\alpha} - \mu q_\alpha + V_\alpha\right) \dot{\psi}_\alpha - \frac{E_\delta}{2} \left[ \left(\frac{1}{q_{\alpha+1}} + \frac{\delta q'_{\alpha+1}}{2 q_{\alpha+1}^2}\right) \dot{\psi}_{\alpha+1} + \left(\frac{1}{q_{\alpha-1}} - \frac{\delta q'_{\alpha-1}}{2 q_{\alpha-1}^2}\right) \dot{\psi}_{\alpha-1} \right] + g_\alpha \left( \dot{\psi}_\alpha^* \psi_\alpha \psi_\alpha + \psi_\alpha^* \dot{\psi}_\alpha \psi_\alpha + \psi_\alpha^* \psi_\alpha \dot{\psi}_\alpha \right) \quad (\text{A.11})$$

$$i\hbar\ddot{\ddot{\psi}}_\alpha = \left(\frac{E_\delta}{q_\alpha} - \mu q_\alpha + V_\alpha\right) \ddot{\psi}_\alpha - \frac{E_\delta}{2} \left[ \left(\frac{1}{q_{\alpha+1}} + \frac{\delta q'_{\alpha+1}}{2 q_{\alpha+1}^2}\right) \ddot{\psi}_{\alpha+1} + \left(\frac{1}{q_{\alpha-1}} - \frac{\delta q'_{\alpha-1}}{2 q_{\alpha-1}^2}\right) \ddot{\psi}_{\alpha-1} \right] + g_\alpha \left( \ddot{\psi}_\alpha^* \psi_\alpha \psi_\alpha + \psi_\alpha^* \ddot{\psi}_\alpha \psi_\alpha + \psi_\alpha^* \psi_\alpha \ddot{\psi}_\alpha + 2\dot{\psi}_\alpha^* \dot{\psi}_\alpha \psi_\alpha + 2\dot{\psi}_\alpha^* \psi_\alpha \dot{\psi}_\alpha + 2\psi_\alpha^* \dot{\psi}_\alpha \dot{\psi}_\alpha \right) \quad (\text{A.12})$$

⋮

We then inject those expressions in the Taylor expansion (A.9). In the differentiation process, since in the manuscript  $\kappa(t)$  is a function that is adiabatically and smoothly ramped to a constant value, we treat the source term as a constant with respect to  $t$ . Whilst the computation of the wavefunction derivatives is straightforward and iterative, terms appearing in the derivatives of the nonlinear term in Eq. (A.10) generally require an important computation time. We may however leverage the specific pattern appearing as we can write the  $n^{\text{th}}$  derivative of the nonlinear term as

$$\frac{d^n}{dt^n} [\psi_\alpha^*(t) \psi_\alpha^2(t)] = \sum_{k=0}^n \binom{n}{k} \frac{d^k}{dt^k} \psi_\alpha^*(t) \frac{d^{n-k}}{dt^{n-k}} \psi_\alpha^2(t), \quad (\text{A.13})$$

where  $\binom{n}{k}$  is the binomial coefficient and the derivative of order  $\nu = (n - k)$  of  $\psi_\alpha^2(t)$  is found to be

$$\frac{d^\nu}{dt^\nu} \psi_\alpha^2(t) = \sum_{\lambda=0}^{\nu} \binom{\nu}{\lambda} \frac{d^\lambda}{dt^\lambda} \psi_\alpha(t) \frac{d^{\nu-\lambda}}{dt^{\nu-\lambda}} \psi_\alpha(t), \quad (\text{A.14})$$

which allows one to cast the  $n^{\text{th}}$  derivative of the nonlinear term into the compact expression

$$\frac{d^n}{dt^n} [\psi_\alpha^*(t) \psi_\alpha^2(t)] = \sum_{k=0}^n \sum_{\lambda=0}^{n-k} \binom{n}{k, \lambda, n-k-\lambda} \frac{d^k}{dt^k} \psi_\alpha^*(t) \frac{d^\lambda}{dt^\lambda} \psi_\alpha(t) \frac{d^{n-k-\lambda}}{dt^{n-k-\lambda}} \psi_\alpha(t), \quad (\text{A.15})$$

where  $\binom{n}{k, \lambda, n-k-\lambda}$  is the trinomial coefficient. An efficient computation of the latter is obtained thanks to Pascal pyramid, where the following recursion relation is used

$$\binom{n}{k, \nu, n-k-\nu} = \binom{n-1}{k-1, \nu, n-k-\nu} + \binom{n-1}{k, \nu-1, n-k-\nu} + \binom{n-1}{k, \nu, n-k-\nu-1}, \quad (\text{A.16})$$

showing that the  $n^{\text{th}}$  level of the pyramid is built from the  $n-1^{\text{th}}$  one, as is shown in FIG. A.1.

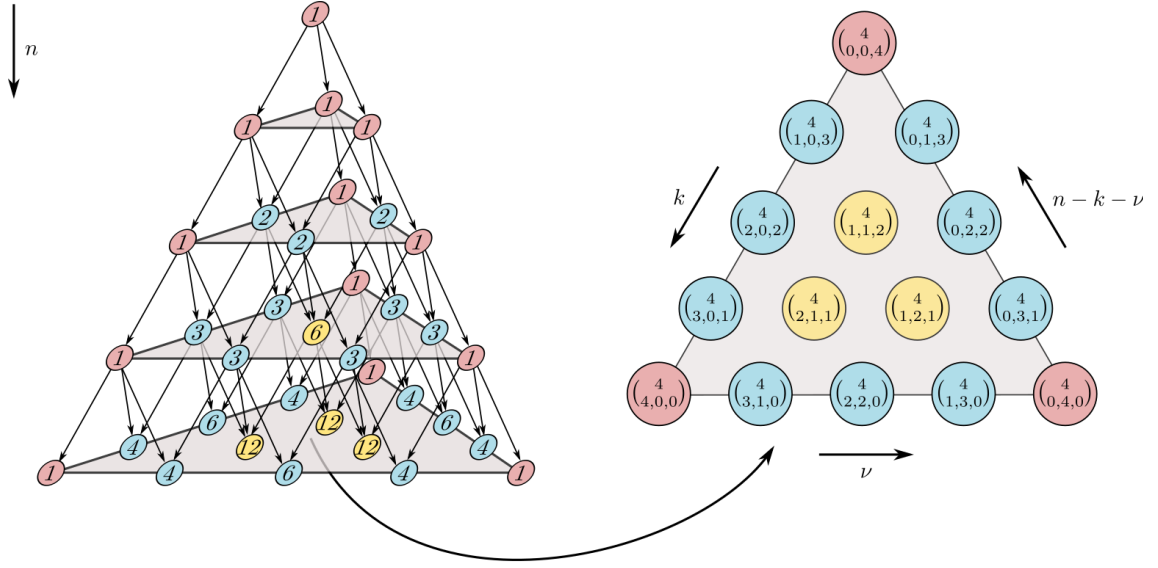


Figure A.1 – Pascal pyramid showing how trinomial coefficients of the  $n^{\text{th}}$  layer of the pyramid can be built recursively from those of the  $n - 1^{\text{th}}$  layer.

The  $n^{\text{th}}$  derivative of the on-site wavefunction  $\psi_\alpha$  is then explicitly written and computed as

$$\begin{aligned}
 i\hbar \frac{d^n}{dt^n} \psi_\alpha(t) &= \left( \frac{E_\delta}{q_\alpha} - \mu q_\alpha + V_\alpha \right) \frac{d^{n-1}}{dt^{n-1}} \psi_\alpha(t) \\
 &- \frac{E_\delta}{2} \left[ \left( \frac{1}{q_{\alpha+1}} + \frac{\delta q'_{\alpha+1}}{2 q_{\alpha+1}^2} \right) \frac{d^{n-1}}{dt^{n-1}} \psi_{\alpha+1}(t) + \left( \frac{1}{q_{\alpha-1}} - \frac{\delta q'_{\alpha-1}}{2 q_{\alpha-1}^2} \right) \frac{d^{n-1}}{dt^{n-1}} \psi_{\alpha-1}(t) \right] \\
 &+ g_\alpha \sum_{k=0}^n \sum_{\lambda=0}^{n-k} \binom{n}{k, \lambda, n-k-\lambda} \frac{d^k}{dt^k} \psi_\alpha^*(t) \frac{d^\lambda}{dt^\lambda} \psi_\alpha(t) \frac{d^{n-k-\lambda}}{dt^{n-k-\lambda}} \psi_\alpha(t), \quad (\text{A.17})
 \end{aligned}$$

where the Pascal pyramid and the related trinomial coefficients are computed and stored at the beginning of the computation for the sake of efficiency.

### A.3 Numerical routine for integrating the one-dimensional field equations resulting from the truncated Wigner method

In this case, the field equations for the classical field  $\psi_\alpha$  at site  $\alpha$ , are very similar to Eq. (A.10) and read

$$\begin{aligned}
 i\hbar \frac{d}{dt} \psi_\alpha(t) &= \left( \frac{E_\delta}{q_\alpha} - \mu q_\alpha + V_\alpha \right) \psi_\alpha(t) + g_\alpha (|\psi_\alpha(t)|^2 - 1) \psi_\alpha(t) + \kappa(t) \sqrt{\mathcal{N}} \delta_{\alpha, \alpha_S} \\
 &- \frac{E_\delta}{2} \left[ \left( \frac{1}{q_{\alpha+1}} + \frac{\delta q'_{\alpha+1}}{2 q_{\alpha+1}^2} \right) \psi_{\alpha+1}(t) + \left( \frac{1}{q_{\alpha-1}} - \frac{\delta q'_{\alpha-1}}{2 q_{\alpha-1}^2} \right) \psi_{\alpha-1}(t) \right] \\
 &+ \chi_{\text{in,L}}(t) \delta_{\alpha, \alpha_L} + \chi_{\text{in,R}}(t) \delta_{\alpha, \alpha_R}, \quad (\text{A.18})
 \end{aligned}$$

where

$$\begin{aligned}\chi_{\text{in,L}}(t) &= E_\delta \sum_{\alpha'=0}^{\alpha_L-1} M_{\alpha'-\alpha_L}(t-t_0)\psi_{\alpha'}(t_0) \\ \chi_{\text{in,R}}(t) &= -E_\delta \sum_{\alpha'=\alpha_R+1}^{\alpha_{\text{out}}} M_{\alpha'-\alpha_R}(t-t_0)\psi_{\alpha'}(t_0)\end{aligned}$$

and with

$$M_\alpha(\tau) = \frac{i^\alpha}{2} \left[ J_{\alpha-1} \left( \frac{E_\delta \tau}{\hbar} \right) + J_{\alpha-1} \left( \frac{E_\delta \tau}{\hbar} \right) \right] e^{-i(E_\delta - \mu)\tau/\hbar} \equiv L_\alpha(\tau) e^{-i(E_\delta - \mu)\tau/\hbar}, \quad (\text{A.19})$$

with  $\alpha_L$  (resp.  $\alpha_R$ ) the first (resp. last) site of the scattering region and  $\alpha_{\text{out}} = \alpha_R + N_{\text{SECS}}$  the last site downstream of the scattering region in the presence of a complex region. These quantum noise terms consist in a summation over all sites required for complex scaling, both in the left and right neighbour regions of the scattering region, of (up to less important factors) products of Bessel functions and initial amplitudes of the classical fields  $\psi_\alpha(t_0)$ . Omitting once again the explicit  $t$  dependence, the derivatives of the propagation equation remain essentially the same and read

$$\begin{aligned}i\hbar\dot{\psi}_\alpha &= \left( \frac{E_\delta}{q_\alpha} - \mu q_\alpha + V_\alpha \right) \dot{\psi}_\alpha - \frac{E_\delta}{2} \left[ \left( \frac{1}{q_{\alpha+1}} + \frac{\delta q'_{\alpha+1}}{2 q_{\alpha+1}^2} \right) \dot{\psi}_{\alpha+1} + \left( \frac{1}{q_{\alpha-1}} - \frac{\delta q'_{\alpha-1}}{2 q_{\alpha-1}^2} \right) \dot{\psi}_{\alpha-1} \right] \\ &\quad + g_\alpha \left( \dot{\psi}_\alpha^* \psi_\alpha \psi_\alpha + \psi_\alpha^* \dot{\psi}_\alpha \psi_\alpha + \psi_\alpha^* \psi_\alpha \dot{\psi}_\alpha \right) - g_\alpha \dot{\psi}_\alpha + \dot{\chi}_{\text{in,L}}(t) \delta_{\alpha,\alpha_L} + \dot{\chi}_{\text{in,R}}(t) \delta_{\alpha,\alpha_R}\end{aligned} \quad (\text{A.20})$$

$$\begin{aligned}i\hbar\ddot{\psi}_\alpha &= \left( \frac{E_\delta}{q_\alpha} - \mu q_\alpha + V_\alpha \right) \ddot{\psi}_\alpha - \frac{E_\delta}{2} \left[ \left( \frac{1}{q_{\alpha+1}} + \frac{\delta q'_{\alpha+1}}{2 q_{\alpha+1}^2} \right) \ddot{\psi}_{\alpha+1} + \left( \frac{1}{q_{\alpha-1}} - \frac{\delta q'_{\alpha-1}}{2 q_{\alpha-1}^2} \right) \ddot{\psi}_{\alpha-1} \right] \\ &\quad + g_\alpha \left( \ddot{\psi}_\alpha^* \psi_\alpha \psi_\alpha + \psi_\alpha^* \ddot{\psi}_\alpha \psi_\alpha + \psi_\alpha^* \psi_\alpha \ddot{\psi}_\alpha \right. \\ &\quad \left. + 2\dot{\psi}_\alpha^* \dot{\psi}_\alpha \psi_\alpha + 2\dot{\psi}_\alpha^* \psi_\alpha \dot{\psi}_\alpha + 2\psi_\alpha^* \dot{\psi}_\alpha \dot{\psi}_\alpha \right) - g_\alpha \ddot{\psi}_\alpha + \ddot{\chi}_{\text{in,L}}(t) \delta_{\alpha,\alpha_L} + \ddot{\chi}_{\text{in,R}}(t) \delta_{\alpha,\alpha_R} \\ &\quad \vdots\end{aligned} \quad (\text{A.21})$$

The derivatives of the noise terms coming from the left,  $\chi_{\text{in}}$ , and the right,  $\chi_{\text{out}}$ , of the system are directly<sup>2</sup> related to the derivatives of  $M_\alpha(\tau)$  which can be themselves related to those of

---

<sup>2</sup>Since  $\dot{\psi}_\alpha(t_0)$  and all higher order derivatives terms are equal to zero.



the Bessel functions of the first kind

$$\begin{aligned} \dot{M}_\alpha(\tau) &= \frac{i^\alpha}{2} \left[ \dot{J}_{\alpha-1} \left( \frac{E_\delta \tau}{\hbar} \right) + \dot{J}_{\alpha+1} \left( \frac{E_\delta \tau}{\hbar} \right) \right] e^{-i(E_\delta - \mu)\tau/\hbar} \\ &\quad + \frac{i^\alpha}{2} [-i(E_\delta - \mu)] \left[ J_{\alpha-1} \left( \frac{E_\delta \tau}{\hbar} \right) + J_{\alpha+1} \left( \frac{E_\delta \tau}{\hbar} \right) \right] e^{-i(E_\delta - \mu)\tau/\hbar} \end{aligned} \quad (\text{A.22})$$

$$\begin{aligned} \ddot{M}_\alpha(\tau) &= \frac{i^\alpha}{2} \left[ \ddot{J}_{\alpha-1} \left( \frac{E_\delta \tau}{\hbar} \right) + \ddot{J}_{\alpha+1} \left( \frac{E_\delta \tau}{\hbar} \right) \right] e^{-i(E_\delta - \mu)\tau/\hbar} \\ &\quad + 2 \frac{i^\alpha}{2} [-i(E_\delta - \mu)] \left[ \dot{J}_{\alpha-1} \left( \frac{E_\delta \tau}{\hbar} \right) + \dot{J}_{\alpha+1} \left( \frac{E_\delta \tau}{\hbar} \right) \right] e^{-i(E_\delta - \mu)\tau/\hbar} \\ &\quad + \frac{i^\alpha}{2} [-i(E_\delta - \mu)]^2 \left[ J_{\alpha-1} \left( \frac{E_\delta \tau}{\hbar} \right) + J_{\alpha+1} \left( \frac{E_\delta \tau}{\hbar} \right) \right] e^{-i(E_\delta - \mu)\tau/\hbar} \end{aligned} \quad (\text{A.23})$$

$$\begin{aligned} \dddot{M}_\alpha(\tau) &= \frac{i^\alpha}{2} \left[ \dddot{J}_{\alpha-1} \left( \frac{E_\delta \tau}{\hbar} \right) + \dddot{J}_{\alpha+1} \left( \frac{E_\delta \tau}{\hbar} \right) \right] e^{-i(E_\delta - \mu)\tau/\hbar} \\ &\quad + 3 \frac{i^\alpha}{2} [-i(E_\delta - \mu)] \left[ \ddot{J}_{\alpha-1} \left( \frac{E_\delta \tau}{\hbar} \right) + \ddot{J}_{\alpha+1} \left( \frac{E_\delta \tau}{\hbar} \right) \right] e^{-i(E_\delta - \mu)\tau/\hbar} \\ &\quad + 3 \frac{i^\alpha}{2} [-i(E_\delta - \mu)]^2 \left[ \dot{J}_{\alpha-1} \left( \frac{E_\delta \tau}{\hbar} \right) + \dot{J}_{\alpha+1} \left( \frac{E_\delta \tau}{\hbar} \right) \right] e^{-i(E_\delta - \mu)\tau/\hbar} \end{aligned} \quad (\text{A.24})$$

$$+ \frac{i^\alpha}{2} [-i(E_\delta - \mu)]^3 \left[ J_{\alpha-1} \left( \frac{E_\delta \tau}{\hbar} \right) + J_{\alpha+1} \left( \frac{E_\delta \tau}{\hbar} \right) \right] e^{-i(E_\delta - \mu)\tau/\hbar} \quad (\text{A.25})$$

⋮

We observe that the  $n^{\text{th}}$  derivative of  $M_\alpha(\tau)$  depends upon the  $n^{\text{th}}$  derivative (and all lower order) derivatives of Bessel functions and that the derivatives of an order  $n' \leq n$ , can be stored in a common factor with a prefactor given by the binomial coefficient  $\binom{n}{n'}$  times  $[i(E_\delta - \mu)]^{(n-n')}$ , which yields

$$\frac{d^n M_\alpha(\tau)}{d\tau^n} = \frac{i^\alpha}{2} \sum_{n'=0}^n \binom{n}{n'} [-i(E_\delta - \mu)]^{(n-n')} \left[ \frac{d^{n'} J_{\alpha-1} \left( \frac{E_\delta \tau}{\hbar} \right)}{d\tau^{n'}} + \frac{d^{n'} J_{\alpha+1} \left( \frac{E_\delta \tau}{\hbar} \right)}{d\tau^{n'}} \right] e^{-i(E_\delta - \mu)\tau/\hbar}. \quad (\text{A.26})$$

The  $n^{\text{th}}$  derivative of  $M_\alpha(\tau)$  can obviously be computed from all lower derivatives and from the derivatives of Bessel functions of the first kind  $J_\nu(z)$  which can all be computed exploiting the following property

$$\frac{dJ_\nu(z)}{dz} = \frac{1}{2} [J_{\nu-1}(z) - J_{\nu+1}(z)]. \quad (\text{A.27})$$

Higher order derivatives of  $J_\nu(z)$  are then given by

$$\frac{d^2 J_\nu(z)}{dz^2} = \frac{1}{4} [J_{\nu-2}(z) - 2J_\nu(z) + J_{\nu+2}(z)] \quad (\text{A.28})$$

$$\frac{d^3 J_\nu(z)}{dz^3} = \frac{1}{8} [J_{\nu-3}(z) - 3J_{\nu-1}(z) + 3J_{\nu+1}(z) - J_{\nu+3}(z)] \quad (\text{A.29})$$

$$\frac{d^4 J_\nu(z)}{dz^4} = \frac{1}{16} [J_{\nu-4}(z) - 4J_{\nu-2}(z) + 6J_\nu(z) - 4J_{\nu+2}(z) + J_{\nu+4}(z)] \quad (\text{A.30})$$

⋮

$$\frac{d^n J_\nu(z)}{dz^n} = \frac{1}{2^n} \sum_{\nu'=0}^n (-1)^{\nu'} \binom{n}{\nu'} J_{\nu+2\nu'-n}(z), \quad (\text{A.31})$$

where  $\binom{n}{\nu'}$  is the binomial coefficient that can be efficiently computed through the building of Pascal triangle. One can further take advantage of the symmetry of the Bessel functions with respect to  $\nu$  that reads

$$J_{-\nu}(z) = (-1)^\nu J_\nu(z) \quad (\text{A.32})$$

to derive the same symmetry property for the  $n^{\text{th}}$  derivative

$$\begin{aligned} \frac{d^n J_{-\nu}(z)}{dz^n} &= \frac{1}{2^n} \sum_{\nu'=0}^n (-1)^{\nu'} \binom{n}{\nu'} J_{-\nu+2\nu'-n}(z) = \frac{1}{2^n} \sum_{\nu'=0}^n (-1)^{\nu'} \binom{n}{\nu'} J_{-(\nu-2\nu'+n)}(z) \\ &= \frac{1}{2^n} \sum_{\nu'=0}^n (-1)^{\nu'} (-1)^{(\nu-2\nu'+n)} \binom{n}{\nu'} J_{\nu-2\nu'+n}(z) \\ &= \frac{1}{2^n} (-1)^{(\nu+n)} \sum_{\nu'=0}^n (-1)^{-\nu'} \binom{n}{\nu'} J_{\nu-2\nu'+n}(z) \\ &= \frac{1}{2^n} (-1)^{(\nu+n)} \sum_{\nu''=n}^0 (-1)^{(\nu''-n)} \binom{n}{n-\nu''} J_{\nu+2\nu''-n}(z) \\ &= \frac{1}{2^n} (-1)^\nu \sum_{\nu''=0}^n (-1)^{\nu''} \binom{n}{\nu''} J_{\nu+2\nu''-n}(z) = (-1)^{\nu+n} \frac{d^n J_\nu(z)}{dz^n}, \end{aligned} \quad (\text{A.33})$$

which is numerically exploited to spare the computation of derivatives related to a negative order.

The  $n^{\text{th}}$  derivative of the noise terms finally reads (where, without loss of generality, we have set  $t_0 = 0$  for the sake of clarity and brevity)

$$\begin{aligned} \frac{d^n \chi_{\text{in,L}}(t)}{dt^n} &= E_\delta \sum_{\alpha'=0}^{\alpha_L-1} \left\{ \frac{i^\alpha}{2} \sum_{n'=0}^n \binom{n}{n'} [i(E_\delta - \mu)]^{(n-n')} \right. \\ &\quad \left[ \frac{1}{2^{n'}} \sum_{\nu'=0}^{n'} (-1)^{\nu'} \binom{n'}{\nu'} J_{\alpha-1+2\nu'-n'} \left( \frac{E_\delta t}{\hbar} \right) \right. \\ &\quad \left. \left. + \frac{1}{2^{n'}} \sum_{\nu'=0}^{n'} (-1)^{\nu'} \binom{n'}{\nu'} J_{\alpha+1+2\nu'-n'} \left( \frac{E_\delta t}{\hbar} \right) \right] e^{i(E_\delta - \mu)t/\hbar} \right\} \psi_{\alpha'}(0) \end{aligned} \quad (\text{A.34})$$

$$\begin{aligned} \frac{d^k \chi_{\text{in,R}}(t)}{dt^n} &= -E_\delta \sum_{\alpha'=\alpha_R+1}^{\alpha_{\text{out}}} \left\{ \frac{i^\alpha}{2} \sum_{n'=0}^n \binom{n}{n'} [i(E_\delta - \mu)]^{(n-n')} \right. \\ &\quad \left[ \frac{1}{2^{n'}} \sum_{\nu'=0}^{n'} (-1)^{\nu'} \binom{n'}{\nu'} J_{\alpha-1+2\nu'-n'} \left( \frac{E_\delta t}{\hbar} \right) \right. \\ &\quad \left. \left. + \frac{1}{2^{k'}} \sum_{\nu'=0}^{n'} (-1)^{\nu'} \binom{n'}{\nu'} J_{\alpha+1+2\nu'-n'} \left( \frac{E_\delta t}{\hbar} \right) \right] e^{i(E_\delta - \mu)t/\hbar} \right\} \psi_{\alpha'}(0). \end{aligned} \quad (\text{A.35})$$

The  $n^{\text{th}}$  derivative of the field amplitudes  $\psi_\alpha$  is then explicitly written and computed as

$$\begin{aligned}
i\hbar \frac{d^n}{dt^n} \psi_\alpha(t) &= \left( \frac{E_\delta}{q_\alpha} - \mu q_\alpha + V_\alpha \right) \frac{d^{n-1}}{dt^{n-1}} \psi_\alpha(t) \\
&- \frac{E_\delta}{2} \left[ \left( \frac{1}{q_{\alpha+1}} + \frac{\delta q'_{\alpha+1}}{2 q_{\alpha+1}^2} \right) \frac{d^{n-1}}{dt^{n-1}} \psi_{\alpha+1}(t) + \left( \frac{1}{q_{\alpha-1}} - \frac{\delta q'_{\alpha-1}}{2 q_{\alpha-1}^2} \right) \frac{d^{n-1}}{dt^{n-1}} \psi_{\alpha-1}(t) \right] \\
&+ g_\alpha \sum_{k=0}^n \sum_{\lambda=0}^{n-k} \binom{n}{k, \lambda, n-k-\lambda} \frac{d^k}{dt^k} \psi_\alpha^*(t) \frac{d^\lambda}{dt^\lambda} \psi_\alpha(t) \frac{d^{n-k-\lambda}}{dt^{n-k-\lambda}} \psi_\alpha(t) - g_\alpha \frac{d^{n-1}}{dt^{n-1}} \psi_\alpha(t) \\
&+ \frac{d^{n-1}}{dt^{n-1}} \chi_{\text{in},L}(t) \delta_{\alpha,\alpha_L} + \frac{d^{n-1}}{dt^{n-1}} \chi_{\text{in},R}(t) \delta_{\alpha,\alpha_R}, \tag{A.36}
\end{aligned}$$

where, once again, Pascal pyramid and the related trinomial coefficients that appear both in the derivatives on the nonlinear term as well as in the derivatives of the quantum noise terms entering the scattering region, are computed and stored at the beginning of the computation.

## A.4 Numerical routine for integrating the two-dimensional field equations

Two-dimensional field equations possess essentially the same structure as the one-dimensional field equations. They are given by

$$\begin{aligned}
i\hbar \frac{d}{dt} \psi_{l,w}(t) &= \left( \frac{2E_\delta}{q_l} - \mu q_l + V_{l,w} \right) \psi_{l,w}(t) \\
&- \frac{E_\delta}{2} \left[ \left( \frac{1}{q_{l+1}} + \frac{\delta q'_{l+1}}{2 q_{l+1}^2} \right) \psi_{l+1,w}(t) + \left( \frac{1}{q_{l-1}} - \frac{\delta q'_{l-1}}{2 q_{l-1}^2} \right) \psi_{l-1,w}(t) \right] \\
&- \frac{E_\delta}{2} [\psi_{l,w+1}(t) + \psi_{l,w-1}(t)] + g_l |\psi_{l,w}(t)|^2 \psi_{l,w}(t) + \kappa(t) \sqrt{\mathcal{N}} \delta_{l,\alpha_S}, \tag{A.37}
\end{aligned}$$

The derivatives are obtained similarly as for the one-dimensional field equations and can be written

$$\begin{aligned}
i\hbar \frac{d^n}{dt^n} \psi_{l,w}(t) &= \left( \frac{2E_\delta}{q_l} - \mu q_l + V_{l,w} \right) \frac{d^{n-1}}{dt^{n-1}} \psi_{l,w}(t) \\
&- \frac{E_\delta}{2} \left[ \left( \frac{1}{q_{l+1}} + \frac{\delta q'_{l+1}}{2 q_{l+1}^2} \right) \frac{d^{n-1}}{dt^{n-1}} \psi_{l+1,w}(t) + \left( \frac{1}{q_{l-1}} - \frac{\delta q'_{l-1}}{2 q_{l-1}^2} \right) \frac{d^{n-1}}{dt^{n-1}} \psi_{l-1,w}(t) \right] \\
&- \frac{E_\delta}{2} \left[ \frac{d^{n-1}}{dt^{n-1}} \psi_{l,w+1}(t) + \frac{d^{n-1}}{dt^{n-1}} \psi_{l,w-1}(t) \right] \\
&+ g_l \sum_{k=0}^n \sum_{\lambda=0}^{n-k} \binom{n}{k, \lambda, n-k-\lambda} \frac{d^k}{dt^k} \psi_{l,w}^*(t) \frac{d^\lambda}{dt^\lambda} \psi_{l,w}(t) \frac{d^{n-k-\lambda}}{dt^{n-k-\lambda}} \psi_{l,w}(t), \tag{A.38}
\end{aligned}$$

where Pascal pyramid and the related trinomial coefficients are computed and stored at the beginning of the computation.

## A.5 Numerical routine for integrating the two-dimensional field equations resulting from the truncated Wigner method

In this case, the field equations for the classical field  $\psi_{l,w}$  at site  $(l, w)$ , are very similar to Eq. (A.37) and read

$$\begin{aligned}
i\hbar \frac{d}{dt} \psi_{l,w}(t) = & \left( \frac{2E_\delta}{q_l} - \mu q_l + V_{l,w} \right) \psi_{l,w}(t) + g_l (|\psi_{l,w}(t)|^2 - 1) \psi_{l,w}(t) + \kappa(t) \sqrt{\mathcal{N}} \delta_{l,\alpha_S} \\
& - \frac{E_\delta}{2} \left[ \left( \frac{1}{q_{l+1}} + \frac{\delta q'_{l+1}}{2 q_{l+1}^2} \right) \psi_{l+1,w}(t) + \left( \frac{1}{q_{l-1}} - \frac{\delta q'_{l-1}}{2 q_{l-1}^2} \right) \psi_{l-1,w}(t) \right] \\
& - \frac{E_\delta}{2} [\psi_{l,w+1}(t) + \psi_{l,w-1}(t)] \\
& + \chi_{l_L,w}(t) \delta_{l_L,w} + \chi_{l_R,w}(t) \delta_{l_R,w},
\end{aligned} \tag{A.39}$$

where the quantum noise terms entering the scattering region are given by

$$\begin{aligned}
\chi_{l_L,w}(t) = & E_\delta \sum_{w'=0}^{W-1} \sum_{l'=-\infty}^{l_L-1} L_{l'-l_L}(t-t_0) T_{w-w'}(t-t_0) e^{-i(2E_\delta-\mu)(t-t_0)/\hbar} \psi_{l',w'}(t_0) \\
\chi_{l_R,w}(t) = & -E_\delta \sum_{w'=0}^{W-1} \sum_{l'=l_R+1}^{\infty} L_{l'-l_R}(t-t_0) T_{w-w'}(t-t_0) e^{-i(2E_\delta-\mu)(t-t_0)/\hbar} \psi_{l',w'}(t_0)
\end{aligned} \tag{A.40}$$

and with

$$L_\lambda(\tau) = \frac{i^\lambda}{2} \left[ J_{\lambda-1} \left( \frac{E_\delta \tau}{\hbar} \right) + J_{\lambda-1} \left( \frac{E_\delta \tau}{\hbar} \right) \right], \tag{A.41}$$

and

$$T_\omega(z) = \frac{1}{W} \sum_{w'=0}^{W-1} e^{iz \cos(\frac{2\pi w'}{W})} e^{\frac{2\pi i \omega w'}{W}} \simeq i^\omega J_\omega(z), \tag{A.42}$$

which are, respectively, convolution kernels in the longitudinal and transverse directions. Eqs. (A.40) can be further simplified performing the substitutions  $l'' = l' - l_R$  and  $l''' = l' - l_L$ , as well as using the periodicity of the classical fields  $\psi_{l''+l_L,w'} = \psi_{l'',w'}$  and  $\psi_{l'''+l_R,w'} = \psi_{l''',w'}$  yielding, after renaming  $l'' \rightarrow l'$  and  $l''' \rightarrow l'$ ,

$$\begin{aligned}
\chi_{l_L,w}(t) = & E_\delta \sum_{w'=0}^{W-1} \sum_{l'=-\infty}^{-1} L_{l'}(t-t_0) T_{w-w'}(t-t_0) e^{-i(2E_\delta-\mu)(t-t_0)/\hbar} \psi_{l',w'}(t_0) \\
\chi_{l_R,w}(t) = & -E_\delta \sum_{w'=0}^{W-1} \sum_{l'=1}^{\infty} L_{l'}(t-t_0) T_{w-w'}(t-t_0) e^{-i(2E_\delta-\mu)(t-t_0)/\hbar} \psi_{l',w'}(t_0).
\end{aligned} \tag{A.43}$$

Further simplifications occur if we take the discrete Fourier transform of the classical fields at initial time, which leaves the noise terms in Eq. (A.43) totally unchanged. As a matter of fact, the discrete Fourier transform of the zero mean and unit variance gaussian random classical fields  $\psi_{l,w}(t_0)$  yields Fourier coefficients  $\eta_{l,k}$  which are random gaussian variables with the same mean and variance. Taking the discrete Fourier transform of  $\psi_{l,j}(t_0)$  allows us

to rewrite Eq. (A.43), for instance for  $\chi_{l_{R,w}}(t)$ , as

$$\begin{aligned}
\chi_{l_{R,w}}(t) &= -E_\delta \sum_{w'=0}^{W-1} \sum_{l'=1}^{\infty} L_{l'}(t-t_0) T_{w-w'}(t-t_0) e^{-i(2E_\delta-\mu)(t-t_0)/\hbar} \psi_{l',w'}(t_0) \\
&= -E_\delta \sum_{w'=0}^{W-1} \sum_{l'=1}^{\infty} L_{l'}(t-t_0) T_{w-w'}(t-t_0) e^{-i(2E_\delta-\mu)(t-t_0)/\hbar} \left( \frac{1}{\sqrt{W}} \sum_{k=0}^{W-1} \eta_{l',k}(t_0) e^{2\pi i k w'/W} \right) \\
&= -E_\delta \sum_{l'=1}^{\infty} \sum_{k=0}^{W-1} L_{l'}(t-t_0) \underbrace{\left( \frac{1}{\sqrt{W}} \sum_{w'=0}^{W-1} T_{w-w'}(t-t_0) e^{2\pi i k (w'-w)/W} \right)}_{T_k(t-t_0)} \\
&\quad \times e^{2\pi i k w/W} e^{-i(2E_\delta-\mu)(t-t_0)/\hbar} \eta_{l',k}(t_0). \tag{A.44}
\end{aligned}$$

This new kernel in the transverse direction is indeed much more convenient to deal with than the previous one since

$$\begin{aligned}
T_k(t-t_0) &= \frac{1}{\sqrt{W}} \sum_{j'=0}^{W-1} T_{w-w'}(t-t_0) e^{2\pi i k (w'-w)/W} = \frac{1}{\sqrt{W}} \sum_{\lambda=0}^{W-1} T_\lambda(t-t_0) e^{2\pi i k \lambda/W} \\
&= \frac{1}{W\sqrt{W}} \sum_{k'=0}^{W-1} \underbrace{\sum_{\lambda=0}^{W-1} e^{2\pi i \frac{\lambda}{W} (k'-k)}}_{W\delta_{kk'}} e^{i(t-t_0) \cos(2\pi k'/W)} = \frac{1}{\sqrt{W}} e^{i(t-t_0) \cos(2\pi k/W)}, \tag{A.45}
\end{aligned}$$

where we have performed the variable substitution  $\lambda = w - w'$  and once again exploited the periodicity of the terms appearing in the kernel. We finally recognise in the form of the noise term

$$\chi_{l_{R,w}}(t) = -E_\delta e^{-\frac{i}{\hbar}(2E_\delta-\mu)(t-t_0)} \sum_{l'=1}^{\infty} L_{l'}(t-t_0) \sum_{k=0}^{W-1} T_k(t-t_0) \eta_{l',k}(t_0) e^{2\pi i k w/W} \tag{A.46}$$

a discrete Fourier transform performed in the transverse direction, allowing us to write the Fourier coefficients associated with the noise term as

$$\hat{\chi}_{l_{R,k}}(t) = -E_\delta e^{-\frac{i}{\hbar}(2E_\delta-\mu)(t-t_0)} T_k(t-t_0) \sum_{l'=1}^{\infty} L_{l'}(t-t_0) \eta_{l',k}(t_0), \tag{A.47}$$

which is much lighter to compute than the expression of the noise term in the direct space, even considering that the inverse Fourier transform of this latter expression should finally be computed, as can be expedited by the use of fast Fourier transform algorithms. It finally allows us to write the Fourier coefficients associated with both noise terms as

$$\begin{aligned}
\hat{\chi}_{l_{L,k}}(t) &= E_\delta e^{-\frac{i}{\hbar}(2E_\delta-\mu)(t-t_0)} T_k(t-t_0) \sum_{l'=-\infty}^{-1} L_{l'}(t-t_0) \eta_{l',k}(t_0) \\
\hat{\chi}_{l_{R,k}}(t) &= -E_\delta e^{-\frac{i}{\hbar}(2E_\delta-\mu)(t-t_0)} T_k(t-t_0) \sum_{l'=1}^{\infty} L_{l'}(t-t_0) \eta_{l',k}(t_0). \tag{A.48}
\end{aligned}$$

We are now in a position to derive the derivative of order  $n$  of the classical field  $\psi_{l,w}$ . The derivatives of the longitudinal convolution kernel have already been calculated and read

$$\frac{d^n L_l(\tau)}{d\tau^n} = \frac{i^l}{2} \left[ \frac{d^n J_{l-1}\left(\frac{E_\delta \tau}{\hbar}\right)}{d\tau^n} + \frac{d^n J_{l+1}\left(\frac{E_\delta \tau}{\hbar}\right)}{d\tau^n} \right], \quad (\text{A.49})$$

where the  $n^{\text{th}}$  derivative of the Bessel function of the first kind has already been evaluated in Eq. (A.31). The derivatives of the transverse convolution kernel can be repeatedly computed using that property

$$\frac{\partial K_\lambda(z)}{\partial z} = \frac{i}{2} [K_{\lambda-1}(z) + K_{\lambda+1}(z)], \quad (\text{A.50})$$

because this relationship allows for the easy calculation of higher order derivatives that follows

$$\frac{d^2 K_\lambda(z)}{dz^2} = \frac{-1}{4} (K_{\lambda-2}(z) + K_\lambda(z) + K_{\lambda+2}(z)), \quad (\text{A.51})$$

$$\frac{d^3 K_\lambda(z)}{dz^3} = \frac{-i}{8} (K_{\lambda-3}(z) + 3K_{\lambda-1}(z) + 3K_{\lambda+1}(z) + K_{\lambda+3}(z)), \quad (\text{A.52})$$

$$\frac{d^4 K_\lambda(z)}{dz^4} = \frac{1}{16} (K_{\lambda-4}(z) + 4K_{\lambda-2}(z) + 6K_\lambda(z) + 4K_{\lambda+2}(z) + K_{\lambda+4}(z)), \quad (\text{A.53})$$

⋮

$$\frac{d^n K_\lambda(z)}{dz^n} = \left(\frac{i}{2}\right)^n \sum_{\lambda'=0}^n \binom{n}{\lambda'} K_{\lambda+2\lambda'-n}(z). \quad (\text{A.54})$$

Furthermore exploiting the property

$$\frac{d^n}{dt^n} A(t)B(t)C(t) = \sum_{k=0}^n \sum_{\lambda=0}^{n-k} \binom{n}{k, \lambda, n-k-\lambda} \frac{d^k}{dt^k} A(t) \frac{d^\lambda}{dt^\lambda} B(t) \frac{d^{n-k-\lambda}}{dt^{n-k-\lambda}} C(t), \quad (\text{A.55})$$

the form of the convolution kernels derivatives and the derivative of the exponential appearing in the noise terms, one can write

$$\frac{d^n}{dt^n} \hat{\chi}_{l_L, k}(t) = E_\delta \left[ \sum_{l'=-\infty}^{-1} \left( \sum_{k=0}^n \sum_{\lambda=0}^{n-k} \binom{n}{k, \lambda, n-k-\lambda} \frac{d^k}{dt^k} L_{l'}(t-t_0) \frac{d^\lambda}{dt^\lambda} T_k(t-t_0) \frac{d^{n-k-\lambda}}{dt^{n-k-\lambda}} e^{-\frac{i}{\hbar}(2E_\delta - \mu)t} \right) \eta_{l', k}(t_0) \right] \quad (\text{A.56})$$

$$\frac{d^n}{dt^n} \hat{\chi}_{l_R, k}(t) = -E_\delta \left[ \sum_{l'=1}^{\infty} \left( \sum_{k=0}^n \sum_{\lambda=0}^{n-k} \binom{n}{k, \lambda, n-k-\lambda} \frac{d^k}{dt^k} L_{l'}(t-t_0) \frac{d^\lambda}{dt^\lambda} T_k(t-t_0) \frac{d^{n-k-\lambda}}{dt^{n-k-\lambda}} e^{-\frac{i}{\hbar}(2E_\delta - \mu)t} \right) \eta_{l', k}(t_0) \right]. \quad (\text{A.57})$$

Finally, the derivatives of the classical fields which are used in the propagation prescribed in Eq. (A.7) are written

$$\begin{aligned}
i\hbar \frac{d^n}{dt^n} \psi_{l,w}(t) = & \left( \frac{2E_\delta}{q_l} - \mu q_l + V_{l,w} \right) \frac{d^{n-1}}{dt^{n-1}} \psi_{l,w}(t) \\
& - \frac{E_\delta}{2} \left[ \left( \frac{1}{q_{l+1}} + \frac{\delta q'_{l+1}}{2 q_{l+1}^2} \right) \frac{d^{n-1}}{dt^{n-1}} \psi_{l+1,w}(t) + \left( \frac{1}{q_{l-1}} - \frac{\delta q'_{l-1}}{2 q_{l-1}^2} \right) \frac{d^{n-1}}{dt^{n-1}} \psi_{l-1,w}(t) \right] \\
& - \frac{E_\delta}{2} \left[ \frac{d^{n-1}}{dt^{n-1}} \psi_{l,w+1}(t) + \frac{d^{n-1}}{dt^{n-1}} \psi_{l,w-1}(t) \right] \\
& + g_l \sum_{k=0}^n \sum_{\lambda=0}^{n-k} \binom{n}{k, \lambda, n-k-\lambda} \frac{d^k}{dt^k} \psi_{l,w}^*(t) \frac{d^\lambda}{dt^\lambda} \psi_{l,w}(t) \frac{d^{n-k-\lambda}}{dt^{n-k-\lambda}} \psi_{l,w}(t) \\
& + \delta_{l_L,w} \frac{d^{n-1}}{dt^{n-1}} \chi_{l_L,w}(t) + \delta_{l_R,w} \frac{d^{n-1}}{dt^{n-1}} \chi_{l_R,w}(t), \tag{A.58}
\end{aligned}$$

where the  $n^{\text{th}}$  derivatives of  $\chi_{l_L,w}(t)$  and  $\chi_{l_R,w}(t)$  are given in Eqs. (A.56) and (A.57), and where we have renamed  $k \rightarrow w$ .





## Appendix B

# Introduction to Green's functions

Green's functions are a convenient mathematical tool that is used to solve initial (or boundary) value problems. It is used to transform the related linear ordinary (or partial) inhomogeneous differential equation into an integral equation. Despite this kind of equation is not necessarily easier to solve analytically – when it is possible to do so – than the original one, it usually suggests to apply a perturbation theory. In this appendix, we briefly present how Green's functions can be used to solve inhomogeneous ordinary differential equations and how this technique readily generalises to partial differential equations. Specifically, we apply this formalism to the Schrödinger equation and develop the underlying Hamiltonian in a perturbative series which most naturally leads to the Dyson equation for the total Green's function.

### B.1 Green's function of an ordinary differential equation

In this section, we follow the discussion in the following (excellent) reference [380]. An initial value (or Cauchy) problem is determined by a linear differential equation of the form

$$\sum_{n=0}^N a_n(t) \frac{d^n}{dt^n} f(t) = \phi(t) \quad (\text{B.1})$$

for a function  $f(t)$  and a source term  $\phi(t)$ , which can also be written in terms of the differential operator

$$\hat{L}(t) = \sum_{n=0}^N a_n(t) \frac{d^n}{dt^n} \quad (\text{B.2})$$

as  $\hat{L}(t)f(t) = \phi(t)$ . The Cauchy problem is completely determined by Eq. (B.1) along with the related initial conditions  $f^{(n)}(t_0) = f_n$ , with  $n = 0, \dots, N - 1$ , on the function of interest. They provide the state of the system at initial time and allow one to determine the integration constants appearing in the general solution. Such problems frequently appear in physics, especially when  $N = 2$ . The most prominent example of which is Newton's law of motion, where the unknown function  $f(t)$  plays the role of the position of the centre of mass of the studied system and the source term corresponds to the net force applied to that centre-of-mass.

The Green's function  $G(t, t')$  of the system described by Eq. (B.1) is the function (or more generally and rigorously, the distribution) that satisfies the same differential equation as the initial one, but where the source term  $\phi(t)$  in the right hand side of Eq. (B.1) is replaced by a Dirac impulse  $\delta(t - t')$ . It is formally yielded as the solution of

$$\sum_{n=0}^N a_n(t) \frac{d^n}{dt^n} G(t, t') = \delta(t - t') \quad (\text{B.3})$$

or equivalently  $\hat{L}(t)G(t, t') = \delta(t - t')$  and satisfies to the same initial conditions as Eq. (B.1) do. This formal definition for the Green's function provides an interpretation in terms of the impulse response of the system described by Eq. (B.1). It contains all the internal dynamics of the system whilst the source term appearing in the right hand side of Eq. (B.1) corresponds to an external excitation of the system.

The original equation (B.1) can be tedious (or even impossible) to solve analytically, whereas Eq. (B.3) is easier to solve. It permits to obtain the solution of Eq. (B.1) systematically by exploiting the linearity of the differential operator  $\hat{L}$ . Indeed, multiplying (B.3) in operator form by  $\phi(t')$  and integrating over  $t'$  yields

$$\int_{-\infty}^{\infty} \hat{L}(t)G(t, t')\phi(t')dt' = \int_{-\infty}^{\infty} \delta(t - t')\phi(t')dt' = \phi(t), \quad (\text{B.4})$$

which highlights a decomposition of the source term as a linear superposition of time-shifted impulses applied at time  $t'$  and weighted by  $\phi(t')$ . Owing to the linearity of the differential operator, it can be taken outside the integral, which motivates to write the (particular) solution of Eq. (B.1) as the same linear superposition of time-shifted impulse responses at time  $t'$ , also weighted by  $\phi(t')$ . This is formally written as the integral form<sup>1</sup>

$$f_p(t) = \int_{-\infty}^{\infty} G(t, t')\phi(t')dt', \quad (\text{B.5})$$

because  $f_p(t)$  solves  $\hat{L}f_p(t) = \phi(t)$ , that is,  $f_p(t)$  is a solution of Eq. (B.1) whose general solution is given by

$$f(t) = f_h(t) + \int_{-\infty}^{\infty} G(t, t')\phi(t')dt', \quad (\text{B.6})$$

where  $f_h(t)$  is the solution of the associated homogeneous equation  $\hat{L}(t)f_h(t) = 0$ . This highlights that once the Green's function of  $\hat{L}(t)$  is computed, any particular solution due to another external excitation  $\phi'(t)$  is obtained by performing the integral in Eq. (B.5). The task amounts thus to determining the proper Green's function, not only determining the solutions of Eq. (B.3), but also choosing amongst those solutions the one which satisfies the initial (or boundary, in case of a partial differential equation) conditions which are imposed by the problem under study. Finding the Green's function that solves Eq. (B.3) is quite easy when the coefficients are constant but becomes more tedious when they are not. To shed more light on this process, we treat the classical spring-mass system as an example.

---

<sup>1</sup>In case the Green's function depends only on the difference between its arguments  $G(t, t') \equiv G(t - t')$ , as is the case in systems which are invariant under translation, then Eq. (B.5) becomes a convolution product.

### B.1.1 Green's function of the classical harmonic oscillator

The motion of a mass  $m$  attached to a spring of stiffness  $k$  obeys a second order ordinary differential equation resulting from Newton's law of motion that reads

$$\left(\frac{d^2}{dt^2} + \omega_0^2\right)x(t) = \frac{F(t)}{m}, \quad (\text{B.7})$$

where  $\omega_0 = \sqrt{k/m}$  is the eigenfrequency of the system. The Green's function of the system obeys

$$\left(\frac{d^2}{dt^2} + \omega_0^2\right)G(t, t') = \delta(t - t'), \quad (\text{B.8})$$

which gives, in the Fourier space, the following algebraic equation

$$(-\omega^2 + \omega_0^2)\mathcal{G}(\omega) = 1, \quad (\text{B.9})$$

whose solution is given by  $\mathcal{G}(\omega) = -1/(\omega^2 - \omega_0^2)$ . This function possesses two simple poles on the real axis at  $\omega = \pm\omega_0$  which renders it, as such, not integrable over the real axis. The inverse Fourier transform gives the solution of Eq. (B.8) in the direct space as

$$G(t, t') = -\frac{1}{2\pi} \int_{-\infty}^{\infty} \frac{e^{i\omega(t-t')}}{\omega^2 - \omega_0^2} d\omega. \quad (\text{B.10})$$

We evaluate this integral by standard residue calculus, namely by closing the real axis with a semi-circle of radius  $R \rightarrow \infty$  in the lower or upper semi-half plane, depending on the sign of  $(t - t')$ , and applying the residue theorem to evaluate

$$-\frac{1}{2\pi} \lim_{R \rightarrow \infty} \oint_{\Gamma^\pm} \frac{e^{i\omega(t-t')}}{\omega^2 - \omega_0^2} d\omega \quad (\text{B.11})$$

along the closed contour contour  $\Gamma^\pm = \gamma_1 \circ \gamma_2^\pm$  parametrised by

$$\begin{aligned} \gamma_1 &: [-R, R] \rightarrow \mathbb{C}, \omega \mapsto \omega \\ \gamma_2^\pm &: [0, \pi] \rightarrow \mathbb{C}, \varphi \mapsto Re^{\pm i\varphi} \end{aligned}$$

in the limit  $R \rightarrow \infty$ . In this limit, the integration along  $\gamma_1$  renders the inverse Fourier transform whilst the integration along  $\gamma_2^\pm$  vanishes, provided the good path is followed to close the contour. The residue theorem is finally applied to expedite the evaluation of (B.11).

However, owing to the presence of the poles lying on the real axis, a more sophisticated contour that circumvents the two poles must be prescribed, for instance by slightly deforming  $\gamma_1$  to add two circles of radius  $\epsilon$  (in the limit  $\epsilon \rightarrow 0$ ) centred on the two poles. Following Feynman's prescription [381], we may equivalently keep the contour  $\gamma^\pm$  unchanged, provided that we instead add a small imaginary part  $\pm i\epsilon$  (still in the limit  $\epsilon \rightarrow 0$ ) to the poles, amounting to displacing them away from the real axis, either in the upper or in the lower half-circle. Applying this prescription, the poles are then slightly modified as  $\omega = \pm(\omega_0 \pm i\epsilon)$  in the limit  $\epsilon \rightarrow 0$ .

Depending on the causal or anticausal feature of the system, we have to introduce the retarded (or causal) Green's function  $G^{(\text{ret})}(t, t')$  that is nonzero only when  $t > t'$  and the advanced (or anticausal) Green's function  $G^{(\text{ad})}(t, t')$  that is nonzero when  $t < t'$ .

For the retarded Green's function  $G^{(\text{ret})}(t, t')$  related the case  $t - t' > 0$ , we choose the contour as  $\Gamma^+ = \gamma_1 \circ \gamma_2^+$ , with the poles slightly shifted in the upper plane yielding the following integral

$$G^{(\text{ret})}(t, t') = -\frac{1}{2\pi} \lim_{R \rightarrow \infty, \epsilon \rightarrow 0} \oint_{\Gamma^+} \frac{e^{i\omega(t-t')}}{(\omega + \omega_0 + i\epsilon)(\omega - \omega_0 + i\epsilon)} d\omega \quad (\text{B.12})$$

which may be computed by means of the residue theorem which states in this case that

$$G^{(\text{ret})}(t, t') = -i \lim_{\epsilon \rightarrow 0} \left( \frac{e^{i\omega(t-t')}}{\omega + \omega_0} \Big|_{\omega=\omega_0+i\epsilon} + \frac{e^{i\omega(t-t')}}{\omega - \omega_0} \Big|_{\omega=-\omega_0+i\epsilon} \right) = \frac{\sin[\omega_0(t-t')]}{\omega_0}, \quad (\text{B.13})$$

because the two simple poles are the only singularities within the path and the integral along the path  $\gamma_2^+$  goes to zero in the limit  $R \rightarrow \infty$ . If  $t - t' < 0$ , the integration is performed along  $\Gamma^- = \gamma_1 \circ \gamma_2^-$  and  $G^{(\text{ret})}(t, t') = 0$ , because of the Cauchy theorem. This reflects the causal feature of the system.

For the advanced Green's function  $G^{(\text{ad})}(t, t')$  related to the case  $t - t' < 0$ , we choose the contour as  $\Gamma^- = \gamma_1 \circ \gamma_2^-$ , with the poles slightly shifted in the lower plane, yielding the following integral

$$G^{(\text{ad})}(t, t') = -\frac{1}{2\pi} \lim_{R \rightarrow \infty, \epsilon \rightarrow 0} \oint_{\Gamma^-} \frac{e^{i\omega(t-t')}}{(\omega + \omega_0 - i\epsilon)(\omega - \omega_0 - i\epsilon)} d\omega \quad (\text{B.14})$$

which may be computed by means of the residue theorem which states in this case that

$$G^{(\text{ad})}(t, t') = i \lim_{\epsilon \rightarrow 0} \left( \frac{e^{i\omega(t-t')}}{\omega + \omega_0} \Big|_{\omega=\omega_0-i\epsilon} + \frac{e^{i\omega(t-t')}}{\omega - \omega_0} \Big|_{\omega=-\omega_0-i\epsilon} \right) = -\frac{\sin[\omega_0(t-t')]}{\omega_0}, \quad (\text{B.15})$$

because the two simple poles are the only singularities within the path and the integral along path  $\Gamma_2^-$  goes to zero in the limit  $R \rightarrow \infty$ . If  $t - t' > 0$ , the integration is performed along  $\Gamma^+ = \gamma_1 \circ \gamma_2^+$  and  $G^{(\text{ad})}(t, t') = 0$ , because of the Cauchy theorem. This reflects the anticausal feature of the system.

To sum up, we obtained two Green's functions that both satisfy Eq. (B.8) and which are referred to as retarded (or causal) and advanced (or anticausal) Green's function. They can be written in the compact form

$$G^{(\text{ret})}(t, t') = \frac{1}{\omega_0} \theta(t - t') \sin[\omega_0(t - t')] = G^{(\text{ad})}(t', t) \quad (\text{B.16})$$

$$G^{(\text{ad})}(t, t') = -\frac{1}{\omega_0} \theta(t' - t) \sin[\omega_0(t - t')] = G^{(\text{ret})}(t', t), \quad (\text{B.17})$$

where the Heaviside step function  $\theta(\cdot)$  ensures that the retarded (resp. advanced) Green's function  $G^{(\text{ret})}(t, t')$  (resp.  $G^{(\text{ad})}(t, t')$ ) is zero if  $t < t'$  (resp.  $t > t'$ ), in agreement with the

causality (resp. anticausality). The choice of the appropriate Green's function is dictated by the problem under study. Since we are here interested in a causal solution, we choose the retarded Green's function  $G^{(\text{ret})}(t, t')$  and the general solution of Eq. (B.7) is then obtained thanks to the integral form provided in Eq. (B.6) which reads

$$x(t) = A \cos(\omega_0 t) + B \sin(\omega_0 t) + \frac{1}{\omega_0} \int_{-\infty}^t \sin[\omega_0(t - t')] \frac{F(t')}{m} dt', \quad (\text{B.18})$$

where  $x_h(t) = A \cos(\omega_0 t) + B \sin(\omega_0 t)$  is the solution of the homogeneous Eq. (B.7), with  $A$  and  $B$  being constants that are determined by the initial conditions.

## B.2 Green's function of a partial differential equation

We now generalise the Green's function technique developed in the familiar world of ordinary differential equations to the much more hostile world of partial differential equations. Whilst those equations turn out to be far more complicated than ordinary differential equations, the conversion from the partial differential equation to an integral equation remains essentially the same. The price to pay for the additional complexity related to the spatial part in those equations materialises when it comes to determining the Green's function related to the problem. To illustrate it, we treat the Schrödinger equation as an example.

### B.2.1 Green's function of the Schrödinger equation

We start from the time-dependent Schrödinger equation

$$i\hbar \frac{\partial}{\partial t} |\psi\rangle = \hat{H} |\psi\rangle, \quad (\text{B.19})$$

with  $\hat{H}$  the Hamiltonian describing the problem under study. A formal solution of Eq. (B.19) is given by

$$|\psi(t)\rangle = \hat{U} |\psi(t')\rangle, \quad (\text{B.20})$$

where  $\hat{U} = \hat{U}^\dagger$  is the unitary time evolution operator that describes the time evolution of the system initially in the state  $|\psi(t')\rangle$  at time  $t = t'$  to the state  $|\psi(t)\rangle$ . Inserting the solution (B.20) into the Schrödinger equation (B.19) yields

$$\left[ i\hbar \frac{\partial}{\partial t} \hat{U} - \hat{H} \hat{U} \right] |\psi(t')\rangle = 0, \quad (\text{B.21})$$

which is valid for any  $|\psi(t')\rangle$  and consequently yields the following differential equation

$$i\hbar \frac{\partial}{\partial t} \hat{U} - \hat{H} \hat{U} = 0 \quad (\text{B.22})$$

which is formally solved by direct integration [380] as

$$\hat{U} = 1 - \frac{i}{\hbar} \int_{t'}^t \hat{H}(\tau) \hat{U}(\tau, t') d\tau. \quad (\text{B.23})$$

In the very common case of a static Hamiltonian, which does not depend upon time, one recovers  $\hat{U} = \exp[-i(t - t')\hat{H}/\hbar]$  and Eq. (B.20) takes on the form

$$|\psi(t)\rangle = e^{-i(t-t')\hat{H}/\hbar} |\psi(t')\rangle. \quad (\text{B.24})$$

In position representation, this equation reads

$$\psi(\mathbf{r}, t) = \int \langle \mathbf{r} | e^{-i(t-t')\hat{H}/\hbar} | \mathbf{r}' \rangle \psi_{t'}(\mathbf{r}') d^3 r', \quad (\text{B.25})$$

which is an integral equation very similar to Eq. (B.5). This analogy stimulates to define the Green's function as the matrix element [382]

$$G(\mathbf{r}, t; \mathbf{r}', t') = \langle \mathbf{r} | e^{-i(t-t')\hat{H}/\hbar} | \mathbf{r}' \rangle = \sum_n \phi_n^*(\mathbf{r}') \phi_n(\mathbf{r}) e^{-iE_n(t-t')/\hbar}, \quad (\text{B.26})$$

with  $E_n$  and  $\phi_n$  the eigenvalues and eigenvectors of the Hamiltonian  $\hat{H}$ . We observe that  $G(\mathbf{r}, t; \mathbf{r}', t')$  provides a lot of information about the differential operator since it requires the full diagonalisation of  $\hat{H}$ . Written under this form, the Green's function describes the propagation from position  $\mathbf{r}'$  at time  $t'$  to position  $\mathbf{r}$  at time  $t$ , with no restriction on the sign of  $t - t'$ . To distinguish between those two possibilities, we introduce the retarded and advanced Green's functions

$$G^{(\text{ret})}(\mathbf{r}, t; \mathbf{r}', t') = \frac{1}{i\hbar} \theta(t - t') \sum_n \phi_n^*(\mathbf{r}') \phi_n(\mathbf{r}) e^{-iE_n(t-t')/\hbar} \quad (\text{B.27})$$

$$G^{(\text{ad})}(\mathbf{r}, t; \mathbf{r}', t') = -\frac{1}{i\hbar} \theta(t' - t) \sum_n \phi_n^*(\mathbf{r}') \phi_n(\mathbf{r}) e^{-iE_n(t-t')/\hbar}, \quad (\text{B.28})$$

following the same approach as for ordinary differential equations. The prefactor  $\pm 1/i\hbar$  has been introduced in order to comply with

$$\left( i\hbar \frac{\partial}{\partial t} - H(\mathbf{r}) \right) G^{(\text{ret/ad})}(\mathbf{r}, t; \mathbf{r}', t') = \delta(\mathbf{r} - \mathbf{r}') \delta(t - t'), \quad (\text{B.29})$$

which is the equation that defines a Green's function for the differential operator of the Schrödinger equation, in formal analogy with Eq. (B.3). The retarded and advanced Green's functions can also be described as operators in the Hilbert space

$$\hat{G}^{(\text{ret/ad})} = \pm \frac{1}{i\hbar} \theta[\pm(t - t')] e^{-i(t-t')\hat{H}/\hbar} \quad (\text{B.30})$$

whose (inverse) Fourier transform defines the propagator, which, in the retarded case, read

$$\hat{G}^{(\text{ret})}(E) = \int_{-\infty}^{\infty} \hat{G}^{(\text{ret})} e^{iE\tau/\hbar} d\tau = \int_0^{\infty} e^{i(E-\hat{H})\tau/\hbar} d\tau, \quad (\text{B.31})$$

where  $\tau = t - t'$ . In order to guarantee the convergence of the integral, we introduce, in formal analogy with ordinary differential equations, the convergence factor  $\pm i\epsilon$  in the limit  $\epsilon \rightarrow 0^+$ . Exploiting the following identity

$$\lim_{\epsilon \rightarrow 0^+} \int_0^{\infty} e^{ik(x \pm i\epsilon)} dk = i \lim_{\epsilon \rightarrow 0^+} \frac{1}{x \pm i\epsilon} \quad (\text{B.32})$$

as well as the introduction of the convergence factor  $\pm i\epsilon$  in the limit  $\epsilon \rightarrow 0^+$  in Eq. (B.31), we formulate the Green's function as

$$\hat{G}^{(\text{ret/ad})}(E) = \lim_{\epsilon \rightarrow 0^+} \frac{1}{E - \hat{H} \pm i\epsilon}. \quad (\text{B.33})$$

Determining the propagator (or the Green's function in a given representation) for  $\hat{H}$  is generally a complicated, when possible, task. However, if the Hamiltonian  $\hat{H}$  describing the system can be written as a sum of an unperturbed Hamiltonian  $\hat{H}_0$  whose eigenvalues and eigenvectors are known, or easy to calculate, and a small perturbation Hamiltonian  $\hat{H}_1$ , it is possible to write a perturbative series for the total Green's function (B.33) in terms of the Green's function  $\hat{G}_0^{(\text{ret/ad})}(E)$  of the unperturbed Hamiltonian and the perturbation  $\hat{H}_1$ . This perturbative series, which is referred to as a Dyson series [383,384], provides information about the eigenenergies and eigenstates of the total Hamiltonian  $\hat{H}$  of the problem.

### B.3 Perturbative series for the full Green's function

We assume that the Hamiltonian describing the problem under consideration can be written  $\hat{H} = \hat{H}_0 + \hat{H}_1$ , where the Hamiltonian  $\hat{H}_1$  is treated as a small perturbation of the unperturbed Hamiltonian  $\hat{H}_0$ . The eigenvalues and eigenvectors of  $\hat{H}_0$  are either known or easy to obtain, as well as the related Green's function

$$\hat{G}_0^{(\text{ret/ad})}(E) = \lim_{\epsilon \rightarrow 0^+} \frac{1}{E - \hat{H}_0 \pm i\epsilon}. \quad (\text{B.34})$$

The total Green's function  $\hat{G}^{(\text{ret/ad})}(E)$  related to the total Hamiltonian  $\hat{H}$  reads, omitting for the moment the term  $\pm i\epsilon$  and the (ret/ad) upper index for the sake of clarity [382,385,386],

$$\begin{aligned} \hat{G}(E) &= \frac{1}{E - \hat{H}} = \frac{1}{E - \hat{H}_0 - \hat{H}_1} = \frac{1}{E - \hat{H}_0 (1 - (E - \hat{H}_0)^{-1} \hat{H}_1)} \\ &= \frac{1}{1 - (E - \hat{H}_0)^{-1} \hat{H}_1} \frac{1}{E - \hat{H}_0} = \frac{1}{1 - \hat{G}_0(E) \hat{H}_1} \hat{G}_0(E) \\ &= (1 + \hat{G}_0(E) \hat{H}_1 + \hat{G}_0(E) \hat{H}_1 \hat{G}_0(E) \hat{H}_1 + \dots) \hat{G}_0(E), \end{aligned}$$

which can be written in the more compact form

$$\hat{G}(E) = \hat{G}_0(E) + \hat{G}_0(E) \hat{H}_1 \hat{G}(E) \quad (\text{B.35})$$

or equivalently

$$\hat{G}(E) = \hat{G}_0(E) + \hat{G}(E) \hat{H}_1 \hat{G}_0(E). \quad (\text{B.36})$$

Those self-consistent equations are referred to as Dyson equations and relate the total Green's function associated with the Hamiltonian  $\hat{H}$  to the Green's function  $\hat{G}_0(E)$  of the unperturbed Hamiltonian  $\hat{H}_0$ .





## Appendix C

# Analytical expression for the quantum noise

### C.1 Propagation on a semi-infinite lattice

Let us consider a semi-infinite lattice described by the following Hamiltonian

$$\hat{H} = \sum_{l=1}^{\infty} E_0 |l\rangle \langle l| - \frac{1}{2} \sum_{l=1}^{\infty} E_1 (|l+1\rangle \langle l| + |l\rangle \langle l+1|), \quad (\text{C.1})$$

where  $E_0$  stands for the on-site energy,  $E_1$  for a nearest-neighbour hopping term and  $|l\rangle$  for the local basis sites. Normalised eigenstates  $|\theta\rangle$  of the lattice, satisfying  $\hat{H}|\theta\rangle = E^{(\theta)}|\theta\rangle$ , are found to be (with  $0 < \theta < \pi$ )

$$|\theta\rangle = \sqrt{\frac{2}{\pi}} \sum_{l=1}^{\infty} \sin(l\theta) |l\rangle, \quad (\text{C.2})$$

where the associated eigenvalues read  $E^{(\theta)} = E_0 - E_1 \cos \theta$ . It allows us to express the  $|l\rangle$  states on the continuous eigenbasis as

$$|l\rangle = \sqrt{\frac{2}{\pi}} \int_0^{\pi} \sin(l\theta) |\theta\rangle d\theta, \quad (\text{C.3})$$

where both discrete  $|l\rangle$  and continuous  $|\theta\rangle$  states form orthonormal bases. The time evolution of the total wavefunction is provided by

$$|\psi(t)\rangle = \sum_{l=1}^{\infty} \psi_l(t) |l\rangle = \int_0^{\pi} \psi^{(\theta)}(t) |\theta\rangle d\theta, \quad (\text{C.4})$$

where

$$\psi^{(\theta)}(t) = \sqrt{\frac{2}{\pi}} \sum_{l=1}^{\infty} \psi_l(t) \sin(l\theta). \quad (\text{C.5})$$

The wavefunction  $\psi^{(\theta)}(t)$  at time  $t$  expressed in the  $|\theta\rangle$  basis can be related to its value at time  $t_0$  through the time evolution operator, which yields

$$\psi^{(\theta)}(t) = \psi^{(\theta)}(t_0) \exp \left[ -\frac{i}{\hbar} E^{(\theta)} (t - t_0) \right], \quad (\text{C.6})$$

and which, given that

$$\psi_l(t) = \sqrt{\frac{2}{\pi}} \int_0^\pi \psi^{(\theta)}(t) \sin(l\theta) d\theta \quad (\text{C.7})$$

allows one to compute  $\psi_l(t)$  knowing the initial condition  $\psi_l(t_0)$ . One has

$$\begin{aligned} \psi_l(t) &= \sqrt{\frac{2}{\pi}} \int_0^\pi \sin(l\theta) \exp\left[-\frac{i}{\hbar}(t-t_0)(E_0 - E_1 \cos \theta)\right] \sqrt{\frac{2}{\pi}} \sum_{l'=1}^\infty \psi_{l'}(t_0) \sin(l'\theta) d\theta \\ &= \frac{2}{\pi} \sum_{l'=1}^\infty \psi_{l'}(t_0) \int_0^\pi \sin(l\theta) \sin(l'\theta) \exp\left(\frac{i}{\hbar}(t-t_0)E_1 \cos \theta\right) d\theta \exp\left(-\frac{i}{\hbar}(t-t_0)E_0\right) \end{aligned} \quad (\text{C.8})$$

By making the substitution  $x = E_1(t-t_0)/\hbar$ , the integral appearing above reads

$$\begin{aligned} \frac{2}{\pi} \int_0^\pi \sin(l\theta) \sin(l'\theta) e^{ix \cos \theta} d\theta &= \frac{1}{\pi} \int_{-\pi}^\pi \frac{1}{(2i)^2} (e^{i\theta} - e^{-i\theta}) (e^{il'\theta} - e^{-il'\theta}) e^{ix \cos \theta} d\theta \\ &= \frac{1}{4\pi} \int_{-\pi}^\pi (i^l e^{-il\varphi} - (-i)^l e^{il\varphi}) (i^{l'} e^{-il'\varphi} - (-i)^{l'} e^{il'\varphi}) e^{ix \sin \varphi} d\varphi \\ &= -\frac{1}{2} (i^{l+l'} J_{l+l'}(x) - i^{l-l'} J_{l-l'}(x) - i^{l-l'} J_{l-l'}(x) + i^{-l-l'} J_{-l-l'}(x)) \\ &= i^{l-l'} J_{l-l'}(x) - i^{l+l'} J_{l+l'}(x), \end{aligned}$$

where we have performed the variable substitution  $\varphi = \frac{\pi}{2} - \theta$  and introduced

$$J_l(x) = \frac{1}{2\pi} \int_{-\pi}^\pi e^{ix \sin \varphi} e^{-il\varphi} d\varphi, \quad (\text{C.9})$$

the Bessel function of the first kind and order  $l$  and finally used the parity of those functions around  $l = 0$ . The wavefunction at time  $t$  then reads

$$\psi_l(t) = \sum_{l'=1}^\infty \psi_{l'}(t_0) \left[ i^{l-l'} J_{l-l'}\left(\frac{E_1(t-t_0)}{\hbar}\right) - i^{l+l'} J_{l+l'}\left(\frac{E_1(t-t_0)}{\hbar}\right) \right] \exp\left(-\frac{i}{\hbar} E_0(t-t_0)\right) \quad (\text{C.10})$$

This equation indicates how the local wavefunction at site  $l$  evolves from the initial wavefunction  $\psi_{l'}(t_0)$  at time  $t_0$  to time  $t$ . In the mean-field approximation, an empty waveguide is modelled by  $\psi_{l'}(t_0) = 0$  for all  $l$ , which results in  $\psi_l(t) = 0$  according to Eq. (C.10). The transport is of course induced by the injection of particles from the source. However, the sampling of the initial state by random classical fields in the truncated Wigner method involves an initial wavefunction such that  $\overline{\psi_l} = 0$  but also  $\overline{|\psi_l|^2} = 1/2$ , where  $\overline{\cdot}$  denotes the average over the initial conditions. As a result of the truncation of the infinite space into a finite scattering region, this equation indicates that a quantum noise is injected into the scattering region due to the initial sampling of the empty waveguide.

## C.2 Quantum noise in two dimensions

In this section, we generalise the expression (C.10) of quantum noise penetrating the scattering region in two dimensions. The Hamiltonian of a 2D discrete system of infinite longitudinal

extension and  $W$  transverse sites, with on-site energy  $E_\delta$  and energy  $E_0$ , reads

$$\hat{H} = \sum_{l=1}^{\infty} \sum_{w=0}^{W-1} \left[ (E_0 + 2E_\delta) |l, w\rangle \langle l, w| - \frac{1}{2} \left( |l+1, w\rangle \langle l, w| + |l, w\rangle \langle l+1, w| \right) - \frac{1}{2} \left( |l, w+1\rangle \langle l, w| + |l, w\rangle \langle l, w+1| \right) \right] \quad (\text{C.11})$$

In the partial Fourier space along the  $y$ -direction, this Hamiltonian becomes diagonal in the  $y$ -direction and reads

$$\hat{H} = \sum_{l=1}^{\infty} \sum_{k=0}^{W-1} \left[ (E_0 + E_k + E_\delta) |l, k\rangle \langle l, k| - \frac{1}{2} \left( |l+1, k\rangle \langle l, k| + |l, k\rangle \langle l+1, k| \right) \right], \quad (\text{C.12})$$

where the energy  $E_k$  is given by

$$\begin{aligned} E_k &= \langle k| \left( |l, w\rangle \langle l, w+1| + |l, w+1\rangle \langle l, w| \right) |k'\rangle \\ &= \frac{1}{W} \sum_{w'=0}^{W-1} \sum_{w''=0}^{W-1} \exp\left(2\pi i \frac{w'k}{W}\right) \langle l, w'| \left( |l, w\rangle \langle l, w+1| \right. \\ &\quad \left. + |l, w+1\rangle \langle l, w| \right) |l, w''\rangle \exp\left(-2\pi i \frac{w''k'}{W}\right) \\ &= \frac{1}{W} \sum_{w'=0}^{W-1} \sum_{w''=0}^{W-1} \exp\left(2\pi i \frac{w'k - w''k'}{W}\right) (\delta_{w, w'} \delta_{w+1, w''} + \delta_{w+1, w'} \delta_{w, w''}) \\ &= \frac{1}{W} \exp\left(2\pi i \frac{w}{W}(k - k')\right) \left[ \exp\left(2\pi i \frac{k}{W}\right) + \exp\left(-2\pi i \frac{k'}{W}\right) \right]. \end{aligned} \quad (\text{C.13})$$

In Fourier representation and using the result (C.10) we have derived in one dimension, the wavefunction  $\tilde{\psi}_{n,k}(t)$  at time  $t$  reads

$$\begin{aligned} \tilde{\psi}_{l,k}(t) &= \sum_{l'=1}^{\infty} \tilde{\psi}_{l',k}(t_0) \left[ i^{l-l'} J_{l-l'} \left( \frac{(t-t_0)}{\hbar} E_\delta \right) + i^{l+l'} J_{l+l'} \left( \frac{(t-t_0)}{\hbar} E_\delta \right) \right] \\ &\quad \times \exp\left[-\frac{i}{\hbar}(t-t_0)(E_0 + E_\delta + E_k)\right], \end{aligned}$$

where the wavefunction  $\tilde{\psi}_{l,k}(t_0)$  at initial time is obtained by taking the 1D Fourier transform of the wavefunction at initial time in the direct space

$$\tilde{\psi}_{l,k}(t_0) = \frac{1}{\sqrt{W}} \sum_{w'=0}^{W-1} \psi_{l,w'}(t_0) \exp\left(-2\pi i \frac{w'k}{W}\right). \quad (\text{C.14})$$

Finally, the wavefunction in the direct space at time  $t$  is obtained by taking the inverse Fourier transform. It yields

$$\begin{aligned}
\psi_{l,w}(t) &= \frac{1}{\sqrt{W}} \sum_{k=0}^{W-1} e^{2\pi i k w / W} \sum_{l'=1}^{\infty} \left[ i^{l-l'} J_{l-l'} \left( \frac{(t-t_0)}{\hbar} E_{\delta} \right) + i^{l+l'} J_{l+l'} \left( \frac{(t-t_0)}{\hbar} E_{\delta} \right) \right] \\
&\quad \times \exp \left( -\frac{i}{\hbar} (t-t_0) (E_0 + 2E_{\delta} - E_{\delta} \cos(2\pi k / W)) \right) \\
&\quad \times \frac{1}{\sqrt{W}} \sum_{w'=0}^{W-1} \psi_{l',w'}(t_0) e^{-2\pi i w' k / W} \\
&= \sum_{w'=0}^{W-1} \sum_{l'=1}^{\infty} \psi_{l',w'}(t_0) \left[ i^{l-l'} J_{l-l'} \left( \frac{(t-t_0)}{\hbar} E_{\delta} \right) + i^{l+l'} J_{l+l'} \left( \frac{(t-t_0)}{\hbar} E_{\delta} \right) \right] \\
&\quad \times \exp \left( -\frac{i}{\hbar} (t-t_0) (E_0 + 2E_{\delta}) \right) \\
&\quad \times \frac{1}{W} \sum_{k=0}^{W-1} \exp \left( \frac{i}{\hbar} (t-t_0) (E_{\delta} \cos(2\pi k / W)) \right) e^{2\pi i (w-w') k / W}. \quad (\text{C.15})
\end{aligned}$$

In this latter context, it appears that  $\psi_{l,w}(t)$  has the same form as in one dimension, multiplied by the following kernel in the transverse direction

$$K_{\lambda}(z) = \frac{1}{W} \sum_{k=0}^{W-1} e^{iz \cos(2\pi k / W)} e^{2\pi i \lambda k / W}, \quad (\text{C.16})$$

where  $\lambda = l - l'$  and  $z = \frac{(t-t_0)E_{\delta}}{\hbar}$ . In the limit  $W \rightarrow \infty$ ,  $K_{\lambda}(z)$  is yielded as

$$\begin{aligned}
K_{\lambda}(z) &\simeq \frac{1}{2\pi} \int_{-\pi}^{\pi} e^{iz \cos \theta} e^{i\lambda \theta} d\theta = \frac{1}{2\pi} \int_{-\pi}^{\pi} e^{iz \sin(\frac{\pi}{2}-\theta)} e^{i\lambda \theta} d\theta \\
&= \frac{1}{2\pi} \int_{-\frac{\pi}{2}}^{\frac{3\pi}{2}} e^{iz \sin \theta'} e^{i\lambda(\frac{\pi}{2}-\theta')} d\theta' = \frac{1}{2\pi} \int_{-\pi}^{\pi} e^{iz \sin \theta'} e^{-i\lambda \theta'} d\theta' e^{i\lambda \frac{\pi}{2}} \\
&= i^{\lambda} J_{\lambda}(z), \quad (\text{C.17})
\end{aligned}$$

where  $J_{\lambda}(z)$  is the Bessel function of the first kind and order  $\lambda$ . The kernel in Eq. (C.16) presents a nice symmetry with respect to  $\lambda$ . This symmetry property reads

$$\begin{aligned}
K_{\lambda}(z) &= \frac{1}{W} \sum_{k=0}^{W-1} e^{iz \cos(2\pi k / W)} e^{2\pi i \lambda k / W} \stackrel{k' \equiv -k}{=} \frac{1}{W} \sum_{k'=W-1}^0 e^{iz \cos(2\pi(-k') / W)} e^{2\pi i \lambda(-k') / W} \\
&= \frac{1}{W} \sum_{k'=W-1}^0 e^{iz \cos(2\pi k' / W)} e^{-2\pi i \lambda k' / W} \\
&\stackrel{k'' \equiv k'+W}{=} \frac{1}{W} \sum_{k''=1}^W e^{iz \cos(2\pi(k''-W) / W)} e^{-2\pi i \lambda(k''-W) / W} \\
&= \frac{1}{W} \sum_{k''=1}^W e^{iz \cos(2\pi k'' / W)} e^{-2\pi i \lambda k'' / W} = K_{-\lambda}(z). \quad (\text{C.18})
\end{aligned}$$

This symmetry also reflects in the limit  $W \rightarrow \infty$  since

$$K_{-\lambda}(z) \simeq i^{-\lambda} J_{-\lambda}(z) = (-i)^\lambda (-1)^\lambda J_\lambda(z) = i^\lambda J_\lambda(z) \simeq K_\lambda(z). \quad (\text{C.19})$$

Besides this nice symmetry property, the first order derivative of that kernel also fulfils

$$\begin{aligned} \frac{\partial K_\lambda(z)}{\partial z} &= \frac{1}{W} \sum_{k=0}^{W-1} i \cos\left(\frac{2\pi k}{W}\right) e^{iz \cos(2\pi k/W)} e^{2\pi i \lambda k/W} \\ &= \frac{i}{2W} \sum_{k=0}^{W-1} \left( e^{2\pi i k/W} + e^{-2\pi i k/W} \right) e^{iz \cos(2\pi k/W)} e^{2\pi i \lambda k/W} \\ &= \frac{i}{2W} \sum_{k=0}^{W-1} e^{iz \cos(2\pi k/W)} \left( e^{2\pi i(\lambda+1)k/W} + e^{2\pi i(\lambda-1)k/W} \right) = \frac{i}{2} (K_{\lambda-1}(z) + K_{\lambda+1}(z)) \\ &= \frac{\partial K_{-\lambda}(z)}{\partial z}, \end{aligned} \quad (\text{C.20})$$

thereby allowing an iterative evaluation of the derivative of order  $k$  from those of order  $k-1$ , which is very useful in view of numerically integrating the quantum noise with the procedure detailed in the appendix A.



## Appendix D

# Derivation of the motion equation for the truncated Wigner method

With the aim of deriving an evolution equation for the Wigner function  $W^{(\hat{\rho})}(\boldsymbol{\alpha}, \boldsymbol{\alpha}^*)$ , we must compute

$$i\hbar \frac{\partial}{\partial t} W^{(\hat{\rho})}(\boldsymbol{\alpha}, \boldsymbol{\alpha}^*) = \frac{1}{\pi^{2N}} \prod_{\alpha=0}^N \iint e^{-\xi_\nu \alpha_\nu^* + \xi_\nu^* \alpha_\nu} i\hbar \frac{\partial}{\partial t} \chi_{\mathcal{W}}(\boldsymbol{\xi}, \boldsymbol{\xi}^*) d^2 \xi_\alpha, \quad (\text{D.1})$$

where the evolution equation for the characteristic function reads

$$i\hbar \frac{\partial}{\partial t} \chi_{\mathcal{W}}(\boldsymbol{\xi}, \boldsymbol{\xi}^*) = \text{Tr} \left\{ \hat{\rho} \left[ \prod_{\nu} e^{\xi_\nu \hat{a}_\nu^\dagger - \xi_\nu^* \hat{a}_\nu}, \hat{H} \right] \right\}, \quad (\text{D.2})$$

with the two-body Hamiltonian

$$\hat{H} = \sum_{\nu=0}^N (E_\nu + V_\nu) \hat{a}_\nu^\dagger \hat{a}_\nu + \sum_{\nu=0}^N \sum_{\vartheta=0}^N t_{\nu\vartheta} \left( \hat{a}_\nu^\dagger \hat{a}_{\nu+1} + \hat{a}_{\nu+1}^\dagger \hat{a}_\nu \right) + \frac{1}{2} \sum_{\nu=0}^N U_\nu \hat{a}_\nu^\dagger \hat{a}_\nu^\dagger \hat{a}_\nu \hat{a}_\nu, \quad (\text{D.3})$$

where  $E_\nu$  is the on-site energy,  $V_\nu$  is the on-site potential, the matrix element  $t_{\nu\vartheta}$  encodes the hopping from site  $\nu$  to  $\vartheta$  and  $U_\nu$  is the on-site two-body interaction term. The Baker–Haussdorff lemma [267]

$$e^{\xi_\nu \hat{a}_\nu^\dagger - \xi_\nu^* \hat{a}_\nu} = e^{\xi_\nu \hat{a}_\nu^\dagger} e^{-\xi_\nu^* \hat{a}_\nu} e^{-|\xi|^2/2} \quad (\text{D.4})$$

can be used to simplify the exponentials appearing in the commutator (D.2). This leads to the computation of

$$[e^{\xi_\nu \hat{a}_\nu^\dagger}, \hat{a}_\nu] = \sum_{k=0}^{\infty} \frac{\xi_\nu^k}{k!} [(\hat{a}_\nu^\dagger)^k, \hat{a}_\nu] = - \sum_{k=0}^{\infty} \frac{k}{k!} \xi_\nu^k (\hat{a}_\nu^\dagger)^{k-1} = -\xi_\nu e^{\xi_\nu \hat{a}_\nu^\dagger} \quad (\text{D.5})$$

$$[e^{-\xi_\nu^* \hat{a}_\nu}, \hat{a}_\nu] = \sum_{k=0}^{\infty} \frac{(-\xi_\nu^*)^k}{k!} [\hat{a}_\nu^k, \hat{a}_\nu] = \sum_{k=0}^{\infty} \frac{k}{k!} (-\xi_\nu^*)^k (\hat{a}_\nu^\dagger)^{k-1} = -\xi_\nu^* e^{\xi_\nu^* \hat{a}_\nu} \quad (\text{D.6})$$

which implies that one can write

$$\left[ e^{\xi_\nu \hat{a}_\nu^\dagger} e^{-\xi_\nu^* \hat{a}_\nu}, \hat{a}_\nu^\dagger \hat{a}_\nu \right] = e^{\xi_\nu \hat{a}_\nu^\dagger} \left( -\xi_\nu^* \hat{a}_\nu - \xi_\nu \hat{a}_\nu^\dagger \right) e^{-\xi_\nu^* \hat{a}_\nu} = \left( \xi_\nu^* \frac{\partial}{\partial \xi_\nu^*} - \xi_\nu \frac{\partial}{\partial \xi_\nu} \right) e^{\xi_\nu \hat{a}_\nu^\dagger} e^{-\xi_\nu^* \hat{a}_\nu}, \quad (\text{D.7})$$

that is the commutator related to the first term in Eq. (D.3). The commutator related to the second term of Eq. (D.3) is given by

$$\begin{aligned} \left[ e^{\xi_\nu \hat{a}_\nu^\dagger} e^{-\xi_\nu^* \hat{a}_\nu} e^{\xi_\vartheta \hat{a}_\vartheta^\dagger} e^{-\xi_\vartheta^* \hat{a}_\vartheta}, \hat{a}_\nu^\dagger \hat{a}_\vartheta + \hat{a}_\vartheta^\dagger \hat{a}_\nu \right] &= e^{\xi_\nu \hat{a}_\nu^\dagger} e^{-\xi_\nu^* \hat{a}_\nu} \left( -\xi_\nu^* \hat{a}_\nu - \xi_\vartheta^* \hat{a}_\vartheta - \xi_\nu \hat{a}_\nu^\dagger - \xi_\vartheta \hat{a}_\vartheta^\dagger \right) e^{-\xi_\nu^* \hat{a}_\nu} e^{-\xi_\vartheta^* \hat{a}_\vartheta} \\ &= \left( \xi_\nu^* \frac{\partial}{\partial \xi_\nu^*} + \xi_\vartheta^* \frac{\partial}{\partial \xi_\vartheta^*} - \xi_\nu \frac{\partial}{\partial \xi_\nu} - \xi_\vartheta \frac{\partial}{\partial \xi_\vartheta} \right) \\ &\quad \times e^{\xi_\nu \hat{a}_\nu^\dagger} e^{-\xi_\nu^* \hat{a}_\nu} e^{\xi_\vartheta \hat{a}_\vartheta^\dagger} e^{-\xi_\vartheta^* \hat{a}_\vartheta}. \end{aligned} \quad (\text{D.8})$$

Finally, the last term in Eq. (D.3) can be rewritten under the form

$$\sum_{\nu=0}^N U_\nu \hat{a}_\nu^\dagger \hat{a}_\nu^\dagger \hat{a}_\nu \hat{a}_\nu = \frac{1}{2} \sum_{\nu=0}^N U_\nu \left( \hat{a}_\nu^\dagger \hat{a}_\nu \hat{a}_\nu \hat{a}_\nu^\dagger - \hat{a}_\nu^\dagger \hat{a}_\nu \right) \quad (\text{D.9})$$

and we compute the related commutator as

$$\left[ e^{\xi_\nu \hat{a}_\nu^\dagger - \xi_\nu^* \hat{a}_\nu}, \hat{a}_\nu^\dagger \hat{a}_\nu \hat{a}_\nu \hat{a}_\nu^\dagger - \hat{a}_\nu^\dagger \hat{a}_\nu \right] = \left( \xi_\nu^* \frac{\partial}{\partial \xi_\nu^*} - \xi_\nu \frac{\partial}{\partial \xi_\nu} \right) \left( \frac{\xi_\nu \xi_\nu^*}{2} - 2 \frac{\partial^2}{\partial \xi_\nu \partial \xi_\nu^*} - 2 \right) e^{\xi_\nu \hat{a}_\nu^\dagger - \xi_\nu^* \hat{a}_\nu}. \quad (\text{D.10})$$

All together, commutators (D.7), (D.8) and (D.10) allow us to formulate the evolution equation for the characteristic function as

$$\begin{aligned} i\hbar \frac{\partial}{\partial t} \chi_{\mathcal{W}}(\boldsymbol{\xi}, \boldsymbol{\xi}^*, t) &= \sum_{\nu=0}^N (E_\nu + V_\nu) \left( \xi_\nu^* \frac{\partial}{\partial \xi_\nu^*} - \xi_\nu \frac{\partial}{\partial \xi_\nu} \right) \chi_{\mathcal{W}}(\boldsymbol{\xi}, \boldsymbol{\xi}^*, t) \\ &\quad + \sum_{\nu=0}^N \sum_{\vartheta=0}^N t_{\nu\vartheta} \left( \xi_\nu^* \frac{\partial}{\partial \xi_\nu^*} + \xi_\vartheta^* \frac{\partial}{\partial \xi_\vartheta^*} - \xi_\nu \frac{\partial}{\partial \xi_\nu} - \xi_\vartheta \frac{\partial}{\partial \xi_\vartheta} \right) \chi_{\mathcal{W}}(\boldsymbol{\xi}, \boldsymbol{\xi}^*, t) \\ &\quad + \sum_{\nu=0}^N U_\nu \left( \xi_\nu^* \frac{\partial}{\partial \xi_\nu^*} - \xi_\nu \frac{\partial}{\partial \xi_\nu} \right) \left( \frac{\xi_\nu \xi_\nu^*}{4} - \frac{\partial^2}{\partial \xi_\nu \partial \xi_\nu^*} - 1 \right) \chi_{\mathcal{W}}(\boldsymbol{\xi}, \boldsymbol{\xi}^*, t) \end{aligned} \quad (\text{D.11})$$

which in turn allows us to write the evolution equation for the Wigner function as

$$\begin{aligned} i\hbar \frac{\partial}{\partial t} W^{(\hat{\rho})}(\boldsymbol{\psi}, \boldsymbol{\psi}^*, t) &= \sum_{\nu=0}^N (E_\nu + V_\nu) \left( \psi_\nu^* \frac{\partial}{\partial \psi_\nu^*} - \psi_\nu \frac{\partial}{\partial \psi_\nu} \right) W^{(\hat{\rho})}(\boldsymbol{\psi}, \boldsymbol{\psi}^*, t) \\ &\quad + \sum_{\nu=0}^N \sum_{\vartheta=0}^N t_{\nu\vartheta} \left( \psi_\nu^* \frac{\partial}{\partial \psi_\nu^*} + \psi_\vartheta^* \frac{\partial}{\partial \psi_\vartheta^*} - \psi_\nu \frac{\partial}{\partial \psi_\nu} - \psi_\vartheta \frac{\partial}{\partial \psi_\vartheta} \right) W^{(\hat{\rho})}(\boldsymbol{\psi}, \boldsymbol{\psi}^*, t) \\ &\quad + \sum_{\nu}^N U_\nu \left[ (|\psi_\nu|^2 - 1) \left( \psi_\nu^* \frac{\partial}{\partial \psi_\nu^*} - \psi_\nu \frac{\partial}{\partial \psi_\nu} \right) \right. \\ &\quad \quad \left. - \frac{1}{4} \left( \psi_\nu^* \frac{\partial^3}{\partial \psi_\nu \partial \psi_\nu^*} - \psi_\nu \frac{\partial^3}{\partial \psi_\nu \partial \psi_\nu^2} \right) \right] W^{(\hat{\rho})}(\boldsymbol{\psi}, \boldsymbol{\psi}^*, t). \end{aligned} \quad (\text{D.12})$$

The last line of this equation includes third order derivatives terms that are neglected in the framework of the truncated Wigner method. This is actually a good approximation provided the on-site density  $|\psi_\nu|^2 \gg 1$  and the interaction parameter  $U_\nu$  remains small enough, as is formally shown in [254].



## Appendix E

# Overview of the numerical integration package

In this appendix, we give a brief insight of the structure of the numerical integration package we developed and used for this work. This package is organised following a traditional data pipeline. Data are first created according to the physical scenarios we model, following the discussions in this manuscript. Once put into the suitable format, they feed the propagation algorithm described in Appendix A. The results produced by this algorithm are finally postprocessed to yield the observables of interest, as described in this manuscript. This data pipeline is best explained with the scheme in FIG. E.1. We note that this structure was suggested by the work of Dr. Julien Dujardin [51] who worked on similar topics.

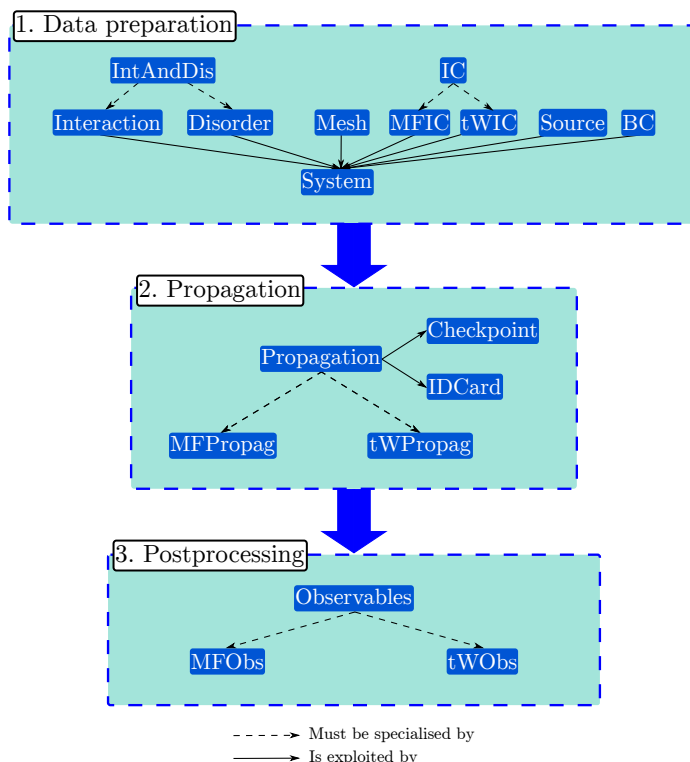


Figure E.1 – Scheme of the data pipeline we implemented to solve the partial differential equations related to the physical scenarios we studied in this work. This pipeline consists in a vertical stack of three layers: a preprocessing layer that puts data in the suitable format, followed by a propagation layer whose output feeds the last layer that postprocesses the results into an exploitable format. Structure inspired from [51].

In the following, we give a brief description of the various classes we implemented in this work.

## E.1 Data preparation layer

The purpose of this layer is to prepare data and to properly setup the system for the propagation. The related classes are written in C++, mainly to facilitate the communication with the following layer, and are devoted to modelling a specific part of the physical system under study.

- **IntAndDis**: this abstract class specifies a number of methods that must be implemented by its subclasses.
  - **Interaction**: this class is inherited from **IntAndDis** and implements the spatial interaction profile.
  - **Disorder**: this class is inherited from **IntAndDis** and implements the spatial disorder profile.

- **Mesh**: this class represents the numerical mesh that results from the finite difference scheme we used to discretise the field equations.
- **IC**: this abstract class is responsible for the implementation of the initial conditions. It must be inherited by subclasses that particularise the initial conditions to the mean-field approximation or to the truncated Wigner method, respectively.
  - **MFIC**: this class is inherited from **IC** and particularises the initial conditions to the mean-field approximation.
  - **tWIC**: this class is inherited from **IC** and particularises the initial conditions to the truncated Wigner method.
- **Source**: this class is responsible for handling the time profile of the source.
- **BC**: this class is responsible for implementing the boundary conditions, including smooth exterior complex scaling.

Most of those classes implement methods that run quite straightforwardly in terms of time and resources. However, the generation of the quantum noise related to the truncated Wigner method in the **tWIC** class can be demanding, especially in two dimensions.

## E.2 Propagation layer

The classes composing this layer are also written in **C++** because numerical efficiency is the determinant factor here. As the name indicates, the propagation layer is devoted to propagating the field equations in time. To that end, an abstract class that must be specialised to the mean-field approximation or to the truncated Wigner method regroups the main part of the work. This layer is also responsible for checkpointing the simulations whose state can consequently be saved and relaunched at certain times. It is particularly useful in exploration phase, when one wants to investigate the state of the system at intermediate times without relaunching the simulation from the beginning. Finally, it also includes a class whose job is to communicate the simulation parameters to whomever it may concern, be it other classes or the user.

- **Propagation**: this abstract class is the skeleton of the propagation and designs how it is achieved. It must be specialised by subclasses dedicated to the propagation of the field equations in the mean-field approximation or in the truncated Wigner method.
  - **MFPropag**: this class is inherited from **Propagation** and particularises it to the mean-field approximation.
  - **tWPropag**: this class is inherited from **Propagation** and particularises it to the truncated Wigner method.
- **IDCard**: this class saves the simulation parameters, either for user purposes or to relaunch an interrupted simulation from a saved state.
- **Checkpoint**: this class saves the state of the system at user-specified times and is also responsible for relaunching the simulation from those times if it has been interrupted

for some reason<sup>1</sup>. This is essentially achieved by querying the simulation parameters from the `IDCard` class and loading the saved system state.

The propagation performed by this layer is numerically demanding, especially for the truncated Wigner method in two dimensions. For that reason, simulations were realised in parallel on the clusters of the Consortium des Équipements de Calcul Intensif (CÉCI) that provides powerful numerical resources, including a large number of CPUs/GPUs and a very large amount of RAM. The most demanding simulations performed in this manuscript typically involved hundreds to thousands of CPUs, with several Gb of RAM per CPU during several hours (~10 hours per job). Those simulations are therefore not conceivable on a classical laptop.

### E.3 Postprocessing layer

This last layer is dedicated to postprocessing the outcome of the propagation and to compute the observables of interest. It involves manipulating thousands to tens of thousands of files containing many complex numbers and to perform various transformations and combinations of them, ranging from basic averaging to computing Fast Fourier Transforms (FFT). The Python language, and more precisely the SciPy ecosystem, is completely appropriate for that purpose owing to its simplicity of use and great versatility.

- **Observables**: this abstract class is used to design how observables should be computed. It must be specialised by subclasses particularising this implementation to mean-field or truncated Wigner observables.
  - **MFObs**: this class inherits from the `Observables` class and specialises it to compute observables related to the mean-field approximation.
  - **tWObs**: this class inherits from the `Observables` class and specialises it to compute observables related to the truncated Wigner method.

---

<sup>1</sup>Typically, a simulation can be stopped by the user to check its integrity or for any other desired reason... But also untimely by SLURM, the resource manager of the clusters, because the user-specified resources required by the job are a bit too optimistic (often not enough required memory or computation time).

# List of publications

Parts the results presented in this manuscript have been published in the following references:

- Renaud Chrétien, Josef Rammensee, Julien Dujardin, Cyril Petitjean, and Peter Schlagheck,  
*Al'tshuler–Aronov–Spivak oscillations of bosonic matter wave beams in the presence of interaction*  
Phys. Rev. A **100**, 033606 (2019).
- Renaud Chrétien and Peter Schlagheck  
*Inversion of coherent backscattering with interacting Bose–Einstein condensates in two–dimensional disorder: A truncated Wigner approach*  
Phys. Rev. A **103**, 033319 (2021).



# Bibliography

- [1] M. Planck, *Wege zur physikalischen Erkenntnis: Reden und Vorträge*. 1933.
- [2] A. Michelson, *Light Waves And Their Uses...* 1903.
- [3] C. Cohen-Tannoudji, B. Diu, and F. Laloë, *Quantum mechanics: 1st ed.* New York, NY: Wiley, 1977. Trans. of: *Mécanique quantique*. Paris: Hermann, 1973.
- [4] R. P. Feynman, R. B. Leighton, and M. Sands, *The Feynman Lectures on Physics, Vol. III*. Basic Books, 2011.
- [5] S. Bose, “Plancks Gesetz und Lichtquantenhypothese,” *Zeitschrift für Physik*, vol. 26, pp. 178–181, Dec 1924.
- [6] A. Einstein, “Quantentheorie des einatomigen idealen Gases,” *Sitzungsberichte der Preussischen Akademie der Wissenschaften*, vol. 22, p. 261, 1924.
- [7] A. Einstein, “Quantentheorie des einatomigen idealen Gases: Zweite Abhandlung,” *Sitzungsberichte der Preussischen Akademie der Wissenschaften*, vol. 1, p. 3, 1925.
- [8] M. H. Anderson, J. R. Ensher, M. R. Matthews, C. E. Wieman, and E. A. Cornell, “Observation of Bose-Einstein condensation in a dilute atomic vapor,” *Science*, vol. 269, p. 198–201, Jul 1995.
- [9] K. B. Davis, M.-O. Mewes, M. R. Andrews, N. J. van Druten, D. S. Durfee, D. M. Kurn, and W. Ketterle, “Bose-Einstein condensation in a gas of sodium atoms,” *Phys. Rev. Lett.*, vol. 75, p. 3969–3973, Nov 1995.
- [10] N. Van Druten, M.-O. Mewes, M. Andrews, D. Durfee, D. Kurn, C. Townsend, and W. Ketterle, “Bose–Einstein condensation and prospects for precision measurements,” in *Proceedings of 20th Biennial Conference on Precision Electromagnetic Measurements*, 1996.
- [11] J. Dunningham, K. Burnett, and W. Phillips, “Bose-Einstein condensates and precision measurements,” *Philosophical transactions. Series A, Mathematical, physical, and engineering sciences*, vol. 363, pp. 2165–75, 10 2005.
- [12] W. Muessel, H. Strobel, D. Linnemann, D. B. Hume, and M. K. Oberthaler, “Scalable spin squeezing for quantum-enhanced magnetometry with Bose–Einstein condensates,” *Phys. Rev. Lett.*, vol. 113, p. 103004, Sep 2014.
- [13] W. C. Burton, C. J. Kennedy, W. C. Chung, S. Vadia, W. Chen, and W. Ketterle, “Coherence times of Bose-Einstein condensates beyond the shot-noise limit via superfluid shielding,” *Phys. Rev. Lett.*, vol. 117, p. 275301, Dec 2016.
- [14] J. I. Cirac, M. Lewenstein, K. Mølmer, and P. Zoller, “Quantum superposition states of Bose–Einstein condensates,” *Phys. Rev. A*, vol. 57, pp. 1208–1218, Feb 1998.

- [15] T. Byrnes, K. Wen, and Y. Yamamoto, “Macroscopic quantum computation using Bose–Einstein condensates,” *Phys. Rev. A*, vol. 85, p. 040306, Apr 2012.
- [16] D. Jaksch, J. J. García-Ripoll, J. I. Cirac, and P. Zoller, *Quantum Computing with Cold Ions and Atoms: Theory*, ch. 23, pp. 483–517. John Wiley & Sons, Ltd, 2016.
- [17] I. Bloch, J. Dalibard, and W. Zwerger, “Many–body physics with ultracold gases,” *Rev. Mod. Phys.*, vol. 80, pp. 885–964, Jul 2008.
- [18] E. R. Elliott, M. C. Krutzik, J. R. Williams, R. J. Thompson, and D. C. Aveline, “NASA’s Cold Atom Lab (CAL): system development and ground test status,” *Nature*, vol. 4, p. 16, 2018.
- [19] D. Aveline, J. Williams, E. Elliott, C. Dutenhoffer, J. Kellogg, J. Kohel, N. Lay, K. Oudrhiri, R. Shotwell, N. Yu, and R. Thompson, “Observation of Bose–Einstein condensates in an Earth-orbiting research lab,” *Nature*, vol. 582, pp. 193–197, 06 2020.
- [20] D. A. R. Dalvit, J. Dziarmaga, and W. H. Zurek, “Decoherence in Bose-Einstein condensates: Towards bigger and better Schrödinger cats,” *Phys. Rev. A*, vol. 62, p. 013607, Jun 2000.
- [21] W. Wang, L. Fu, and X. Yi, “Effect of decoherence on the dynamics of Bose-Einstein condensates in a double-well potential,” *Physical Review A*, vol. 75, 05 2007.
- [22] B. Dalton, “Decoherence effects in Bose-Einstein condensate interferometry,” *Annals of Physics*, vol. 326, no. 3, pp. 668 – 720, 2011.
- [23] E. M. Bookjans, A. Vinit, and C. Raman, “Quantum phase transition in an antiferromagnetic spinor Bose-Einstein condensate,” *Phys. Rev. Lett.*, vol. 107, p. 195306, Nov 2011.
- [24] A. Vinit, E. M. Bookjans, C. A. R. Sá de Melo, and C. Raman, “Antiferromagnetic spatial ordering in a quenched one-dimensional spinor gas,” *Phys. Rev. Lett.*, vol. 110, p. 165301, Apr 2013.
- [25] R. Howl, C. Sabín, L. Hackermüller, and I. Fuentes, “Quantum decoherence of phonons in Bose-Einstein condensates,” *Journal of Physics B: Atomic, Molecular and Optical Physics*, vol. 51, p. 015303, nov 2017.
- [26] K. Pawłowski, M. Fadel, P. Treutlein, Y. Castin, and A. Sinatra, “Mesoscopic quantum superpositions in bimodal Bose-Einstein condensates: Decoherence and strategies to counteract it,” *Phys. Rev. A*, vol. 95, p. 063609, Jun 2017.
- [27] F. Schäfer, T. Fukuhara, S. Sugawa, Y. Takasu, and Y. Takahashi, “Tools for quantum simulation with ultracold atoms in optical lattices,” *Nat Rev Phys*, vol. 2, pp. 411–425, 2020.
- [28] C. N. Cohen-Tannoudji, “Nobel lecture: Manipulating atoms with photons,” *Rev. Mod. Phys.*, vol. 70, pp. 707–719, Jul 1998.
- [29] C. J. Pethick and H. Smith, *Bose–Einstein Condensation in Dilute Gases*. Cambridge: Cambridge University Press, 2 ed., 2008.
- [30] J. Dalibard, F. Gerbier, G. Juzeliūnas, and P. Öhberg, “Colloquium: Artificial gauge potentials for neutral atoms,” *Rev. Mod. Phys.*, vol. 83, pp. 1523–1543, Nov 2011.
- [31] N. Goldman, G. Juzeliūnas, P. Öhberg, and I. B. Spielman, “Light-induced gauge fields for ultracold atoms,” *Reports on Progress in Physics*, vol. 77, no. 12, p. 126401, 2014.
- [32] A. Micheli, A. J. Daley, D. Jaksch, and P. Zoller, “Single atom transistor in a 1D optical lattice,” *Phys. Rev. Lett.*, vol. 93, p. 140408, Oct 2004.



- [33] B. T. Seaman, M. Krämer, D. Z. Anderson, and M. J. Holland, “Atomtronics: Ultracold-atom analogs of electronic devices,” *Phys. Rev. A*, vol. 75, p. 023615, Feb 2007.
- [34] J. A. Stickney, D. Z. Anderson, and A. A. Zozulya, “Transistorlike behavior of a Bose-Einstein condensate in a triple-well potential,” *Phys. Rev. A*, vol. 75, p. 013608, Jan 2007.
- [35] R. A. Pepino, J. Cooper, D. Z. Anderson, and M. J. Holland, “Atomtronic circuits of diodes and transistors,” *Phys. Rev. Lett.*, vol. 103, p. 140405, Sep 2009.
- [36] L. Amico, M. Boshier, G. Birkel, A. Minguzzi, C. Miniatura, L. C. Kwek, D. Aghamalyan, V. Ahufinger, N. Andrei, A. S. Arnold, M. Baker, T. A. Bell, T. Bland, J. P. Brantut, D. Cassettari, F. Chevy, R. Citro, S. D. Palo, R. Dumke, M. Edwards, R. Folman, J. Fortagh, S. A. Gardiner, B. M. Garraway, G. Gauthier, A. Günther, T. Haug, C. Hufnagel, M. Keil, W. von Klitzing, P. Ireland, M. Lebrat, W. Li, L. Longchambon, J. Mompert, O. Morsch, P. Naldesi, T. W. Neely, M. Olshanii, E. Orignac, S. Pandey, A. Pérez-Obiol, H. Perrin, L. Piroli, J. Polo, A. L. Pritchard, N. P. Proukakis, C. Rylands, H. Rubinsztein-Dunlop, F. Scazza, S. Stringari, F. Tosto, A. Trombettoni, N. Victorin, D. Wilkowski, K. Khani, and A. Yakimenko, “Roadmap on atomtronics: State of the art and perspective,” *arXiv:2008.04439*, 2021.
- [37] M. F. Gonzalez-Zalba, S. N. Shevchenko, S. Barraud, J. R. Johansson, A. J. Ferguson, F. Nori, and A. C. Betz, “Gate-sensing coherent charge oscillations in a silicon field-effect transistor,” *Nano Letters*, vol. 16, pp. 1614–1619, Mar 2016.
- [38] S. Datta, *Electronic Transport in Mesoscopic Systems*. Cambridge University Press, 1995.
- [39] E. Akkermans and G. Montambaux, *Mesoscopic Physics of Electrons and Photons*. Cambridge University Press, 2007.
- [40] I. Carusotto, “Nonlinear atomic Fabry–Perot interferometer: From the mean-field theory to the atom blockade effect,” *Phys. Rev. A*, vol. 63, p. 023610, Jan 2001.
- [41] Y. Aharonov and D. Bohm, “Significance of electromagnetic potentials in the quantum theory,” *Phys. Rev.*, vol. 115, pp. 485–491, Aug 1959.
- [42] R. A. Webb, S. Washburn, C. P. Umbach, and R. B. Laibowitz, “Observation of  $\frac{h}{e}$  Aharonov–Bohm oscillations in normal–metal rings,” *Phys. Rev. Lett.*, vol. 54, pp. 2696–2699, Jun 1985.
- [43] A. D. Stone and Y. Imry, “Periodicity of the Aharonov–Bohm effect in normal–metal rings,” *Phys. Rev. Lett.*, vol. 56, pp. 189–192, Jan 1986.
- [44] S. Washburn and R. A. Webb, “Aharonov–Bohm effect in normal metal quantum coherence and transport,” *Advances in Physics*, vol. 35, no. 4, pp. 375–422, 1986.
- [45] J.-P. Brantut, J. Meineke, D. Stadler, S. Krinner, and T. Esslinger, “Conduction of ultracold fermions through a mesoscopic channel,” *Science*, vol. 337, p. 1069, 2012.
- [46] D. Stadler, S. Krinner, J. Meineke, J.-P. Brantut, and T. Esslinger, “Observing the drop of resistance in the flow of a superfluid fermi gas,” *Nature*, vol. 491, pp. 736–739, Nov 2012.
- [47] J.-P. Brantut, C. Grenier, J. Meineke, D. Stadler, S. Krinner, C. Kollath, T. Esslinger, and A. Georges, “A thermoelectric heat engine with ultracold atoms,” *Science*, vol. 342, no. 6159, pp. 713–715, 2013.

- [48] S. Krinner, D. Stadler, D. Husmann, J.-P. Brantut, and T. Esslinger, “Observation of quantized conductance in neutral matter,” *Nature*, vol. 517, pp. 64–67, Dec 2014.
- [49] M. Büttiker, “Four-terminal phase-coherent conductance,” *Phys. Rev. Lett.*, vol. 57, pp. 1761–1764, Oct 1986.
- [50] B. J. van Wees, H. van Houten, C. W. J. Beenakker, J. G. Williamson, L. P. Kouwenhoven, D. van der Marel, and C. T. Foxon, “Quantized conductance of point contacts in a two-dimensional electron gas,” *Phys. Rev. Lett.*, vol. 60, pp. 848–850, Feb 1988.
- [51] J. Dujardin, *Coherence and many-body effects in the transport of Bose–Einstein condensates*. PhD thesis, University Of Liège, 2015.
- [52] B. L. Altshuler, D. Khmel’nitzkii, A. I. Larkin, and P. A. Lee, “Magnetoresistance and Hall effect in a disordered two-dimensional electron gas,” *Phys. Rev. B*, vol. 22, pp. 5142–5153, Dec 1980.
- [53] G. Bergmann, “Weak localization in thin films: a time-of-flight experiment with conduction electrons,” *Physics Reports*, vol. 107, no. 1, pp. 1–58, 1984.
- [54] P.-E. Wolf and G. Maret, “Weak localization and coherent backscattering of photons in disordered media,” *Phys. Rev. Lett.*, vol. 55, pp. 2696–2699, Dec 1985.
- [55] Akkermans, E., Wolf, P.E., Maynard, R., and Maret, G., “Theoretical study of the coherent backscattering of light by disordered media,” *J. Phys. France*, vol. 49, no. 1, pp. 77–98, 1988.
- [56] Wolf, P.E., Maret, G., Akkermans, E., and Maynard, R., “Optical coherent backscattering by random media: an experimental study,” *J. Phys. France*, vol. 49, no. 1, pp. 63–75, 1988.
- [57] F. Jendrzejewski, K. Müller, J. Richard, A. Date, T. Plisson, P. Bouyer, A. Aspect, and V. Josse, “Coherent backscattering of ultracold atoms,” *Phys. Rev. Lett.*, vol. 109, p. 195302, Nov 2012.
- [58] G. Labeyrie, T. Karpiuk, J.-F. Schaff, B. Grémaud, C. Miniatura, and D. Delande, “Enhanced backscattering of a dilute Bose-Einstein condensate,” *EPL (Europhysics Letters)*, vol. 100, p. 66001, dec 2012.
- [59] T. Wellens and B. Grémaud, “Nonlinear coherent transport of waves in disordered media,” *Phys. Rev. Lett.*, vol. 100, p. 033902, Jan 2008.
- [60] M. Hartung, T. Wellens, C. A. Müller, K. Richter, and P. Schlagheck, “Coherent backscattering of Bose–Einstein condensates in two-dimensional disorder potentials,” *Phys. Rev. Lett.*, vol. 101, p. 020603, July 2008.
- [61] T. Hartmann, J. Michl, C. Petitjean, T. Wellens, J.-D. Urbina, K. Richter, and P. Schlagheck, “Weak localization with nonlinear bosonic matter waves,” *Ann. Phys.*, vol. 327, pp. 1998–2049, Aug. 2012.
- [62] T. Geiger, A. Buchleitner, and T. Wellens, “Microscopic scattering theory for interacting bosons in weak random potentials,” *New J. Phys.*, vol. 15, no. 11, p. 115015, 2013.
- [63] R. A. Pepino, “Advances in atomtronics,” *Entropy*, vol. 23, no. 5, 2021.
- [64] Lord Rayleigh, “XV. on the light from the sky, its polarization and colour,” *The London, Edinburgh, and Dublin Philosophical Magazine and Journal of Science*, vol. 41, no. 271, pp. 107–120, 1871.

- [65] Lord Rayleigh, “X. on the electromagnetic theory of light,” *The London, Edinburgh, and Dublin Philosophical Magazine and Journal of Science*, vol. 12, no. 73, pp. 81–101, 1881.
- [66] Lord Rayleigh, “XXXIV. on the transmission of light through an atmosphere containing small particles in suspension, and on the origin of the blue of the sky,” *The London, Edinburgh, and Dublin Philosophical Magazine and Journal of Science*, vol. 47, no. 287, pp. 375–384, 1899.
- [67] Lord Rayleigh, “Colours of sea and sky1,” *Nature*, vol. 83, pp. 48–50, Mar 1910.
- [68] G. Mie, “Beiträge zur Optik trüber Medien, speziell kolloidaler Metallösungen,” *Annalen der Physik*, vol. 330, no. 3, pp. 377–445, 1908.
- [69] D. A. Wharam, T. J. Thornton, R. Newbury, M. Pepper, H. Ahmed, J. E. F. Frost, D. G. Hasko, D. C. Peacock, D. A. Ritchie, and G. A. C. Jones, “One-dimensional transport and the quantisation of the ballistic resistance,” *Journal of Physics C: Solid State Physics*, vol. 21, pp. L209–L214, mar 1988.
- [70] N. Goel, J. Graham, J. Keay, K. Suzuki, S. Miyashita, M. Santos, and Y. Hirayama, “Ballistic transport in insb mesoscopic structures,” *Physica E: Low-dimensional Systems and Nanostructures*, vol. 26, no. 1, pp. 455 – 459, 2005. International Conference on Quantum Dots.
- [71] B. Hackens, S. Faniel, F. Delfosse, C. Gustin, H. Boutry, I. Huynen, X. Wallart, S. Bol-laert, A. Cappy, and V. Bayot, “Long dephasing time and high temperature ballistic transport in an InGaAs open quantum dot,” *Physica E: Low-dimensional Systems and Nanostructures*, vol. 17, pp. 143 – 146, 2003. Proceedings of the International Conference on Superlattices, Nano-structures and Nano-devices ICSNN 2002 o-structures and Nano-devices ICSNN 2002.
- [72] S. Faniel, B. Hackens, A. Vlad, L. Moldovan, C. Gustin, B. Habib, S. Melinte, M. Shayegan, and V. Bayot, “Dephasing time of two-dimensional holes in GaAs open quantum dots: Magnetotransport measurements,” *Phys. Rev. B*, vol. 75, p. 193310, May 2007.
- [73] C. T. White and T. N. Todorov, “Carbon nanotubes as long ballistic conductors,” *Nature*, vol. 393, pp. 240–242, May 1998.
- [74] T. Mutat, J. Adler, and M. Sheintuch, “Single species transport and self diffusion in wide single-walled carbon nanotubes,” *The Journal of Chemical Physics*, vol. 136, p. 234902, June 2012.
- [75] J. Baringhaus, M. Ruan, F. Edler, A. Tejada, M. Sicot, A. Taleb-Ibrahimi, A.-P. Li, Z. Jiang, E. H. Conrad, C. Berger, C. Tegenkamp, and W. A. de Heer, “Exceptional ballistic transport in epitaxial graphene nanoribbons,” *Nature*, vol. 506, pp. 349–354, Feb. 2014.
- [76] N. Cherroret, *Coherent multiple scattering: from atomic matter waves to light and vice versa*. Habilitation à diriger des recherches, Sorbonne Université, Nov. 2018.
- [77] P. W. Anderson, “Absence of diffusion in certain random lattices,” *Phys. Rev.*, vol. 109, pp. 1492–1505, Mar. 1958.
- [78] T. Wellens and M. Walter, “Lecture on quantum transport,” 2013.
- [79] P. Drude, “Zur Elektronentheorie der Metalle,” *Annalen der Physik*, vol. 306, no. 3, pp. 566–613, 1900.

- [80] P. Drude, “Zur Elektronentheorie der Metalle; II. Teil. Galvanomagnetische und thermomagnetische Effecte,” *Annalen der Physik*, vol. 308, no. 11, pp. 369–402, 1900.
- [81] N. Ashcroft and N. Mermin, *Solid state physics*. Brooks/Cole Publishing Company, 1976.
- [82] S. Chandrasekhar, *Radiative transfer*. Dover Publications Inc., 1950.
- [83] E. E. Salpeter and H. A. Bethe, “A relativistic equation for bound-state problems,” *Phys. Rev.*, vol. 84, pp. 1232–1242, Dec 1951.
- [84] M. Piraud, L. Pezzé, and L. Sanchez-Palencia, “Quantum transport of atomic matter waves in anisotropic two-dimensional and three-dimensional disorder,” *New Journal of Physics*, vol. 15, p. 075007, 07 2013.
- [85] T. Ihn, *Electronic Quantum Transport in Mesoscopic Semiconductor Structures*. Springer Tracts in Modern Physics, 2004.
- [86] C. Miniatura, R. C. Kuhn, D. Delande, and C. A. Müller, “Quantum diffusion of matter waves in 2D speckle potentials,” *The European Physical Journal B*, vol. 68, pp. 353–364, Apr 2009.
- [87] J. Richard, *Propagation d’atomes ultra-froids en milieu désordonné - Étude dans l’espace des impulsions de phénomènes de diffusion et de localisation*. PhD thesis, 2015.
- [88] T. Ihn, *Semiconductor Nanostructures: Quantum states and electronic transport*. Oxford University Press, 2009.
- [89] F. Jendrzejewski, *Quantum transport of ultracold atoms in disordered potentials*. PhD thesis, 2012.
- [90] T. Wellens, “Nonlinear coherent backscattering,” *Applied Physics B*, vol. 95, pp. 189–193, May 2009.
- [91] L. Gor’kov, A. Larkin, and D. E. Khmel’nitskii, “Particle conductivity in a two-dimensional random potential,” *JETP Lett.*, vol. 30, p. 228, 1979.
- [92] E. Akkermans and R. Maynard, “Weak localization of waves,” *J. Physique Lett.*, vol. 46, pp. 1045–1053, 1985.
- [93] M. P. Van Albada and A. Lagendijk, “Observation of weak localization of light in a random medium,” *Phys. Rev. Lett.*, vol. 55, pp. 2692–2695, Dec 1985.
- [94] D. Y. Sharvin and Y. V. Sharvin, “Magnetic-flux quantization in a cylindrical film of a normal metal,” *JETP Lett.*, vol. 34, p. 272, 1981.
- [95] B. L. Altshuler, A. G. Aronov, and B. Z. Spivak, “The Aharonov–Bohm effect in disordered conductors,” *Pis’ma Zh. Eksp. Teor. Fiz.*, vol. 33, no. 2, p. 101, 1981.
- [96] B. L. Al’tshuler, A. G. Aronov, and B. Z. Spivak, “The Aharonov–Bohm effect in disordered conductors,” *JETP Lett.*, vol. 33, p. 94, 1981.
- [97] D. J. Bishop, R. C. Dynes, and D. C. Tsui, “Magnetoresistance in Si metal-oxide-semiconductor field-effect transistors: Evidence of weak localization and correlation,” *Phys. Rev. B*, vol. 26, pp. 773–779, Jul 1982.
- [98] L. Van den dries, C. Van Haesendonck, Y. Bruynseraede, and G. Deutscher, “Two-dimensional localization in thin copper films,” *Phys. Rev. Lett.*, vol. 46, pp. 565–568, Feb 1981.

- [99] H. Beckmann, T. Fulmer, D. Garrett, M. Hossain, and G. Bergmann, “Weak localization in thin Cs films,” *Phys. Rev. B*, vol. 59, pp. 7724–7731, Mar 1999.
- [100] M. Oszałdowski, T. Berus, and V. K. Dugaev, “Weak localization in insb thin films heavily doped with lead,” *Phys. Rev. B*, vol. 65, p. 235418, May 2002.
- [101] B. Hapke, “Bidirectional reflectance spectroscopy: The coherent backscatter opposition effect and anisotropic scattering,” *Icarus*, vol. 157, no. 2, pp. 523 – 534, 2002.
- [102] D. S. Wiersma, M. P. van Albada, B. A. van Tiggelen, and A. Lagendijk, “Experimental evidence for recurrent multiple scattering events of light in disordered media,” *Phys. Rev. Lett.*, vol. 74, pp. 4193–4196, May 1995.
- [103] B. A. van Tiggelen, A. Lagendijk, and A. Tip, “Multiple-scattering effects for the propagation of light in 3D slabs,” *Journal of Physics: Condensed Matter*, vol. 2, pp. 7653–7677, sep 1990.
- [104] A. Tourin, A. Derode, P. Roux, B. A. van Tiggelen, and M. Fink, “Time-dependent coherent backscattering of acoustic waves,” *Phys. Rev. Lett.*, vol. 79, pp. 3637–3639, Nov 1997.
- [105] J. de Rosny, A. Tourin, and M. Fink, “Coherent backscattering of an elastic wave in a chaotic cavity,” *Phys. Rev. Lett.*, vol. 84, pp. 1693–1695, Feb 2000.
- [106] A. Derode, V. Mamou, F. Padilla, F. Jenson, and P. Laugier, “Dynamic coherent backscattering in a heterogeneous absorbing medium: Application to human trabecular bone characterization,” *Applied Physics Letters*, vol. 87, no. 11, p. 114101, 2005.
- [107] L. Margerin, “Chapter 1 coherent back-scattering and weak localization of seismic waves,” in *Earth Heterogeneity and Scattering Effects on Seismic Waves*, vol. 50 of *Advances in Geophysics*, pp. 1–19, Elsevier, 2008.
- [108] L. Margerin, M. Campillo, B. A. Van Tiggelen, and R. Hennino, “Energy partition of seismic coda waves in layered media: Theory and application to pinyon flats observatory,” *Geophysical Journal International*, vol. 177, no. 2, pp. 571–585, 2009.
- [109] G. Labeyrie, F. de Tomasi, J.-C. Bernard, C. A. Müller, C. Miniatura, and R. Kaiser, “Coherent backscattering of light by cold atoms,” *Phys. Rev. Lett.*, vol. 83, pp. 5266–5269, Dec 1999.
- [110] N. Cherroret, T. Karpiuk, C. A. Müller, B. Grémaud, and C. Miniatura, “Coherent backscattering of ultracold matter waves: Momentum space signatures,” *Phys. Rev. A*, vol. 85, p. 011604, Jan 2012.
- [111] N. Finlayson and G. I. Stegeman, “Spatial switching, instabilities, and chaos in a three-waveguide nonlinear directional coupler,” *Applied Physics Letters*, vol. 56, no. 23, pp. 2276–2278, 1990.
- [112] D. Hennig and G. Tsironis, “Wave transmission in nonlinear lattices,” *Physics Reports*, vol. 307, no. 5, pp. 333–432, 1999.
- [113] T. Chanelière, D. Wilkowski, Y. Bidet, R. Kaiser, and C. Miniatura, “Saturation-induced coherence loss in coherent backscattering of light,” *Phys. Rev. E*, vol. 70, p. 036602, Sep 2004.
- [114] V. M. Agranovich and V. E. Kravtsov, “Nonlinear backscattering from opaque media,” *Phys. Rev. B*, vol. 43, pp. 13691–13694, Jun 1991.
- [115] T. Geiger, A. Buchleitner, and T. Wellens, “Microscopic scattering theory for interacting bosons in weak random potentials,” *New J. Phys.*, vol. 15, p. 115015, Nov 2013.

- [116] T. Scoquart, T. Wellens, D. Delande, and N. Cherroret, “Quench dynamics of a weakly interacting disordered Bose gas in momentum space,” *Phys. Rev. Research*, vol. 2, p. 033349, Sep 2020.
- [117] N. Mott, “Electrons in disordered structures,” *Advances in Physics*, vol. 16, no. 61, pp. 49–144, 1967.
- [118] N. Mott, *Metal–Insulator Transitions*. Taylor and Francis, 1990.
- [119] A. Ioffe and A. Regel, “Non–crystalline, amorphous and liquid electronic semiconductors,” *Progress in Semiconductors*, vol. 4, pp. 237–291, 1960.
- [120] D. Vollhardt and P. Wölfle, “Chapter 1 - self–consistent theory of Anderson localization,” in *Electronic Phase Transitions* (W. Hanke and Y. Kopayev, eds.), vol. 32 of *Modern Problems in Condensed Matter Sciences*, pp. 1–78, Elsevier, 1992.
- [121] E. Abrahams, P. W. Anderson, D. C. Licciardello, and T. V. Ramakrishnan, “Scaling theory of localization: Absence of quantum diffusion in two dimensions,” *Phys. Rev. Lett.*, vol. 42, pp. 673–676, Mar 1979.
- [122] D. Thouless, “Electrons in disordered systems and the theory of localization,” *Physics Reports*, vol. 13, no. 3, pp. 93–142, 1974.
- [123] P. Sierant, D. Delande, and J. Zakrzewski, “Thouless time analysis of Anderson and many–body localization transitions,” *Phys. Rev. Lett.*, vol. 124, p. 186601, May 2020.
- [124] F. Wegner, “Exact density of states for lowest Landau level in white noise potential superfield representation for interacting systems,” *Zeitschrift für Physik B Condensed Matter*, vol. 51, pp. 279–285, Dec 1983.
- [125] D. Vollhardt and P. Wölfle, “Scaling equations from a self–consistent theory of Anderson localization,” *Phys. Rev. Lett.*, vol. 48, pp. 699–702, Mar 1982.
- [126] A. Lagendijk, B. Tiggelen, and D. Wiersma, “Fifty years of Anderson localization,” *Phys. Today*, vol. 62, pp. 24–29, 08 2009.
- [127] M. Filoche and S. Mayboroda, “Universal mechanism for Anderson and weak localization,” *Proceedings of the National Academy of Sciences*, vol. 109, no. 37, pp. 14761–14766, 2012.
- [128] M. L. Lyra, S. Mayboroda, and M. Filoche, “Dual landscapes in Anderson localization on discrete lattices,” *EPL (Europhysics Letters)*, vol. 109, p. 47001, feb 2015.
- [129] D. S. Wiersma, P. Bartolini, A. Lagendijk, and R. Righini, “Localization of light in a disordered medium,” *Nature*, vol. 390, no. 6661, pp. 671–673, 1997.
- [130] A. A. Chabanov, M. Stoytchev, and A. Z. Genack, “Statistical signatures of photon localization,” *Nature*, vol. 404, pp. 850–853, Apr 2000.
- [131] T. Schwartz, G. Bartal, S. Fishman, and M. Segev, “Transport and Anderson localization in disordered two–dimensional photonic lattices,” *Nature*, vol. 446, p. 52–55, Mar 2007.
- [132] R. Weaver, “Anderson localization of ultrasound,” *Wave Motion*, vol. 12, no. 2, pp. 129–142, 1990.
- [133] H. Hu, A. Strybulevych, J. H. Page, S. E. Skipetrov, and B. A. van Tiggelen, “Localization of ultrasound in a three–dimensional elastic network,” *Nature Phys.*, vol. 4, pp. 945–948, Oct 2008.

- [134] A. A. Chabanov, Z. Q. Zhang, and A. Z. Genack, “Breakdown of diffusion in dynamics of extended waves in mesoscopic media,” *Phys. Rev. Lett.*, vol. 90, p. 203903, May 2003.
- [135] J. Billy, V. Josse, Z. Zuo, A. Bernard, B. Hambrecht, P. Lugan, D. Clément, L. Sanchez-Palencia, P. Bouyer, and A. Aspect, “Direct observation of Anderson localization of matter waves in a controlled disorder.,” *Nature*, vol. 453, p. 891, June 2008.
- [136] G. Roati, C. D’Errico, L. Fallani, M. Fattori, C. Fort, M. Zaccanti, G. Modugno, M. Modugno, and M. Inguscio, “Anderson localization of a non-interacting Bose–Einstein condensate.,” *Nature*, vol. 453, p. 895, June 2008.
- [137] F. Moore, J. Robinson, C. Bharucha, B. Sundaram, and M. Raizen, “Atom optics realization of the quantum  $\delta$ -kicked rotor,” *Phys. Rev. Lett.*, vol. 75, p. 4598, Dec 1995.
- [138] J. Chabé, G. Lemarié, B. Grémaud, D. Delande, P. Szriftgiser, and J. Garreau, “Experimental observation of the Anderson metal–insulator transition with atomic matter waves,” *Phys. Rev. Lett.*, vol. 101, p. 255702, Dec 2008.
- [139] N. Cherroret, T. Karpiuk, B. Grémaud, and C. Miniatura, “Thermalization of matter waves in speckle potentials,” *Phys. Rev. A*, vol. 92, p. 063614, Dec 2015.
- [140] S. Ghosh, D. Delande, C. Miniatura, and N. Cherroret, “Coherent backscattering reveals the Anderson transition,” *Phys. Rev. Lett.*, vol. 115, p. 200602, Nov 2015.
- [141] T. Karpiuk, N. Cherroret, K. L. Lee, B. Grémaud, C. A. Müller, and C. Miniatura, “Coherent forward scattering peak induced by Anderson localization,” *Phys. Rev. Lett.*, vol. 109, p. 190601, Nov 2012.
- [142] V. Josse, *Propagation cohérente d’atomes ultra-froids: Laser à atomes guidés et localisation d’Anderson*. Habilitation à diriger des recherches, Université Paris–Sud, Apr 2015.
- [143] S. Ghosh, N. Cherroret, B. Grémaud, C. Miniatura, and D. Delande, “Coherent forward scattering in two-dimensional disordered systems,” *Phys. Rev. A*, vol. 90, p. 063602, Dec 2014.
- [144] T. Micklitz, C. A. Müller, and A. Altland, “Strong Anderson localization in cold atom quantum quenches,” *Phys. Rev. Lett.*, vol. 112, p. 110602, Mar 2014.
- [145] K. L. Lee, B. Grémaud, and C. Miniatura, “Dynamics of localized waves in one-dimensional random potentials: Statistical theory of the coherent forward scattering peak,” *Phys. Rev. A*, vol. 90, p. 043605, Oct 2014.
- [146] T.-L. Dao, A. Georges, J. Dalibard, C. Salomon, and I. Carusotto, “Measuring the one-particle excitations of ultracold fermionic atoms by stimulated raman spectroscopy,” *Phys. Rev. Lett.*, vol. 98, p. 240402, Jun 2007.
- [147] G. Lemarié, C. A. Müller, D. Guéry-Odelin, and C. Miniatura, “Coherent backscattering and forward-scattering peaks in the quantum kicked rotor,” *Phys. Rev. A*, vol. 95, p. 043626, Apr 2017.
- [148] C. Barenghi and N. G. Parker, *A Primer on Quantum Fluids*. Springer International Publishing, 2016.
- [149] R. Tolman, *The Principles of Statistical Mechanics*. Dover Publications, 1938.
- [150] L. Landau and E. Lifshitz, *Course of Theoretical Physics: Statistical Physics*. Butterworth-Heinemann, 1980.
- [151] C. Cohen-Tannoudji, “Condensation de Bose–Einstein des gaz atomiques ultrafroids.” Cours du Collège de France, 1998.

- [152] J. Dalibard, “Cohérence et superfluidité dans les gaz atomiques.” Cours du Collège de France, 2016.
- [153] L. P. Pitaevski and S. Stringari, *Bose–Einstein condensation*. Oxford: Oxford University Press, 2016.
- [154] F. Dalfovo, S. Giorgini, L. P. Pitaevskii, and S. Stringari, “Theory of Bose–Einstein condensation in trapped gases,” *Rev. Mod. Phys.*, vol. 71, pp. 463–512, Apr 1999.
- [155] D. S. Durfee and W. Ketterle, “Experimental studies of Bose-Einstein condensation,” *Opt. Express*, vol. 2, pp. 299–313, Apr 1998.
- [156] E. A. Cornell and C. E. Wieman, “Nobel lecture: Bose–Einstein condensation in a dilute gas, the first 70 years and some recent experiments,” *Rev. Mod. Phys.*, vol. 74, pp. 875–893, Aug 2002.
- [157] D. G. Fried, T. C. Killian, L. Willmann, D. Landhuis, S. C. Moss, D. Kleppner, and T. J. Greytak, “Bose-Einstein condensation of atomic hydrogen,” *Phys. Rev. Lett.*, vol. 81, pp. 3811–3814, Nov 1998.
- [158] A. Robert, O. Sirjean, A. Browaeys, J. Poupard, S. Nowak, D. Boiron, C. I. Westbrook, and A. Aspect, “A Bose-Einstein condensate of metastable atoms,” *Science*, vol. 292, no. 5516, pp. 461–464, 2001.
- [159] F. Pereira Dos Santos, J. Léonard, J. Wang, C. J. Barrelet, F. Perales, E. Rasel, C. S. Unnikrishnan, M. Leduc, and C. Cohen-Tannoudji, “Bose-Einstein condensation of metastable helium,” *Phys. Rev. Lett.*, vol. 86, pp. 3459–3462, Apr 2001.
- [160] F. Schreck, L. Khaykovich, K. L. Corwin, G. Ferrari, T. Bourdel, J. Cubizolles, and C. Salomon, “Quasipure Bose-Einstein condensate immersed in a Fermi sea,” *Phys. Rev. Lett.*, vol. 87, p. 080403, Aug 2001.
- [161] C. C. Bradley, C. A. Sackett, J. J. Tollett, and R. G. Hulet, “Evidence of Bose-Einstein condensation in an atomic gas with attractive interactions,” *Phys. Rev. Lett.*, vol. 75, p. 1687–1690, Aug 1995.
- [162] G. Salomon, L. Fouché, S. Lepoutre, A. Aspect, and T. Bourdel, “All-optical cooling of  $^{39}\text{K}$  to Bose-Einstein condensation,” *Phys. Rev. A*, vol. 90, p. 033405, Sep 2014.
- [163] S. Kraft, F. Vogt, O. Appel, F. Riehle, and U. Sterr, “Bose-Einstein condensation of alkaline Earth atoms:  $^{40}\text{Ca}$ ,” *Phys. Rev. Lett.*, vol. 103, p. 130401, Sep 2009.
- [164] G. Modugno, G. Ferrari, G. Roati, R. J. Brecha, A. Simoni, and M. Inguscio, “Bose-Einstein condensation of potassium atoms by sympathetic cooling,” *Science*, vol. 294, no. 5545, pp. 1320–1322, 2001.
- [165] A. Griesmaier, J. Werner, S. Hensler, J. Stuhler, and T. Pfau, “Bose-Einstein condensation of chromium,” *Phys. Rev. Lett.*, vol. 94, p. 160401, Apr 2005.
- [166] S. L. Cornish, N. R. Claussen, J. L. Roberts, E. A. Cornell, and C. E. Wieman, “Stable  $^{85}\text{Rb}$  Bose-Einstein condensates with widely tunable interactions,” *Phys. Rev. Lett.*, vol. 85, pp. 1795–1798, Aug 2000.
- [167] S. Stellmer, M. K. Tey, B. Huang, R. Grimm, and F. Schreck, “Bose-Einstein condensation of strontium,” *Phys. Rev. Lett.*, vol. 103, p. 200401, Nov 2009.
- [168] S. Stellmer, M. K. Tey, R. Grimm, and F. Schreck, “Bose-Einstein condensation of  $^{86}\text{Sr}$ ,” *Phys. Rev. A*, vol. 82, p. 041602, Oct 2010.



- [169] P. G. Mickelson, Y. N. Martinez de Escobar, M. Yan, B. J. DeSalvo, and T. C. Killian, “Bose-Einstein condensation of  $^{88}\text{Sr}$  through sympathetic cooling with  $^{87}\text{Sr}$ ,” *Phys. Rev. A*, vol. 81, p. 051601, May 2010.
- [170] D. J. McCarron, H. W. Cho, D. L. Jenkin, M. P. Köppinger, and S. L. Cornish, “Dual-species Bose-Einstein condensate of  $^{87}\text{Rb}$  and  $^{133}\text{Cs}$ ,” *Phys. Rev. A*, vol. 84, p. 011603, Jul 2011.
- [171] T. Weber, J. Herbig, M. Mark, H.-C. Nägerl, and R. Grimm, “Bose-Einstein condensation of Cesium,” *Science*, vol. 299, pp. 232–235, Dec 2003.
- [172] Y. Tang, N. Q. Burdick, K. Baumann, and B. L. Lev, “Bose-Einstein condensation of  $^{162}\text{Dy}$  and  $^{160}\text{Dy}$ ,” *New J. Phys.*, vol. 17, no. 4, p. 045006, 2015.
- [173] M. Lu, N. Q. Burdick, S. H. Youn, and B. L. Lev, “Strongly dipolar Bose-Einstein condensate of dysprosium,” *Phys. Rev. Lett.*, vol. 107, p. 190401, Oct 2011.
- [174] K. Aikawa, A. Frisch, M. Mark, S. Baier, A. Rietzler, R. Grimm, and F. Ferlaino, “Bose-Einstein condensation of erbium,” *Phys. Rev. Lett.*, vol. 108, p. 210401, May 2012.
- [175] T. Fukuhara, S. Sugawa, and Y. Takahashi, “Bose-Einstein condensation of an ytterbium isotope,” *Phys. Rev. A*, vol. 76, p. 051604, Nov 2007.
- [176] Y. Takasu, K. Maki, K. Komori, T. Takano, K. Honda, M. Kumakura, T. Yabuzaki, and Y. Takahashi, “Spin-Singlet Bose-Einstein condensation of two-electron atoms,” *Phys. Rev. Lett.*, vol. 91, p. 040404, Jul 2003.
- [177] B. Pasquiou, A. Bayerle, S. M. Tzanova, S. Stellmer, J. Szczepkowski, M. Parigger, R. Grimm, and F. Schreck, “Quantum degenerate mixtures of strontium and rubidium atoms,” *Phys. Rev. A*, vol. 88, p. 023601, Aug 2013.
- [178] M. L. Harris, P. Tierney, and S. L. Cornish, “Magnetic trapping of a cold Rb–Cs atomic mixture,” *Journal of Physics B: Atomic, Molecular and Optical Physics*, vol. 41, p. 035303, Jan 2008.
- [179] B. A. Lippmann and J. Schwinger, “Variational principles for scattering processes,” *Phys. Rev.*, vol. 79, pp. 469–480, Aug 1950.
- [180] M. Born, “Quantenmechanik der Stoßvorgänge,” *Zeitschrift für Physik*, vol. 38, pp. 803–827, Nov 1926.
- [181] M. Koshino and T. Ando, “Transport in bilayer graphene: Calculations within a self-consistent born approximation,” *Phys. Rev. B*, vol. 73, p. 245403, Jun 2006.
- [182] J. E. Gubernatis, E. Domany, J. A. Krumhansl, and M. Huberman, “The Born approximation in the theory of the scattering of elastic waves by flaws,” *Journal of Applied Physics*, vol. 48, no. 7, pp. 2812–2819, 1977.
- [183] E. Fermi, “Motion of neutrons in hydrogenous substances,” *Ric. Sci.*, vol. 7, no. 13.
- [184] H. Feshbach, “A unified theory of nuclear reactions,” *Annals of Physics*, vol. 5, no. 4, pp. 357–390, 1958.
- [185] H. Feshbach, “A unified theory of nuclear reactions,” *Annals of Physics*, vol. 19, no. 2, pp. 287–313, 1962.
- [186] C. Chin, R. Grimm, P. Julienne, and E. Tiesinga, “Feshbach resonances in ultracold gases,” *Rev. Mod. Phys.*, vol. 82, pp. 1225–1286, Apr 2010.

- [187] A. J. Moerdijk, B. J. Verhaar, and A. Axelsson, “Resonances in ultracold collisions of  $^6\text{Li}$ ,  $^7\text{Li}$ , and  $^{23}\text{Na}$ ,” *Phys. Rev. A*, vol. 51, pp. 4852–4861, Jun 1995.
- [188] E. P. Gross, “Structure of a quantized vortex in boson systems,” *Il Nuovo Cimento*, vol. 20, pp. 454–477, May 1961.
- [189] L. P. Pitaevskii, “Vortex lines in an imperfect Bose gas,” *Zh. Eksp. Teor. Fiz.*, p. 451, 1961.
- [190] M. Johansson, G. Kopidakis, S. Lepri, and S. Aubry, “Transmission thresholds in time-periodically driven nonlinear disordered systems,” *EPL (Europhysics Letters)*, vol. 86, p. 10009, apr 2009.
- [191] S. E. Skipetrov and R. Maynard, “Instabilities of waves in nonlinear disordered media,” *Phys. Rev. Lett.*, vol. 85, pp. 736–739, Jul 2000.
- [192] B. Spivak and A. Zyuzin, “Mesoscopic sensitivity of speckles in disordered nonlinear media to changes of the scattering potential,” *Phys. Rev. Lett.*, vol. 84, pp. 1970–1973, Feb 2000.
- [193] I. Bloch, “Ultracold quantum gases in optical lattices,” *Nature Physics*, vol. 1, pp. 23–30, Oct 2005.
- [194] L. Khaykovich, “Formation of a matter-wave bright soliton,” *Science*, vol. 296, p. 1290–1293, May 2002.
- [195] A. Smerzi, S. Fantoni, S. Giovanazzi, and S. R. Shenoy, “Quantum coherent atomic tunneling between two trapped Bose–Einstein condensates,” *Phys. Rev. Lett.*, vol. 79, pp. 4950–4953, Dec. 1997.
- [196] S. Giovanazzi, A. Smerzi, and S. Fantoni, “Josephson effects in dilute Bose–Einstein condensates,” *Phys. Rev. Lett.*, vol. 84, pp. 4521–4524, May 2000.
- [197] I. Bloch, T. W. Hänsch, and T. Esslinger, “Measurement of the spatial coherence of a trapped Bose gas at the phase transition,” *Nature*, vol. 403, pp. 166–170, Jan 2000.
- [198] M. R. Andrews, C. G. Townsend, H.-J. Miesner, D. S. Durfee, D. M. Kurn, and W. Ketterle, “Observation of interference between two Bose condensates,” *Science*, vol. 275, no. 5300, pp. 637–641, 1997.
- [199] M.-O. Mewes, M. R. Andrews, D. M. Kurn, D. S. Durfee, C. G. Townsend, and W. Ketterle, “Output coupler for Bose–Einstein condensed atoms,” *Phys. Rev. Lett.*, vol. 78, pp. 582–585, Jan. 1997.
- [200] B. P. Anderson and M. A. Kasevich, “Macroscopic quantum interference from atomic tunnel arrays,” *Science*, vol. 282, no. 5394, pp. 1686–1689, 1998.
- [201] E. W. Hagley, “A well-collimated quasi-continuous atom laser,” *Science*, vol. 283, pp. 1706–1709, Mar. 1999.
- [202] I. Bloch, T. W. Hänsch, and T. Esslinger, “Atom laser with a cw output coupler,” *Phys. Rev. Lett.*, vol. 82, pp. 3008–3011, Apr. 1999.
- [203] L. Dobrek, M. Gajda, M. Lewenstein, K. Sengstock, G. Birkl, and W. Ertmer, “Optical generation of vortices in trapped Bose–Einstein condensates,” *Phys. Rev. A*, vol. 60, pp. R3381–R3384, Nov 1999.
- [204] A. Micheli, A. J. Daley, D. Jaksch, and P. Zoller, “Single atom transistor in a 1D optical lattice,” *Phys. Rev. Lett.*, vol. 93, p. 140408, 2004.

- [205] B. T. Seaman, M. Krämer, D. Z. Anderson, and M. J. Holland, “Atomtronics: Ultracold-atom analogs of electronic devices,” *Phys. Rev. A*, vol. 75, p. 023615, 2007.
- [206] R. A. Pepino, J. Cooper, D. Z. Anderson, and M. J. Holland, “Atomtronic circuits of diodes and transistors,” *Phys. Rev. Lett.*, vol. 103, p. 140405, 2009.
- [207] M. Bruderer and W. Belzig, “Mesoscopic transport of fermions through an engineered optical lattice connecting two reservoirs,” *Phys. Rev. A*, vol. 85, p. 013623, 2012.
- [208] L. Kristinsdóttir, O. Karlström, J. Bjerlin, J. Cremon, P. Schlagheck, A. Wacker, and S. Reimann, “Total current blockade in an ultracold dipolar quantum wire,” *Phys. Rev. Lett.*, vol. 110, p. 085303, Feb 2013.
- [209] S. Martellucci, A. Chester, A. Aspect, and M. Inguscio, *Bose–Einstein Condensates and Atom Lasers*. Springer, Boston, MA, 2002.
- [210] G. M. Moy, J. J. Hope, and C. M. Savage, “Atom laser based on Raman transitions,” *Phys. Rev. A*, vol. 55, pp. 3631–3638, May 1997.
- [211] N. P. Robins, C. Figl, S. A. Haine, A. K. Morrison, M. Jeppesen, J. J. Hope, and J. D. Close, “Achieving peak brightness in an atom laser,” *Phys. Rev. Lett.*, vol. 96, p. 140403, Apr 2006.
- [212] W. Guerin, J.-F. Riou, J. P. Gaebler, V. Josse, P. Bouyer, and A. Aspect, “Guided quasicontinuous atom laser,” *Phys. Rev. Lett.*, vol. 97, p. 200402, Nov. 2006.
- [213] V. Bolpasi, N. K. Efremidis, M. J. Morrissey, P. C. Condylis, D. Sahagun, M. Baker, and W. von Klitzing, “An ultra-bright atom laser,” *New J. Phys.*, vol. 16, p. 033036, Mar. 2014.
- [214] G. L. Gattobigio, A. Couvert, M. Jeppesen, R. Mathevet, and D. Guéry-Odelin, “Multimode-to-monomode guided-atom lasers: An entropic analysis,” *Phys. Rev. A*, vol. 80, p. 041605, Oct. 2009.
- [215] T. Ernst, T. Paul, and P. Schlagheck, “Transport of ultracold Bose gases beyond the Gross–Pitaevskii description,” *Phys. Rev. A*, vol. 81, p. 013631, Jan. 2010.
- [216] J. Dujardin, A. Argüelles, and P. Schlagheck, “Elastic and inelastic transmission in guided atom lasers: A truncated Wigner approach,” *Phys. Rev. A*, vol. 91, p. 033614, Mar 2015.
- [217] J.-F. Riou, Y. Le Coq, F. Impens, W. Guerin, C. J. Bordé, A. Aspect, and P. Bouyer, “Theoretical tools for atom-laser-beam propagation,” *Phys. Rev. A*, vol. 77, p. 033630, Mar. 2008.
- [218] J. Dujardin, A. Saenz, and P. Schlagheck, “A study of one-dimensional transport of Bose-Einstein condensates using exterior complex scaling,” *Appl. Phys. B*, vol. 117, pp. 765–773, Apr 2014.
- [219] T. Shibata, “Absorbing boundary conditions for the finite-difference time-domain calculation of the one-dimensional Schrödinger equation,” *Phys. Rev. B*, vol. 43, pp. 6760–6763, Mar 1991.
- [220] R. Kosloff and D. Kosloff, “Absorbing boundaries for wave propagation problems,” *J. Comput. Phys.*, vol. 63, pp. 363–376, Apr. 1986.
- [221] U. V. Riss and H.-D. Meyer, “The transformative complex absorbing potential method: a bridge between complex absorbing potentials and smooth exterior scaling,” *Journal of Physics B: Atomic, Molecular and Optical Physics*, vol. 31, pp. 2279–2304, may 1998.

- [222] E. Balslev and J. Combes, “Spectral properties of many-body Schrödinger operators with dilatation-analytic interactions,” *Commun. Math. Phys.*, vol. 22, pp. 280–294, Dec. 1971.
- [223] S. Barry, “Resonances in n-body quantum systems with dilatation analytic potentials and the foundations of time-dependent perturbation theory,” *Ann. Math.*, vol. 97, no. 2, p. 247, 1973.
- [224] W. P. Reinhardt, “Complex coordinates in the theory of atomic and molecular structure and dynamics,” *Annu. Rev. Phys. Chem.*, vol. 33, pp. 223–255, Oct. 1982.
- [225] B. Junker, “Recent computational developments in the use of complex scaling in resonance phenomena,” *Adv. Atom. Mol. Phys.*, vol. 18, p. 207, 1982.
- [226] Y. Ho, “The method of complex coordinate rotation and its applications to atomic collision processes,” *Phys. Rep.*, vol. 99, pp. 1–68, Oct. 1983.
- [227] P.-O. Löwdin, “On the change of spectra associated with unbounded similarity transformations of a many-particle Hamiltonian and the occurrence of resonance states in the method of complex scaling. Part I. general theory,” *Adv. Quant. Chem.*, vol. 19, p. 87, 1988.
- [228] P. Schlagheck and T. Paul, “Complex-scaling approach to the decay of Bose–Einstein condensates,” *Phys. Rev. A*, vol. 73, p. 23619, Feb. 2006.
- [229] S. Wimberger, P. Schlagheck, and R. Mannella, “Tunnelling rates for the nonlinear Wannier–Stark problem,” *J. Phys. B*, vol. 39, p. 729–740, Jan 2006.
- [230] P. Schlagheck and S. Wimberger, “Nonexponential decay of Bose–Einstein condensates: a numerical study based on the complex scaling method,” *Appl. Phys. B*, vol. 86, pp. 385–390, Dec. 2006.
- [231] S. Barry, “The definition of molecular resonance curves by the method of exterior complex scaling,” *Phys. Lett. A*, vol. 71, pp. 211–214, Apr. 1979.
- [232] N. Rom, E. Engdahl, and N. Moiseyev, “Tunneling rates in bound systems using smooth exterior complex scaling within the framework of the finite basis set approximation,” *J. Chem. Phys.*, vol. 93, no. 5, p. 3413, 1990.
- [233] K. Kato, “Resonances and continuum states in the complex scaling method,” *Journal of Physics: Conference Series*, vol. 49, p. 73–78, Oct 2006.
- [234] S. Haroche and J.-M. Raimond, *Exploring the Quantum: Atoms, Cavities, and Photons*. Oxford: Oxford University Press, 2006.
- [235] L. Landau and E. Lifshitz, *Course of Theoretical Physics: Mechanics*. Butterworth-Heinemann, 1982.
- [236] L. Landau and E. Lifshitz, *Course of Theoretical Physics: Quantum Mechanics*. Butterworth-Heinemann, 1983.
- [237] T. L. Curtright, D. B. Fairlie, and C. K. Zachos, *A Concise Treatise on Quantum Mechanics in Phase Space*. World Scientific, 2014.
- [238] A. Polkovnikov, “Phase space representation of quantum dynamics,” *Ann. Phys.*, vol. 325, pp. 1790–1852, Aug 2010.
- [239] P. Blakie, A. Bradley, M. Davis, R. Ballagh, and C. Gardiner, “Dynamics and statistical mechanics of ultra-cold Bose gases using c-field techniques,” *Advances in Physics*, vol. 57, no. 5, pp. 363–455, 2008.

- [240] E. Wigner, *Gruppentheorie und ihre Anwendung auf die Quantenmechanik der Atom-spektren*. Wiesbaden: Vieweg+Teubner Verlag, 1931.
- [241] E. Wigner, “On the quantum correction for thermodynamic equilibrium,” *Phys. Rev.*, vol. 40, pp. 749–760, June 1932.
- [242] E. C. G. Sudarshan, “Equivalence of semiclassical and quantum mechanical descriptions of statistical light beams,” *Phys. Rev. Lett.*, vol. 10, pp. 277–279, Apr 1963.
- [243] R. J. Glauber, “Coherent and incoherent states of the radiation field,” *Phys. Rev.*, vol. 131, pp. 2766–2788, Sep 1963.
- [244] K. Husimi, “Some formal properties of the density matrix,” *Proceedings of the Physico-Mathematical Society of Japan. 3rd Series*, vol. 22, no. 4, pp. 264–314, 1940.
- [245] L. Cohen, “Generalized phase-space distribution functions,” *Journal of Mathematical Physics*, vol. 7, no. 5, pp. 781–786, 1966.
- [246] L. Cohen, “Quantization problem and variational principle in the phase-space formulation of quantum mechanics,” *Journal of Mathematical Physics*, vol. 17, no. 10, pp. 1863–1866, 1976.
- [247] U. Leonhardt, *Measuring the Quantum State of Light*. Cambridge University Press, 1997.
- [248] A. Kenfack and K. Yczkowski, “Negativity of the Wigner function as an indicator of non-classicality,” *J. Opt. B*, vol. 6, p. 396–404, Aug 2004.
- [249] W. Rossmann, *Lie Groups - An Introduction Through Linear Groups*. Oxford Science Publications, 2002.
- [250] B. Hall, *Lie Groups, Lie Algebras, and Representations An Elementary Introduction*. Springer, 2015.
- [251] C. W. Gardiner and P. Zoller, *Quantum Noise: a handbook of stochastic methods for physics, chemistry and the natural sciences*. Berlin: Springer-Verlag, 3 ed., 2004.
- [252] D. J. Watts and S. H. Strogatz, “Collective dynamics of ‘small-world’ networks,” *Nature*, vol. 393, pp. 440–442, Jun 1998.
- [253] V. Latora and M. Marchiori, “Efficient behavior of small-world networks,” *Phys. Rev. Lett.*, vol. 87, p. 198701, Oct 2001.
- [254] A. Sinatra, C. Lobo, and Y. Castin, “The truncated Wigner method for Bose-condensed gases: limits of validity and applications,” *J. Phys. B*, vol. 35, pp. 3599–3631, Sept. 2002.
- [255] K. E. Cahill and R. J. Glauber, “Density operators and quasiprobability distributions,” *Phys. Rev.*, vol. 177, pp. 1882–1902, Jan. 1969.
- [256] C. Gardiner and P. Zoller, *The Quantum World of Ultra-Cold Atoms and Light Book III: Ultra-Cold Atoms*. World Scientific (Europe), 2017.
- [257] J. Dujardin, T. Engl, and P. Schlagheck, “Breakdown of Anderson localization in the transport of Bose-Einstein condensates through one-dimensional disordered potentials,” *Phys. Rev. A*, vol. 93, p. 013612, Jan 2016.
- [258] A. Polkovnikov, “Quantum corrections to the dynamics of interacting bosons: Beyond the truncated wigner approximation,” *Phys. Rev. A*, vol. 68, p. 053604, Nov. 2003.
- [259] A. Polkovnikov and V. Gritsev, “Breakdown of the adiabatic limit in low-dimensional gapless systems,” *Nature Physics*, vol. 4, pp. 477–481, Jun 2008.

- [260] A. A. Norrie, R. J. Ballagh, and C. W. Gardiner, “Quantum turbulence and correlations in bose-einstein condensate collisions,” *Phys. Rev. A*, vol. 73, p. 043617, Apr 2006.
- [261] P. D. Drummond and A. D. Hardman, “Simulation of quantum effects in raman-active waveguides,” *Europhysics Letters (EPL)*, vol. 21, pp. 279–284, jan 1993.
- [262] G. Vidal, “Efficient classical simulation of slightly entangled quantum computations,” *Phys. Rev. Lett.*, vol. 91, p. 147902, Oct 2003.
- [263] F. Verstraete, D. Porras, and J. I. Cirac, “Density matrix renormalization group and periodic boundary conditions: A quantum information perspective,” *Phys. Rev. Lett.*, vol. 93, p. 227205, Nov 2004.
- [264] G. Vidal, “Efficient simulation of one-dimensional quantum many-body systems,” *Phys. Rev. Lett.*, vol. 93, p. 040502, Jul 2004.
- [265] S. R. White, “Density matrix formulation for quantum renormalization groups,” *Phys. Rev. Lett.*, vol. 69, pp. 2863–2866, Nov 1992.
- [266] J. I. Cirac and F. Verstraete, “Renormalization and tensor product states in spin chains and lattices,” *Journal of Physics A: Mathematical and Theoretical*, vol. 42, p. 504004, dec 2009.
- [267] J. J. Sakurai, *Modern Quantum Mechanics*. Revised ed ed., 1994.
- [268] D. J. Griffiths, *Introduction to Quantum Mechanics (2nd Edition)*. Pearson Prentice Hall, 2nd ed., Apr. 2004.
- [269] C. Cohen-Tannoudji, B. Diu, and F. Laloë, *Mécanique Quantique, volume I and II*, vol. 67. Hermann, Paris, 1977.
- [270] W. Ehrenberg and R. E. Siday, “The refractive index in electron optics and the principles of dynamics,” *Proceedings of the Physical Society. Section B*, vol. 62, no. 1, p. 8, 1949.
- [271] C. G. Kuper, *The Ehrenberg-Siday-Aharonov-Bohm Effect*, pp. 239–247. Berlin, Heidelberg: Springer Berlin Heidelberg, 2000.
- [272] Y. Aharonov and D. Bohm, “Further considerations on electromagnetic potentials in the quantum theory,” *Phys. Rev.*, vol. 123, pp. 1511–1524, Aug 1961.
- [273] A. J. Leggett, “Macroscopic Quantum Systems and the Quantum Theory of Measurement,” *Progress of Theoretical Physics Supplement*, vol. 69, pp. 80–100, 03 1980.
- [274] S. Olariu and I. I. Popescu, “The quantum effects of electromagnetic fluxes,” *Rev. Mod. Phys.*, vol. 57, pp. 339–436, Apr 1985.
- [275] L. Vaidman, “Role of potentials in the Aharonov–Bohm effect,” *Phys. Rev. A*, vol. 86, p. 040101, Oct 2012.
- [276] R. Weder, “The electric Aharonov–Bohm effect,” *Journal of Mathematical Physics*, vol. 52, no. 5, p. 052109, 2011.
- [277] R. G. Chambers, “Shift of an electron interference pattern by enclosed magnetic flux,” *Phys. Rev. Lett.*, vol. 5, pp. 3–5, Jul 1960.
- [278] F. Strocchi and A. S. Wightman, “Proof of the charge superselection rule in local relativistic quantum field theory,” *Journal of Mathematical Physics*, vol. 15, no. 12, pp. 2198–2224, 1974.
- [279] P. Bocchieri and A. Loinger, “Nonexistence of the Aharonov–Bohm effect.,” *Nuov Cim A*, vol. 47, 1978.

- [280] P. Bocchieri, A. Loinger, and G. Siragusa, “Nonexistence of the Aharonov–Bohm effect.—ii,” *Nuov Cim A*, vol. 51, 1979.
- [281] S. M. Roy, “Condition for nonexistence of Aharonov–Bohm effect,” *Phys. Rev. Lett.*, vol. 44, pp. 111–114, Jan 1980.
- [282] P. Bocchieri and A. Loinger, “Incompatibility of the Aharonov–Bohm effect with the quantum laws,” *Lett. Nuov. Cim.*, vol. 35, 1982.
- [283] S. Roy and V. Singh, “Time–dependent Aharonov–Bohm hamiltonian and admissibility criteria of quantum wave functions,” *Nuov Cim A*, vol. 79, 1984.
- [284] A. Tonomura, N. Osakabe, T. Matsuda, T. Kawasaki, J. Endo, S. Yano, and H. Yamada, “Evidence for Aharonov–Bohm effect with magnetic field completely shielded from electron wave,” *Phys. Rev. Lett.*, vol. 56, pp. 792–795, Feb 1986.
- [285] Y. Gefen, Y. Imry, and M. Y. Azbel, “Quantum oscillations and the Aharonov–Bohm effect for parallel resistors,” *Phys. Rev. Lett.*, vol. 52, pp. 129–132, Jan 1984.
- [286] M. Büttiker, Y. Imry, and M. Y. Azbel, “Quantum oscillations in one–dimensional normal–metal rings,” *Phys. Rev. A*, vol. 30, pp. 1982–1989, Oct 1984.
- [287] Y. Aharonov and A. Casher, “Topological quantum effects for neutral particles,” *Phys. Rev. Lett.*, vol. 53, pp. 319–321, Jul 1984.
- [288] A. Cimmino, G. I. Opat, A. G. Klein, H. Kaiser, S. A. Werner, M. Arif, and R. Clothier, “Observation of the topological Aharonov–Casher phase shift by neutron interferometry,” *Phys. Rev. Lett.*, vol. 63, pp. 380–383, Jul 1989.
- [289] Y. Imry and R. A. Webb, “Quantum interference and the Aharonov–Bohm effect,” *Sci. Am.*, vol. 260, p. 36, 1989.
- [290] E. Xypakis, J.-W. Rhim, J. H. Bardarson, and R. Ilan, “Perfect transmission and Aharonov–Bohm oscillations in topological insulator nanowires with nonuniform cross section,” *Phys. Rev. B*, vol. 101, p. 045401, Jan 2020.
- [291] W. Gou, T. Chen, D. Xie, T. Xiao, T.-S. Deng, B. Gadway, W. Yi, and B. Yan, “Tunable nonreciprocal quantum transport through a dissipative Aharonov–Bohm ring in ultracold atoms,” *Phys. Rev. Lett.*, vol. 124, p. 070402, Feb 2020.
- [292] M. Todorčić, B. Klajn, D. Jukić, and H. Buljan, “Berry phase for a Bose gas on a one–dimensional ring,” *Phys. Rev. A*, vol. 102, p. 013322, Jul 2020.
- [293] K. Shinohara, T. Aoki, and A. Morinaga, “Scalar Aharonov–Bohm effect for ultracold atoms,” *Phys. Rev. A*, vol. 66, p. 042106, Oct 2002.
- [294] T. Aoki, M. Yasuhara, and A. Morinaga, “Atomic multiple–wave interferometer phase–shifted by the scalar Aharonov–Bohm effect,” *Phys. Rev. A*, vol. 67, p. 053602, May 2003.
- [295] A. Morinaga, T. Aoki, and M. Yasuhara, “Dependence of berry’s phase for atom on a sign of the  $g$  factor in the rotating magnetic field,” *Phys. Rev. A*, vol. 71, p. 054101, May 2005.
- [296] A. Tokuno, M. Oshikawa, and E. Demler, “Dynamics of one–dimensional bose liquids: Andreev–like reflection at  $y$  junctions and the absence of the Aharonov–Bohm effect,” *Phys. Rev. Lett.*, vol. 100, p. 140402, Apr 2008.
- [297] M. Aidelsburger, M. Atala, M. Lohse, J. T. Barreiro, B. Paredes, and I. Bloch, “Realization of the Hofstadter Hamiltonian with ultracold atoms in optical lattices,” *Phys. Rev. Lett.*, vol. 111, p. 185301, Oct 2013.

- [298] M.-X. Huo, W. Nie, D. A. W. Hutchinson, and L. C. Kwek, “A solenoidal synthetic field and the non-Abelian Aharonov-Bohm effects in neutral atoms,” *Scientific Reports*, vol. 4, p. 5992, Aug 2014.
- [299] A. Noguchi, Y. Shikano, K. Toyoda, and S. Urabe, “Aharonov-bohm effect in the tunnelling of a quantum rotor in a linear Paul trap,” *Nature Communications*, vol. 5, p. 3868, May 2014.
- [300] L. Duca, T. Li, M. Reitter, I. Bloch, M. Schleier-Smith, and U. Schneider, “An Aharonov-Bohm interferometer for determining Bloch band topology,” *Science*, vol. 347, no. 6219, pp. 288–292, 2015.
- [301] N. Goldman, J. C. Budich, and P. Zoller, “Topological quantum matter with ultracold gases in optical lattices,” *Nature Physics*, vol. 12, pp. 639–645, Jul 2016.
- [302] C. Gross and I. Bloch, “Quantum simulations with ultracold atoms in optical lattices,” *Science*, vol. 357, no. 6355, pp. 995–1001, 2017.
- [303] L. Amico, A. Osterloh, and F. Cataliotti, “Quantum many particle systems in ring-shaped optical lattices,” *Phys. Rev. Lett.*, vol. 95, p. 063201, Aug 2005.
- [304] A. Ramanathan, K. C. Wright, S. R. Muniz, M. Zelan, W. T. Hill, C. J. Lobb, K. Helmerson, W. D. Phillips, and G. K. Campbell, “Superflow in a toroidal Bose-Einstein condensate: An atom circuit with a tunable weak link,” *Phys. Rev. Lett.*, vol. 106, p. 130401, Mar 2011.
- [305] M. V. Berry, “Quantal phase factors accompanying adiabatic changes,” *Proceedings of the Royal Society of London. A. Mathematical and Physical Sciences*, vol. 392, no. 1802, pp. 45–57, 1984.
- [306] B. Juliá-Díaz, D. Dagnino, K. J. Günter, T. Graß, N. Barberán, M. Lewenstein, and J. Dalibard, “Strongly correlated states of a small cold-atom cloud from geometric gauge fields,” *Phys. Rev. A*, vol. 84, p. 053605, Nov 2011.
- [307] B. Juliá-Díaz, T. Graß, N. Barberán, and M. Lewenstein, “Fractional quantum hall states of a few bosonic atoms in geometric gauge fields,” *New Journal of Physics*, vol. 14, p. 055003, may 2012.
- [308] M.-X. Huo, W. Nie, D. A. W. Hutchinson, and L. C. Kwek, “A solenoidal synthetic field and the non-Abelian Aharonov-Bohm effects in neutral atoms,” *Scientific reports*, vol. 4, p. 5992, 2014.
- [309] N. Moiseyev, “Quantum theory of resonances: calculating energies, widths and cross-sections by complex scaling,” *Phys. Rep.*, vol. 302, pp. 212–293, Sept. 1998.
- [310] R. Peierls, “Zur Theorie des Diamagnetismus von Leitungselektronen,” *Zeitschrift für Physik*, vol. 80, pp. 763–791, Nov 1933.
- [311] D. R. Hofstadter, “Energy levels and wave functions of Bloch electrons in rational and irrational magnetic fields,” *Phys. Rev. B*, vol. 14, pp. 2239–2249, Sep 1976.
- [312] M. Olshanii, “Atomic scattering in the presence of an external confinement and a gas of impenetrable bosons,” *Phys. Rev. Lett.*, vol. 81, pp. 938–941, Aug 1998.
- [313] T. Paul, K. Richter, and P. Schlagheck, “Nonlinear resonant transport of Bose-Einstein condensates,” *Phys. Rev. Lett.*, vol. 94, p. 020404, Jan. 2005.
- [314] T. Paul, M. Hartung, K. Richter, and P. Schlagheck, “Nonlinear transport of Bose-Einstein condensates through mesoscopic waveguides,” *Phys. Rev. A*, vol. 76, p. 063605, Dec. 2007.



- [315] E. Strambini, L. Chirulli, V. Giovannetti, F. Taddei, R. Fazio, V. Piazza, and F. Beltram, “Coherent detection of electron dephasing,” *Phys. Rev. Lett.*, vol. 104, p. 170403, Apr 2010.
- [316] H. Sigurdsson, O. Kibis, and I. Shelykh, “Aharonov-Bohm effect induced by circularly polarized light,” *Superlattices and Microstructures*, vol. 87, pp. 149 – 153, 2015. Proceedings of the 16th International Conference on the Physics of Light–Matter Coupling in Nanostructures, PLMCN 2015 (Medellín, Colombia), 3-8 February, 2015.
- [317] S. Cho, B. Dellabetta, R. Zhong, J. Schneeloch, T. Liu, G. Gu, M. J. Gilbert, and N. Mason, “Aharonov–Bohm oscillations in a quasi–ballistic three–dimensional topological insulator nanowire,” *Nature Communications*, vol. 6, p. 7634, Jul 2015.
- [318] S. Russo, J. B. Oostinga, D. Wehenkel, H. B. Heersche, S. S. Sobhani, L. M. K. Vander-sypen, and A. F. Morpurgo, “Observation of Aharonov–Bohm conductance oscillations in a graphene ring,” *Phys. Rev. B*, vol. 77, p. 085413, Feb 2008.
- [319] R. Berkovits and Y. Avishai, “Interacting electrons in disordered potentials: Conductance versus persistent currents,” *Phys. Rev. Lett.*, vol. 76, pp. 291–294, Jan 1996.
- [320] S. Ihnatsenka and I. V. Zozoulenko, “Interacting electrons in the Aharonov–Bohm interferometer,” *Phys. Rev. B*, vol. 77, p. 235304, Jun 2008.
- [321] Y. Komijani, R. Yoshii, and I. Affleck, “Interaction effects in Aharonov–Bohm–Kondo rings,” *Phys. Rev. B*, vol. 88, p. 245104, Dec 2013.
- [322] T. Chakraborty, A. Manaselyan, and M. Barseghyan, “Irregular Aharonov–Bohm effect for interacting electrons in a ZnO quantum ring,” *Journal of Physics: Condensed Matter*, vol. 29, p. 075605, dec 2016.
- [323] T. Haug, H. Heimonen, R. Dumke, L.-C. Kwek, and L. Amico, “Aharonov-Bohm effect in mesoscopic Bose-Einstein condensates,” *Phys. Rev. A*, vol. 100, p. 041601, Oct 2019.
- [324] T. Haug, R. Dumke, L.-C. Kwek, and L. Amico, “Andreev-reflection and Aharonov–Bohm dynamics in atomtronic circuits,” *Quantum Science and Technology*, vol. 4, p. 045001, jul 2019.
- [325] T. Haug, “Quantum transport with cold atoms,” 2020.
- [326] R. Chrétien, J. Rammensee, J. Dujardin, C. Petitjean, and P. Schlagheck, “Al’tshuler-aronov-spivak oscillations of bosonic matter-wave beams in the presence of interaction,” *Phys. Rev. A*, vol. 100, p. 033606, Sep 2019.
- [327] T. Paul, P. Leboeuf, N. Pavloff, K. Richter, and P. Schlagheck, “Nonlinear transport of Bose–Einstein condensates through waveguides with disorder,” *Phys. Rev. A*, vol. 72, p. 063621, Dec. 2005.
- [328] N. Osakabe, T. Matsuda, T. Kawasaki, J. Endo, A. Tonomura, S. Yano, and H. Yamada, “Experimental confirmation of Aharonov–Bohm effect using a toroidal magnetic field confined by a superconductor,” *Phys. Rev. A*, vol. 34, pp. 815–822, Aug 1986.
- [329] I. O. Kulik *JETP*, vol. 5, p. 345, 1967.
- [330] L. Gunther and Y. Imry, “Flux quantization without off–diagonal long range order in a thin hollow cylinder,” *Solid State Communications*, vol. 7, no. 18, pp. 1391 – 1394, 1969.
- [331] M. Büttiker, “Role of quantum coherence in series resistors,” *Phys. Rev. B*, vol. 33, pp. 3020–3026, Mar 1986.

- [332] S. Datta, M. R. Melloch, S. Bandyopadhyay, R. Noren, M. Vaziri, M. Miller, and R. Reifenberger, “Novel interference effects between parallel quantum wells,” *Phys. Rev. Lett.*, vol. 55, pp. 2344–2347, Nov 1985.
- [333] V. Chandrasekhar, M. J. Rooks, S. Wind, and D. E. Prober, “Observation of Aharonov–Bohm electron interference effects with periods  $\frac{h}{e}$  and  $\frac{h}{2e}$  in individual micron-size, normal-metal rings,” *Phys. Rev. Lett.*, vol. 55, pp. 1610–1613, Oct 1985.
- [334] J. M. Gordon, “Quantum phase sensitivity to macroscopic boundaries: Al cylinders and wires,” *Phys. Rev. B*, vol. 30, pp. 6770–6773, Dec 1984.
- [335] B. Pannetier, J. Chaussy, R. Rammal, and P. Gandit, “Magnetic flux quantization in the weak–localization regime of a nonsuperconducting metal,” *Phys. Rev. Lett.*, vol. 53, pp. 718–721, Aug 1984.
- [336] B. Pannetier, J. Chaussy, R. Rammal, and P. Gandit, “First observation of Al’tshuler–Aronov–Spivak effect in gold and copper,” *Phys. Rev. B*, vol. 31, pp. 3209–3211, Mar 1985.
- [337] B. Douçot and R. Rammal, “Interference effects and magnetoresistance oscillations in normal–metal networks. 2. periodicity of the probability distribution,” *J. Phys. France*, vol. 48, no. 6, pp. 941–956, 1987.
- [338] D. Weinmann, A. Müller-Groeling, J.-L. Pichard, and K. Frahm, “ $h/2e$  oscillations for correlated electron pairs in disordered mesoscopic rings,” *Phys. Rev. Lett.*, vol. 75, pp. 1598–1601, Aug 1995.
- [339] M. Murat, Y. Gefen, and Y. Imry, “Ensemble and temperature averaging of quantum oscillations in normal–metal rings,” *Phys. Rev. B*, vol. 34, pp. 659–668, Jul 1986.
- [340] D. Takai and K. Ohta, “Structure of  $h/2e$  oscillations in a one–dimensional mesoscopic ring,” *Physics Letters A*, vol. 189, no. 3, pp. 211 – 217, 1994.
- [341] I. A. Shelykh, N. T. Bagraev, N. G. Galkin, and L. E. Klyachkin, “Interplay of  $h/e$  and  $h/2e$  oscillations in gate–controlled Aharonov–Bohm rings,” *Phys. Rev. B*, vol. 71, p. 113311, Mar 2005.
- [342] S. Kawabata and K. Nakamura, “ $h/2e$  oscillations and quantum chaos in ballistic Aharonov–Bohm billiards,” *Phys. Rev. B*, vol. 57, pp. 6282–6285, Mar 1998.
- [343] L. C. Mur, C. J. P. M. Harmans, and W. G. van der Wiel, “Competition between  $h/e$  and  $h/2e$  oscillations in a semiconductor aharonov–bohm interferometer,” *New Journal of Physics*, vol. 10, p. 073031, jul 2008.
- [344] J. Wei, P. Cadden-Zimansky, and V. Chandrasekhar, “Observation of large  $h/2e$  and  $h/4e$  oscillations in a proximity dc superconducting quantum interference device,” *Applied Physics Letters*, vol. 92, no. 10, p. 102502, 2008.
- [345] T. Ihn, “Oscillations in the ribbons,” *Nature Materials*, vol. 9, pp. 187–188, Mar 2010.
- [346] H. Li, T. Kottos, and B. Shapiro, “Half–period Aharonov–Bohm oscillations in disordered rotating optical ring cavities,” *Phys. Rev. A*, vol. 94, p. 031801, Sep 2016.
- [347] T. Kottos and U. Smilansky, “Quantum chaos on graphs,” *Phys. Rev. Lett.*, vol. 79, pp. 4794–4797, Dec 1997.
- [348] T. Kottos and U. Smilansky, “Periodic orbit theory and spectral statistics for quantum graphs,” *Annals of Physics*, vol. 274, no. 1, pp. 76 – 124, 1999.
- [349] T. Kottos and U. Smilansky, “Chaotic scattering on graphs,” *Phys. Rev. Lett.*, vol. 85, pp. 968–971, Jul 2000.

- [350] T. Paul, M. Albert, P. Schlagheck, P. Leboeuf, and N. Pavloff, “Anderson localization of a weakly interacting one-dimensional Bose gas,” *Phys. Rev. A*, vol. 80, p. 033615, Sep 2009.
- [351] W. Lee, “Aharonov–bohm oscillations in the conductance of a disordered mesoscopic ring with superconducting inclusions,” *Solid State Communications*, vol. 109, no. 4, pp. 257–262, 1998.
- [352] R. Chrétien and P. Schlagheck, “Inversion of coherent backscattering with interacting Bose–Einstein condensates in two-dimensional disorder: A truncated Wigner approach,” *Phys. Rev. A*, vol. 103, p. 033319, Mar 2021.
- [353] I. Georgescu, “Rubidium round-the-clock,” *Nature Chemistry*, vol. 7, pp. 1034–1034, Dec 2015.
- [354] C. D’Errico, M. Zaccanti, M. Fattori, G. Roati, M. Inguscio, G. Modugno, and A. Simoni, “Feshbach resonances in ultracold  $^{39}\text{K}$ ,” *New Journal of Physics*, vol. 9, pp. 223–223, jul 2007.
- [355] A. Marte, T. Volz, J. Schuster, S. Dürr, G. Rempe, E. G. M. van Kempen, and B. J. Verhaar, “Feshbach resonances in rubidium 87: Precision measurement and analysis,” *Phys. Rev. Lett.*, vol. 89, p. 283202, Dec 2002.
- [356] J. Rammensee, “Semiclassical treatment of interference phenomena in bosonic quantum many-body systems,” September 2019.
- [357] J. E. Lye, L. Fallani, M. Modugno, D. S. Wiersma, C. Fort, and M. Inguscio, “Bose–Einstein condensate in a random potential,” *Phys. Rev. Lett.*, vol. 95, p. 070401, Aug 2005.
- [358] C. Fort, L. Fallani, V. Guarrera, J. E. Lye, M. Modugno, D. S. Wiersma, and M. Inguscio, “Effect of optical disorder and single defects on the expansion of a Bose–Einstein condensate in a one-dimensional waveguide,” *Phys. Rev. Lett.*, vol. 95, p. 170410, Oct 2005.
- [359] T. Schulte, S. Drenkelforth, J. Kruse, W. Ertmer, J. Arlt, K. Sacha, J. Zakrzewski, and M. Lewenstein, “Routes towards Anderson–like localization of Bose–Einstein condensates in disordered optical lattices,” *Phys. Rev. Lett.*, vol. 95, Oct 2005.
- [360] D. Clément, A. F. Varón, M. Hugbart, J. A. Retter, P. Bouyer, L. Sanchez-Palencia, D. M. Gangardt, G. V. Shlyapnikov, and A. Aspect, “Suppression of transport of an interacting elongated Bose–Einstein condensate in a random potential,” *Phys. Rev. Lett.*, vol. 95, p. 170409, Oct 2005.
- [361] A. Couvert, M. Jeppesen, T. Kawalec, G. Reinaudi, R. Mathevet, and D. Guéry-Odelin, “A quasi-monomode guided atom laser from an all-optical Bose–Einstein condensate,” *Europhys. Lett.*, vol. 83, p. 50001, Sept. 2008.
- [362] G. L. Gattobigio, A. Couvert, B. Georgeot, and D. Guéry-Odelin, “Exploring classically chaotic potentials with a matter wave quantum probe,” *Phys. Rev. Lett.*, vol. 107, p. 254104, Dec. 2011.
- [363] F. Vermersch, C. M. Fabre, P. Cheiney, G. L. Gattobigio, R. Mathevet, and D. Guéry-Odelin, “Guided–atom laser: Transverse mode quality and longitudinal momentum distribution,” *Phys. Rev. A*, vol. 84, p. 043618, Oct 2011.
- [364] T. Hartmann, *Transport of Bose–Einstein condensates through two dimensional cavities*. PhD thesis, Universität Regensburg, 2014.

- [365] T. Paul, M. Albert, P. Schlagheck, P. Leboeuf, and N. Pavloff, “Anderson localization of a weakly interacting one-dimensional Bose gas,” *Phys. Rev. A*, vol. 80, p. 033615, Sept. 2009.
- [366] N. Moiseyev and L. S. Cederbaum, “Resonance solutions of the nonlinear Schrödinger equation: Tunneling lifetime and fragmentation of trapped condensates,” *Phys. Rev. A*, vol. 72, p. 33605, Sept. 2005.
- [367] M. Rontani, G. Eriksson, S. Åberg, and S. M. Reimann, “On the renormalization of contact interactions for the configuration-interaction method in two-dimensions,” *J. Phys. B: At. Mol. Opt. Phys.*, vol. 50, p. 065301, 2017.
- [368] R. C. Kuhn, O. Sigwarth, C. Miniatura, D. Delande, and C. A. Müller, “Coherent matter wave transport in speckle potentials,” *New Journal of Physics*, vol. 9, pp. 161–161, jun 2007.
- [369] I. Freund, M. Rosenbluh, R. Berkovits, and M. Kaveh, “Coherent backscattering of light in a quasi-two-dimensional system,” *Phys. Rev. Lett.*, vol. 61, pp. 1214–1217, Sep 1988.
- [370] H. Van de Hulst, *Multiple Light Scattering*. Academic Press, 1980.
- [371] M. Hartung, *Transport and Coherent Backscattering of Bose-Einstein Condensates in Mesoscopic Systems*. PhD thesis, Universität Regensburg, 2009.
- [372] R. G. Scott and D. A. W. Hutchinson, “Incoherence of Bose-Einstein condensates at supersonic speeds due to quantum noise,” *Phys. Rev. A*, vol. 78, p. 063614, Dec 2008.
- [373] K. W. Wilsmann, L. H. Ymai, A. P. Tonel, J. Links, and A. Foerster, “Control of tunneling in an atomtronic switching device,” *Communications Physics*, vol. 1, p. 91, Dec 2018.
- [374] H.-D. Meyer, “Theory of the Liapunov exponents of Hamiltonian systems and a numerical study on the transition from regular to irregular classical motion,” *The Journal of Chemical Physics*, vol. 84, no. 6, pp. 3147–3161, 1986.
- [375] R. E. Wengert, “A simple automatic derivative evaluation program,” *Commun. ACM*, vol. 7, p. 463–464, Aug. 1964.
- [376] D. Barton, I. M. Willers, and R. V. M. Zahar, “Taylor series methods for ordinary differential equations — An evaluation,” in *Mathematical Software* (J. Rice, ed.), pp. 369–390, New York: Academic Press, 1971.
- [377] M. Bartholomew-Biggs, S. Brown, B. Christianson, and L. Dixon, “Automatic differentiation of algorithms,” *Journal of Computational and Applied Mathematics*, vol. 124, no. 1, pp. 171 – 190, 2000. Numerical Analysis 2000. Vol. IV: Optimization and Non-linear Equations.
- [378] M. Bücker, G. Corliss, P. Hovland, U. Naumann, and B. Norris, *Automatic Differentiation: Applications, Theory, and Implementations (Lecture Notes in Computational Science and Engineering)*. Berlin, Heidelberg: Springer-Verlag, 2006.
- [379] U. Naumann, *The Art of Differentiating Computer Programs: An Introduction to Algorithmic Differentiation*. USA: Society for Industrial and Applied Mathematics, 2012.
- [380] C. Aslangul, *Mathématiques pour physiciens*. École normale supérieure, 2012.
- [381] R. Feynman and A. Hibbs, *Quantum Mechanics and Path Integrals*. McGraw-Hill, New York, 1965.

- [382] E. Economou, *Green's functions in Quantum Physics*. Berlin: Springer, 1983.
- [383] S. Weinberg, *The Quantum Theory of Fields*, vol. 1. Cambridge University Press, 1995.
- [384] M. E. Peskin and D. V. Schroeder, *An Introduction to Quantum Field Theory*. Westview Press, 1995.
- [385] H. Bruus and K. Flensberg, *Introduction to many-body quantum theory in condensed matter physics*. Oxford Graduate Press, 2004.
- [386] M. Cottam and Z. Haghshenasfard, *Many-body theory of condensed matter systems*. Cambridge University Press, 2020.